MONTE CARLO SIMULATIONS OF CONFINED NEMATIC SYSTEMS

CHARLIE WAND

PHD

THE UNIVERSITY OF YORK

DEPARTMENT OF CHEMISTRY

SEPTEMBER 2013

ABSTRACT

In this thesis, a systematic Monte Carlo simulation study of confined nematic and cholesteric systems is carried out. A simple off-lattice model is developed to explore a range of confined systems. Double emulsion nematic shells are investigated with planar anchoring which is then extended to solid particles of different geometries with nematic coatings before progressing to single and *n*-fold toroidal droplets.

For shells and coatings with planar anchoring the total topological charge on both surfaces must be +2. A bipolar structure is found in thick shells and four *s*=+1/2 defects are found for thin nematic shells. A metastable defect configuration comprising of two *s*=+1/2 and one *s*=+1 defects is occasionally observed for intermediate thicknesses. With the addition of chirality, a transition to a twisted bipolar director configuration is observed at all thicknesses.

A single toroidal droplet with planar anchoring has a defect free ground state. Previous work has predicted the presence of a twisted director configuration ground state. The relative stabilities of the twisted and untwisted configurations are investigated here. It was found that, for all the systems investigated, the twisted director configuration is only stable for a cholesteric torus. For multiple tori system, with each additional handle the total topological charge on the surface decreases by 2. In a non-chiral nematic system the constraint on the topological charge on the surface is fulfilled by the required number of *s*=-1 defects located at either the innermost surface of a handle or the join between two tori. With increasing chirality, the *s*=-1 defects detach from the surface and migrate to form *s*=-1/2 disclination lines through the cholesteric. In handled droplets with homeotropic anchoring, two *s*=+1/2 disclination lines are found that, with the addition of chirality form a helical structure around the tube.

TABLE OF CONTENTS

TABLE OF TABLES

TABLE OF FIGURES

ACKNOWLEDGEMENTS

I would like to thank my supervisor, Dr. Martin Bates for all his guidance and input in my research without which I could not have managed to produce this work. I would also like to thank Dr. Martin Walker for all his support and help with coming to grips with Linux and always being ready for a cup of tea. My thanks also go to the other members, both past and present, of the advanced materials group for their support.

Finally I would like to thank my friends and family, in particular wonderful future wife, Harri, whose ongoing support and encouragement I have relied on.

DECLARATION

I hereby declare that I am the sole author of the work presented in this thesis and that no work from this thesis has been published previously, or has been accepted for publication. All sources are explicitly acknowledged via the references that accompany the text.

Charlie Wand

September 2013

1 INTRODUCTION

1.1 LIQUID CRYSTAL MESOPHASES

The term liquid crystal is used to describe a state of matter that flows like a liquid but possesses some degree of orientational order; it covers a large range of mesophases which can be formed by a wide variety of materials. Molecules that form liquid-crystalline phases, known as mesogens, can be broadly divided into two categories; thermotropic and lyotropic liquid crystals. In this work, we focus on thermotropic liquid crystals whose phase behaviour is dependent on the temperature of the system[1] and tend to be water immiscible. Indeed, the nematic shells that occur in double emulsion droplets and other systems that are studied in this thesis often depend on their immiscibility with water.

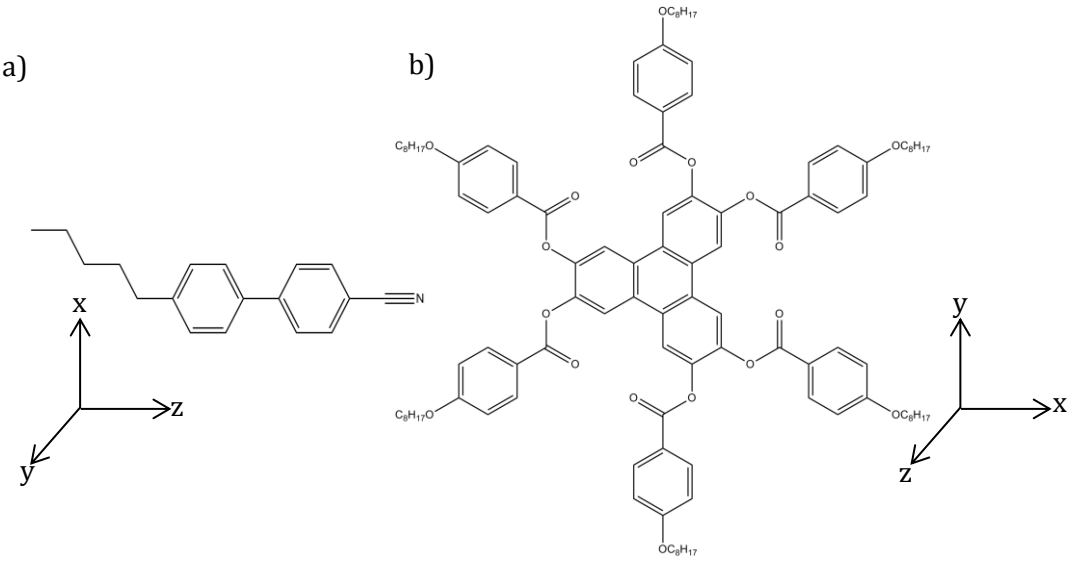

Figure 1.1.1 Examples of common a) calamitic and b) discotic molecules

A liquid crystal phase arises due to anisotropic interactions between the molecules which can include intermolecular interactions such as π-stacking and hydrogen bonding, however the most common reason that molecules form a liquid crystal phase is thought to be shape anisotropy. The simplest case of shape anisotropy is when one molecular dimension differs from the other two, *e.g.* $x = y \neq z$. When $x = y < z$, the molecule is rod shaped, or

calamitic (Figure 1.1.1a) and when $x = y > z$, the molecule is disc shaped or discotic (Figure 1.1.1b). Other, more complicated molecular shapes also form liquid crystalline phases including board shaped molecules ($x \neq y \neq z$) and bent-core or banana-shaped molecules[2].

In this thesis the two simplest mesophases formed by calamitic liquid crystals are focused on, the nematic phase and its chiral analogue, the chiral nematic phases. Calamitic liquid crystals also form other phases, such as the smectic phase that include positional order where the molecules pack into two dimensional layers. Similarly, discotic molecules form columnar mesophases in which the molecules stack in one-dimensional columns.

1.1.1 *THE NEMATIC MESOPHASE*

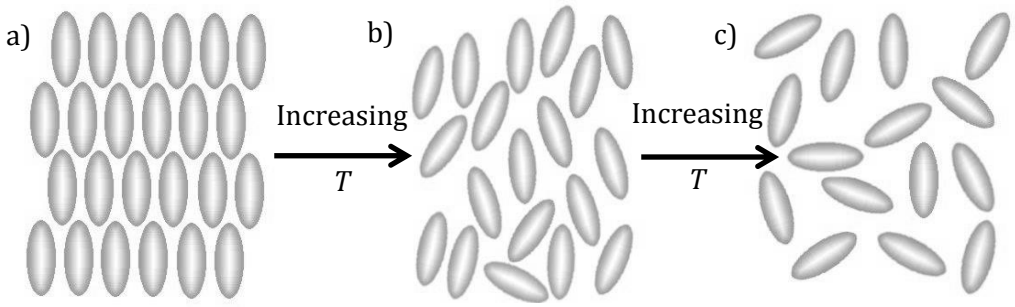

Figure 1.1.2 A schematic showing the phase progression with increasing temperature from a) a solid crystal to b) a nematic liquid crystal and c) an isotropic liquid

In a nematic mesophase, there is local orientational order but no local positional order, meaning that the molecules are free to diffuse through the phase; they tend to point in a single direction (Figure 1.1.2). The molecules are free to rotate about both their long and short molecular axes, although the relaxation time for rotations about the short axis is much longer ($\approx 10^5 - 10^6$ times per second) than the relaxation time for rotations about the long molecular axis ($\approx 10^{11} - 10^{12}$ times per second)[3].

1.1.1.1 Order in Nematics

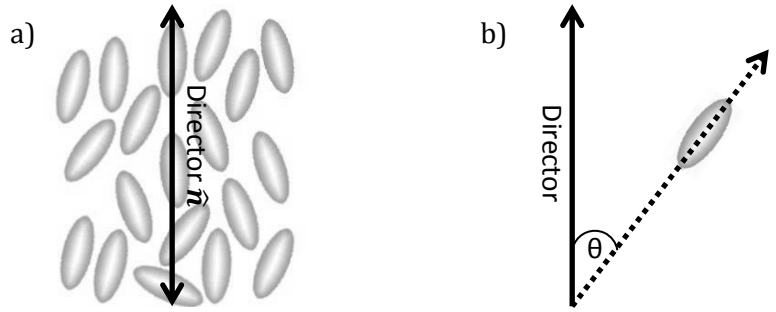

Figure 1.1.3 Schematics of a) the director of a nematic phase and b) the angle between the local director and the long axis of the molecule.

The direction that the long molecular axis of the molecule statistically favours is known as the director and is usually represented by the unit vector $\hat{\boldsymbol{n}}$, where $\hat{\boldsymbol{n}} = -\hat{\boldsymbol{n}}$ as the nematic phase is non-polar (Figure 1.1.3a). The degree of orientational order present with respect to a given axis, *e.g.* the director in a nematic phases is quantified by the order parameter,

$$S = \langle P_2(\cos\theta)\rangle = \langle \tfrac{3}{2}\cos^2\theta - \tfrac{1}{2}\rangle \qquad (1.1.1)$$

where θ is the angle between the long axis of the molecule and the local director (Figure 1.1.3b). The second Legendre polynomial is used rather than the first because the director is a headless vector and the quadratic term in the second Legendre polynomial is independent on the sign of θ. The first Legendre polynomial,

$$\langle P_1(\cos\theta)\rangle = \langle\cos\theta\rangle \qquad (1.1.2)$$

is a measure of polarity of the system and is equal to zero for a nematic phase. Other even terms of the Legendre expansion can also be employed and the fourth and sixth Legendre polynomials are;

$$P_4(x) = \tfrac{1}{8}(35x^4 - 30x^2 + 3) \qquad (1.1.3)$$

$$P_6(x) = \tfrac{1}{16}(231x^6 - 315x^4 + 105x^2 - 5) \qquad (1.1.4)$$

where $x = \cos\theta$ and are often used to measure the amount of order in mesophases as the Legendre polynomials, P_L, are part of an infinite sum in the expansion of the orientational distribution which gives the probability of finding a molecule at the angle θ to the director.

The order parameter can be measured from a macroscopic quantity, *i.e.* optical birefringence or measured using a wide range of analytical techniques including nuclear magnetic resonance[4] or Raman scattering[5].

1.1.1.2 Elasticity in Nematics

Due to the fluid nature of the nematic phase, it can be deformed which increases the energy per unit volume of the system from a non-deformed state by

$$\begin{aligned} F_V = {} & \tfrac{1}{2}K_1[\nabla \cdot \hat{\boldsymbol{n}}]^2 + \tfrac{1}{2}K_2[\hat{\boldsymbol{n}} \cdot (\boldsymbol{\nabla} \times \hat{\boldsymbol{n}})]^2 + \tfrac{1}{2}K_3|\hat{\boldsymbol{n}} \times (\boldsymbol{\nabla} \times \hat{\boldsymbol{n}})|^2 \\ & - (K_2 + K_{24})[\boldsymbol{\nabla} \cdot (\hat{\boldsymbol{n}}\boldsymbol{\nabla} \cdot \hat{\boldsymbol{n}} + \hat{\boldsymbol{n}} \times \boldsymbol{\nabla} \times \hat{\boldsymbol{n}})] \\ & + K_{13}[\boldsymbol{\nabla} \cdot (\hat{\boldsymbol{n}}\boldsymbol{\nabla} \cdot \hat{\boldsymbol{n}})] \end{aligned} \qquad (1.1.5)$$

which is known as the Frank elastic energy[6] and $\hat{\boldsymbol{n}}$ is the director of unit length and ∇ is the Laplace operator, $\nabla = \hat{\boldsymbol{x}}\frac{\partial}{\partial x} + \hat{\boldsymbol{y}}\frac{\partial}{\partial y} + \hat{\boldsymbol{z}}\frac{\partial}{\partial z}$. There are three types of bulk-like distortions and two surface-like distortions. The three bulk-like deformations are the splay, twist and the bend, measured using elastic constants K_1, K_2 and K_3 respectively (Figure 1.1.4) and the two surface-like distortions are K_{24} and K_{13} or the saddle-splay and splay-bend. The surface-like terms in (1.1.5) are often ignored in bulk systems as the contribution to the total energy for the surface is much smaller than that of the bulk.

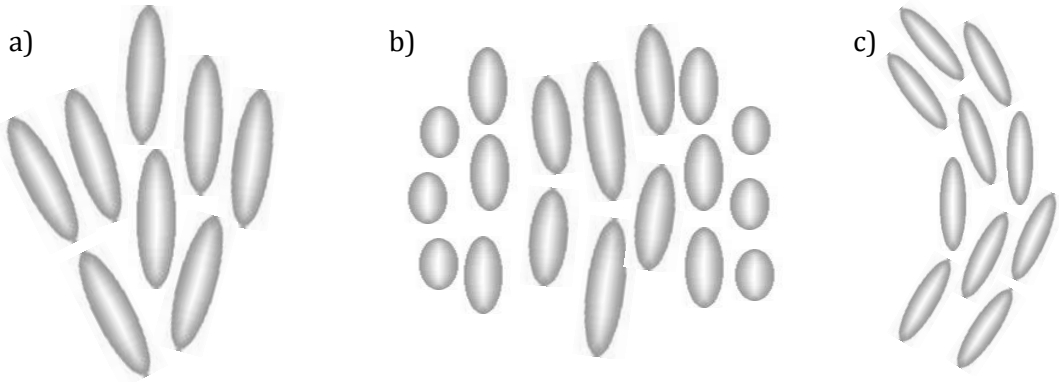

Figure 1.1.4 A schematic representation of a) the splay, b) the twist and c) the bend deformations

The elastic constants decrease with increasing temperature. At T_{N-I} the three bulk-like elastic constants decompose to one elastic constant. For a common mesogen, 5CB (Figure 1.1.1a) when 18 ºC below T_{N-I}, $K_1 = 7.8 \times 10^{-12}$ N, $K_2 = 4.8 \times 10^{-12}$ N and $K_3 = 11.2 \times 10^{-12}$ N which decrease to $K_1 = 3.6 \times 10^{-12}$ N, $K_2 = 2.4 \times 10^{-12}$ N and $K_3 = 4.3 \times 10^{-12}$ N at 2 ºC below T_{N-I} [7]. Note that the magnitudes of K_1, K_2 and K_3 are similar which often leads to the one elastic constant approach in theoretical calculations where $K_1 = K_2 = K_3 = K$.

1.1.2 *Chiral Systems*

1.1.1.3 The Chiral Nematic Phase

With the introduction of chirality into a nematic, a helical twist perpendicular to the director is introduced and the symmetry of the phase is reduced from $D_{\infty h}$ to D_{∞} (Figure 1.1.5). The chiral nematic phase is also known as a cholesteric phase as historically the first chiral nematic was seen in derivatives of cholesterol[1].

A chiral nematic phase can be formed by either a chiral mesogen or doping a non-chiral nematic phase with a small amount of a chiral dopant. The pitch length of a chiral nematic is defined as the length for the director to rotate by 360^{o}, which decreases with increasing concentration of the chiral dopant. In general, the pitch length of a system decreases with increasing temperature[8] which has many applications in thermochromic devices.

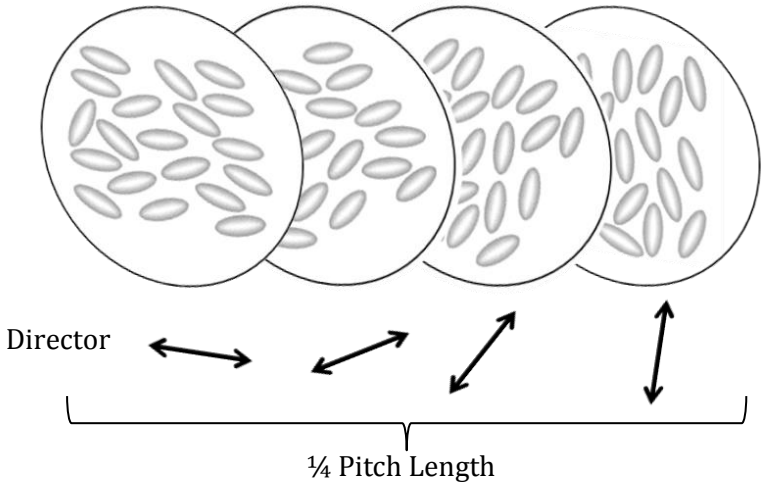

Figure 1.1.5 A schematic of a chiral nematic phase showing a rotation of a quarter of a pitch length

Whilst the pitch length of a chiral nematic is heavily dependent on the both the composition of the bulk and the temperature, the pitch length tends to be similar to the wavelength of visible light (400-700nm)[9]. The presence of the inherent helix with a pitch length similar to that of visible light has been widely used for display purposes[10].

1.1.1.4 Blue phases

Blue phases are examples of a frustrated phase. Blue phases referred to in this thesis are known as cholesteric blue phases as they are found between a chiral nematic and an isotropic phase. Smectic blue phases also exist but are not considered here. Blue phases consist of double twist cylinders (Figure 1.1.6a) which pack together in one of three ways to form distinct blue phases (BP). In BPI the cylinders pack in a face centred lattice and in BPII as a simple cubic lattice (Figure 1.1.6b). The cubic arrays cannot completely fill space and

defects are formed where three double twist cylinders meet (Figure 1.1.6c) in a cubic array. The third blue phase, BPIII, the packing structure of the double twist cylinders is not known and it possesses the same symmetry as the isotropic phase[11].

The temperature range that a blue phase exists over is very small, between 0.5-2°C and research to stabilise and increase the temperature range in which blue phases occur is on-

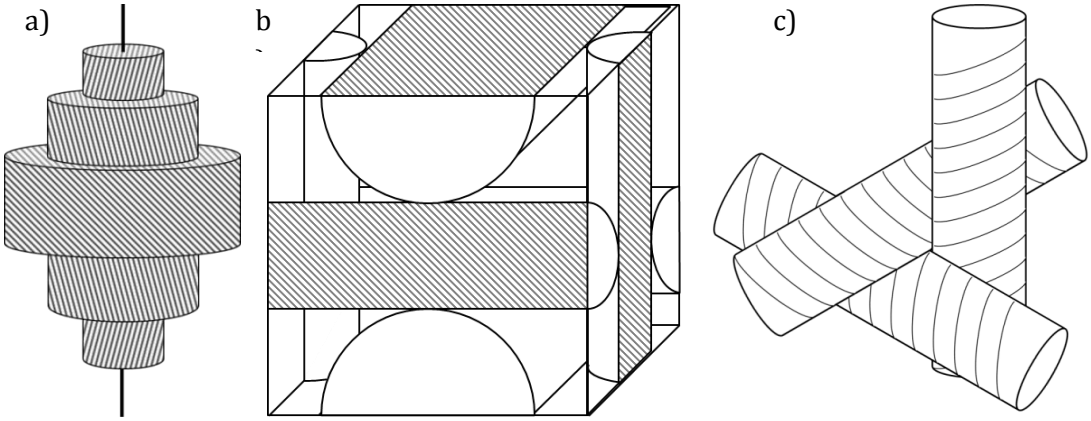

Figure 1.1.6 Schematics of a) a blue phase double helix, b) the packing of double helix cylinders in BPII and c) a defect between three double helix cylinders

going and polymer networks[12] have been employed to stabilize the cubic lattice as well as the fabrication of new exotic molecules that form a blue phase over a wide temperature range[13].

Blue phases are of technological interest as the presence of a cubic array of defects means that a photonic crystal[14] (see section 1.2.4) is formed on the with a selective wavelength similar to that of visible light, indeed blue phases got their name as early examples appeared blue when in thin films[15].

1.1.3 *DEFECTS IN LIQUID CRYSTALS*

Due to the fluid nature inherent in a nematic, areas where the director is undefined occur due to frustration between opposing regions of order. These isotropic regions where the order parameter is approximately zero are known as defects. Defects can be either point defects (zero dimensional), disinclination lines (one dimensional) or sheets/planes (two dimensional). Sheet defects are considered unstable and not discussed here[16]. The geometry of the system may impose the presence of defects in the lowest energy ground state of the system, as in the nematic shells formed in a double emulsion investigated in this thesis. Additional defects may also be formed due to the kinetics of the transition from the isotropic to the nematic phase and may or may not remain present when the system has reached equilibrium.

Both disclination lines and point defects can be classified by the amount that the director rotates on circling the defect core in a clockwise rotation. The strength (s) of a point defect is measured by the angle at which the director rotates about it, or $2s\pi$. For example, if the director rotates clockwise by 360 degrees, it has strength +1, whereas if the director rotates by 180 degrees anti-clockwise, it has strength -1/2 (Figure 1.1.7).

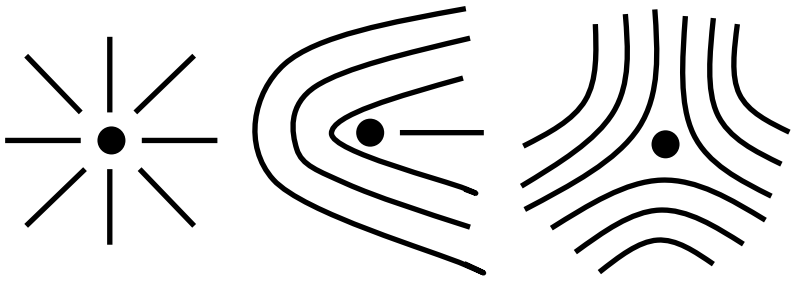

s = +1 s = +1/2 s =-1/2

Figure 1.1.7 Defects of varying strengths around an axial defect, viewed down the defect

Due to the distortion in the director field, the presence of defects increases the energy of the system with respect to a defect free state. The free energy per unit length for an axial disclination line being proportional to s^2[1]. For example, a disclination line with s=+1 is unstable with respect to two s=+1/2 disclination lines. For a s=+1 disclination of length L the energy is proportional to L, however, for two s=+1/2 the energy is proportional $L/2$. Defects of the same sign repel each other, minimising the elastic energy of the system and defects of opposing signs attract one another and annihilate on contact, reducing the energy of the system.

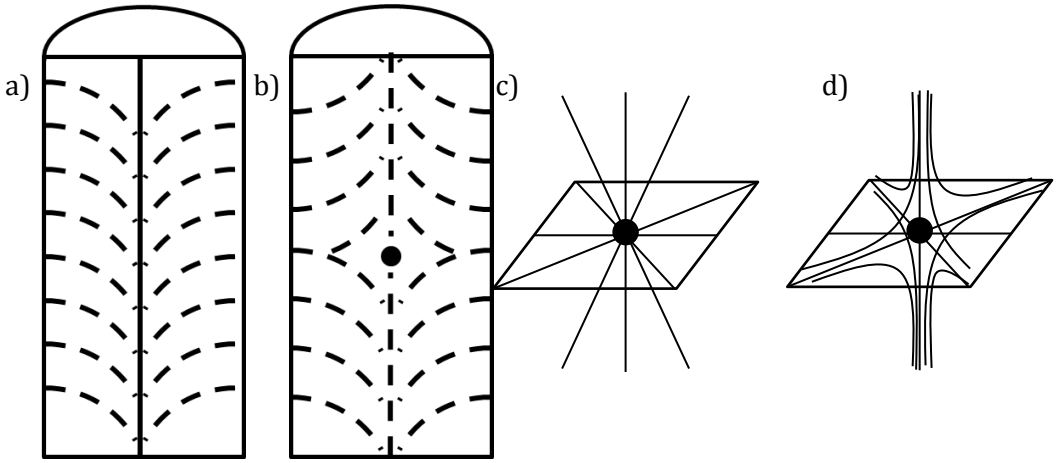

Figure 1.1.8 a) and b) show a cross section of a nematic in a capillary with homeotropic anchoring with a s=+1 disclination line and a s=+1 point defect that has escaped into the third dimension respectively. c) and d) show a radial and hyperbolic hedgehog.

Point defects can be thought of as disclinations that have escaped into the third dimension and, whilst are uncommon in a bulk system can be found in confined systems and at surfaces. A classic example of a confined system in which a defect can escape into the third dimension is of a nematic in a capillary tube with strong homeotropic anchoring. In this case due to the boundary conditions imposed by the surface, a s=+1 axial disclination line can form in the centre of the tube (Figure 1.1.8a). A s=+1 point defect that has escaped into the third dimension (Figure 1.1.8b) may be formed instead in order to decrease the region of disorder and minimise the energy of the system.

Only defects with a strength of ± 1 have been seen experimentally as escaped structures. These defects are also known as hedgehog defects[17] and can be found either on the surface or in the bulk nematic. There are two distinct hedgehog defects, the radial hedgehog and the hyperbolic hedgehog corresponding to a *s*=+1 and *s*=-1 defect respectively (Figure 1.1.8c and d).

Related to hedgehog defects are boojums, a term first coined by Mermin taken from a Lewis Carroll poem[18]. A boojum is a pair of half-hedgehog type defects located at the surface (*e.g.* Figure 1.2.2a). and unlike hedgehog defects, a boojum cannot be found in the bulk.

1.2 CONFINEMENT OF NEMATIC AND CHIRAL NEMATIC MESOPHASES

1.2.1 *MOLECULAR ALIGNMENT AT SURFACES*

Due to the inherent anisotropic nature of molecules that form a nematic or chiral nematic phase, when confined there are three distinct ways the molecules can orient with respect to the interface, either parallel, perpendicularly or at a tilted angle. In this thesis, systems with planar or perpendicular anchoring are considered. The interface can be between a nematic and a solid (*e.g.* between two glass slides), the air-nematic interface (*e.g.* a free standing film) or between the nematic phase and an immiscible liquid, as shown in Figure 1.2.1.

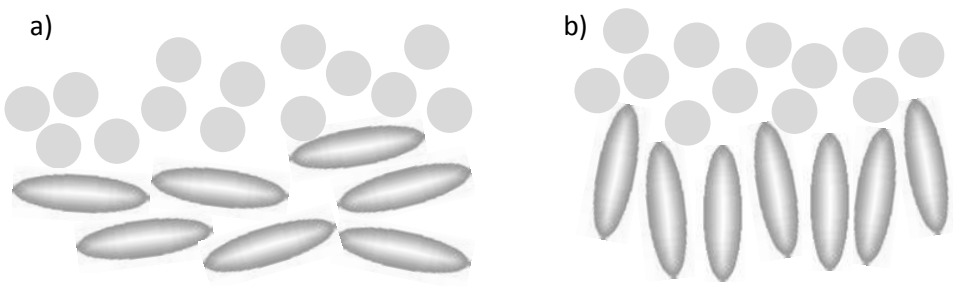

Figure 1.2.1 Schematic of nematic (ellipsoids) - water (circles) interface showing a) planar anchoring and b) homeotropic anchoring

When the long molecular axis of the mesogens is at right angles to the surface normal, the anchoring type is described as tangential or planar anchoring (Figure 1.2.1a). If there is no preferred orientation of the mesogens on the surface it is known as planar degenerate anchoring. When the long molecular axis is parallel to the surface normal the anchoring type is described as normal or homeotropic anchoring (Figure 1.2.1b). The type of anchoring favoured can be controlled by the mesogens used or by the addition of a surfactant[19] or ions into the aqueous solution to promote one type of anchoring over the other. For example, in the aqueous phase nematic droplets of 5CB favour planar anchoring. The anchoring at the surface of the nematic droplets may be switched to homeotropic anchoring by the addition of iodides or thiocyanate anions into the aqueous solvent[20].

The diagrams shown in Figure 1.2.1 and the anchoring discussed previously is known as strong anchoring, that is all the molecules lie in the preferred orientation with respect to the surface normal. Weak anchoring may occur when the interactions at the surface are insufficient to drive all the molecules at the surface to lie in the preferred orientation. The potential interactions used throughout this work is at the strong anchoring limit, that is all the mesogens are parallel to the surface in systems with planar anchoring or perpendicular to the surface in systems with homeotropic anchoring.

1.2.2 *NEMATIC AND CHIRAL NEMATIC DROPLETS*

The most simple confined nematic system is that of a sphere or single droplet. Much work has been done on nematic droplets both experimentally and theoretically with both planar and homeotropic anchoring. Nematic droplets have been made using a wide range of techniques including templating[21], photopolymerisation[22] and micro fluidics[23]. One of the most challenging aspects of fabricating nematic spheres is controlling the size distribution of the sample as for many applications a monodisperse system is desired.

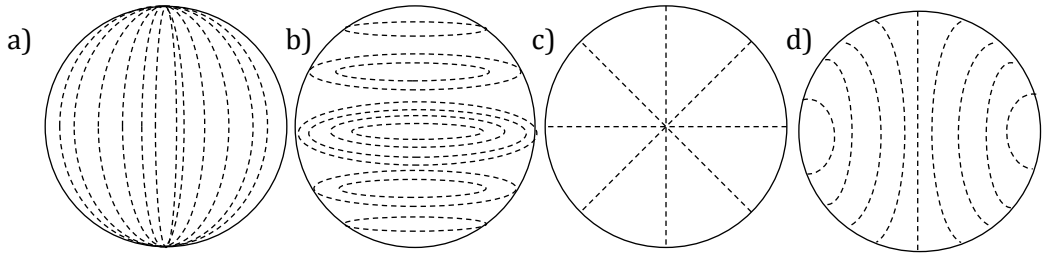

Figure 1.2.2 Four typical director configurations found in nematic droplets. a) The bipolar and b) axial director configurations are found in droplets with planar anchoring whereas c) the radial and d) equatorial director configurations are found for droplets with homeotropic anchoring.

There are four typical director configurations for nematic droplets (Figure 1.2.2), two found with homeotropic anchoring and two found with planar anchoring. The director configuration formed depends on both the strength of the surface anchoring and the ratio of the elastic constants[24].

For nematic droplets with planar anchoring, the total topological charge on the surface is equal to +2 in all cases. It is not geometrically possible to coat a sphere with rods without forming defects with a total topological charge of +2, this is known as the Poincaré-Hopf theorem[25].

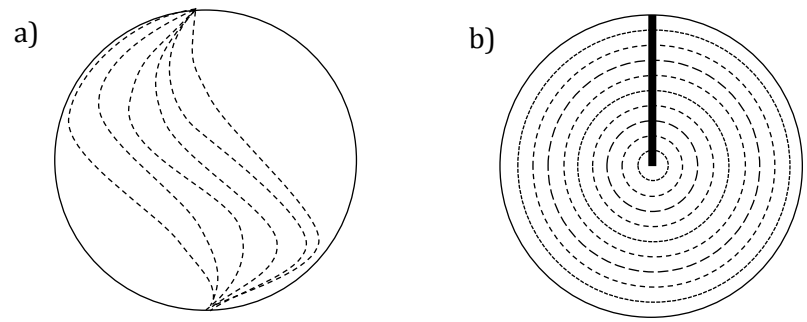

Figure 1.2.3 A schematic representation of two possible director configurations for a of nematic droplet with planar anchoring showing a) the twisted bipolar director configuration and b) the Frank-Pryce structure

Chiral nematic droplets with planar anchoring have also undergone much research and the director configuration was found to be highly dependent on both the ratio of the pitch length and the diameter of the droplet[26]. In systems where the pitch length is much longer than the droplet diameter, a twisted bipolar director configuration is observed (Figure 1.2.3), whereas for highly chiral systems where the pitch length is smaller than the droplet diameter a Frank-Pryce defect structure is found (Figure 1.2.3). A Frank-Pryce defect structure is characterised as a *s*=+2 disclination line attached to a central hedgehog defect.

1.2.3 *NEMATIC SHELLS*

A slightly more complex case than a nematic droplet is when either a water droplet or spherical colloidal particle is encased in a nematic droplet producing a nematic shell. The presence of four =+1/2 defects was first proposed by Lubensky and Prost[27], however, recent interest into spherical shells has been sparked by Nelson's[28] seminal paper predicting that a tetrahedral defect arrangement may be seen for nematic shells with planar anchoring which in turn may be employed to form tetrahedral arrays of the shells.

It has been found that if the radius of the nematic droplet is much larger than the radius of the water droplet, the system acts in a similar way to a pure nematic droplet without the inclusion of the inner water droplet (Figure 1.2.4b), however in thin nematic shells a rich

variety of director configurations can be seen, including four *s*=+1/2 defects in a tetrahedral arrangement as shown in Figure 1.2.4a. Nematic shells have been made experimentally[29] *via* microfluidics in which the diameter of the nematic shells are approximately 200 microns with the shell thicknesses ranging from approximately one hundred to ten microns.

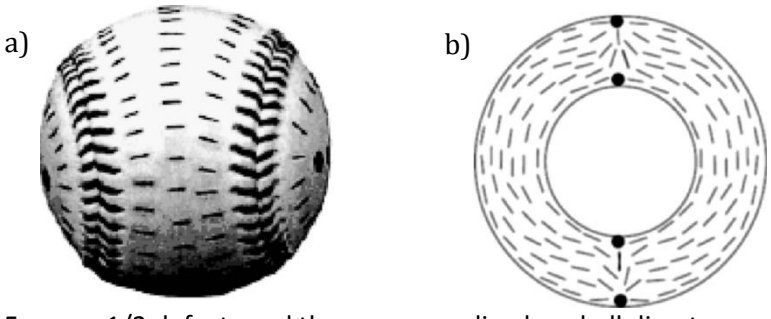

Figure 1.2.4 a) Four *s*=+1/2 defects and the corresponding baseball director configuration found for thin nematic shells and b) a bipolar defect configuration found for thick nematic shells. Taken from Vitelli and Nelson[30]

In nematic shells with homeotropic anchoring, it is possible to form a defect-free ground state, similar to the radial configuration of a nematic droplet (Figure 1.2.5) with the inner surface taking the place of the central hedgehog defect.

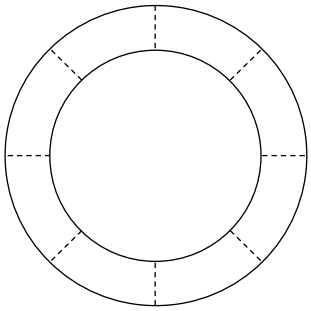

Figure 1.2.5 Schematic of a nematic shell with homeotropic anchoring

In nematic shells with planar anchoring, as stated earlier, the total topological charge on the surface of a sphere must be equal to +2. In a nematic shell, there are two spherical surfaces, the inner surface and the outer surface both of which must obey the constraint

on the total topological charge. In equilibrated systems, three defect configurations were seen consisting of; 1) four $s = +\frac{1}{2}$ defects, 2) two $s = +\frac{1}{2}$ and one $s = +1$ or 3) two $s = +1$ defects. In nematic shells that have not yet reached equilibrium, a larger number of defects some with negative topological charge may be present and the total topological charge is conserved, *i.e.* equal to +2, with the addition of corresponding positively charged defects to balance the negatively charged defects.

It has been found experimentally that for thick nematic shells, a bipolar defect configuration consisting of a boojum at each pole is seen (Figure 1.2.4a), whereas for thin shells four *s*=+1/2 axial disclination lines are seen (Figure 1.2.4b). At intermediate thicknesses, a third defect configuration was seen, consisting of one *s*=+1 and two *s*=+1/2 defects[31](Figure 1.2.6). It has been suggested theoretically that the switch over between thick shell behaviour and thin shell behaviour is dependent on the elastic constant ratios[30], with the bipolar structure being favoured in pure splay or bend systems and within the one elastic constant approach occurs at[32]

$$h/R \approx 0.67 \qquad (1.2.1)$$

where *h* is the shell thickness and *R* is the outer shell radius.

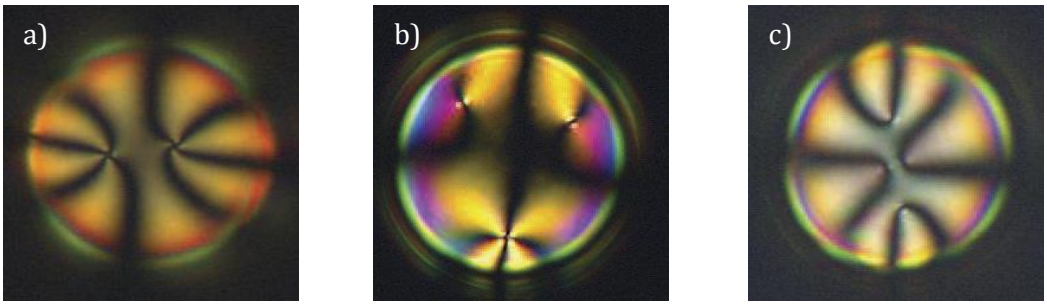

Figure 1.2.6 Cross polarized images of a nematic shell with planar anchoring showing a) two b) three and c) four defects. Taken from Fernandez-Nieves *et al*[29]

Due to the potential application of nematic shells relying on the tetrahedral arrangement in thin shells, work has focussed on systems in the thin shell regime, indeed, many published results have ignored the influence of thickness and investigated a two-dimensional nematic on the surface of a sphere[33, 34]. Whilst for a one elastic constant approach a tetrahedral defect is expected, maximising the distance between defects of the same sign[35], this is not the case when $K_1 \neq K_3$. Both Bates[33] and Shin *et al*[35] found that when the elastic constants were not equal, a defect configuration in which all the defects are located around the great circle of the sphere is seen. Dhakal *et al*[34] have also found that the tetrahedral arrangement is preferable at higher temperatures and the great circle arrangement at low temperatures.

The great circle defect configuration can be thought of as bisecting the bipolar configuration seen in director configuration of pure splay ($^{K_3}/_{K_1} \rightarrow \infty$) system. In these systems, there is no energy penalty associated with splitting the *s*=+1 defects, creating two *s*=+1/2 defects with an uninterrupted nematic region between them. These two hemispheres can then be rotated to form an infinite number of defect configurations in which all the defects are located on the great circle of the sphere.

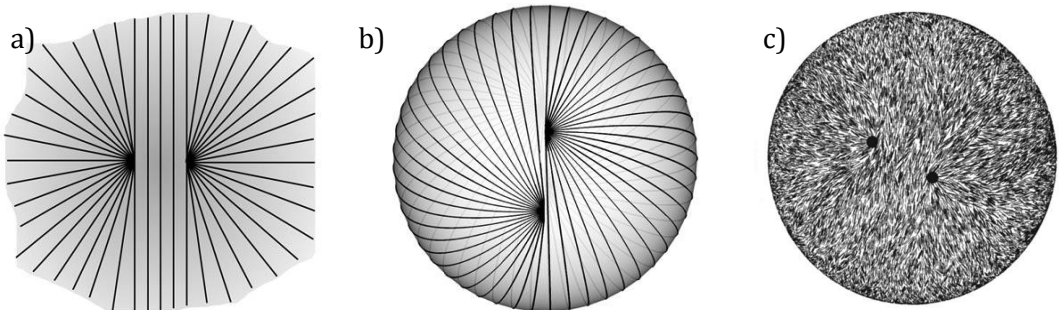

Figure 1.2.7 a) At the limit of $^{K_3}/_{K_1} \rightarrow \infty$ the separation of a *s*=+1 into two *s*=+1/2 defects has no energy penalty. b) and c) two examples of a great circle defect configuration. a) and b) are taken from Shin *et al* [35] and c) from Bates[33]

Nematic shells produced experimentally are of inhomogeneous thickness due to the slight difference in density between the nematic phase and the inner water droplet. The defect configurations observed in the non-uniform thickness shells differ from those predicted in uniform thickness nematic shells. For bipolar defect configurations with two *s*=+1 defects the effect of shifting the inner water droplet was investigated and a transformation from the bipolar defect structure seen in uniform thickness shells to a defect configuration with both defects at the thinnest part of the nematic shell[36] was found. The transition from a bipolar, or deconfined structure to a confined defect configuration where both defects are confined to one hemisphere is dependent on both the average thickness and the relative amount shifted.

Seyednejad *et al*[32] propose that the three defect configuration is stabilised by shifting the central water droplet, with the boojum found at the thinnest part of the nematic shell splitting to form two *s*=+1/2 defects. In thin shells of inhomogeneous thickness the defects are not located in a tetrahedral arrangement but rather are located at the thinnest part of the nematic shell, minimising the length of the disclination lines as the energy of a defect is proportional to the length of the defect.

The behaviour of nematic shells in the presence of an external electric field[37] and nematic shells with different boundary conditions at the inner and outer surfaces have also been investigated[38]. For thin nematic shells, that form four *s*=+1/2 defects with no external electric field, when a homogenous external electric field is applied the bipolar configuration is stabilised, with the poles in the direction of the electric field. Higher order and inhomogeneous external electric fields result in more complex defect configurations containing both positive and negative strength defects. For nematic shells in which planar anchoring is favoured at the inner surface and homeotropic anchoring at the outer surface,

a hybrid director configuration is seen with two *s*=+1 defects on the inner surface and a defect free outer surface.

Smectic shells and the transition from the nematic phase to the smectic phase have also been investigated in double emulsion systems[39, 40]. At temperatures just above the nematic-smectic transition temperature, $K_3 \gg K_1$ and the great circle defect configuration is observed, as found in the simulations of an infinitely thin shell of hard rods[35].

Only very recently have chiral nematic shells been fabricated[41]. A single *s*=+2 defect is observed in the shells, indicating a similar director configuration as those found for filled chiral droplets in which the radius of the droplet is much smaller than the pitch length of the cholesteric phase. The chiral nematic shells were fabricated *via* microfluidics used to encapsulate dyes. The monodisperse nature of the resulting chiral nematic shells allowed for a close packed array to be formed, however the position of the defect was different in each shell.

Little work has been done into non-spherical nematic shells produced by encapsulating a non-spherical colloidal particle with research focussing on spheres that have been deformed by elongating in one or two directions[42, 43] that form four *s*=+1/2 defects. For uniaxial prolate ellipsoidal particles (*i.e.* $x = y < z$), the defects form in pairs at the ends of the longest particle axis, merging and forming a single *s*=+1 defect for very long ellipsoids[43]. For uniaxial oblate ellipsoidal particles (*i.e.* $x = y > z$) the defects tend to locate around the waist of the particle rather than the relatively flat faces of the particle, however Bates *et al*[42] found that the defects were off-set and found slightly on the faces.

1.2.4 *APPLICATIONS OF NEMATIC SHELLS*

Nematic shells with planar anchoring have many different applications due to the presence of defects in the ground state. Double emulsion systems are predicted to self-assemble through the defects and when a solid particle is encapsulated with a nematic shell, it is possible to selectively functionalise the surface of the particle through the defect sites.

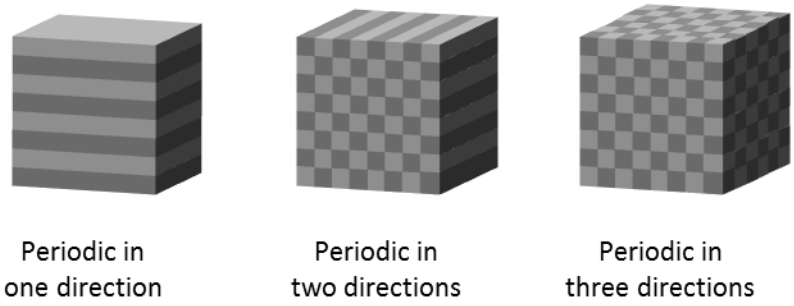

Figure 1.2.8 Photonic crystals periodic in one, two and three directions

It is predicted that two or more nematic shells will interact with each other through the defect sites[28], leading to an ordered system on the micrometre scale. For bipolar droplets, this would lead to strings of droplets. Such behaviour is also seen with colloidal particles[44] or water droplets suspended in a bulk nematic phase[45]. For nematic shells with four defects in a tetrahedral arrangement this would lead to a three-dimensional lattice similar to that found in diamond and the regular array of nematic shells around water droplets acts as a photonic crystal. Recently, chiral nematic shells have been shown to act as a photonic crystal and used to modulate light produced by a laser[41].

A photonic crystal is a material consisting of a periodic array of nanostructures of differing dielectric permittivity[46]. These nanostructures can be formed from a wide variety of building blocks, including silica as found in opals, block copolymers[47] and the nematic shells discussed here. The periodicity of the crystal can be in one, two or three dimensions. One-dimensional photonic crystals are relatively simple to fabricate whereas three-

dimensional photonic crystals with a complete photonic band gap are much more complex (Figure 1.2.8) and have only recently been fabricated on a large scale[48].

The periodic array means that wavelengths of light approximately equal to twice the distance between the nanostructures cannot propagate through the material due to destructive interference from scattering. The wavelengths that pass through the crystal are known as modes and form bands and the disallowed wavelengths form band gaps. This leads to a band structure similar to the electronic band structure in semiconductors such as amorphous silicon (Figure 1.2.9).

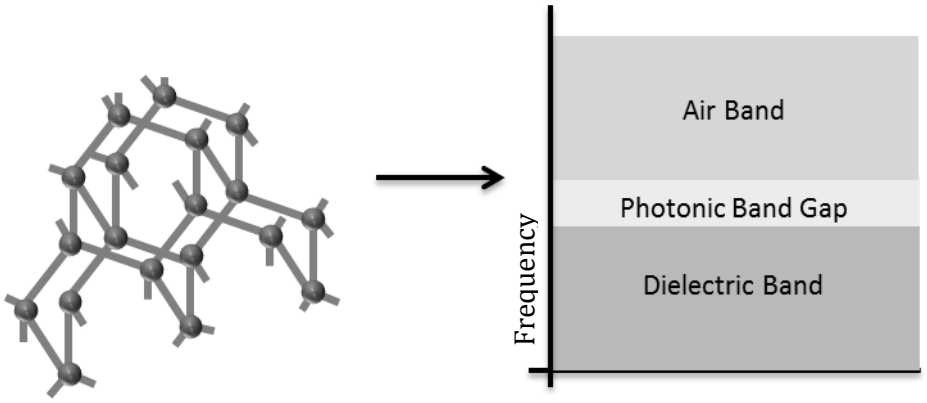

Figure 1.2.9 Three dimensional diamond structure and schematic of a band diagram for a photonic crystal

With the ability to selectively manipulate the flow of light, the main use of photonic crystals is in display devices. One-dimensional photonic crystals have commercial applications including optical coatings (*e.g.* anti-reflective coatings) and spatial filters. Two-dimensional photonic crystals have recently been used commercially as photonic crystal fibres. Possible commercial applications of three-dimensional photonic crystals, include optical computers. When three-dimensional photonic crystals are used in conjunction with wave guides they can be used to manipulate light including guiding light round sharp bends and splitting light[49].

The defect configurations seen for nematic shells with planar anchoring can be thought of as atom-like structures, *i.e.* the bipolar structure seen for thick shells is analogous to an *sp* hybridised carbon whereas the tetrahedral defect configuration seen for thin shells is analogous to an sp^3 hybridised carbon atom. These atom-like structures can be used to investigate the self-assembly found on a microscopic scale in biological systems [50].

For solid particles encapsulated within a nematic shell, it is proposed that the addition of foreign media into the nematic shell, such as polymers or DNA linkers, would lead to a selective functionalization on the inner particle through the defects. The added non-mesogenic molecules migrate to the defects to maintain the nematic ordering in the spherical shell[28]. These selectively functionalised colloids can be used in catalysis, for example, by attaching one linker to a planar substrate leaving a three-valent colloidal particle[28, 51].

1.2.5 *COLLOIDAL PARTICLES IN A BULK NEMATIC PHASE*

There has been a plethora of research into spherical colloidal particles in a bulk nematic system, with both planar and homeotropic anchoring, however there has been relatively little research into non-spherical particles and faceted particles in a bulk nematic.

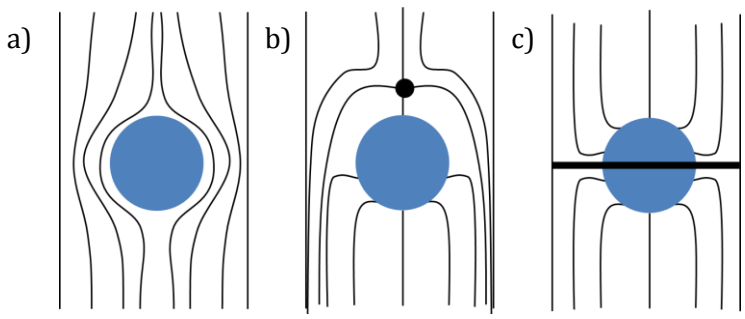

Figure 1.2.10 Schematics of a spherical colloidal particle in a nematic with a) planar anchoring or b) and c) homeotropic anchoring, with a dipole and Saturn ring defect respectively.

For a spherical colloidal particle with planar anchoring in a bulk nematic a boojum is formed around the colloidal particle[52] (Figure 1.2.10a). For spherical colloidal particles with homeotropic anchoring in a bulk nematic, there are two limiting defect structures[53], either a dipole (Figure 1.2.10b) or a Saturn ring (Figure 1.2.10c).

As with the nematic shells discussed in section 1.2.3, the colloidal particles in a bulk nematic self-assemble through the defects. For colloids with planar anchoring, the self-assembly process occurs through the boojums to two-dimensional arrays of colloidal particles, whereas particles with homeotropic can self-assemble through the defects to form both chains[54] and two-dimensional arrays[55] . Recently, work has focussed on defect lines surrounding two or more spherical colloidal particles in a bulk cholesteric[56] or nematic liquid crystal, forming many intricate defect line "knots" around the colloidal particles[57].

Whilst work has primarily focussed on spherical colloidal particles in a bulk liquid crystal phase, it is possible to fabricate colloidal particles in a variety of geometries[58] and only recently have non-spherical colloidal particles been considered. Faceted nanoparticles that are cubic or triangular prisms have been investigated with homeotropic anchoring[59], as have larger, two-dimensional squares[60]. The defect lines surrounding the cubic and triangular prisms were shown to form along the edges, with the triangular prisms aligning with the director.

Other, non-spherical geometry particles have been considered with planar anchoring, including platelets with three to five sides[61, 62], star-shaped particles[63] and more complex colloidal particles which possess handles[64]. The ground state of both polygonal platelets and the star-shaped particles are dependent on the number of edges, or arms in the case of the star shaped particles. For systems with an odd number of sides/arms, *e.g.* triangular platelets or five-armed stars, the particles orient with one side/arm aligning parallel the

director, whereas particles with an even number of sides/arms, *e.g.* a square platelet orient with each side/arm at 45° to the director. In all cases, the defects are located at the vertices of the platelets.

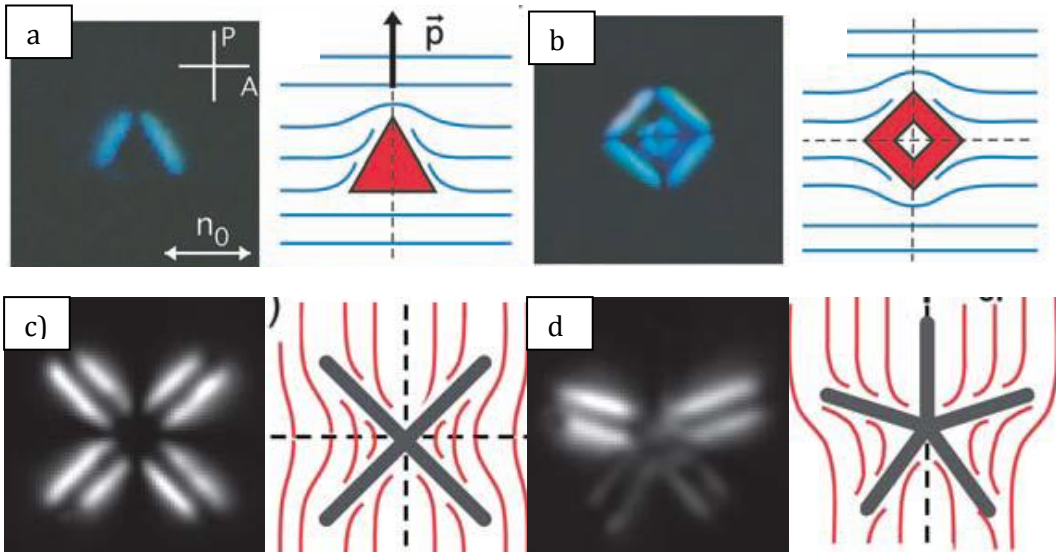

Figure 1.2.11 a) and b) show a triangular and square platelet respectively, taken from Lapointe *et al*[61]. c) and d) show star shaped particles with four and five arms respectively. All show an optical microscopy image under crossed polarisers and a schematic of the director configuration and are taken from Lapointe *et al*[63]

1.2.6 *NEMATIC AND CHIRAL NEMATICS CONFINED IN NON-SPHERICAL GEOMETRIES*

Whilst a sphere minimises the surface area and is the ground state for a liquid droplet, there are many other possible geometries of droplets possible, such as a torus. A torus is a doughnut-like shape and is the product of two circles (Figure 1.2.12).

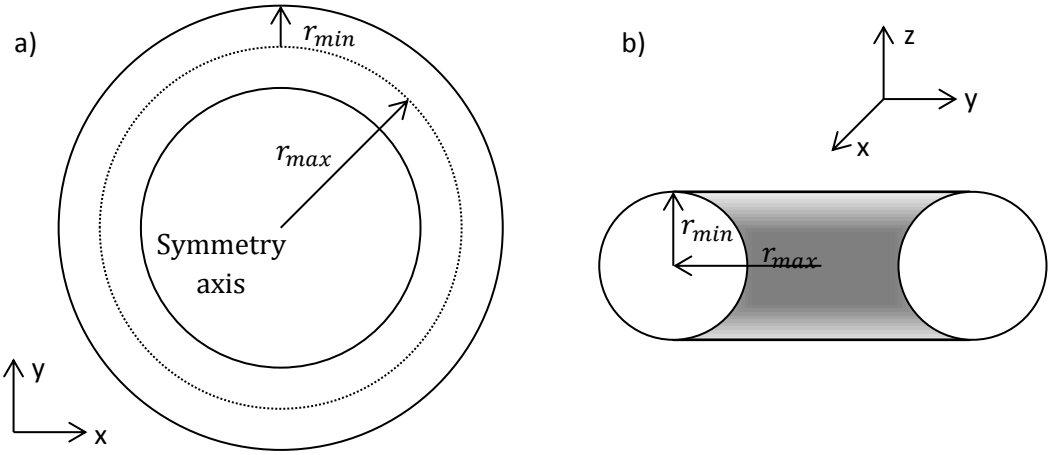

Figure 1.2.12 Parameters used to define a torus. a) Shows the torus from above and b) shows a cross section of the torus

Unlike an ellipsoid or even a cube it is not possible to transform a sphere into a torus without cutting it, this is because a torus has a different Euler characteristic to that of a sphere. The Euler characteristic (χ) of a sphere is 2, whereas for a single torus $\chi = 0$. The Euler characteristic of a body with handles is

$$\chi = 2(1 - g) \tag{1.2.2}$$

where *g* is the number of handles. For example, the Euler characteristic of a system with two handles (*g* = 2), otherwise known as a double torus is

$$\chi = 2(1 - 2) = -2 \tag{1.2.3}$$

The Euler characteristic for a polygon is given by

$$\chi = V - E + F \tag{1.2.4}$$

where *V, E* and *F* are the number of vertices, edges and faces respectively. From (1.2.4), it is possible to see that a cube has the same Euler characteristic as a sphere, which can be considered as having no handles, *i.e.* $g = 0$.

$$\chi = 8 - 12 + 6 = +2 \qquad (1.2.5)$$

A cube is in fact one of five platonic solids[65], the others being a tetrahedron (four sided), an octahedron (eight sided) a dodecahedron (twelve sided) and an icosahedron (twenty sided). A platonic solid is a regular (*i.e.* all edges and angles are equal), convex polyhedron with $\chi = +2$.

Although toroidal droplets are unstable, they can be stabilised by external force and are found in nature, *e.g.* in raindrops[66] or the packing of DNA in sperm[67] . Both isotropic[68] and nematic[69] tori have been created experimentally by stabilising the toroidal droplet in a gel matrix, as have multiple handled bodies (*e.g.* double and triple tori).

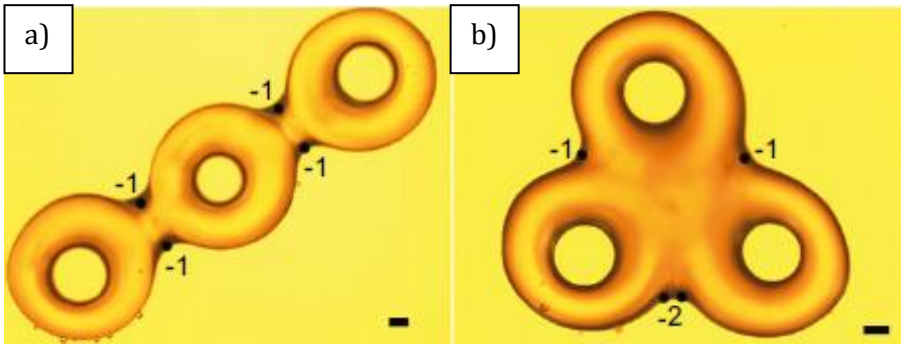

Figure 1.2.13 A linear and triangular triple torus with planar anchoring showing four *s*=-1 defects, equal to the Euler characteristic for a body with three handles ($\chi = -4$). Taken from Pairam *et al* [69]

In nematic droplets with handles with planar anchoring, the total topological charge on the surface is equal to the Euler characteristic meaning that a defect-free ground state is expected for a nematic torus with planar anchoring and the total topological defect charge on the surface to decrease by -2 for each additional handle. Pairam *et al*[69] found that a

single torus does have a defect-free ground state and that a double torus has two *s*=-1 defects at the join between two of the tori. For a toroidal colloidal particle in a nematic, Liu *et al*[64] found both a defect-free structure and one where two *s*=+1 defects and two *s*=-1 defects located on the outer and innermost surfaces respectively were introduced, corresponding to a total topological charge on the surface of torus of 0.

For a single nematic torus with planar anchoring, the director in fat tori (large r_{min}) was seen to spontaneously twist whereas thinner tori (small r_{min}) the director runs axially along the tube of the torus. Kulic *et al*[70] proposed that the presence of the twisted state is dependent on the on the ratio of the twist and bend elastic constants, K_2/K_3, with the twisted director configuration found when K_2/K_3 is small. Further work by Pairam *et al*[69] however, suggests that the director configuration is dependent on the saddle-splay elastic constant, K_{24} (Figure 1.2.14).

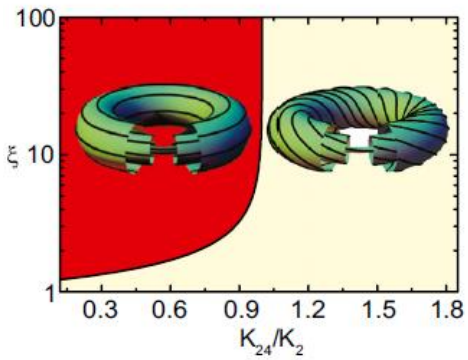

Figure 1.2.14 The regimes where the twisted and untwisted axial director configurations for a nematic torus with planar anchoring are seen. ξ is the aspect ratio of $\xi = r_{max}/r_{min}$. Taken from Pairam *et al*[69]

There has been very little research into nematic tori with homeotropic anchoring, however Stelzer and Bernhard[71] performed a finite element study into the stability of three possible director configurations both with and without the presence of an external magnetic field.

The three director configurations considered were; a *s*=+1 disclination line along the centre of the tube, two *s*=+1/2 disclination lines along the tube or an escaped *s*=+1 defect structure. It was found that with no external magnetic field the director configuration with two *s*=+1/2 defects running along the tube was favoured.

1.3 COMPUTER SIMULATION OF LIQUID CRYSTALS

Computers were first used to simulate liquid crystals in the 1970s, although prior to this theoretical work was done, including work by Onsager[72] in the 1940s based on hard rods, and Maier and Saupe[73] using mean field theory in the 1960s. It was not until the 1990s when the power of computers had increased significantly that real progress in liquid crystal simulations has occurred. Atomistic simulations model each atom separately. Due to the large computational cost atomistic modelling can only be used for small systems. To overcome this problem, coarse-grained modelling is used. In this technique, groups of atoms, or whole molecules are modelled as single particles[74] (Figure 1.3.1). The particles in coarse-grained modelling can be of any shape, generally for liquid crystal mesogens either rods, spherocylinders (cylinders with spherical ends), ellipsoids or discs[75]. Three examples of coarse grained simulations, hard rods and spherocylinders, the Gay-Berne[76] model and the Lebwohl-Lasher[77] model, are discussed below.

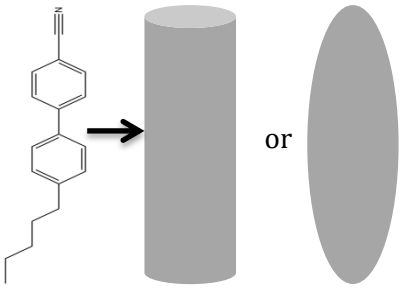

Figure 1.3.1 An example of coarse graining

The Maier-Saupe mean field theory for a nematic phase is based on the long range dispersion forces and ignores shorter range forces treating surrounding particles as one, known as the molecular mean field approximation. The Maier-Saupe mean field theory has the form

$$U(\cos\theta) = \overline{u_2}\,\overline{P_2}P_2(\cos\theta) \qquad (1.3.1)$$

where θ is the angle between the long molecular axis and the director (Figure 1.1.3b) and P_2 is the second Legendre polynomial (1.1.1). $\overline{P_2}$ is the ensemble average of P_2 and $\overline{u_2}$ is the averaged anisotropic interaction parameters. There is only one unknown, P_2, in (1.3.1) and the Maier-Saupe theory successfully predicts the order properties and order-disorder (*e.g.* nematic-isotropic) transition observed in many experimental systems[78].

Unlike the Maier-Saupe mean field theory, Onsager considered a three-dimensional gas of hard spherocylinders which ignores the long-range dispersion interactions however takes into account the short-range anisotropic interactions. Onsager theory states that the phase transition from an isotropic to a nematic phase with increasing pressure is entropically driven. There are two coupled contributions to the entropy, the orientational order found in a gas and the translational entropy from the excluded volume of two rods found parallel to one another. At low densities, the orientational contribution to the entropy is dominant and an isotropic phase is formed, however at higher densities the translational contribution to the entropy is dominant and a nematic phase is seen.

Whilst Onsager theory is only valid for infinitely long rods ($^{L}/_{D} \rightarrow \infty$) computer simulations of hard rods, spherocylinders, and hard ellipsoids have found that both a nematic and smectic phase[79] may be formed and the phase diagram for hard spherocylinders has been mapped by Bolhuis and Frenkel[80]. The relative simplicity of systems of hard rods has lent itself to the investigation of many different systems, including two-dimensional nematics[81], confined systems[82], binary mixtures[83] and polydisperse systems[84].

The Gay-Berne[76] model is an anisotropic form of the Lennard-Jones potential that has been widely used to investigate the nematic phase and takes into account both short- and long-range interactions. The potential is based on ellipsoidal particles of length *l* and breadth *d* where, for prolate particles *l*>*d* , σ_e and σ_s are the end-to-end and the side-to-side diameters respectively and ε_e and ε_s the end-to-end and side-to-side well depths. The potential is given by [76];

$$U(\boldsymbol{p}_i, \boldsymbol{p}_j, \boldsymbol{r}_{ij}) = 4\varepsilon(\boldsymbol{p}_i, \boldsymbol{p}_j, \hat{\boldsymbol{r}}_{ij}) \left[\left(\frac{\sigma_s}{r_{ij} - \sigma(\boldsymbol{p_i}, \boldsymbol{p_j}, \hat{\boldsymbol{r}}_{\boldsymbol{ij}}) + \sigma_s} \right)^{12} - \left(\frac{\sigma_s}{r_{ij} - \sigma(\boldsymbol{p_i}, \boldsymbol{p_j}, \hat{\boldsymbol{r}}_{\boldsymbol{ij}}) + \sigma_s} \right)^{6} \right] \tag{1.3.2}$$

Where $\boldsymbol{p}_i$ and $\boldsymbol{p}_j$are unit vectors representing the orientations of the molecules and $\boldsymbol{r_{ij}}$ the separation between the molecules. The orientation dependent part of the Gay-Berne potential is;

$$\sigma(\boldsymbol{p_i}, \boldsymbol{p_j}, \hat{\boldsymbol{r}}_{\boldsymbol{ij}}) = {}^{\sigma_s}\Bigg/\sqrt{1 - \frac{\chi}{2}\left\{ \frac{\left[\hat{\boldsymbol{r}}_{ij} \cdot (\boldsymbol{p}_i + \boldsymbol{p}_j)\right]^2}{1 + \chi(\boldsymbol{p}_i \cdot \boldsymbol{p}_j)} + \frac{\left[\hat{\boldsymbol{r}}_{ij} \cdot (\boldsymbol{p}_i - \boldsymbol{p}_j)\right]^2}{1 - \chi(\boldsymbol{p}_i \cdot \boldsymbol{p}_j)} \right\}} \tag{1.3.3}$$

For spherical particles this reduces to σ_s which is the spherical diameter, or $\sqrt{2}d$[85].

$\varepsilon(\boldsymbol{p}_i, \boldsymbol{p}_j, \hat{\boldsymbol{r}}_{ij})$ affects the well depths in the potential.

$$\varepsilon(\boldsymbol{p}_i, \boldsymbol{p}_j, \hat{\boldsymbol{r}}_{ij}) = \varepsilon_s \boldsymbol{\varepsilon}'^{\nu}(\boldsymbol{p}_i, \boldsymbol{p}_j)\varepsilon''^{\mu}(\boldsymbol{p}_i, \boldsymbol{p}_j, \hat{\boldsymbol{r}}_{ij}) \tag{1.3.4}$$

$$\varepsilon'(\boldsymbol{p_i}, \boldsymbol{p_j}) = 1 \Big/ \sqrt{1 - \chi^2(\boldsymbol{p}_i \cdot \boldsymbol{p}_j)^2} \tag{1.3.5}$$

$$\boldsymbol{\varepsilon}''(\boldsymbol{p_i}, \boldsymbol{p_j}, \hat{\boldsymbol{r}}_{\boldsymbol{ij}}) = 1 - \frac{\chi'}{2}\left\{\frac{[\hat{\boldsymbol{r}}_{ij} \cdot (\boldsymbol{p}_i + \boldsymbol{p}_j)]^2}{1 + \chi'(\boldsymbol{p}_i \cdot \boldsymbol{p}_j)} + \frac{[\hat{\boldsymbol{r}}_{ij} \cdot (\boldsymbol{p}_i - \boldsymbol{p}_j)]^2}{1 - \chi'(\boldsymbol{p}_i \cdot \boldsymbol{p}_j)}\right\} \tag{1.3.6}$$

$$\chi = \frac{\kappa^2 - 1}{\kappa^2 + 1} \text{ and } \chi' = \frac{\kappa^{\frac{1}{\mu}} - 1}{\kappa^{\frac{1}{\mu}} + 1} \tag{1.3.7}$$

where $\kappa = \frac{\sigma_e}{\sigma_s}$ and $\kappa = \frac{\varepsilon_s}{\varepsilon_e}$.

In the original paper, values of $\kappa = 3, \kappa' = 5, \mu = 2 \text{ and } \nu = 1$ or GB(3,5,2,1) where GB(κ,κ',μ,ν), were used and both a nematic and isotropic phase is seen in bulk systems. Whilst simulations using GB(3,5,2,1) form an ordered liquid phase, the length-to-breadth ratio is much smaller than that found for many mesogens. Luckhurst and Simmonds[86] proposed a set of parameters, GB(4.4,20,1,1), based on the dimensions of *p*-terphenyl, which although not mesogenic in itself, has a similar molecular structure to many common calamitic mesogens. For GB(4.4,20,1,1))[87] a smetic phase is observed in addition to the isotropic and nematic phases found using the original parameters.

The final model for nematics discussed here is the Lebwohl-Lasher model[77] . The Lebwohl-Lasher model is a lattice-based version of the Maier-Saupe mean-field model discussed previously. The Lebwohl-Lasher model consists of a cubic lattice of uniaxial particles which are free to rotate. The particles interact with the nearest neighbours and that the pair potential

$$U_{ij} = -\varepsilon P_2(\cos\beta_{ij}) \tag{1.3.8}$$

where β_{ij} is the angle between nearest neighbours *i* and *j* and ε is a positive coupling parameter. In the bulk[88], a nematic phase is formed at temperatures below $T^* = kT/\varepsilon =$

1.232. It is possible to introduce interfaces with specific alignment by using a layer of ghost particles located at the interface[89].

1.3.1 *The Monte Carlo Method (MC)*

The Monte Carlo technique was developed in the 1940's by Metropolis *et al*[90] and is so called due to the random numbers used in the calculations. However, similar techniques had been used long before the invention of computers and employed various techniques to generate random numbers, e.g. a pack of cards or throwing a dart at a board. Today however, a random number generator program is used.

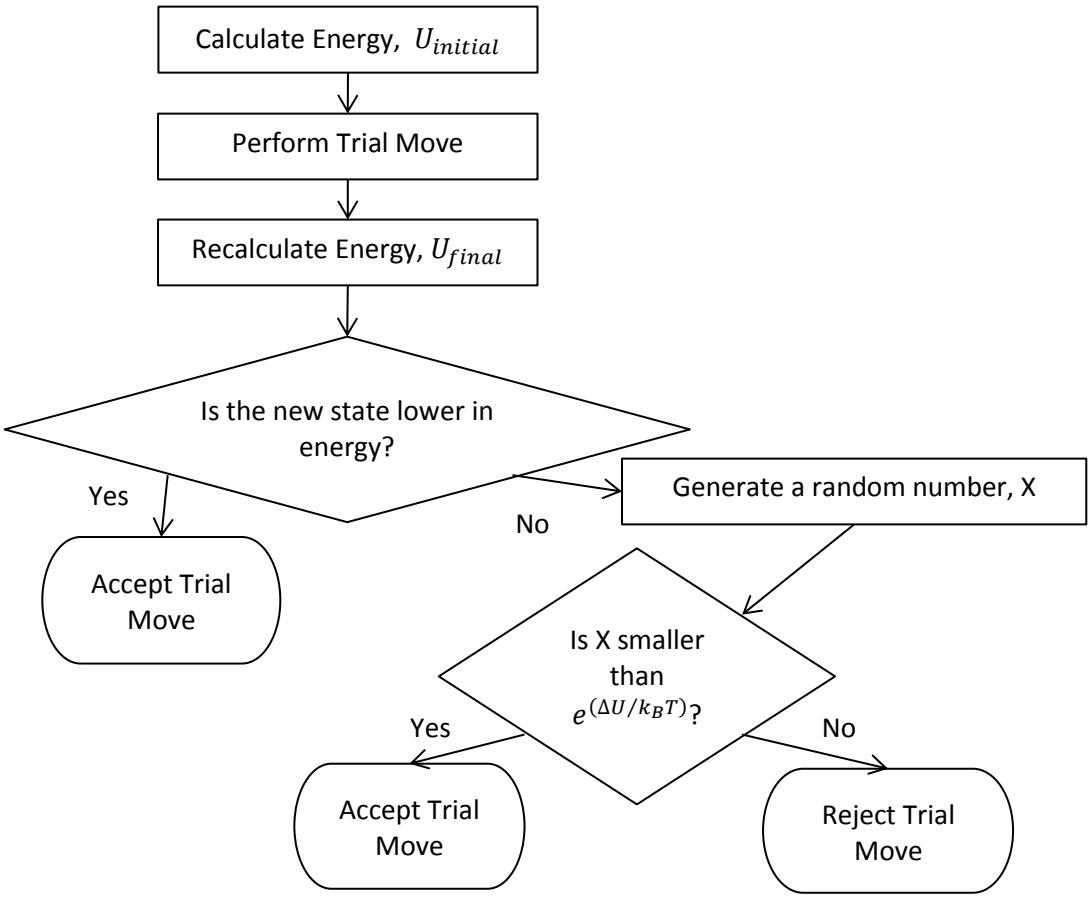

Figure 1.3.2 Flow chart of a Monte Carlo move

Monte Carlo is an importance sampling technique that works by setting up a Markov chain of states which satisfy the conditions that each trial belongs to a finite set of outcomes which is only based on the outcome of the trial that immediately precedes it. An importance sampling technique means that the function evaluation is concentrated in regions of the state space that make important contributions to the integral being investigated.

After a trial rearrangement has occurred, if the energy has decreased then the move is accepted, this is known as a downhill move. If the energy of the system is increased, then a random number is generated and compared to the Boltzmann factor of the energy difference of the two states.

$$e^{(\Delta U/k_B T)} \; where \; \Delta U = U_{final} - U_{initial} \qquad (1.3.9)$$

If the random number is smaller than the Boltzmann factor, then the move is accepted as an uphill move, if not the move is rejected (Figure 1.3.2) and the state recounted. An MC cycle is *N* trial move attempts, where *N* is the number of particles in the simulation.

1.3.2 *Trial Moves*

The trial move selected in a MC simulation can be; a change in volume (isothermal-isobaric systems or *NPT*), a particle exchange or a particle displacement (a constant number, volume and temperature system or *NVT*). In this research, all simulations are a *NVT* type simulation and so moves are either particle exchange or displacement.

In this thesis, there are four types of trial move are attempted for mesogens;

1. A translation by a random amount along a random vector
2. A rotation by a random vector on a sphere
3. A new random orientation
4. A combination of 1. and 2.

For water particles, trial moves were a translation by a random amount along a random vector (1 above). The resulting position ($\boldsymbol{r}_n$) of the particle after a random translation (as in 1 and 4 above) is

$$\boldsymbol{r}_n = \boldsymbol{r}_o + d_1\boldsymbol{t} \tag{1.3.10}$$

where $\boldsymbol{r}_o$ is the initial position of the particle and for both $r_{n\alpha}$ and $r_{o\alpha}$ where $\alpha = x, y, z$ is between zero and the simulation box length. $\boldsymbol{t}$ is a random vector in a cube and $d_1$is a constant between 0.01 and 0.5, *i.e.* the maximum translational displacement is 0.5σ and the minimum translational displacement is 0.01σ.

The resulting orientation ($\boldsymbol{p}_n$) of a particle after a random rotation (as in 2 and 4 above) may be written in a similar way as

$$\boldsymbol{p}_n = \boldsymbol{p}_o + \frac{d_2\boldsymbol{t}}{t} \tag{1.3.11}$$

where $\boldsymbol{p}_o$ is the initial orientation of the particle and $\boldsymbol{t}$ is again a random vector on a sphere with length t. d_2 is a constant between 0.1 and 5.

For simulations of mesogens surrounding a solid particle, an additional type of trial move was made in which the positions of a randomly chosen mesogen and water particle were exchanged and the orientation of the mesogen was replaced by a random vector.

1.3.3 *Acceptance Ratio*

In a Monte Carlo simulation, the number of accepted trial moves is optimised *via* the parameters d_1 and d_2. For large values of d_1, resulting in large displacements, the simulation may be advanced faster than with a lower value of d_1. However, large displacements are more likely to be rejected, *e.g.* a large displacement may cause a mesogen in the centre of the bulk to be displaced into the bulk water which would be very unfavourable and result in the move being rejected. Conversely small displacements lead to a large number of trial moves being accepted however the number needed to

equilibrate the system is much greater than for a larger value of d_1. In order to optimize the Monte Carlo simulation, the acceptance ratio,

$$p_{acc} = \frac{N_{acc}}{N_{trial}} \tag{1.3.12}$$

where N_{acc} and N_{trial} are the number of trial moves accepted and attempted respectively, is calculated and d_1 is altered to maintain p_{acc}between 0.4 and 0.6. Note that, in (1.3.13), both N_{acc} and N_{tot} refer to only those trial moves in which a translation has taken place (moves 1 and 4). An analogous ratio is calculated for trial rotations by a random vector on a sphere and d_2 is varied to maintain an acceptance ratio between 0.4 and 0.6.

1.3.4 *Periodic Boundary Conditions*

In all simulations cubic periodic boundary conditions were used (Figure 1.3.3). By utilising periodic boundary conditions, surface effects may be avoided by replicating the simulation cell to form an infinite lattice. When a particle moves out of the simulation cell, a copy of the particle enters the simulation cell from the opposite face. This removes the 'walls' of the simulation cell and so removes any surface effects[91].

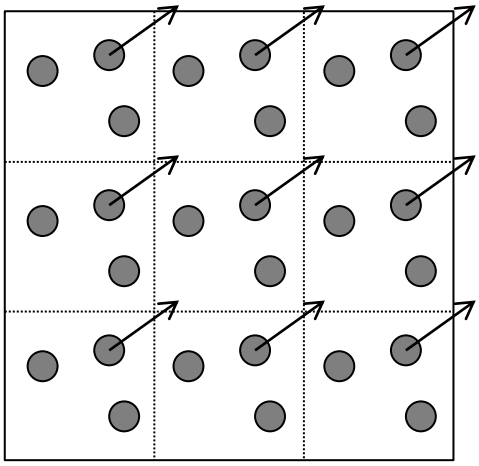

Figure 1.3.3 Schematic of periodic boundary conditions in two dimensions

1.3.5 *NEIGHBOUR LIST*

A linked cell neighbour list is used to greatly reduce the simulation time. When no neighbour list is used, in each trial it is necessary to calculate the energy between one particle every other particle (even if that energy is zero as it is beyond the cut off distance), meaning the time taken per MC cycle scales as N^2 where *N* is the number of particles in the system. Using a neighbour list means that a much smaller number of interactions need to be calculated for each trial.

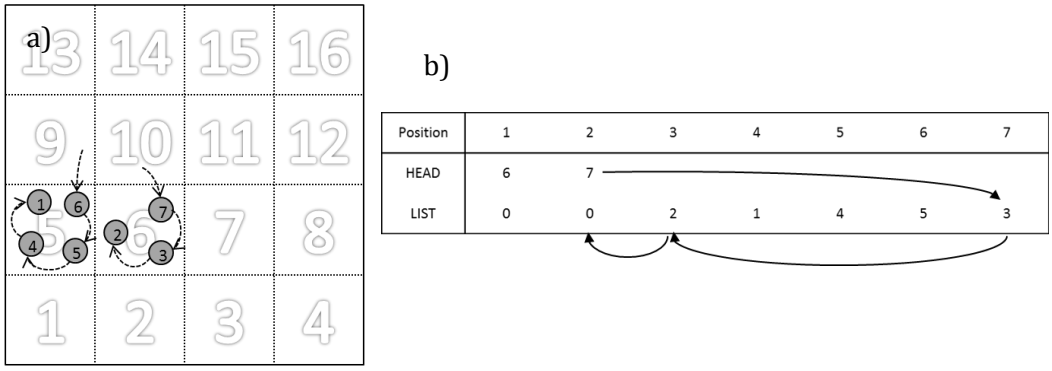

Figure 1.3.4 a) A diagram showing simulation cell split into smaller analysis cells and the numbered particles that are linked in b). The potential energy cut off for particle 7 is also shown. b) shows the linked list table corresponding to the dotted arrow shown in a).

A linked cell neighbour list works by dividing the simulation cell into smaller cubic cells[91]. These smaller analysis cells must have sides equal to or larger than the potential energy cut off used (Figure 1.3.4a), meaning that a particle in one cell can only interact with other particles in that cell or one of the neighbouring 26 cells.

At the start of a simulation, the position and cell that each particle is in is stored. The cell each particle is in is tracked and updated throughout the simulation. The highest number particle in each analysis cell is placed in the HEAD array. This states the position of the next particle number in the LIST array, which in turn states the position of the next particle in

the LIST array and so on. When all the particles in each cell are accounted for, a '0' is used to donate the end of the cell (Figure 1.3.4b).

1.4 ANALYSIS OF SIMULATIONS

Once the simulations have reach equilibrium, the systems were analysed in a variety of ways. By monitoring the energy of the simulation, it was possible to tell when a system had reached equilibrium as the energy of the simulation was constant. For example, simulations started from an isotropic phase showed a sharp decrease in energy on the formation of a nematic phase whereas simulations started from a perfect crystal showed an increase in energy as the order of the system was lost on the formation of a nematic. For bulk systems, other parameters such as the nematic order parameter, $\bar{P}_2$, can be monitored to investigate equilibration.

1.4.1 *BULK ORDER PARAMETER*

The bulk order parameter (1.1.1) was calculated over the simulation box to classify the phase in some of the systems investigated. The order parameter was calculated for each analysis cell and also a global order parameter was calculated for bulk mesogen-only systems, 'slab'-like systems and confined cylinders. The global bulk order parameter was not calculated in the majority of the confined systems as it is meaningless due to the spherical or toroidal geometry of the system.

The bulk order parameter was calculated by calculating the a ***Q***-tensor over all of the mesogens in the system;

$$\boldsymbol{Q}_{\alpha\beta}(\boldsymbol{r}) = \frac{1}{N}\sum_{i=1}^{N}\left(p_{i\alpha}p_{i\beta} - \frac{1}{3}\delta_{\alpha\beta}\right) \qquad (1.4.1)$$

where $\alpha, \beta = x, y, z$ and $\delta_{\alpha\beta}$ is the Kronecker delta. The ***Q***-tensor is then diagonalised

$$\boldsymbol{Q}_{diag} = \begin{pmatrix} \lambda_1 & 0 & 0 \\ 0 & \lambda_2 & 0 \\ 0 & 0 & \lambda_3 \end{pmatrix} \tag{1.4.2}$$

so that $\lambda_1 \geq \lambda_2 \geq \lambda_3$ and the bulk order parameter is taken to be

$$\langle P_2(\cos\theta)\rangle = -3\lambda_2 \tag{1.4.3}$$

1.4.2 *VISUALISATION*

For many of the confined geometries investigated, as stated previously, the bulk order parameter does not provide any meaningful information. For these geometries a measure of the local order is required to locate the defects. To do this, the simulation cell is split into cubic analysis cells that are set to be the same as the cubic cells used in the neighbour list. The size of the analysis cells was a balance between two main factors; smaller analysis cell size meaning the visualisation and position of the defects is of higher resolution whilst a larger analysis cell size means there are more particles in each analysis cell and so less MC cycles are need in order to gain any statistical data about the local order and direction of the director.

In order to visualise the systems simulated and locate the defects, the method proposed by Callan-Jones *et al*[92] was employed and then visualised using Paraview version 3.10.1. This method uses a modified order parameter tensor to calculate three Westin Metrics which are used to represent the linear, planar and spherical order[93].

In each analysis cell a $\boldsymbol{Q}$-tensor was calculated for each analysis cell (1.4.1)and diagonalised to give a matrix in the form

$$\boldsymbol{Q}_{diag} = \begin{pmatrix} \frac{2}{3}S & 0 & 0 \\ 0 & -\frac{1}{3}S + \eta & 0 \\ 0 & 0 & -\frac{1}{3}S - \eta \end{pmatrix} \tag{1.4.4}$$

where *S* is the order parameter and η is the biaxiality parameter (in a uniaxial nematic, η=0) and is equivalent to that shown in (1.4.2). In order to visualise the simulations, the tensor used must be greater than or equal to zero at all points. To achieve this, a modified tensor is used;

$$\boldsymbol{D}_{diag} = \boldsymbol{Q}_{diag} - \frac{1}{3}\boldsymbol{I} = \begin{pmatrix} \lambda_1 & 0 & 0 \\ 0 & \lambda_2 & 0 \\ 0 & 0 & \lambda_3 \end{pmatrix} \quad (1.4.5)$$

where $\lambda_1 \geq \lambda_2 \geq \lambda_3$ and $\lambda_1 + \lambda_2 + \lambda_3 = 1$ From $\boldsymbol{D}_{diag}$, the three Westin metrics, c_l, c_p and c_s, can be calculated.

$$c_l = \lambda_1 - \lambda_2 = S - \eta \quad (1.4.6)$$

$$c_p = 2(\lambda_2 - \lambda_3) = 4\eta \quad (1.4.7)$$

$$c_s = 3\lambda_3 = 1 - S - \eta \quad (1.4.8)$$

The three Westin metrics must all have values between 0 and 1, and $c_l + c_p + c_s = 1$. In a well ordered uniaxial nematic phase, $\lambda_1 \gg \lambda_2 \approx \lambda_3$ and $c_l = 1$. In an isotropic phase ($S = 0, \eta = 0$), $\lambda_1 \approx \lambda_2 \approx \lambda_3$ and so $c_s = 1$ and $c_l = 0$ which is equivalent to a sphere. In reality, c_l is always slightly above zero for a small system due to the presence of some degree of orientational order in a liquid. The same is true for $\bar{P}_2$ for an isotropic phase in a small system.In this thesis only uniaxial molecules were investigated, *i.e.* $\eta = 0$ (as η is a measure of biaxiality), and so $c_p = 0$.

1.4.3 *Director Visualisation*

The director was visualised using stream lines whose trajectory sweeps along the eigenvector field corresponding to λ_1. The streamlines were started from random points in the simulation cell and were chosen so they passed through all regions where there is a non-zero density of mesogens. The director stream lines were used to detect the locations of any escaped defects with *s*=+1 that were not found using the method below. The stream

lines were also used to distinguish between defects of s=$+\frac{1}{2}$ and s=$-\frac{1}{2}$ by studying how the director rotates around the defects (Figure 1.1.7).

1.4.4 *Defect Detection*

The defects were defined as areas where there was density of mesogens, but c_l is less than a threshold value. The threshold value was chosen as it showed a surface in the defect locations but not at the nematic-water interface. The threshold value used was dependent on the temperature of the system. For simulations run at ${T^*}/{T^*_{N-I}} = 0.90$, a threshold of $c_l < 0.15$ was used unless otherwise stated. For simulations run at a higher temperature a much lower threshold value was used as the system was much more disordered and the reverse is true for systems at a lower temperature.

Using this method to detect the defects was very successful for defects of strength $\pm\frac{1}{2}$, it was not always possible to detect defects of strength s=$\pm$1. The s=+1/2 defects were easier to detect due to the different nature of the s=$\pm\frac{1}{2}$ defects and the s=$\pm$1. The half strength defects are axial disclination lines through the nematic whereas the s=$\pm$1 defects are escaped defects on the surface. The defects on the surface are point-like in two dimensions and so tend to have a smaller region of disorder than the axial s=$\pm\frac{1}{2}$ defects.

2 THE INTERACTION POTENTIAL

In this chapter the basic features of the mesogen-mesogen interaction used in this thesis are given, as well as the mesogen-water and water-water interactions used for studying nematic shells. A simple model based on hard spheres with an embedded orientation vector allows for large system sizes of approximately 100,000 particles to be investigated. The chapter then goes on to discuss some preliminary results testing the behaviour of our proposed model with bulk systems and slab-like systems with flat interfaces. An off-lattice model allows for deformation of the spherical shell to occur. By using an off-lattice model, unlike the lattice based analogues, it is also possible to vary the elastic constant ratios.

2.1 MESOGEN-MESOGEN INTERACTION POTENTIAL

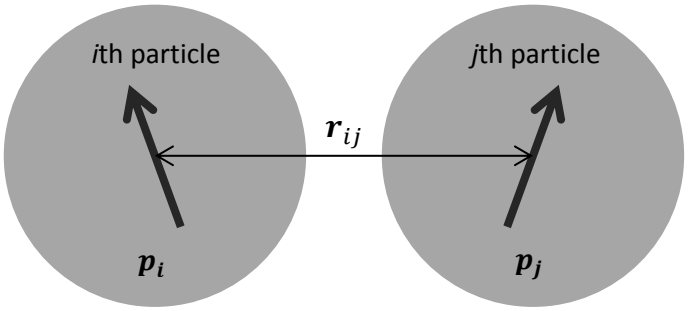

Figure 1.4.1 A schematic of two mesogen particles where $\boldsymbol{p_i}$ and $\boldsymbol{p_j}$ are unit vectors along the direction of the particle and $\boldsymbol{r_{ij}}$ is the unit vector between the centre of particles *i* and *j*.

The key feature of any interaction potential used to model a liquid-crystalline phase is that the interaction between a pair of particles that are parallel is more favourable than for a pair of non-parallel particles, suggesting a simple model

$$U^{LC-LC}(\boldsymbol{p}_i, \boldsymbol{p}_j) = \begin{cases} r \leq \sigma, & \infty \\ \sigma < r < 1.5\sigma, & U^{LC-LC}(\boldsymbol{p}_i, \boldsymbol{p}_j) \\ 1.5\sigma \leq r, & 0 \end{cases} \qquad (2.1.1)$$

where $\boldsymbol{p_i}$ and $\boldsymbol{p_j}$ are unit vectors embedded at the centre of particle *i* and *j* respectively (Figure 1.4.1).

Particles *i* and *j* are hard spheres with a diameter of *σ* and *r* is the distance between the centres of *i* and *j* and

$$U^{LC-LC}(\boldsymbol{p_i}, \boldsymbol{p_j}) = -\varepsilon(\boldsymbol{p}_i \cdot \boldsymbol{p}_j)^2 \quad (2.1.2)$$

with $\varepsilon > 0$. $U^{LC-LC}(\boldsymbol{p_i}, \boldsymbol{p_j})$ is an off-lattice version the Lebwohl-Lasher[77] model. By using spherical cores as opposed to elongated particles such as spherocylinders or rods the system will equilibrate much faster as rotational trial moves are not rejected due to overlap. The mesogen-mesogen potential used is also a simple model, allowing for large system sizes to be investigated. In (2.1.2), $(\boldsymbol{p}_i \cdot \boldsymbol{p}_j)^2 = (\cos\theta)^2$ where θ is the angle between orientation vectors and is lowest in energy when $\theta = 0$ and the particles are aligned. The square is used as there is no polarity in a nematic, *.i.e.* ↑↑=↑↓=↓↓. In order to make this potential more general an expanded form with terms up to $\boldsymbol{p}_{i(j)}^2$ is used. Note that only the even powers are used as, due to the lack of polarity in a nematic phase, the terms with odd powers are all equal to zero.

$$U^{LC-LC}(\boldsymbol{p}_i, \boldsymbol{p}_j, \boldsymbol{r}_{ij}) = -\varepsilon\Big[J_1(\boldsymbol{p}_i \cdot \boldsymbol{p}_j)^2 - 2J_2(\boldsymbol{p}_i \cdot \boldsymbol{p}_j)(\boldsymbol{p}_i \cdot \hat{\boldsymbol{r}}_{ij})(\boldsymbol{p}_j \cdot \hat{\boldsymbol{r}}_{ij}) + J_3(\boldsymbol{p}_i \cdot \hat{\boldsymbol{r}}_{ij})^2(\boldsymbol{p}_j \cdot \hat{\boldsymbol{r}}_{ij})^2\Big] \quad (2.1.3)$$

Where J_x $x = 1,2,3$ are constants, allowing the potential to be based on the orientation of the intermolecular vector, $\boldsymbol{r}_{ij}$ (Figure 1.4.1).

Table 2.1.1 J_1, $J_2$and J_3 values for potentials used.

Potential	J_1	J_2	J_3
1	1.00	0.00	0.00
2	1.00	0.50	1.00
A1	1.00	0.125	0.00
A2	1.00	0.25	0.00
A3	1.00	0.375	0.00
B1	0.75	-0.125	0.00
B2	0.50	-0.25	0.00
B3	0.25	-0.375	0.00

The range of parameters used is chosen so that the interactions between two mesogens are always attractive and the energy at the most favoured particle interaction is -1.

Based on the values of J_1, J_2 and J_3, there are three main classes of $U^{LC-LC}(\boldsymbol{p_i}, \boldsymbol{p_j}, \boldsymbol{r_{ij}})$;

1. Side-side interactions are equal to end-end interactions $(2J_2 = J_3)$ *e.g.* potential 1 and 2.
2. Side-side interactions are favoured over end-end interactions $(2J_2 > J_3)$ *e.g.* potentials A1-A3
3. Side-side interactions are less favoured than end-end interactions $(2J_2 < J_3)$ *e.g.* potentials B1-B3

The difference in energy between side-side interactions and end-end interactions for parallel particles, *i.e.* $\left(\boldsymbol{p}_i.\boldsymbol{p}_j\right)^2 = 1$, can be illustrated by plotting the graphs of $cos(\phi)$ vs. $U^{LC-LC}\left(\boldsymbol{p}_i, \boldsymbol{p}_j, \boldsymbol{r}_{ij}\right)$,where ϕ is the angle between $\boldsymbol{p}_i$and $\hat{\boldsymbol{r}}_{ij}$ where $\hat{\boldsymbol{r}}_{ij} = {\boldsymbol{r}_{ij}}/{r}$ (Figure 2.1.2). In both potentials 1 and 2, side-side interactions and end-end interactions are equal, however in potential 2 there is a barrier to rotation between a side-side and end-end arrangement that is not present in the simpler potential 1 and $U^{LC-LC}\left(\boldsymbol{p}_i, \boldsymbol{p}_j, \boldsymbol{r}_{ij}\right) = -1$ for all values of ϕ.

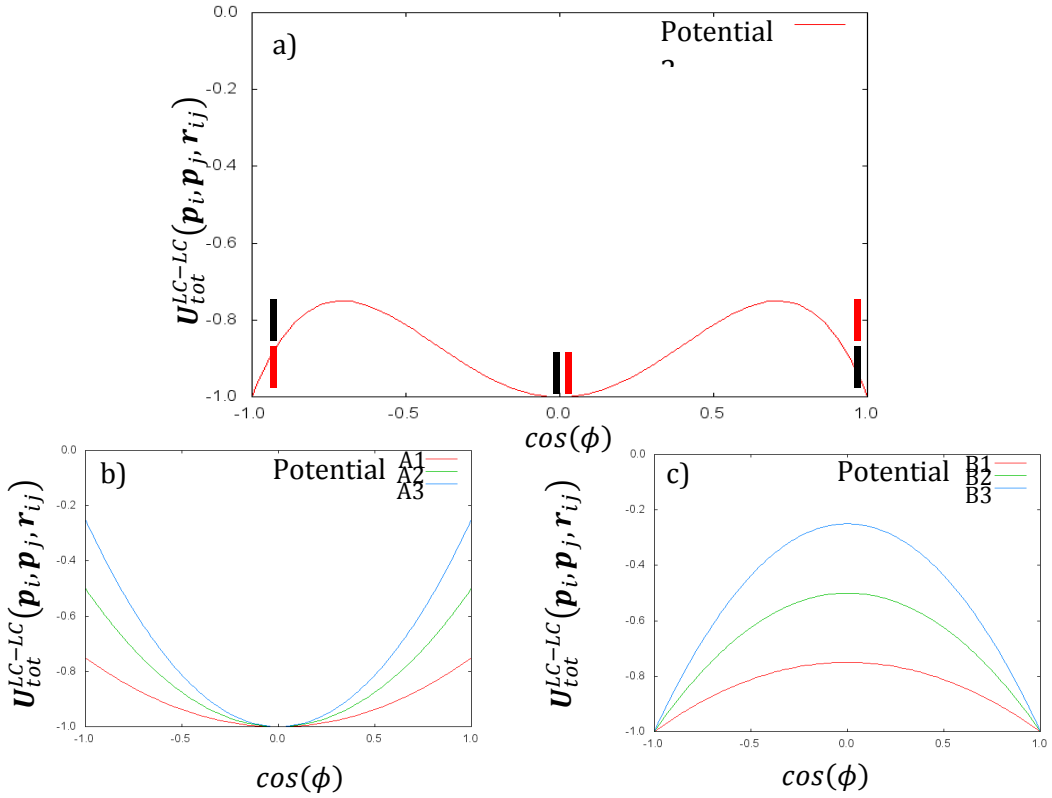

Figure 2.1.2 Graphs of mesogen-mesogen potential interactions vs.cos ϕ for a) potential 2, b) potential A1-3 and c) potential B1-3

2.1.1 *THE CHIRAL INTERACTION POTENTIAL*

It is possible to take into account the chirality of a molecule to investigate the chiral nematic phase. In chapters 4, 6 and 7 chiral shells and toroidal systems are investigated. In order to do this, an additional chiral term[94] was added to the mesogen – mesogen interaction potential (2.1.3),

$$U^{LC-LC}(\boldsymbol{p}_i, \boldsymbol{p}_j, \boldsymbol{r}_{ij}) = \begin{cases} r \leq \sigma, & \infty \\ \sigma < r < 1.5\sigma, & U^{LC-LC}(\boldsymbol{p}_i, \boldsymbol{p}_j, \boldsymbol{r}_{ij}) + U^{LC-LC}_{chiral}(\boldsymbol{p}_i, \boldsymbol{p}_j, \boldsymbol{r}_{ij}) \\ 1.5\sigma \leq r, & 0 \end{cases} \quad (2.1.4)$$

Where

$$U^{LC-LC}_{chiral}(\boldsymbol{p_i}, \boldsymbol{p_j}, \boldsymbol{r_{ij}}) = -\varepsilon_c[\hat{\boldsymbol{r}}_{\boldsymbol{ij}} \cdot (\boldsymbol{p_i} \times \boldsymbol{p_j})][(\boldsymbol{p}_i \cdot \boldsymbol{p}_j)] \quad (2.1.5)$$

And $\varepsilon_c > 0$ where ε_c is the chiral strength parameter. When $\boldsymbol{p_i}$ and $\boldsymbol{p_j}$ are in the same plane, the cross product ($\boldsymbol{p_i} \times \boldsymbol{p_j}$) is orthogonal to $\hat{\boldsymbol{r}}_{\boldsymbol{ij}}$, meaning that the resulting dot product ($\hat{\boldsymbol{r}}_{\boldsymbol{ij}} \cdot (\boldsymbol{p_i} \times \boldsymbol{p_j})$) is zero. Conversely, when $\boldsymbol{p_i}$ and $\boldsymbol{p_j}$ are not in the same plane, the potential causes a helical twist to be favoured [95].

2.2 WATER-WATER INTERACTION POTENTIAL

In the following two chapters, shells formed as a double emulsion of liquid crystals in water will be investigated and so a water-water interaction and the cross mesogen-water interaction need to be defined. Unlike mesogen particles, water particles do not have any orientation dependence as the resulting liquid phase is isotropic. The potential used was a simple square well potential;

$$U^{W-W}(\boldsymbol{r}_{ij}) = \begin{cases} r \leq \sigma, & \infty \\ \sigma < r < 1.5\sigma, & -\varepsilon_W \\ 1.5\sigma \leq r, & 0 \end{cases} \quad (2.2.1)$$

Where $\varepsilon_W > 0$ and is the potential well depth. Preliminary simulations of nematic shells and flat surfaces were run varying ε_W from 0.0 to -0.5. Importantly, no crystallisation of

water occurs at the reduced temperatures studied and it was found that for all interaction potential well depths less than 0.0 gave very similar configurations for the defects in the droplet shell. The magnitude of the water-water interaction is not influential on the structure of the water.

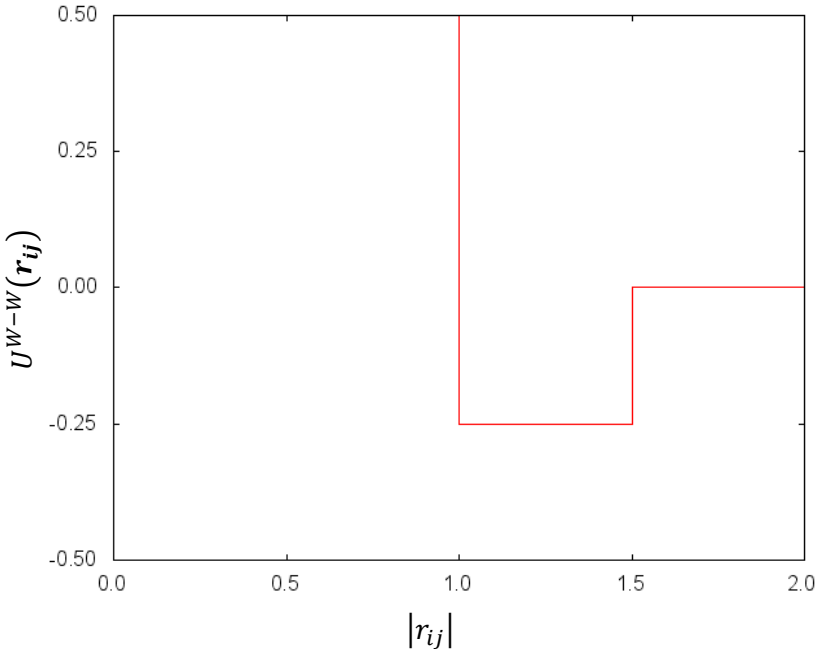

Figure 2.2.1 Graph of $U^{W-W}(\boldsymbol{r}_{ij})$ where $\varepsilon_W = 0.25$

2.3 MESOGEN-WATER INTERACTION POTENTIAL

The mesogen-water interaction governs the anchoring type and strength at the interfaces. We take the mesogen-water potential to have a similar square well form

$$U^{LC-W}(\boldsymbol{p}_i, \boldsymbol{r}_{ij}) = \begin{cases} r \leq \sigma, & \infty \\ \sigma < r < 1.5\sigma, & U^{LC-W}(\boldsymbol{p}_i, \boldsymbol{r}_{ij}) \\ 1.5\sigma \leq r, & 0 \end{cases} \tag{2.3.1}$$

where

$$U^{LC-W}(\boldsymbol{p}_i, \boldsymbol{r}_{ij}) = \varepsilon_{LC-W} + \varepsilon_A(\boldsymbol{p}_i \cdot \hat{\boldsymbol{r}}_{ij})^2 \tag{2.3.2}$$

$$U^{LC-W}(\boldsymbol{p}_i, \boldsymbol{r}_{ij}) = (\varepsilon_A + \varepsilon_{LC-W}) - \varepsilon_A(\boldsymbol{p}_i \cdot \hat{\boldsymbol{r}}_{ij})^2 \quad (2.3.3)$$

For planar and homeotropic anchoring respectively. ε_A and ε_{LC-W} are both positive constants, where ε_A is the anchoring strength and ε_{LC-W} the repulsion between the mesogen and water particles that induces phase separation. As in the mesogen-mesogen interaction potential, $(\boldsymbol{p}_i.\hat{\boldsymbol{r}}_{ij})^2 = (cos\,\theta)^2$ and θ is the angle between $\boldsymbol{p}_i$and $\hat{\boldsymbol{r}}_{ij}$ where $\hat{\boldsymbol{r}}_{ij} = {\boldsymbol{r}_{ij}}/{r}$. By using the interaction potentials (2.3.2) and (2.3.3), the energy of the interaction varies from ε_{LC-W} to $\varepsilon_{LC-W} + \varepsilon_A$ (Figure 2.3.1).

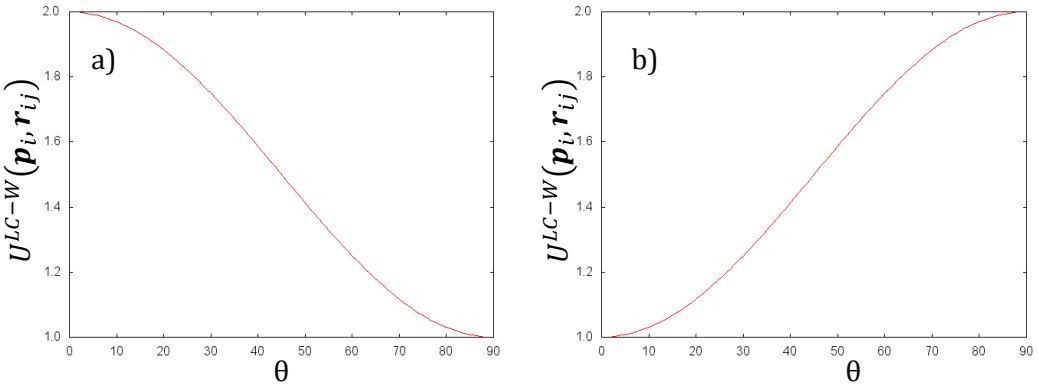

Figure 2.3.1 Graphs of the angle between $\boldsymbol{p}_i$and $\hat{\boldsymbol{r}}_{ij}$ vs. $U^{LC-W}(\boldsymbol{p}_i, \boldsymbol{r}_{ij})$ for $\varepsilon_{LC-W} = 1$ and $\varepsilon_A = 1$ for a) planar and b) homeotropic anchoring

2.4 Preliminary Bulk Simulations

2.4.1 *Bulk Transition Temperatures*

For each potential, a series of simulations of 10368 mesogens in a cubic simulation cell of sides 24, corresponding to $\rho^* = 0.75$ where

$$\rho^* = \frac{N\sigma^3}{V} \quad (2.4.1)$$

were run at different reduced temperatures, T^*, where

$$T^* = \frac{k_B T}{\varepsilon} \quad (2.4.2)$$

to calculate the nematic – isotropic transition temperature, T^*_{N-I}.

The density of $\rho^* = 0.75$ was used as this corresponds to a dense liquid phase for hard spheres, just below the density of liquid-solid coexistence ($\rho_L^* = 0.9375$)[96] and was used to ensure that a liquid phase with no voids were formed in the simulation. By fixing the density, it is assumed the density at the nematic-isotropic transition does not change significantly.

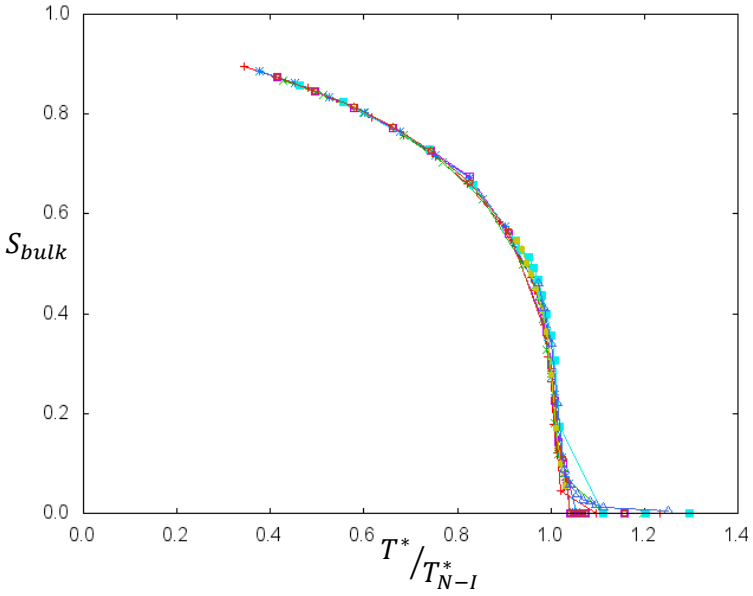

Figure 2.4.1 A graph showing the change order parameter, S_{bulk}, with increasing temperature for all models

The simulations were run from both a cubic lattice and an isotropic phase and the bulk order parameter was calculated throughout the simulation. The bulk order parameter, S_{bulk}, is

$$S_{bulk} = \langle P_2(\cos\theta)\rangle = \langle \frac{3}{2}\cos^2\theta - \frac{1}{2}\rangle \qquad (2.4.3)$$

For a nematic phase at a temperature much lower than the nematic-isotropic transition temperature, the order parameter is relatively constant during a simulation, for simulations at $T^*/T^*_{N-I} = 0.9$ using the models described previously, $S_{bulk} \approx 0.6$. However, as the temperature approaches the transition temperature *S* decreases until at T_{N-I} it drops to zero for an isotropic liquid (Figure 2.4.1).

Table 2.4.1 Nematic - isotropic transition temperatures (T^*) for each potential used

Potential	T^*_{N-I}
1	1.46
2	1.17
A1	1.33
A2	1.21
A3	1.08
B1	1.21
B2	0.97
B3	0.72

2.4.2 *ELASTIC CONSTANT CALCULATIONS*

To calculate the elastic constants the method developed previously by Allen *et al*[97] was employed, allowing for the calculation of ${}^{K_1}/_{K_3}$ and ${}^{K_2}/_{K_3}$. By calculating the ratios, any fluctuations in the absolute values are removed. The method is briefly summarised below;

An ordering tensor in real space (2.4.4) is first calculated, as is the Fourier transform in reciprocal space (2.4.5), which is wave-vector dependent.

$$Q_{\alpha\beta}(\boldsymbol{r}) = \frac{V}{N}\sum_i \left(\tfrac{3}{2}\boldsymbol{p}_{i\alpha}\boldsymbol{p}_{i\beta} - \tfrac{1}{2}\delta_{\alpha\beta}\right)\delta(\boldsymbol{r}-\boldsymbol{r_i}) \qquad (2.4.4)$$

$$\hat{Q}_{\alpha\beta}(\boldsymbol{k}) = \frac{V}{N}\sum_i \left(\tfrac{3}{2}\boldsymbol{p}_{i\alpha}\boldsymbol{p}_{i\beta} - \tfrac{1}{2}\delta_{\alpha\beta}\right)\exp(i\boldsymbol{k}\cdot\boldsymbol{r}) \qquad (2.4.5)$$

Where $\boldsymbol{p}_i$ is a unit orientational vector for particle *i* (as before) and $\alpha, \beta = x, y, z$ and $\delta_{\alpha\beta}$ is the Kronecker delta. When the system is unperturbed, the orientation density is independent of position meaning that for an unperturbed system;

$$\langle \boldsymbol{Q}(\boldsymbol{r}) \rangle = \langle \boldsymbol{Q} \rangle = \frac{\langle \widehat{\boldsymbol{Q}}(\boldsymbol{k}=\boldsymbol{0}) \rangle}{V} = \text{constant} \qquad (2.4.6)$$

where $\langle \dots \rangle$ indicated equilibrium ensemble averages. As in previous simulations, the order parameter, P_2 is taken to be the highest eigenvalue of $\langle \boldsymbol{Q} \rangle$. Taking the director to be parallel with the *z*-axis, ($\widehat{\boldsymbol{n}} = (0,0,1)$), a new axis system **1,2,3** can be taken so that $\langle \boldsymbol{Q} \rangle$ is diagonal with the director. A wave vector ($\boldsymbol{k}$) is taken to lie in the 1-3 plane, so that $\boldsymbol{k} = (k_1, 0, k_3)$. Static orientational fluctuations can be described in terms of $\widehat{\boldsymbol{Q}}$ in the **1,2,3** coordinate system as;

$$\langle \hat{Q}_{13}(\boldsymbol{k}) \hat{Q}_{13}(-\boldsymbol{k}) \rangle \equiv \langle \left| \hat{Q}_{13}(\boldsymbol{k}) \right|^2 \rangle = \frac{\frac{9}{4}\overline{P_2^2} V k_B T}{K_1 k_1^2 + K_3 k_3^2} \qquad (2.4.7)$$

$$\langle \hat{Q}_{23}(\boldsymbol{k}) \hat{Q}_{23}(-\boldsymbol{k}) \rangle \equiv \langle \left| \hat{Q}_{23}(\boldsymbol{k}) \right|^2 \rangle = \frac{\frac{9}{4}\overline{P_2^2} V k_B T}{K_2 k_1^2 + K_3 k_3^2} \qquad (2.4.8)$$

These equations are only valid in the low limit of *k,* as the elastic constants are defined for long wavelength director fluctuations. It is not possible to directly calculate $k = 0$, so it is necessary to extrapolate to this point using

$$E_{13}(k_1^2, k_3^2) \equiv \frac{\frac{9}{4}\overline{P_2^2} V k_B T}{\langle \left| \hat{Q}_{13}(\boldsymbol{k}) \right|^2 \rangle} \rightarrow K_1 k_1^2 + K_3 k_3^2 \; as \; k \rightarrow 0 \qquad (2.4.9)$$

$$E_{23}(k_1^2, k_3^2) \equiv \frac{\frac{9}{4}\overline{P_2^2} V k_B T}{\langle \left| \hat{Q}_{23}(\boldsymbol{k}) \right|^2 \rangle} \rightarrow K_2 k_1^2 + K_3 k_3^2 \; as \; k \rightarrow 0 \qquad (2.4.10)$$

In principle, these should be linear functions of k_1^2 and k_3^2 in the limit of $k \rightarrow 0$, however in practice at finite *k*, the higher order terms are not negligible. To account for this the polynomial

$$f(k_1^2, k_3^2) =$$

$$\frac{c + c_1 k_1^2 + c_2 k_3^2 + c_{11}(k_1^2)^2 + c_{12} k_1^2 k_3^2 + c_{22}(k_3^2)^2 + c_{111}(k_1^2)^3 + c_{112}(k_1^2)^2 k_3^2 + c_{122} k_1^2 (k_3^2)^2 + c_{222}(k_3^2)^3}{1 + d_{11}(k_1^2)^2 + d_{12} k_1^2 k_3^2 + d_{22}(k_3^2)^2 + d_{111}(k_1^2)^3 + d_{112}(k_1^2)^2 k_3^2 + d_{122} k_1^2 (k_3^2)^2 + d_{222}(k_3^2)^3} \qquad (2.4.11)$$

Is used where ${c_1}/{c_2} = {K_x}/{K_3}$ and $\mathrm{x} = 1,2$. In order for the director to be parallel to the *z*-axis, a small field was applied in this direction. This was achieved by including an extra term in the energy potential [98].

$$U_{field}(\boldsymbol{p}_i, \boldsymbol{r}_{ij}) = \varepsilon_{field}[1 - (\boldsymbol{p}_i \cdot \boldsymbol{E})^2] \quad (2.4.12)$$

Where ε_{field} is the field strength and $\boldsymbol{E}$ is the field unit vector, in this case $\boldsymbol{E} = (0,0,1)$.

The ratios ${K_1}/{K_3}$ and ${K_2}/{K_3}$ were calculated for all the potentials. Simulations of bulk nematics were run at $T^* = 0.9 \times T^*_{N-I}$ for values of $\varepsilon_{field} = 0.01 - 0.10$ and it was found that the elastic constant ratios were independent on the field strength used. The simulations were run for a short time and both *S* and the total energy of the system were monitored. Once equilibrated, the simulations were run for 4×10^6 MC cycles to determine the elastic constant ratios (Table 2.4.2).

As can be seen from Table 2.4.2, for potentials 1 and 2 the elastic constants are approximately equal, $K_1 \approx K_2 \approx K_3 = K$. Both the A and B potential series have two elastic constants where, $K_1 \approx K_3 \neq K_2$, for A $(K_1 \approx K_3) < K_2$ and for B $(K_1 \approx K_3) > K_2$.

Although K_2 is found to vary, it is important to note that ${K_1}/{K_3}$ is constant at 1 (*i.e.* $K_1 = K_3$). For simulations of non-spherical particles, *e.g.* hard rods or ellipsoids as found in the Gay-Berne model[97], $K_3 > K_1$ which is proposed effects the location of the defects in infinitely thin shells with four *s*=+1/2 defects[33, 35].

Table 2.4.2 Calculated values for K_1/K_3 and K_2/K_3, averaged over all simulations varying ε_{field} at $T^*/T^*_{N-I} = 0.9$.

Potential	K_1/K_3	K_2/K_3
1	1.038	0.985
2	1.005	1.095
A1	1.014	1.064
A2	1.056	1.151
A3	0.968	1.232
B1	1.012	0.933
B2	0.993	0.860
B3	0.998	0.717

By including the higher terms in the potential, it was hoped that the elastic constant ratios would vary for the different potentials used, particularly the splay and bend ratio, K_1/K_3 to examine how the elastic constants affect the director configuration in nematic shells. Unfortunately, this is not the case and $K_1/K_3 = 1$ for all models studied.

For $\varepsilon_{field} = 0.04$, the temperature dependence of the elastic constants was investigated and a series of simulations were run at $T^* = 0.75, 0.80, 0.85 \text{ and } 0.95 \times T^*_{NI}$ and $\rho^* = 0.75$. It was found that K_1/K_3 and K_2/K_3 were very similar for all T^* used. It was found that whilst the values for the constants in the polynomial used were dependent on the temperature of the simulation, the ratios K_1/K_3 and K_2/K_3 were independent of T^*.

Table 2.4.3 Calculated values for K_1/K_3 and K_2/K_3 for potential 1 with $\varepsilon_{field} = 0.04$

T^*/T^*_{N-I}	K_1/K_3	K_2/K_3
0.75	1.016	1.011
0.80	1.087	1.087
0.85	0.976	1.016
0.90	0.971	0.977
0.95	1.025	1.020

2.5 PRELIMINARY SLAB SIMULATIONS

2.5.1 *NEMATIC SLAB SIMULATIONS*

A system with two flat liquid crystal-water interfaces was initially investigated using the potentials detailed in Table 2.1.1 at $T^*/T^*_{N-I} = 0.8 - 1.05$ in order to parameterise the anchoring potential. The simulation cell contained a slab of liquid crystal along the *z*-axis with water to the right and left (Figure 2.5.1).

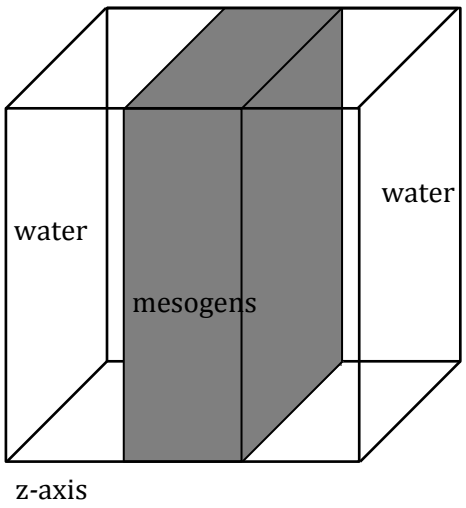

Figure 2.5.1 Schematic of slab simulations

To analyse the systems, the simulation cell was split into slices of 0.75 one along the *z*-axis. For each slice, the density of mesogens (ρ_{LC}) and water (ρ_W) particles were calculated along with the bulk order parameter, S_{bulk} as given in (2.4.3) and the local order parameter with respect to the *z*-axis given by

$$S_z = \langle P_2(\cos\phi)\rangle = \langle \tfrac{3}{2} {p_{iz}}^2 - \tfrac{1}{2} \rangle \qquad (2.5.1)$$

where p_{iz} is the *z*-component of the unit orientational vector of particle *i*. Two order parameters were calculated; S_{bulk} was calculated as it gave a measure of the bulk orientation (i.e. if a nematic was formed), whereas S_z gave a measure of the strength of the anchoring at the interfaces (*i.e.* if the nematic was aligned parallel or perpendicularly to the surface and how strongly). Both planar alignment and homeotropic alignment were run for several different anchoring strengths. The predicted value of S_z is that predicted for perfect alignment multiplied by S_{bulk}. For perfect planar anchoring, S_z is predicted to be

$$\phi = 90^\circ \qquad S_z = \left({}^3/_2 \times 0\right) - {}^1/_2 = {}^{-1}/_2 \qquad (2.5.2)$$

whereas for perfect homeotropic anchoring S_z is predicted to be

$$\phi = 0^\circ \qquad S_z = \left({}^3/_2 \times 1\right) - {}^1/_2 = 1 \qquad (2.5.3)$$

It was found that phase separation is maintained and that the slab does not drift significantly from its initial point in the centre of the simulation cell (Figure 2.5.2a). A small amount of mixing is seen at interfaces, but this is to be expected due to diffusion. The amount of mixing between the liquid crystal and solvent phases increases with increasing temperature as the particles have more thermal energy, however at all temperatures phase separation is seen.

It was found that the presence of the nematic-water interface did not significantly shift the nematic-isotropic transition temperature. Simulations run at $T^*/T^*_{N-I} = 0.9$ all showed a nematic phase with $S_{bulk} \approx 0.6$ (Figure 2.5.2b and c), with S_z dependent on the anchoring at the surface. For planar anchoring, $S_z \approx -0.3$ whereas in systems with homeotropic anchoring, $S_z \approx 0.6$, in agreement with that predicted.

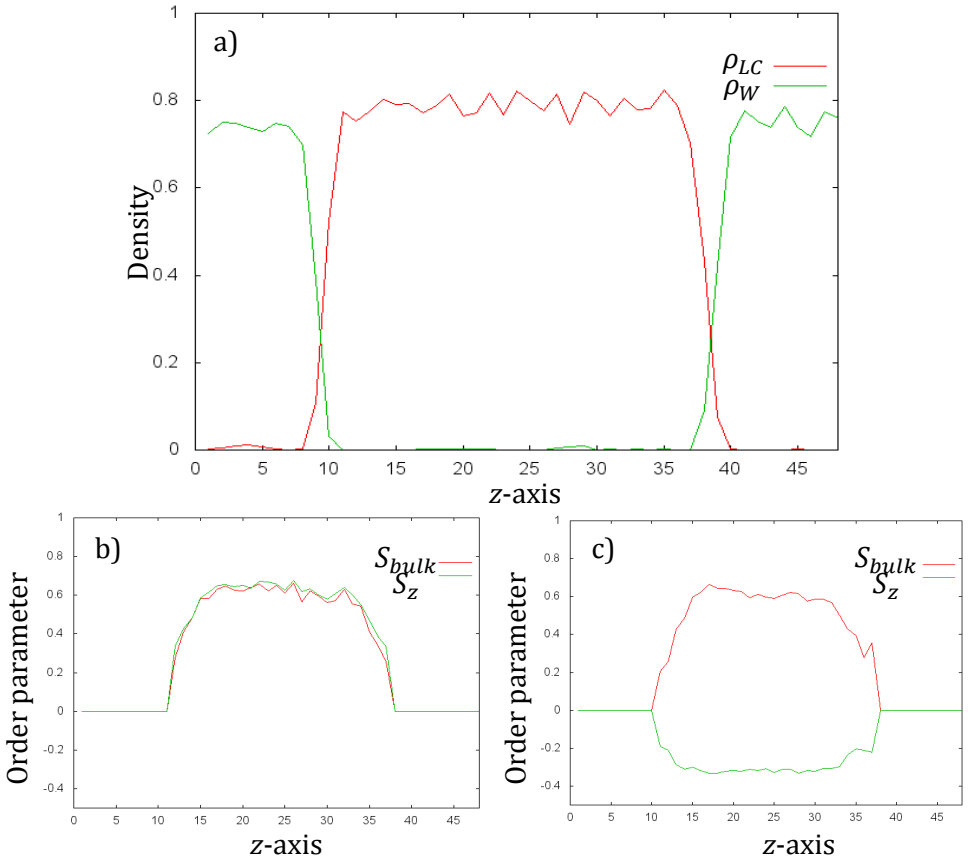

Figure 2.5.2 Graphs for a slab of thickness 30σ at $T^*/T^*_{N-I} = 0.9$ showing a) the density of mesogens and water particles and b) and c) show the order parameters S_{bulk} and S_z for homeotropic and planar anchoring respectively

2.5.2 *CHIRAL NEMATIC SLABS*

Simulations of the flat interface with planar anchoring were also run for the chiral nematic interaction potential (2.1.4) for ${T^*}/{T^*_{N-I}} = 0.9$ for potentials 1 and B3. Both S_{bulk} and the angle between the director at both surfaces and the centre was calculated, in order to determine the pitch length of the chiral nematic. It is not possible to use bulk simulations to calculate the pitch of the chiral nematic as the periodic boundary conditions impose a constraint that the ends of the director at opposing boundaries must meet meaning that only half integer pitch lengths are possible in the simulation cell. Thus calculation of the chiral nematic pitch length is unfeasible unless incredibly large systems, of the dimensions of multiple pitch lengths, are used.

A more direct route is to use a slab with planar degenerate anchoring at the surfaces. The chiral interaction potential used is known to have a linear relationship between the slab thickness and the twist angle[99] and it is possible to extrapolate to an infinite slab thickness to calculate the pitch length. Slabs of chiral nematic were run with planar anchoring varying both the thickness of the slab and ε_c .

For all chiral nematic slab simulations, as with the non-chiral slab simulations, the liquid-crystalline slab did not significantly drift from the centre of the box, and a small amount of mixing is seen at the interfaces between liquid crystal phase and water. The inherent twist perpendicular to the director in the chiral nematic phase can be seen in Figure 2.5.3.

The first interface was taken as the first slab analysed with a mesogen density of above 0.4 allowing for any diffusion or drifting of the slab, the second interface was taken to be the last slab analysed with a mesogen density of above 0.4. The angle with the centre of the slab is calculated to test if there was more than half a pitch length in the slab. These angles were calculated throughout the simulation and the mean value from an equilibrated system was used to calculate the final pitch length shown in Figure 2.5.4a.

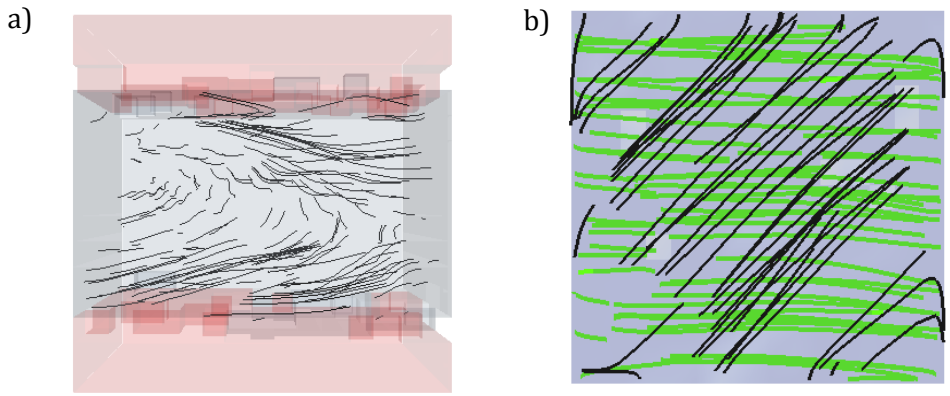

Figure 2.5.3 Slab thickness of 15σ for potential 1 with $\varepsilon_c = 0.15$, showing a) director twist viewed down the *x*-axis and b) the director at the two interfaces.

It was found that at high values of ε_c, the planar anchoring was not preserved and a blue phase structure was formed. The value of ε_c at which the loss of the desired surface anchoring occurred was highly dependent on both the slab thickness and the nematic potential used. For example, for potential B3, in a thin slab of thickness 10σ, $\varepsilon_c = 0.39$ still produced planar alignment at both water-mesogen interfaces, however for potential 1 in a thicker slab of thickness 25σ, planar alignment was not conserved for $\varepsilon_c > 0.18$.

Simulations were performed varying the anchoring strength with $\varepsilon_A = 1, 5, 7.5 \text{ and } 10$ in (2.3.2) for potential 1 to investigate the effect of anchoring strength on the pitch length. The pitch length was found to be independent of the anchoring strength used as the helical twist is inherent to the chiral nematic and is a bulk property. The loss of planar anchoring at

the surfaces, however, occurred at lower ε_c values for smaller anchoring strengths as the energy penalty for unfavourable surface interactions was lower.

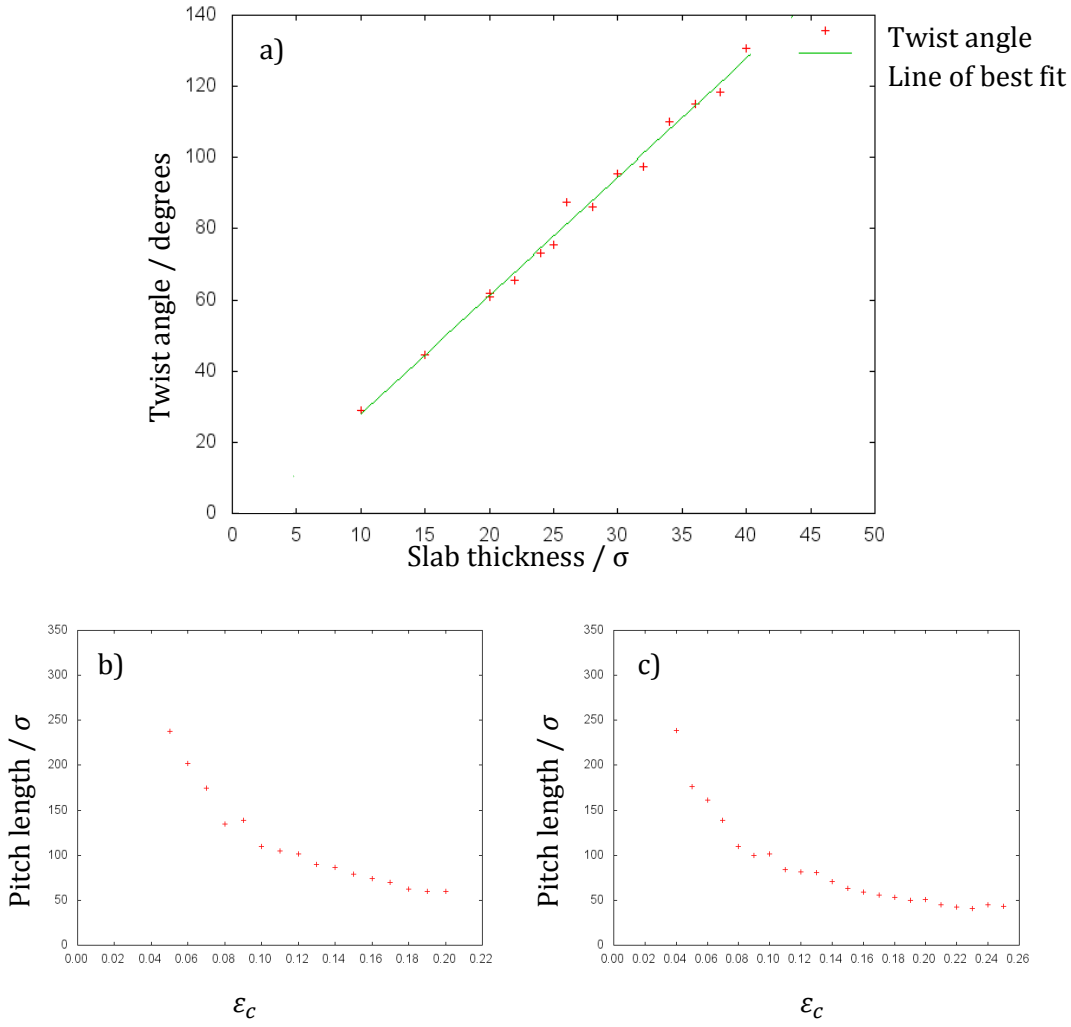

Figure 2.5.4 a) Twist angle vs. slab thickness for potential 1 for $\varepsilon_c = 0.10$ with a linear trend line from which the pitch is calculated. b) and c) show the calculated pitch lengths for potentials 1 and B3 respectively

It is not possible to calculate the temperature at which the transition from a chiral nematic to an isotropic phase occurs for a bulk system as the periodic boundary conditions impose a constraint that there must be half integer values of pitch length in the system. Whilst the presence of the extra chiral term in the potential means that the transition temperature

will have altered from the non-chiral nematic case, it is assumed that the nematic-isotropic transition temperature does not deviate greatly from that of a non-chiral system.

Slab type simulations were also performed at $T^*/T^*_{N-I} = 0.80, 0.90 \text{ and } 0.95$ for potential 1 to investigate how the chiral pitch length varies with temperature. It was found that the chiral pitch length did not vary greatly with temperature (Figure 2.5.5). Experimentally, in general, the pitch length is dependent on temperature, with the pitch length decreasing with increasing temperature.[4]

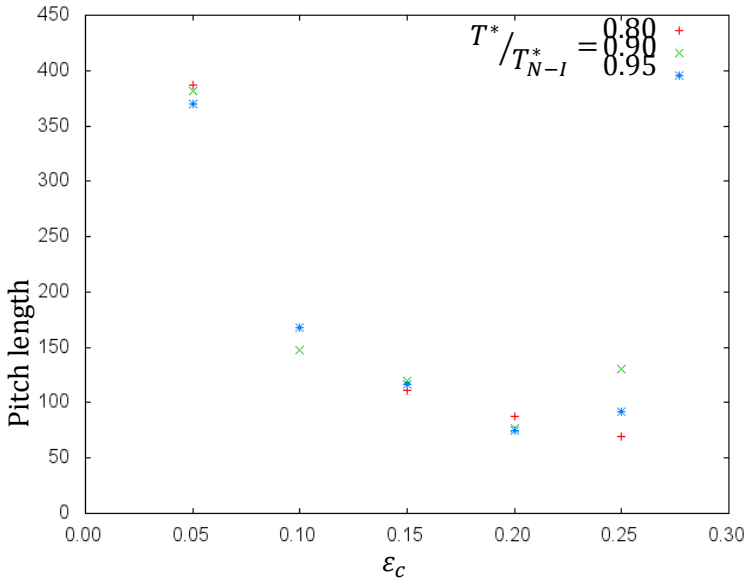

Figure 2.5.5 A graph showing how the pitch lengths vary with T^*/T^*_{N-I} for potential 1

2.5.3 *PHASE SEPARATION*

To ensure the pre-prepared slab geometry did not bias the phase separation observed, a simulation of a randomly distributed mixture comprising of 10% mesogen particles and 90% water particles were run in a cubic box with sides of 24σ where $\rho^* = 0.75$ and $T^*/T^*_{N-I} = 0.9$ was run. For all potentials, the simulations very rapidly showed phase separation to form small nematic droplets which slowly condensed thus proving the selected parameters induce phase separation between the liquid crystal and the water.

3 NEMATIC SHELLS

3.1 INTRODUCTION

Nematic shells are of interest as the confined geometry leads to unusual director configurations with the spherical geometry leading to the presence of defects in the ground state[100]. Experimentally, nematic shells produced are of inhomogeneous thickness due to the slight difference in density between the nematic and water droplet a thinning at the top of the nematic shell and a thickening of the nematic shell at the base is seen.

Nematic shells with homeotropic anchoring at both surfaces can form a defect-free director configuration and are spherical in symmetry. Nematic droplets with homeotropic anchoring has a hedgehog defect located at the centre of the droplet[101], but the removal of the liquid crystal from the centre removes this defect, leaving the defect-free shell (section 1.2.2 and 1.2.3). The defect-free nature and the spherical symmetry of nematic shells with homeotropic anchoring at both surfaces are relatively uninteresting in comparison with nematic shells with planar anchoring at both surfaces and so are only briefly considered.

For nematic shells with planar anchoring, it is geometrically impossible to form a defect-free nematic on the surface. The Poincaré-Hopf theorem[25] states that the total topological defect charge on the surface of a sphere must equal +2. The presence of four s=+1/2 defects to fulfil the constraint on the total topological charge on the surface of a sphere was first proposed by Lubensky and Prost[27], however recent work into spherical nematic shells with planar anchoring on both surfaces has been sparked by Nelson[28], who predicted the presence of a tetrahedral defect arrangement analogous to an sp^3 – hybridised carbon atom on the micrometre scale, which can have applications as photonic displays and bioassays. These double-emulsion systems have been created experimentally[29] *via* micro-fluidics. Simulations have been performed of infinitely thin

shells of hard spherocylinders[33, 35] and of shells of finite thickness using the Lebwohl-Lasher lattice-based model[37, 42].

The defect configurations seen in nematics shells with planar anchoring are thought to be dependent on the relative magnitudes of K_1 and K_3 [30, 35], with the bipolar defect configuration being favoured in pure bend or splay regimes. Previous computer simulations of nematic shells of finite thickness carried out using lattice-based models[37, 42] and numerical studies[32] have utilised a one elastic constant approach where $K_1 = K_2 = K_3 = K$ and have been unable to investigate the dependence of the defect configuration on the elastic constants. In contrast, previous computer simulations of an infinitely thin shell of hard spherocylinders have looked at the dependence of the defect configuration on K_1/K_3. By using the model described previously it is possible to vary relative energies of end-to-end and side-to-side interactions and slightly alter both K_1/K_3 and K_2/K_3 whilst taking into account the thickness of the shell.

In this chapter simulations employing a Monte Carlo technique (MC) are performed of both uniform and non-uniform thickness nematic shells, utilising an off-lattice potential described in chapter 2. In this chapter the research focusses on systems with planar anchoring although some systems with homeotropic anchoring are also investigated in uniform thickness shells.

3.2 SIMULATION PARAMETERS

All simulations were run from an initial isotropic phase at $T^*/T^*_{N-I} = 0.9$ in a cubic simulation cell with sides 48σ and N=82944, corresponding to $\rho^* = 0.75$ unless otherwise stated.

To recap, the systems have two types of particles - mesogens and water particles, leading to three interaction potentials discussed in chapter 2. The mesogen-mesogen interaction potential is

$$U^{LC-LC}(\boldsymbol{p}_i, \boldsymbol{p}_j, \boldsymbol{r}_{ij}) = \begin{cases} r \leq \sigma, & \infty \\ \sigma < r < 1.5\sigma, & U^{LC-LC}(\boldsymbol{p}_i, \boldsymbol{p}_j, \boldsymbol{r}_{ij}) \\ 1.5\sigma \leq r, & 0 \end{cases} \quad (3.2.1)$$

where $\boldsymbol{p_i}$ and $\boldsymbol{p_j}$ are unit vectors embedded at the centre of particle *i* and *j* respectively, $\boldsymbol{r}_{ij}$ is the intermolecular vector and

$$\begin{aligned} U^{LC-LC}(\boldsymbol{p}_i, \boldsymbol{p}_j, \boldsymbol{r}_{ij}) \\ = -\varepsilon \Big[J_1 (\boldsymbol{p}_i \cdot \boldsymbol{p}_j)^2 - 2J_2 (\boldsymbol{p}_i \cdot \boldsymbol{p}_j)(\boldsymbol{p}_i \cdot \hat{\boldsymbol{r}}_{ij})(\boldsymbol{p}_j \cdot \hat{\boldsymbol{r}}_{ij}) \\ + J_3 (\boldsymbol{p}_i \cdot \hat{\boldsymbol{r}}_{ij})^2 (\boldsymbol{p}_j \cdot \hat{\boldsymbol{r}}_{ij})^2 \Big] \end{aligned} \quad (3.2.2)$$

where ε is a positive constant and the values of $J_x$used in this chapter are given by Table 2.1.1. The water-water interaction potential is

$$U^{W-W}(\boldsymbol{r}_{ij}) = \begin{cases} r \leq \sigma, & \infty \\ \sigma < r < 1.5\sigma, & -\varepsilon_W \\ 1.5\sigma \leq r, & 0 \end{cases} \quad (3.2.3)$$

where $\varepsilon_W = 0.25$ unless otherwise stated. The mesogen-water interaction for planar anchoring is

$$U^{LC-W}(\boldsymbol{p}_i, \boldsymbol{r}_{ij}) = \varepsilon_{LC-W} + \varepsilon_A (\boldsymbol{p}_i \cdot \hat{\boldsymbol{r}}_{ij})^2 \quad (3.2.4)$$

where $\varepsilon_{LC-W} = 1$ and $\varepsilon_A = 5$ unless otherwise stated. Several preliminary simulations of uniform nematic shells with planar anchoring at both surfaces were run with values of

$\varepsilon_A = 1,2,3,4,5,10 \text{ and } 20$ for a nematic shell thickness of 10σ and 6σ. As ε_A increases, the repulsion between the mesogen and water particles increases leading to a small contraction of the nematic shell away from the surrounding water, however this contraction did not greatly alter the defect configurations seen.

Table 3.2.1 J_1, $J_2$and J_3 values for potentials used.

Potential	J_1	J_2	J_3
1	1.00	0.00	0.00
2	1.00	0.50	1.00
A1	1.00	0.125	0.00
A2	1.00	0.25	0.00
A3	1.00	0.375	0.00
B1	0.75	-0.125	0.00
B2	0.50	-0.25	0.00
B3	0.25	-0.375	0.00

The starting configurations were produced in the following way. Firstly, the simulation cell was filled with hard spheres on a simple cubic lattice at $\rho^* = 1.0$ from which particles were removed at random so that $\rho^* = 0.75$. A short simulation was then run in order to produce a bulk liquid state that filled the simulation cell uniformly. The shells were then created by carving out two spheres and assigning the particles between the spheres as mesogens.

For the uniform nematic shells, both the spheres used to carve out the shell were centred in the simulation box (Figure 3.2.1a). For the non-uniform nematic shell, the outer largest sphere was still centred in the simulation box, but the centre of the smaller inner sphere was displaced along the *z*-direction (Figure 3.2.1b). For all simulations, the radius of the

droplet (r_{out}) was equal to 20σ. The thickness of the nematic shell was varied by varying the radius of the inner water droplet (r_{in}).

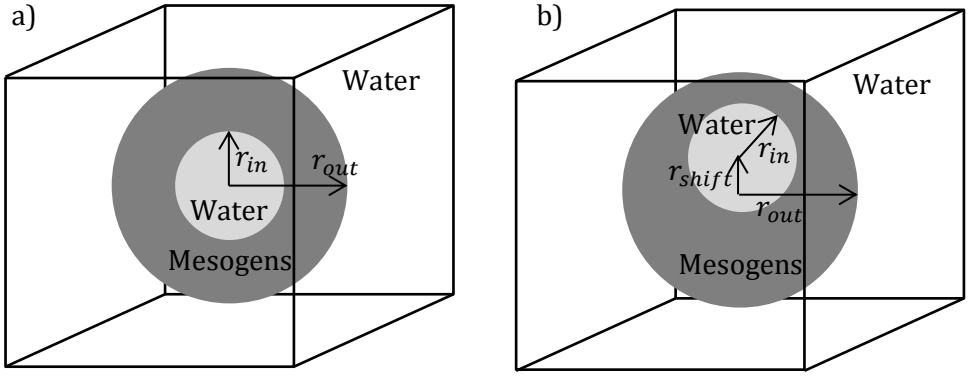

Figure 3.2.1 A schematic representation of the starting configuration for a) uniform and b) non-uniform thickness nematic shells. r_{in} and r_{out} are the radii of the inner and outer spheres respectively. r_{shift} is the amount the centre of the inner sphere is shifted in the *z*-direction in the non-uniform nematic shell systems.

For uniform thickness nematic shells, the radius of the inner sphere (r_{in}) was varied from 6σ to 14σ, corresponding to a nematic shell thickness of 14-6σ. For non-uniform thickness nematic shells, the inner sphere was shifted so that

$$r_{shift} + r_{in} \leq 16 \qquad (3.2.5)$$

as shells thinner than this 'popped' and formed a nematic droplet.

To gain statistically accurate information, each scenario was run for ten simulations started using different random number seeds.

3.3 OPTIMIZING MC FOR NEMATIC SHELL SIMULATIONS

In the systems investigated, the nematic shell forms only a small part of the system and for the thinnest shells, only 20.4% of particles in the system are mesogens. Whilst the water particles near the interfaces play an important role in the simulation controlling the type and strength of anchoring, the water particles away from the interface have negligible effect on the nematic shell.

Preliminary simulations of a nematic shell with planar anchoring that started from an isotropic phase, showed a rapid decrease in energy at the start of the simulation which may be due to the formation of the nematic phase. A similar initial fast decrease in energy was seen for all systems containing both mesogen and water particles when started from an isotropic phase. For preliminary simulations of uniform nematic shells, after in initial fast decrease in energy, the energy continued to decrease very slowly due to the slow movement of the defects through the nematic. The progression of defects through the shells can be seen by looking at areas of disorder throughout the simulation. Within 5000 MC steps after starting, four defects can be observed for all shell thicknesses. Then, as the simulation progresses, the defects move and in the case of the thicker shells, combine to form s=+1 defects.

To decrease the time taken for the simulations to reach equilibrium, the water particles in the simulation were separated into two groups; those inside a biasing cut off radius of 23σ from the centre of the simulation cell, and those outside it. A radius of 23σ was used as this was considered large enough to comfortably encompass the whole nematic shell, allowing for any small movement fluctuations that may have occurred. Preliminary investigations into the percentage of trial moves attempted for the water particles in the outer spheres showed the outermost water particles could not be completely frozen. A value of p = 0.25 in (3.3.2)and (3.3.3)was used.

The MC sampling technique had to be adjusted to account for moves crossing the biasing cut off boundary to maintain the number of water particles inside the cut off sphere. The number of water particles within the cut off sphere would artificially decrease because the close particles have a higher probability of passing outside the cut off area than the outside particles passing into the cut off area. The acceptance factor for an uphill trial move was multiplied by α, which for in-in and out-out moves is[91]

$$\alpha = 1 \tag{3.3.1}$$

whereas for in-out moves,

$$\alpha = {}^{p}/_{[1-(1-p)/N']} \tag{3.3.2}$$

and for out-in moves

$$\alpha = {}^{1}/_{p[1+(1-p)/N']} \tag{3.3.3}$$

where $N' = pN + (1-p)N_{in}$ and N_{in} is the number of particles inside the cut off sphere in the initial state. Simulations were run using this modified technique with 25% of trial moves attempted for water particles outside the cut off sphere with a radius of 23σ gave concordant results to those run using the slower unmodified technique.

3.4 UNIFORM THICKNESS NEMATIC SHELLS

In preliminary simulations, the density of the mesogens in thin shells from the central point was analysed ($g_{LC}(r)$)

$$g_{LC}(r) = \frac{N_{LC}dr}{4\pi r^2} \qquad (3.4.1)$$

Where *r* is the distance from the centre of the simulation cell, N_{LC} is the number of mesogens in a given shell and *dr* was taken to be 0.25*σ*.

All the simulations show that a spherical uniform nematic shell is maintained and that the spherical shell has not drifted from the starting position or been noticeably deformed (Figure 3.4.1). By maintaining a spherical uniform nematic shell the surface area of the nematic-water surface is minimised along with the repulsive interactions between the mesogen and water particles. Nematic shells of thicknesses less than 6*σ* were found to be unstable and 'pop', forming a bulk nematic droplet in the centre of the simulation cell.

For uniform nematic shells with planar anchoring at both surfaces, shell thicknesses ranging from 14*σ* to 6*σ* were investigated for the potentials given in Table 2.1.1.

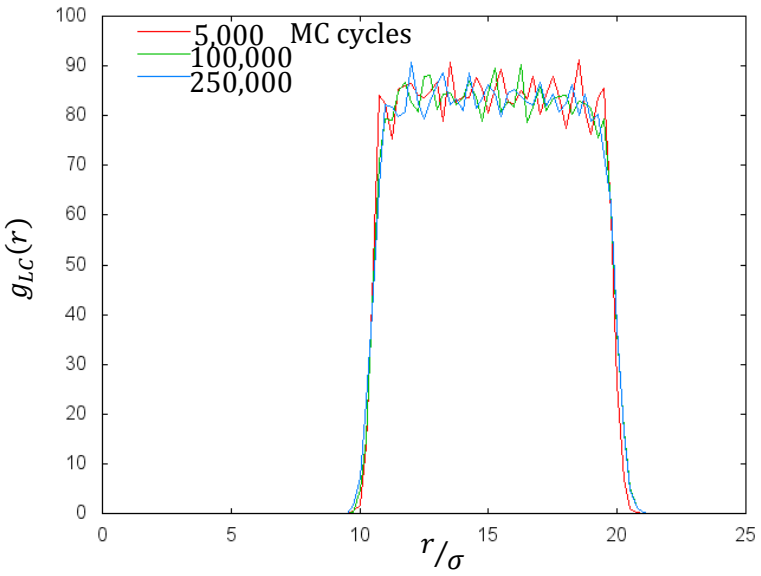

Figure 3.4.1 A graph showing $g_{LC}(r)$ for a shell of thickness 10*σ* for potential 1 after 5,000 (red), 100,000 (green) and 250,000 (blue) MC cycles

3.4.1 *UNIFORM THICKNESS NEMATIC SHELLS WITH PLANAR ANCHORING*

In all uniform thickness nematic shells with planar anchoring, the total topological charge on the inner and outer surfaces was +2, fulfilling the Poincaré-Hopf constraint. The type, number and position of defects seen in nematic shells with planar anchoring are dependent on the thickness of the nematic shell and two thickness regimes are defined dependent on the number of defects formed, thick shells and thin shells. Note that a shell with a particular thickness can behave as either a thin or thick shell dependent on the potential used.

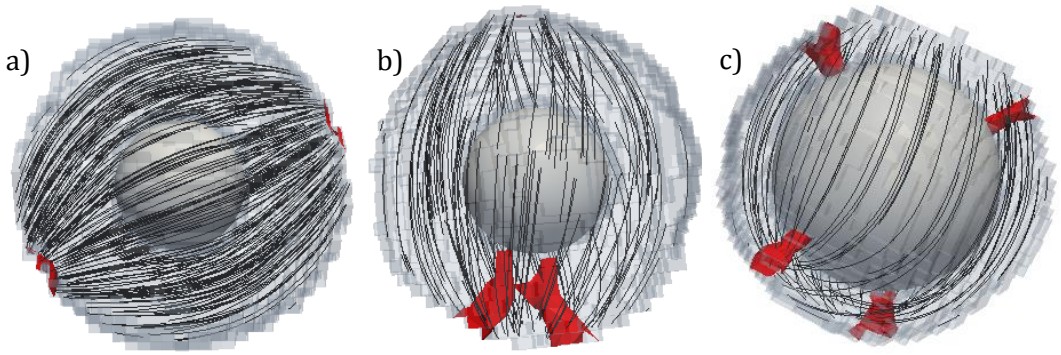

Figure 3.4.2 Potential 1 nematic shell thicknesses of a) 12σ, b) 11σ and c)9σ

For thick shells, a bipolar structure with two *s*=+1 defects was seen (Figure 3.4.2a), whereas for thin shells four *s*=+1/2 defects were seen (Figure 3.4.2c). At intermediate shell thicknesses a third defect configuration was occasionally seen consisting of one *s*=+1 and two *s*=+1/2 defects (Figure 3.4.2b). The three different defect configurations seen for equilibrated nematic shells of uniform thickness with planar anchoring are discussed in detail in the following sections. Table 3.4.1 shows the regions of thick and thin shell behaviour for potentials 1,2, A1, A3, B1 and B3.

Table 3.4.1Thick and thin shell behaviour for systems investigated where red=thick, green=thin and amber=intermediate thickness

Potential	**Nematic shell thickness/σ**							
	14	13	12	11	10	9	8	6
1								
2								
A1								
A3								
B1								
B3								

The switch in behaviour for potentials 1 and 2 occurred at a shell thickness of 9σ, or $h_c \approx 0.45$ where

$$h = {}^{r_{in}}/_{r_{out}} \tag{3.4.2}$$

And h_c is the threshold value below which a bipolar structure is formed and above which four *s*=+1/2 defects are seen. The calculated value of h_c for the systems in which the end-end and side-side interactions are of equal energy is slightly below the value found by Seyednejad *et al*[32] who found $h_c \approx 0.66$ and that seen experimentally by Fernandez-Nieves *et al*[29] who found $h_c \approx 0.50$. The value of h_c is governed by the size of the defect core (r_c) by[30]

$$h_c \approx e^4\sqrt{r_{out}r_c} \tag{3.4.3}$$

Which is when the energy of the boojums found in the thick shells and the four *s*=+1/2 defects are equal. The deviation away from the value of h_c found experimentally could be due to the relative thickness of the nematic shell to the size of the particle. In the simulations performed here, the nematic shell is of the order of ten particles thick whereas

experimentally the nematic shells are tens of thousands of times thicker than the length of the mesogen, *e.g.* the thin shells of 5CB produced *via* microfluidics by Fernandez-Nieves *et al*[29] are in the region of 50μm whereas the molecular length of 5CB is approximately 2nm in length. For the B series of potentials, the transition from a thick shell behaviour to a thin shell behaviour was seen for thicker nematic shells, increasing h_c and for potential B3 $h_c \approx 0.65$ suggesting that the potentials favouring end-end interactions give slightly more realistic results. Conversely, the A series of potentials favoured side-side interactions and for potential A3 $h_c \approx 0.40$.

3.4.2 *THICK NEMATIC SHELLS WITH PLANAR ANCHORING*

For shells which exhibited thick shell behaviour, two *s*=+1 defects, known as boojums are located at the poles of the droplet. A boojum consists of two *s*=+1 defects on the surface that are half-hedgehog defects. In the case of nematic shells, the defects on the inner surface are hyperbolic half-hedgehog defects, whereas on the outer surface the *s*=+1 defects are radial half-hedgehog defects[52]. The boojums are found at the poles of the shell as this maximises the distance between the defects, minimising the distortion of the director field between them.

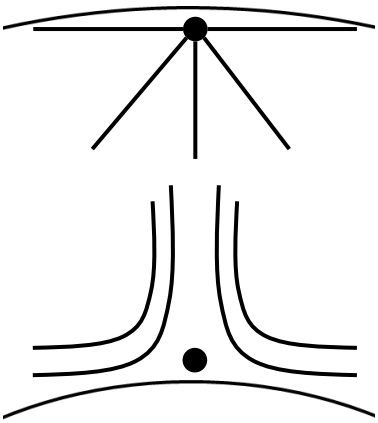

Figure 3.4.3 A schematic representation of a boojum showing a radial (top) and hyperbolic (bottom) half hedgehog defects

In a boojum there are only two regions of disorder at the centre of the two half hedgehogs on the surfaces, surrounded by a much larger region of some nematic order where the director is not planar to the surface. The small size of the disordered region means that the *s*=+1 defects were very hard to locate purely using a threshold of c_l and it was not possible to locate the hyperbolic half hedgehog defects on the inner in this manner. Using a threshold value of $c_l < 0.25$ did pick up the hyperbolic half hedgehog at the inner surface (Figure 3.4.4b), however the radial half hedgehog was then much wider. When a value of $c_l < 0.35$ (Figure 3.4.4c) was used regions on the outer surface away from the defects were also found possibly due to the lower liquid crystal density in some analysis boxes close to the surface leading to a lower order parameter than the analysis boxes further within the nematic shell. The local order parameter in the nematic shell was approximately 0.6, which is similar to that seen in the preliminary simulations of a nematic confined between two flat interfaces (section 2.5.1). It was, however, easy to locate the boojums visually with the aid of the director streamlines. Due to the difficulty in locating both constituent half hedgehogs in a boojum, it was not possible to analyse the angles between the defects to verify the bipolar nature of the droplet seen by eye in the visualisations.

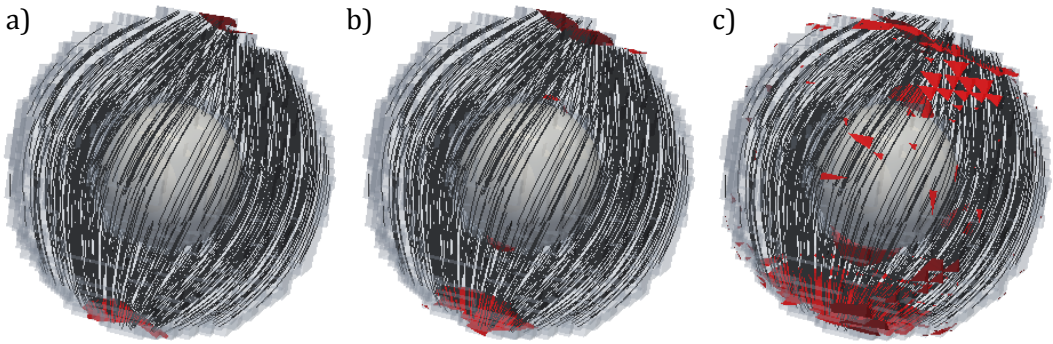

Figure 3.4.4 A nematic shell of thickness 11σ showing two *s*=+1 defects with a) $c_l < 0.15$, b) $c_l < 0.25$ and c) $c_l < 0.35$

As shown in Table 3.4.1, For potentials 1 and 2, where the end-end and side-side interactions are equally favoured, the bipolar structure was only found for shells of with a thickness of 10σ or greater (Figure 3.4.2a). It was found that, for potentials where the side-side interaction was favoured (potentials A1-3), the bipolar configuration was observed in thinner shells and for potential A3 where the difference in energy between the side-side and end-end interactions was the greatest, the bipolar defect configuration was seen in shells as thin as 8σ. Conversely, for potentials where the end-end interaction was favoured (potentials B1-3), the bipolar defect configuration was only seen in very thick shells. For potential B3 where the end-end interaction is much lower in energy than the side-side interaction, the bipolar configuration is only seen for shells of thickness 13σ and above.

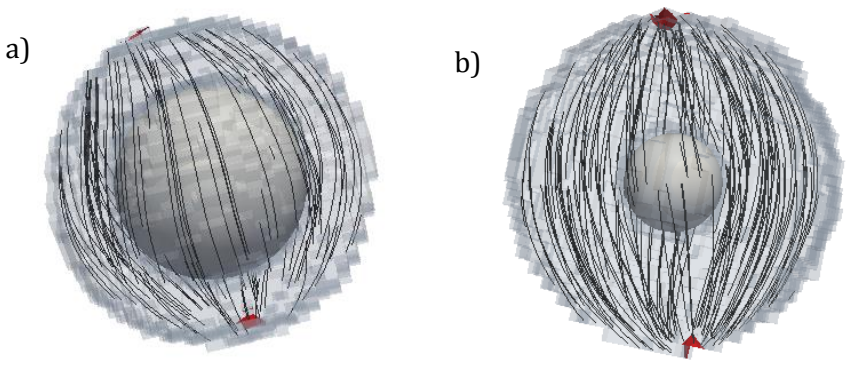

Figure 3.4.5 The Bipolar configuration in a nematic shell with planar anchoring for a) potential A3 with a shell thickness of 8σ and b)potential B3 with a shell thickness of 14σ

The lack of thick shell behaviour exhibited by the B potential series can be explained in the following manner. As shown in Figure 3.4.3, the boojum has a region between the two half hedgehogs on the surfaces where the director is perpendicular to the surfaces. As stated previously, the nematic shells are only a few particles thick meaning that the number of end-end interactions at the region between the half hedgehogs is much fewer than the side-side interactions. Conversely, the s=+1/2 disclination lines do not have this region where the director is perpendicular to the surfaces and so the cross over from a bipolar

defect configuration to four *s*=+1/2 defects is seen much earlier in the potentials where end-end interactions are lower in energy than side-side interactions.

3.4.3 *THIN NEMATIC SHELLS WITH PLANAR ANCHORING*

For thin nematic shells with planar anchoring, four *s*=+1/2 defects (Figure 3.4.2c) were found. Unlike the boojums seen for thick nematic shells, the *s*=+1/2 defects are disclination lines running through the nematic bulk from the inner to the outer surface. Four *s*=+1/2 defects were seen for simulations using potential 1 and 2 for shells of 10σ or thinner. As seen in section 3.4.2, for simulations where the side-side interactions were favoured, the switch from a bipolar structure in thick shells to four *s*=+1/2 defects occurred in thinner shells than those run with where the side-side and end-end interactions were equal in energy. For potential A3, only in the very thinnest shells of thickness 8σ or below were any *s*=+1/2 defects observed. The converse was true for systems that preferred end-end interactions and four *s*=+1/2 defects were seen in shells of thickness 13σ or thinner for potential B3.

Due to the nature of the *s*=+1/2 defects, it was easy to locate the defects using a threshold of $c_l \leq 0.15$. In order to minimise the distortion in the director and the elastic energy of the system, the defects repel each other. The configuration that maximises the distance between defects is when the defects are located at the vertices of a tetrahedron in an analogous arrangement to the hydrogen atoms around the central carbon atom seen in methane.

It was possible to investigate the angles between *s*=+1/2 defects in order to quantify the defect configuration in thin shells with four *s*=+1/2 defects. Two different angles were calculated, the angle between two defects and the centre (Figure 3.4.6a) and the angle between three defects (Figure 3.4.6b).

a) b)

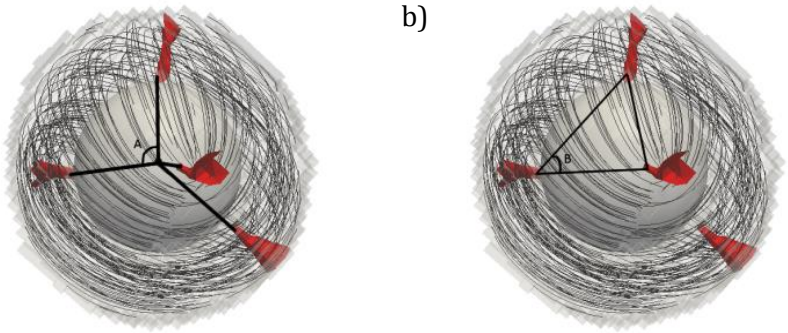

Figure 3.4.6 Diagram showing a) the internal angle between defects in a four s=+1/2 configuration and b) the torsional angle between three defects (B).

The defects were located by defining any regions where four or more adjacent analysis cells with $c_l < 0.15$. It was possible to calculate angle A between two defects and the centre in three ways;

1. The position of the defect on the inner surface
2. The position of the defect on the outer surface
3. The inertia tensor of the defect

The position of the defect on either surface was taken as the middle of the defect when looking at cubic analysis cells whose centre was less than 2σ away from the surface in question. For angle B between three defects it was only possible to use the positions on either surface but not using the inertia tensor. For each scenario investigated, ten simulations were run with a different initial random number seed. It was found that the resulting histogram of angles was very similar using all three defect definitions and the results reported here are from method 3 as the standard deviation tended to be slightly lower, *e.g.* for a nematic shell of thickness 9σ using potential 1 the standard deviation was 23.7^o, 22.8^o and 22.0^o using method 1 to 3 respectively.

For each scenario investigated, a distribution of defect configurations was seen. Snapshots from a simulation of shell thickness 8σ for potential 1 are shown in Figure 3.4.7. For a tetrahedral defect configuration the angle between two defects and the centre is 109.5^o

and the angle between three defects is 60° whereas for the great circle defect configuration, similar to that shown in Figure 3.4.7b it is expected that both angular distributions $f(A)$and $f(B)$ will peak at 90°. For uniform nematic shells with planar anchoring all the angle distribution seen for both the angle between two defects and the centre and between three defects gave a normal distribution, to which a Gaussian curve was fitted to calculate the mean angle.

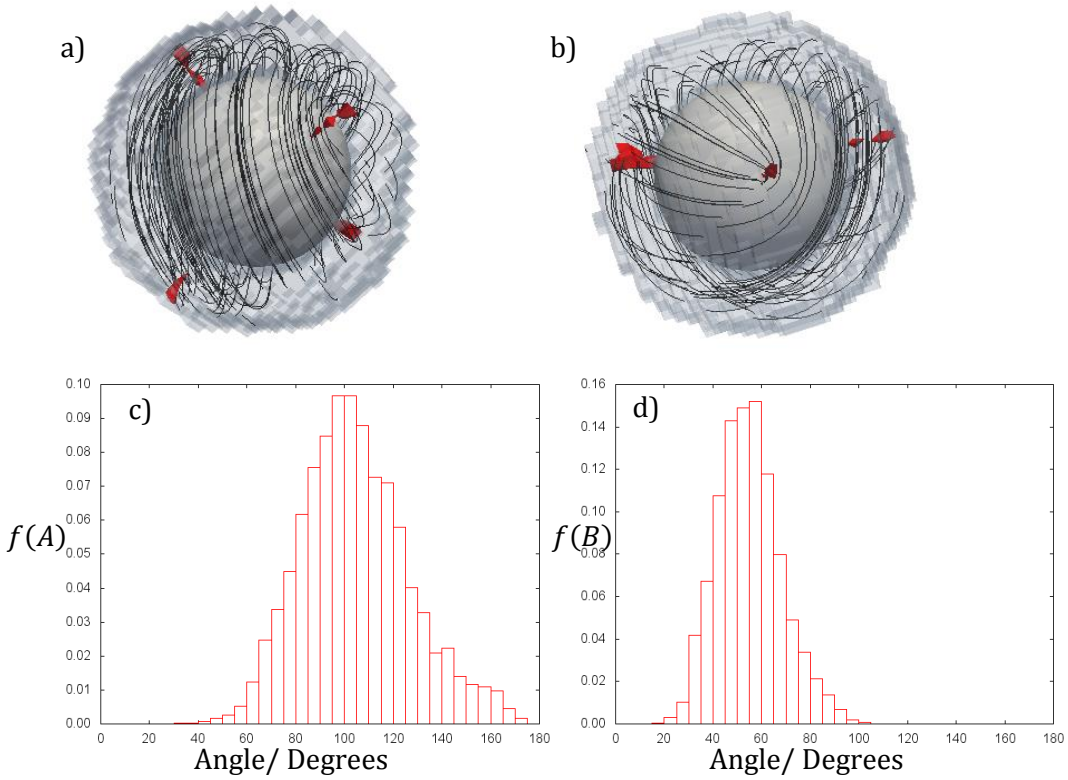

Figure 3.4.7 a) and b) show a uniform nematic shell of thickness 8σ with planar anchoring for potential 1 with four *s*=+1/2 defects in a tetrahedral and great circle arrangement respectively. c) and d) are the angle distributions for the angle between two defects and the centre and three defects respectively.

The resulting histograms of both $f(A)$ and $f(B)$ for a nematic shell thickness of 8σ for potential 1 show that the average defect configuration is roughly tetrahedral in nature. Similar results are seen for all thicknesses where thin behaviour (*i.e.* four *s*=+1/2 defects) is observed for all potentials. Previously, it has been observed that whilst the tetrahedral defect configuration is favoured when the elastic constants are equal, as ${}^{K_3}/_{K_1} \rightarrow \infty$ at

temperatures just above the nematic-smectic transition[40], a great circle configuration in which all the defects are located at the 'waist' of the droplet is favoured[34]. It is likely that for the potentials employed in this chapter the difference between the elastic constants K_1 and K_3 is not large enough to drive the defect configuration to favour an arrangement with the defects located on the great circle of the sphere.

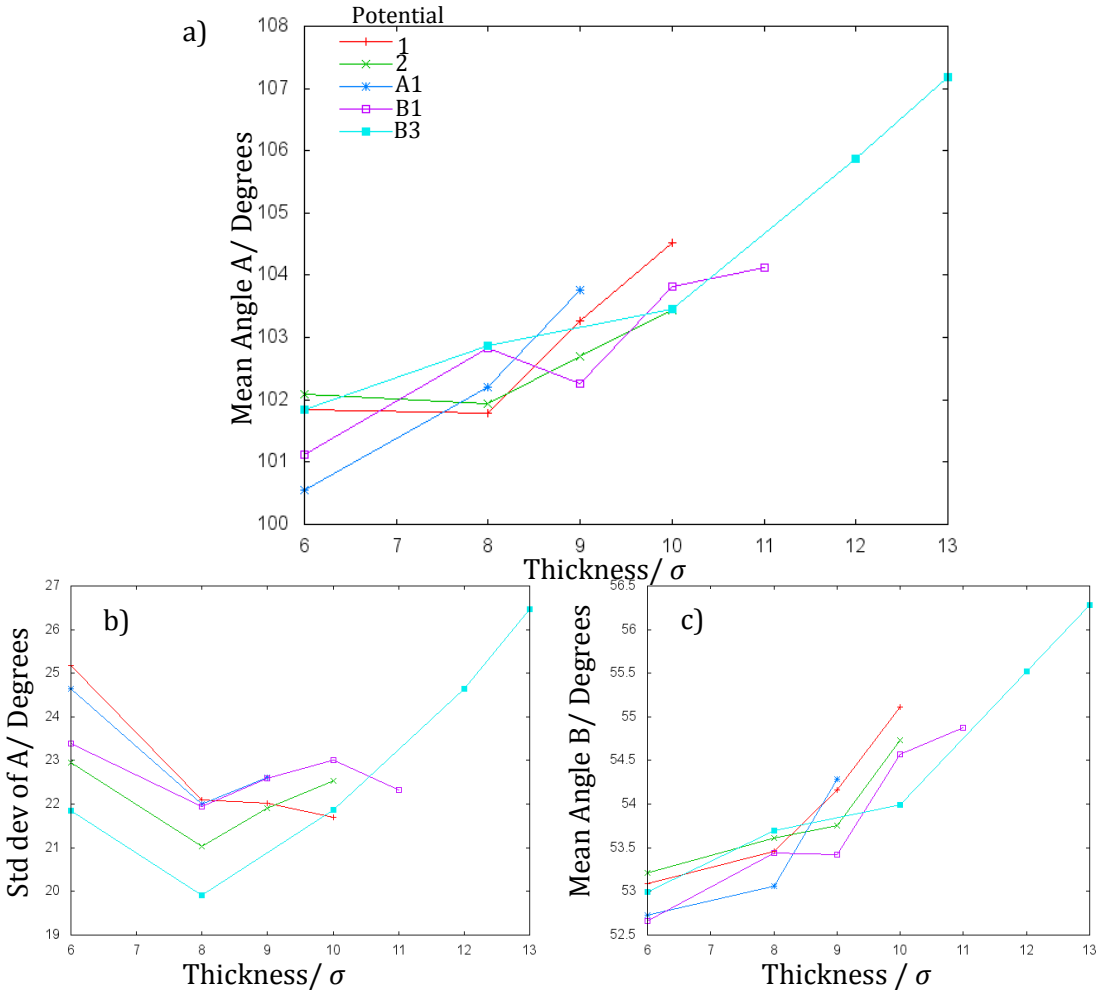

Figure 3.4.8 Graphs showing the variation of a) mean angle A b) the standard deviation of A and c) the mean angle B with shell thickness for each potential

For all potentials investigated, the mean angle between two defects and the centre, angle A, (Figure 3.4.8a) and the mean angle between three defects, angle B, (Figure 3.4.8c) decreases with decreasing thickness of the nematic shell whilst the standard deviation is nearly constant across the shell thicknesses investigated (Figure 3.4.8b). The decrease in the angle between two defects and the centre is most apparent in potential B3 which

shows thin shell behaviour over the widest range of nematic shell thicknesses. The decrease angle A could be due to the decreasing length of the defects as the nematic shell thins. The free energy of a disclination line is proportional to the length of the disclination meaning greater repulsion between pairs of defects is felt in thicker shells where the *s*=+1/2 defects are longer.

3.4.4 *INTERMEDIATE THICKNESS NEMATIC SHELLS WITH PLANAR ANCHORING*

In nematic shells with planar anchoring at both surfaces of thicknesses highlighted in amber in Table 3.4.1, a third defect configuration consisting of one *s*=+1 and two *s*=+1/2 defects was occasionally seen along with both the bipolar and four defect configurations (Figure 3.4.2b). The third metastable defect configuration is only seen in thicknesses between thick and thin shell behaviour along with both the bipolar and four defect structures, highlighting the similarity in energy between two *s*=+1/2 and one *s*=+12 defect at these nematic shell thicknesses.

3.4.5 *TEMPERATURE DEPENDENCE*

In simulations run at $T^*/T^*_{N-I} = 0.9$ all the nematic shells with planar anchoring regardless of thickness, when started from an isotropic system initially formed four *s*=+1/2 defects. The four defects either remained (in thin shells) or coalesced to form either one (intermediate thickness shells) or two (thick shells) *s*=+1 defects. The presence of the four *s*=+1/2 defects at the outset in shells of all thicknesses could indicate that the four *s*=+1/2 defects are a metastable state of the thicker shells or it could merely be that *s*=+1/2 defects form faster than *s*=+1 defects but are less energetically favourable. In order to determine if four *s*=+1/2 defects are a metastable state in thick nematic shells with planar anchoring, simulations were run at lower temperatures in an attempt to stabilise four defect

configuration in the thicker shells. Simulations were run for potentials 0, 19, A1, A3, and B1 at ${T^*}/{T^*_{N-I}} = 0.4 - 0.8$ in 0.1 intervals for a nematic shell of thickness 10σ.

At ${T^*}/{T^*_{N-I}} = 0.5$ and above, four *s*=+1/2 defects are initially seen which then coalesce to form the expected bipolar configuration, suggesting that the four *s*=+1/2 defect configuration is not metastable.

At ${T^*}/{T^*_{N-I}} = 0.40$ a bipolar configuration was not seen unlike higher temperatures and the director lines do not align with the surface instead running straight through the shell. The lack of anchoring at the mesogen-water interface is due to the contraction of the mesogen away from the surface leaving a void surrounding the shell, as seen in preliminary simulations of systems with a large solid particle (section 5.2.3). The contraction away from the surface is not seen at higher temperatures as the kinetic energy of the mesogens overcomes the repulsion between the mesogen and water particles at the surface.

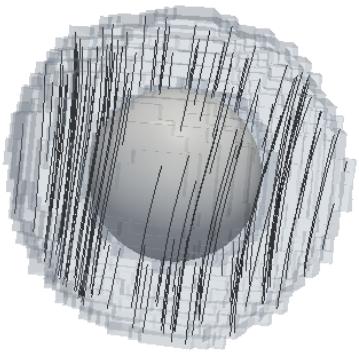

Figure 3.4.9 Director configuration for potential 2 with a nematic shell of thickness 10σ at ${T^*}/{T^*_{N-I}} = 0.40$

3.4.6 *HOMEOTROPIC ALIGNMENT*

In sections 3.4.1 to 3.4.5 the anchoring at both surfaces of the nematic shell has been planar in nature. In this section, nematic shells with homeotropic anchoring at both surfaces are investigated. As noted earlier, homeotropic anchoring at both surfaces should lead to a hedgehog type director configuration with no defects and is spherical in symmetry. Simulations using

$$U^{LC-W}\left(\boldsymbol{p}_i, \boldsymbol{r}_{ij}\right) = \left(\varepsilon_{LC-W} + \varepsilon_A\right) - \varepsilon_A\left(\boldsymbol{p}_i \cdot \hat{\boldsymbol{r}}_{ij}\right)^2 \qquad (3.4.4)$$

were performed with $\varepsilon_{LC-W} = 1$ and $\varepsilon_A = 1, 5 \text{ and } 10$ for all potentials listed in Table 2.1.1 for nematic shells thicknesses of 10σ and 6σ. The resulting director configuration was as expected and can be seen in Figure 3.4.10.

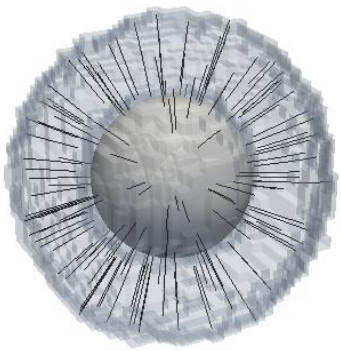

Figure 3.4.10 A nematic shell with homeotropic anchoring at both surfaces showing a defect free director configuration for potential 1, nematic shell thickness of 10σ

3.5 NON-UNIFORM THICKNESS NEMATIC SHELLS

In nematic shells created experimentally *via* microfluidics[29], the slight difference in density between the inner water droplet and the surrounding nematic shell causes the inner droplet to travel to the top of the nematic shell, which in turn causes a thickening at the base of the droplet and a thinning at the top of the nematic shell. In the non-uniform nematic shells produced, the four *s*=+1/2 defects observed in thin shells are no longer located at the vertices of a tetrahedron, rather they are all located at the thinnest part of the nematic shell. In order to investigate systems that are more akin to those seen experimentally, simulations of non-uniform nematic shells with planar anchoring at both surfaces were run.

Simulations were run using potentials 1, 2, A1, A3, B1 and B3 for the systems with $r_{out} = 20\sigma, r_{in} = 10, 11, 12 \text{ and } 13\sigma$ and $r_{in} + r_{shift} = 16\sigma$ in addition to $r_{in} = 11\sigma$ and $r_{shift} = 4\sigma$. Non-uniform nematic shells in which in which $r_{in} + r_{shift} > 16\sigma$ 'popped'. As with the uniform nematic shell systems investigated, all simulations were started from an isotropic phase and run at $T^*/T^*_{N-I} = 0.9$ unless otherwise stated. A schematic of the starting configuration can be seen in Figure 3.2.1b, where the thinnest part of the nematic shell is in the positive *z*-direction (at the 'top' of the simulation box) and the thickest part of the nematic shell in the negative *z*-direction (at the 'bottom' of the simulation box) .

3.5.1 *NON-UNIFORM THICKNESS NEMATIC SHELLS WITH PLANAR ANCHORING*

It was found in all the simulation of non-uniform thickness nematic shells that, as in the uniform nematic shell simulations, the inner water droplet did not move significantly through the duration of the simulations.

As with the uniform thickness nematic shells a transition from a bipolar defect configuration consisting of two *s*=+1, known as thick shell behaviour, to four *s*=+1/2 defects, known as thin shell behaviour was seen for non-uniform thickness nematic shells. The type of behaviour exhibited for each scenario investigated is detailed in Table 3.5.1.

Table 3.5.1 Thick and thin shell behaviour for systems investigated where red=thick, green=thin and amber=intermediate thickness

Potential	$r_{in} = 10\sigma$, $r_{shift} = 6\sigma$	$r_{in} = 11\sigma$, $r_{shift} = 5\sigma$	$r_{in} = 11\sigma$, $r_{shift} = 4\sigma$	$r_{in} = 12\sigma$, $r_{shift} = 4\sigma$	$r_{in} = 13\sigma$, $r_{shift} = 3\sigma$
1					
2					
A1					
A3					
B1					
B3					

A similar trend in the stability of thin and thick behaviour across the interaction potentials is observed for non-uniform thickness nematic shells as in uniform thickness nematic shells with planar anchoring at both surfaces. For potentials 1 and 2 in which the side-side and end-end interactions are equal in energy, purely thin shell behaviour is seen for $r_{in} = 11\sigma$ whereas for the B series of potentials where the end –end interactions are favoured four *s*=+1/2 defects were seen for all values of r_{in} investigated in non-uniform thickness

nematic shells. Conversely, the A series of potentials investigated where side-side interactions are favoured showed thick shell behaviour to a larger value of r_{in}, again in agreement with that shown in uniform thickness nematic shells. All the defect configurations seen in non-uniform thickness nematic shells with planar anchoring at both surfaces fulfil the constraint on the total topological charge located on the inner and outer surfaces, being equal to +2.

Whilst in both uniform and non-uniform nematic shells with planar anchoring the A

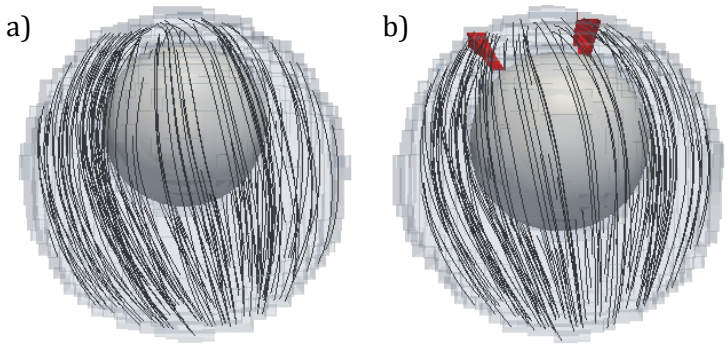

Figure 3.5.1 Non-uniform nematic shells with planar anchoring for potential A3 for a) $r_{in} = 10\sigma$ and $r_{shift} = 6\sigma$ and b) $r_{in} = 11\sigma$ and $r_{shift} = 4\sigma$

interaction potential series favoured the formation of *s*=+1 defects, by shifting the inner droplet away from the centre, the three defect director configuration was stabilised (Figure 3.5.1b). Indeed, for potential A3, in uniform thickness nematic shells only shells of thickness 6σ, corresponding $r_{in} = 14\sigma, r_{shift} = 0\sigma$, showed any *s*=+1/2 defects however in non-uniform nematic shells with planar anchoring when $r_{in} = 11\sigma, r_{shift} = 4\sigma$ and 5σ the defect configuration with one *s*=+1 and two *s*=+1/2 defects were observed in 55% of the simulations. The three defect configuration is also stabilised with respect to both the two and four defect configuration in the case of $r_{in} = 10\sigma, r_{shift} = 6\sigma$ compared to the un-shifted shell, $r_{in} = 10\sigma, r_{shift} = 0\sigma$, for potentials 1, 2 and A1 (Table 3.5.2).

Table 3.5.2 The percentages of two, three or four defects observed for $r_{in} = 10\sigma$ in uniform and non-uniform nematic shells

Potential	% of two *s*=+1 defects		% of one *s*=+1 and two *s*=+1/2 defects		% of four *s*=+1/2 defects	
	$r_{shift} = 0\sigma$	$r_{shift} = 6\sigma$	$r_{shift} = 0\sigma$	$r_{shift} = 6\sigma$	$r_{shift} = 0\sigma$	$r_{shift} = 6\sigma$
1	0	0	10	30	90	70
2	10	0	30	50	60	50
A1	20	10	20	50	60	40

In systems with two *s*=+1 defects, the director configuration was very similar to that seen in uniform thickness nematic shells with planar anchoring where the defects are boojums located at the poles of the droplet (Figure 3.4.5). In all non-uniform nematic shells with planar anchoring that formed a bipolar defect configuration; one defect is located at the top of the simulation at the thinnest part of the shell and one at the thickest part of the nematic shell at the bottom of the simulation (Figure 3.5.1a).

In a theoretical study by Koning *et al*[36] it is predicted that at some values of Δ, where

$$\Delta = {}^{r_{shift}}/_{r_{out}} \qquad (3.5.1)$$

the *s*=+1 boojum located at the thickest part of the nematic shell will migrate to the top of the simulation, producing what was termed the "confined configuration" as the two defects are confined to the thinnest hemisphere. The Δ value at which the confined and deconfined, where the defects are not confined to one hemisphere *i.e.* a bipolar configuration, can be seen is dependent on *h,* where *h* is as defined in (3.4.2). In the systems investigated here, $h = 0.5$ for $r_{in} = 10\sigma$, and the critical value of Δ where only the deconfined (bipolar) configuration is predicted, Δ_d, is approximately 0.7. The value of Δ_d

calculated is larger than Δ for any systems investigated so only a deconfined (bipolar) defect configuration is predicted, and indeed no confined defect configurations were observed for any potentials.

In systems with four *s*=+1/2 defects, the defects migrate away from a tetrahedral

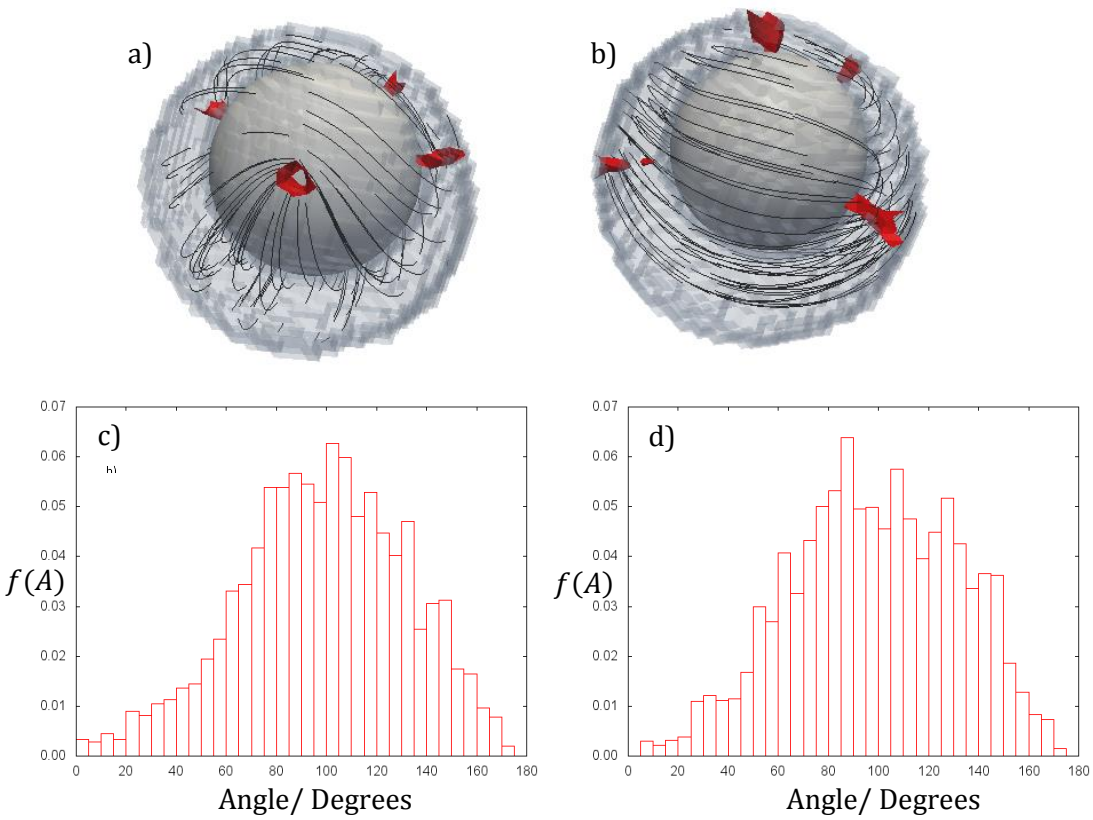

Figure 3.5.2 Non-uniform thickness nematic shells with planar anchoring where a) $r_{in} = 13\sigma, r_{shift} = 3\sigma$ b) $r_{in} = 11\sigma, r_{shift} = 5\sigma$ .c) and d) show the distributions of angles between two defects and the centre for a) and b) respectively.

arrangement to the thinnest part of the nematic shell. The driving force of the migration to the thinnest part of the nematic shell is the minimisation of the total energy of the disclination lines as the energy of a disclination line is proportional to the length which overcomes the long range repulsion between the defects. As in systems with uniform thickness nematic shells with four *s*=+1/2 defects, the distribution of angles between two defects and the centre and between three defects was calculated. Whereas for uniform nematic shells the angle distribution between two defects and the centre was a normal

distribution centred on approximately the predicted angle for the defects located in a perfect tetrahedron, for non-uniform nematic shells this is not the case. Figure 3.5.2c and d clearly show an increasing peak for larger values for the angle between two defects and the centre, rather than the normal distribution seen in uniform thickness nematic shells with the same r_{in}, indeed when a Gaussian function is fitted to the non-uniform nematic shells, the standard deviation is approximately 35^{o} compared to 22^{o} for the uniform thickness nematic shells.

3.6 CONCLUSIONS

In this chapter, both uniform and non-uniform thickness nematic shells have been investigated using an off-lattice model based on hard spheres with an embedded orientation vector. It has been shown that for nematic shells with homeotropic anchoring at both surfaces, a defect-free ground state similar to a hedgehog is observed in all systems. In nematic shells with planar anchoring at both surfaces defects much occur such that the total topological charge on both the inner and outer surface must be equal to +2, this is known as the Poincaré-Hopf constraint.

For nematic shells with planar anchoring at both surfaces the type, number and position of defects seen is highly dependent on the thickness of the nematic shell, with two *s*=+1 defects being seen for thick shells and four *s*=+1/2 defects being seen for thin shells. For nematic shells of intermediate thickness a third metastable defect configuration consisting of one *s*=+1 and two *s*=+1/2 defects is occasionally observed, in agreement with experimentally obtained results[30].

For thick nematic shells with planar anchoring at both surfaces a bipolar configuration consisting of two *s*=+1 boojums are seen at the poles of the shell for both uniform and non-uniform shell thicknesses. These boojums consist of a hyperbolic half hedgehog and a radial half hedgehog on the inner and outer surfaces respectively.

For thin nematic shells with planar anchoring at both surfaces four *s*=+1/2 defects were found. These defects were disclination lines through the nematic shell. In uniform nematic shells, these defects tended to be found in a tetrahedral arrangement, although due to the fluid nature of the system other defect configurations were also occasionally seen, including a distorted tetrahedron and a great circle defect configuration in which the defects are located in one plane through the centre of the droplet. In non-uniform nematic shells, the four *s*=+1/2 defects migrated to the thinnest part of the nematic shell, in

agreement to that seen in experimental systems where the shells produced are of non-uniform thickness. The movement of the defects to the thinnest part of the nematic shell occurs as the reduction in energy due to the short length of the defects overcomes the repulsion felt between the defects.

For nematic shells with planar anchoring for intermediate thicknesses a combination of thin (four s=+1/2) and thick shell (two *s*=+1) behaviour is seen, along with a metastable hybrid defect configuration consisting of one *s*=+1 and two *s*=+1/2 defects. In non-uniform nematic shells, this intermediate defect configuration is stabilised, with the boojum at the thinnest part of the nematic shell splitting into two *s*=+1/2 defects.

Eight different mesogen-mesogen interaction potentials were employed and whilst the interaction potentials gave broadly similar results, the thickness at which the transition from thick to thin behaviour in nematic shells with planar anchoring at both surfaces occurred was dependent on the potential used. In simulations run with potentials 1 and 2, where the end-end and side-side interactions are equally favoured, the bipolar defect configuration was seen for shells of thickness 10σ or greater, however for potentials A1-3 which favoured the side-side interactions, the bipolar configuration was more stabilised with respect to the thin shell behaviour and for potential A3 was seen in shells as thin as 8σ. Conversely, for potentials B1-3 where end-end interactions are favoured, thin shell behaviour was more stable and for potential B3 the bipolar defect configuration was only seen in shells of thickness 13σ and greater.

4 CHIRAL NEMATIC SHELLS

4.1 INTRODUCTION

A chiral nematic or cholesteric phase is the chiral analogue of the nematic phase and is produced from either a chiral molecule or doping a nematic phase with a small amount of a chiral dopant. In the cholesteric phase, the $D_{\infty h}$ symmetry of the nematic phase is reduced to D_{∞} due to an inherent twist perpendicular to the director. The pitch length of a chiral nematic phase is defined as the length for the helix perpendicular to the director to rotate by 2π radians.

There has been a wide range of research into the effect of chirality on the director configurations in liquid-crystalline filled droplets with planar anchoring[102]. It has been found that, at a low chirality where the pitch is much larger than the droplet radius, a chiral nematic droplet forms a twisted bipolar structure (Figure 1.2.3a) in place of the usual bipolar structure[26] (Figure 1.2.2a) due to the intrinsic twist present in the chiral nematic. At higher chirality, when the pitch is shorter than the droplet a Frank-Pryce structure is seen consisting of a *s*=+2 defect line connected to a hedgehog defect at the centre of the droplet (Figure 1.2.3b). All the director configurations seen in cholesteric droplets with planar anchoring have a total topological charge on the surface equal to +2, fulfilling the Poincaré-Hopf constraint[25].

Only very recently have chiral nematic shells been fabricated by Uchida *et al*[41] *via* microfluidics and a number of different dyes have been encapsulated within the chiral nematic shells in order to investigate the photonic properties of an array of such systems. Uchida *et al* found a single disclination line of *s*=+2, similar to that seen in a Frank-Pryce structure seen in filled cholesteric droplets.

In this chapter the simple off-lattice model used in the previous chapters based on hard spheres with a centred orientation vector is employed with an additional chiral term. An off-lattice model is needed to investigate chiral nematic shells as, although it is possible to model chiral nematics using a lattice model, the direction of the helical twist is constrained to be along one of the three axes of the lattice. Whilst this constraint does not matter in bulk systems, in confined systems such as the shells investigated in this chapter and the toroidal droplets investigated in subsequent chapters the constraint on the direction of the helical twist could lead to a resulting unrealistic director configuration. An off-lattice model has no such constraints on the orientation of the twist.

4.1.1 *Simulation Parameters*

The interaction potential used to simulate a chiral nematic phase is detailed in chapter 2, along with the calculated associated pitch lengths. To recap, an additional chiral term[94] was added to the mesogen – mesogen interaction potential used in the previous chapter for non-chiral nematic shells.

$$U^{LC-LC}(\boldsymbol{p}_i, \boldsymbol{p}_j, \boldsymbol{r}_{ij}) = \begin{cases} r \leq \sigma, & \infty \\ \sigma < r < 1.5\sigma, & U^{LC-LC}(\boldsymbol{p}_i, \boldsymbol{p}_j, \boldsymbol{r}_{ij}) + U^{LC-LC}_{chiral}(\boldsymbol{p}_i, \boldsymbol{p}_j, \boldsymbol{r}_{ij}) \\ 1.5\sigma \leq r, & 0 \end{cases} \quad (4.1.1)$$

Where

$$U^{LC-LC}(\boldsymbol{p}_i, \boldsymbol{p}_j, \boldsymbol{r}_{ij}) = -\varepsilon \left[J_1 (\boldsymbol{p}_i \cdot \boldsymbol{p}_j)^2 - 2J_2 (\boldsymbol{p}_i \cdot \boldsymbol{p}_j)(\boldsymbol{p}_i \cdot \hat{\boldsymbol{r}}_{ij})(\boldsymbol{p}_j \cdot \hat{\boldsymbol{r}}_{ij}) + J_3 (\boldsymbol{p}_i \cdot \hat{\boldsymbol{r}}_{ij})^2 (\boldsymbol{p}_j \cdot \hat{\boldsymbol{r}}_{ij})^2 \right] \quad (4.1.2)$$

In this chapter, both potentials 1 and B3 were investigated. Potential 1 is the simplest potential used with $J_1 = 1, J_2 = 0$ and $J_3 = 0$ whereas potential B3 favoured end to end interactions with $J_1 = 0.25, J_2 = -0.375$ and $J_3 = 0$. In potential 1, the elastic constants

are approximately equal, whereas for potential B3, $K_1 = K_3 > K_2$. Potential B3 was investigated as it formed the tetrahedral arrangement of four *s*=+1/2 defects in much thicker nematic shells than the potentials (see chapter 3).

The additional chiral term used in the interaction potential was

$$U_{chiral}^{LC-LC}(\boldsymbol{p_i}, \boldsymbol{p_j}, \hat{\boldsymbol{r}}_{\boldsymbol{ij}}) = \varepsilon_c[\hat{\boldsymbol{r}}_{\boldsymbol{ij}} \cdot (\boldsymbol{p_i} \times \boldsymbol{p_j})][(\boldsymbol{p}_i \cdot \boldsymbol{p}_j)] \quad (4.1.3)$$

When $\boldsymbol{p_i}$ and $\boldsymbol{p_j}$ are in the same plane, the cross product ($\boldsymbol{p_i} \times \boldsymbol{p_j}$) is orthogonal to $\hat{\boldsymbol{r}}_{\boldsymbol{ij}}$, meaning that the resulting dot product ($\hat{\boldsymbol{r}}_{\boldsymbol{ij}} \cdot (\boldsymbol{p_i} \times \boldsymbol{p_j})$) is zero. Conversely, when $\boldsymbol{p_i}$ and $\boldsymbol{p_j}$ are not in the same plane, the potential causes a helical twist to be favoured [95].

The water-water and mesogen-water interaction potentials used in this chapter are

$$U^{W-W}(\boldsymbol{r}_{ij}) = \begin{cases} r \leq \sigma, & \infty \\ \sigma < r < 1.5\sigma, & -\varepsilon_W \\ 1.5\sigma \leq r, & 0 \end{cases} \quad (4.1.4)$$

$$U^{LC-W}(\boldsymbol{p}_i, \boldsymbol{r}_{ij}) = \begin{cases} r \leq \sigma, & \infty \\ \sigma < r < 1.5\sigma, & \varepsilon_{LC-W} + \varepsilon_A(\boldsymbol{p}_i \cdot \hat{\boldsymbol{r}}_{ij})^2 \\ 1.5\sigma \leq r, & 0 \end{cases} \quad (4.1.5)$$

where $\varepsilon_W = 0.5$, $\varepsilon_{LC-W} = 1$ and $\varepsilon_A = 10$ unless otherwise stated.

The same simulation parameters are used as for the non-chiral nematic shells (Chapter 3), that is, a cubic simulation cell with sides of 48σ and *N*=82944 corresponding to $\rho^* = 0.75$. All simulations were run at ${T^*}/{T_{N-I}^*} = 0.9$ from an isotropic phase unless otherwise stated. The starting configurations were produced as stated in section 3.2, with the radius of the outer sphere (r_{out}) equal to 20σ and the thickness of the liquid-crystalline shell was altered by varying the radius of the inner sphere (r_{in}).

As in the previous chapter a biased Monte Carlo scheme was used so that the water particles in the outer region of the simulation cell were sampled less frequently than the

mesogens and water particles in the centre of the simulation cell and a biasing cut off of 23σ was used (section 3.3).

4.2 TWIST ANALYSIS OF BIPOLAR SHELLS

As found for non-chiral nematic shells, the bipolar configuration is a common director configuration for cholesteric shells. For bipolar shells with 2 *s*=+1 defects located at the poles, the angle that the director twists around the droplet is of interest. The locations of the defects was found using the method as outlined in section 1.4.4, using a threshold value of $c_l < 0.25$. The larger values of c_l threshold compared to that utilised previously ($c_l < 0.15$) due to the nature of the *s*=+1 defects. The *s*=+1 defects are boojums consisting of a hyperbolic and radial half hedgehog defect on the inner and outer surfaces respectively (Figure 3.4.3). The three-dimensional nature of the boojum means the director field near the defect is less disordered than that near an *s*=+1/2 disclination line.

The hemispheres centred on each defect were treated separately as, in some cases, the two *s*=+1 defects are not directly opposite one another (Figure 4.2.1a).

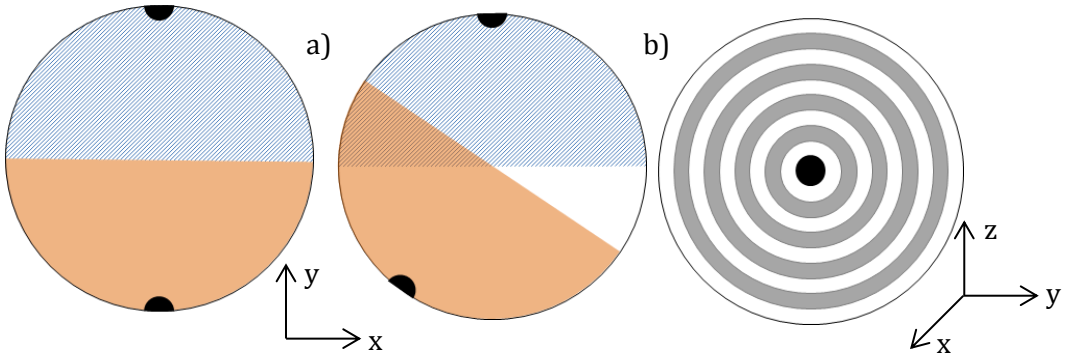

Figure 4.2.1 a) A schematic representation of the two hemispheres used in the twist angle analysis for the defects at the poles the defects off-set. b) A schematic representation of how the droplet is analysed for the twist angle analysis showing the shells viewed down the defect axis

The analysis cells used are cubic cells of the same size as those used in the visualisations (section 1.4.2), with a side of length 1.5σ. For each analysis cell, the distance from the centre of the simulation box to the centre of the analysis cell was calculated and used to split the simulation cell into concentric shells (Figure 4.2.1b). By doing this it is possible to monitor the twist progression through the shell from the inner to outer surface.

The analysis cells near the defect, as specified by the angle between the axis and the centre of the analysis cell (Figure 4.2.2a) are discarded as the presence of the defect caused the nematic order to become distorted and there is no longer planar anchoring at the surfaces.

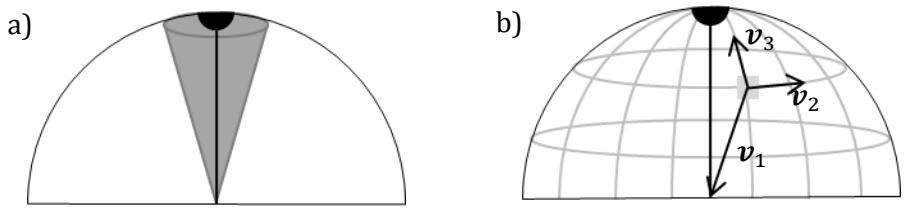

Figure 4.2.2 A schematic representation showing a) the area excluded from the twist angle analysis and b) the vectors $\boldsymbol{v}_1, \boldsymbol{v}_2$ and $\boldsymbol{v}_3$

For each analysis cell within the hemisphere, a modified axis system was created using $\boldsymbol{v}_1, \boldsymbol{v}_2$ and $\boldsymbol{v}_3$. $\boldsymbol{v}_1$is the vector between the centre of the analysis cell and the simulation cell, $\boldsymbol{v}_2$ is the vector running clockwise around the surface of the droplet is calculated and $\boldsymbol{v}_3$ is a vector tangential to the surface towards the defect, normal to both $\boldsymbol{v}_1$and $\boldsymbol{v}_2$ (Figure 4.2.2b).

Finally, the director ($\hat{\boldsymbol{n}}$) in each analysis cell is calculated along and from this two angles were calculated to analyse the twist. The angle α is defined as

$$\alpha = \tan^{-1}\left(\frac{(\hat{\boldsymbol{n}} \cdot \boldsymbol{v}_2)}{(\hat{\boldsymbol{n}} \cdot \boldsymbol{v}_3)}\right) \qquad (4.2.1)$$

which is used to monitor the twist of the director on the surface of the spherical cuts with respect to the meridian of the sphere. If α is zero then the director is parallel to the

meridian whereas when α is 90°, the director runs circularly around the sphere (Figure 4.2.3).

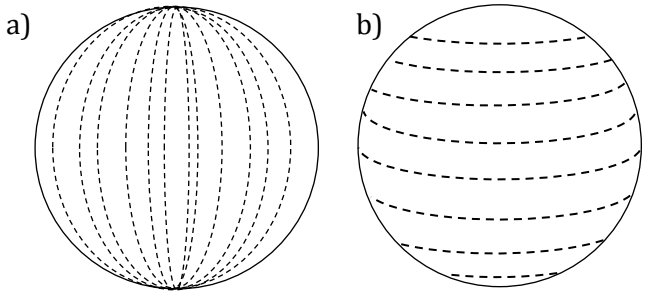

Figure 4.2.3 A schematic representation of the director configuration when a) α = 0° and b) α=90°

The second angle, β, is defined as

$$\beta = \tan^{-1}\left(\frac{(\hat{\boldsymbol{n}} \cdot \boldsymbol{v}_1)}{(\hat{\boldsymbol{n}} \cdot \boldsymbol{v}_2)}\right) \qquad (4.2.2)$$

which is used to monitor the twist of the director off the spherical surfaces. If β is zero then the director only twists along a direction parallel to the radius, *i.e.* between the two surfaces.

For analysis cells with no mesogens present, the director is undefined leading to $\alpha, \beta = 0$. The inner and outer surfaces were taken to be the shell closest to the centre with $N_{LC} > N_W$ where N_{LC} and N_W are the number of mesogen and water particles in the shells.

4.3 UNIFORM CHIRAL NEMATIC SHELLS

A series of simulations were initially performed of uniform nematic shells of thickness ranging from 6σ to 12σ for potential 1, for values of ε_c = 0.05, 0.10, 0.15, 0.20, 0.25 and 0.30 corresponding to pitch lengths ranging from approximately 240σ to 55σ (section 2.5.2). The behaviour of the systems with increasing chirality can be split into three broad regimes dependent on the thickness of the shell, discussed separately below.

The three regimes seen are:

1. Very thin shells where four *s*=+1/2 defects are seen for all values of ε_c
2. Thin shells which show a transition from four *s*=+1/2 defects at low values of ε_c to two *s*=+1 defects at larger ε_c
3. Thick shells that form two *s*=+1 defects at all values of ε_c.

4.3.1 *VERY THIN CHIRAL NEMATIC SHELLS*

For the thinnest shells investigated (of thickness 6σ) four *s*=+1/2 defects were seen with director configurations very similar to those observed when $\varepsilon_c = 0$. The absence of the transition to a twisted bipolar structure could be due to the stabilisation of the *s*=+1/2 defects due to the strong anchoring interactions at the surfaces. The energy of a *s*=+1/2 disclination line is proportional to the length of the defect, *i.e.* the thickness of the nematic shell, whereas due to the escaped nature of the boojums, it is relatively independent of the thickness, being point-like on the surface.

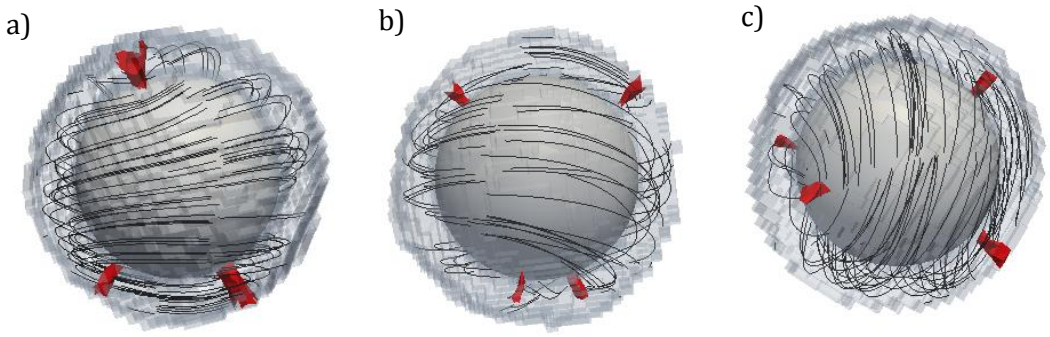

Figure 4.3.1 A chiral nematic shell of thickness 6σ with a) $\varepsilon_c = 0.00$, b) $\varepsilon_c = 0.15$ and c)$\varepsilon_c = 0.20$, showing four *s*=+1/2 defects

The director twisted slightly through the shell, as can be seen by the fact that the director streamlines at the outer surface in Figure 4.3.1b&c are not superimposed on the streamlines on the inner surface as seen in a non-chiral nematic shell when $\varepsilon_c = 0$ (Figure

4.3.1a). However, due to the presence and slow motion of the defects through the shell due to the fluid nature, it was not possible to analyse this twisting angle quantitatively.

4.3.2 *THIN CHIRAL NEMATIC SHELLS*

Shells of thicknesses ranging from 10σ to 8σ formed four *s*=+1/2 defects in a tetrahedral arrangement for a non-chiral nematic shell (section 3.4). As the chirality of the system increased, a transition from four *s*=+1/2 to a bipolar configuration was seen (Figure 4.3.2). The value of ε_c that the transition from four *s*=+1/2 to two *s*=+1 defect occurred at was dependent on the thickness of the chiral nematic shell (Table 4.3.1).

Table 4.3.1 The chirality at which the switch from four *s*=+1/2 to two *s*=+1 defect occurs for chiral nematic shells of intermediate thickness for potential 1

Chiral nematic shell thickness (σ)	ε_c and pitch length (σ) at which change from tetrahedral to bipolar configuration occurs
10	0.06 (202)
9	0.10 (109)
8	0.13 (89)

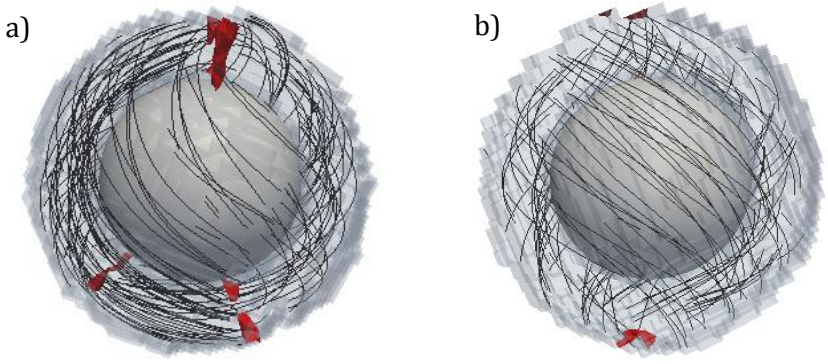

Figure 4.3.2 Chiral nematic shells of thickness 8σ with a) $\varepsilon_c = 0.12$ showing four *s*=+1/2 defects and b) $\varepsilon_c = 0.13$ showing two *s*=+1 defects

For shell thicknesses of 8σ and 9σ, the switch between defect configurations occurs when the pitch length is approximately ten times the thickness of the nematic shell. For the slightly thicker shell (thickness of 10σ), the transition to a twisted bipolar configuration occurs much earlier, when the pitch length is approximately twenty times the thickness of the shell. The reason that the switch occurs much earlier in the thicker shell could be because this thickness is closer to the region where two *s*=+1 defects are formed for a non-chiral nematic. Indeed, for lower anchoring strengths the bipolar configuration was found for non-chiral nematic shells of the same thickness (Table 3.4.1).

For defect configurations with four *s*=+1/2 defects, the angle between two defects and the centre was calculated using the method described in section 3.4.3, in order to investigate if, before the transition to two *s*=+1 defects, the four *s*=+1/2 defects are distorted from the preferred tetrahedral arrangement seen in non-chiral thin nematic shells. To recap, the defects were identified as regions where four or more adjacent analysis cells have $c_l < 0.15$. There are three ways to define the defects; by the position on the inner or outer surfaces or the inertia tensor of the defect. The results for all three ways of defining the defects are very similar and in this chapter, as with the previous chapter, the inertia tensor of the defect is used to calculate the angle between two defects and the centre.

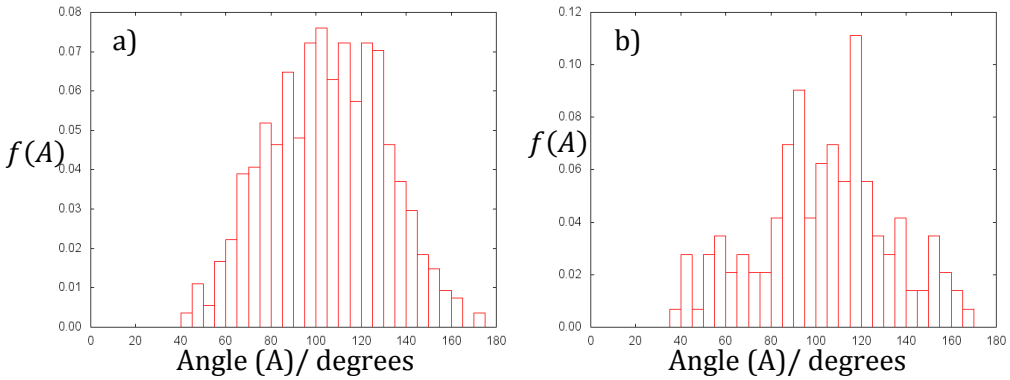

Figure 4.3.3 Histograms showing the distribution of angles between two defects and the centre for a) $\varepsilon_c = 0.10$ and b) $\varepsilon_c = 0.12$

As can be seen in Figure 4.3.3, as ε_c increases, the distribution of the angle between two defects and the centre broadens when compared to that seen in the non-chiral nematic shells. For a shell thickness of 8σ, the mean and standard deviation of a Gaussian function fitted to the distribution of angles between two defects and the centre for a non-chiral nematic shell is 101.8^{o} and 22.1^{o} respectively (Figure 3.4.7) whereas for $\varepsilon_c = 0.11$, the mean angle and standard deviation are 103.9^{o} and 29.5^{o}. The mean angle is very similar for all values of ε_c, indicating that the tetrahedral defect arrangement is most stable for all pitch lengths where four *s*=+1/2 defects are seen. The standard deviation for $\varepsilon_c = 0.10$ to 0.12 is approximately equal, again suggesting that, below the threshold value for the transition to a bipolar defect configuration, the defect configuration is independent from the chirality of the system. The slight increase in the standard deviation with respect to that seen for the non-chiral system is due to the slightly different parameters used in the interactions potentials.

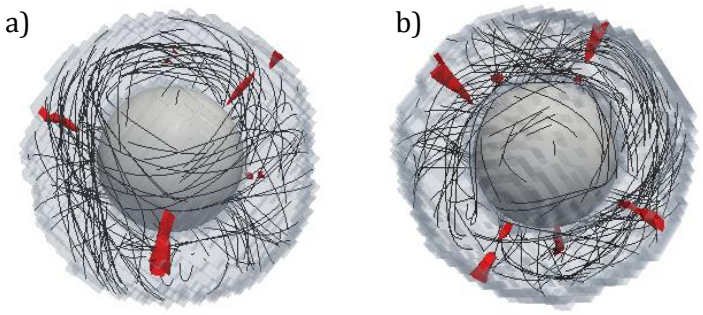

Figure 4.3.4 A shell of thickness 10σ with$\varepsilon_c = 0.20$ showing a blue phase with a) four *s*=-1/2 defects and four *s*=+1 defects and b) six *s*=-1/2 defects and five *s*=+1 defects

For simulations with a very high chirality, additional defects were seen (Figure 4.3.4), however the total topological defect charge of +2 for both the inner and outer surfaces, as stated by the Poincaré-Hopf theorem, was conserved. The defects are geometrically ordered due to the formation of a cubic blue phase. As with the transition from four *s*+1/2 defects to two *s*=+1 defects, the formation of a blue phase occurs at higher ε_c for thinner

shells. The blue phase is formed when the planar anchoring of the surface is overcome by the intrinsic helical twist perpendicular to the director. The transition to a blue phase was not investigated in depth however, for a shell of thickness *10σ* a blue phase is observed for $\varepsilon_c > 0.2$, which corresponds to a pitch length of approximately 60*σ* (Figure 4.3.4).

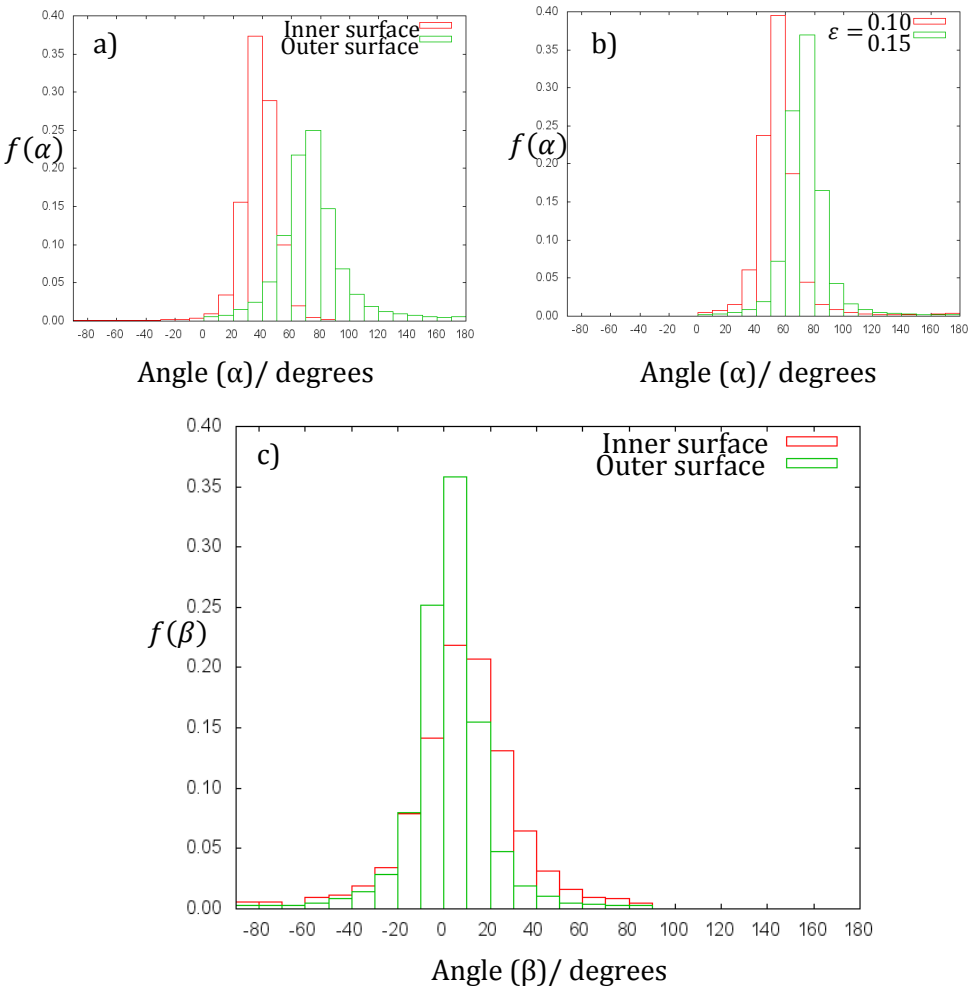

Figure 4.3.5 A histogram showing the distribution of α for a)the inner (red) and outer (green) surfaces for a shell of thickness of 8*σ*,$\varepsilon_c = 0.15$ and b) the outer surface for a shell of thickness 10*σ* at $\varepsilon_c = 0.10$ (red) and $\varepsilon_c = 0.15$ (green). c) shows the distribution of β for a thickness of 9*σ*, $\varepsilon_c = 0.15$

For the bipolar shells with two *s*=+1 defects, the twist angle between the director and the meridian of the spherical surface (α) and the out of plane twist from the spherical surface (β) were analysed with respect to distance from the centre of the simulation box (section 4.2).

For a non-chiral nematic shell in which a bipolar confiugration is observed, $\alpha = 0^0$ at both the inner and outer surfaces. However, for a chiral nematic shell with two *s*=+1 defects at the poles, the director twists away from the meridian at both surfaces. It was found for all systems that formed a bipolar configuration that the twist angle α is greater at the outer surface than the inner surface, demonstrating that there is some twist through the shell. As the chirality (ε_c) increases, the twist angle α also increases, this is because as the pitch length decreases, the ratio of thickness to pitch length increases. For example, by fitting a Gaussian function to the histograms in Figure 4.3.5b, it can be seen that the mean twist angle between defects increases from 55.3° at $\varepsilon_c = 0.10$ to 75.3° at $\varepsilon_c = 0.15$ at the outer surface for a shell of thickness 10σ.

To investigate if the increase in chirality causes the director to twist out of plane twist angle β is calculated. As can be seen in Figure 4.3.5c, away from the defect itself throughout the shell there is very little deviation in the director from the spherical surface.

4.3.3 *THICK CHIRAL NEMATIC SHELLS*

Nematic shells with planar anchoring at both surfaces of thickness 11σ and above all formed a bipolar structure for a non-chiral nematic shell and therefore no transition from a tetrahedral configuration was observed. With the addition of chirality to the system, the director twists around the waist of the shell between the two defects. The amount of twist observed increases with decreasing pitch length. In accordance with the behaviour seen in thin shells, at high values of ε_c a chiral nematic phase is no longer formed and a cubic blue phase is observed.

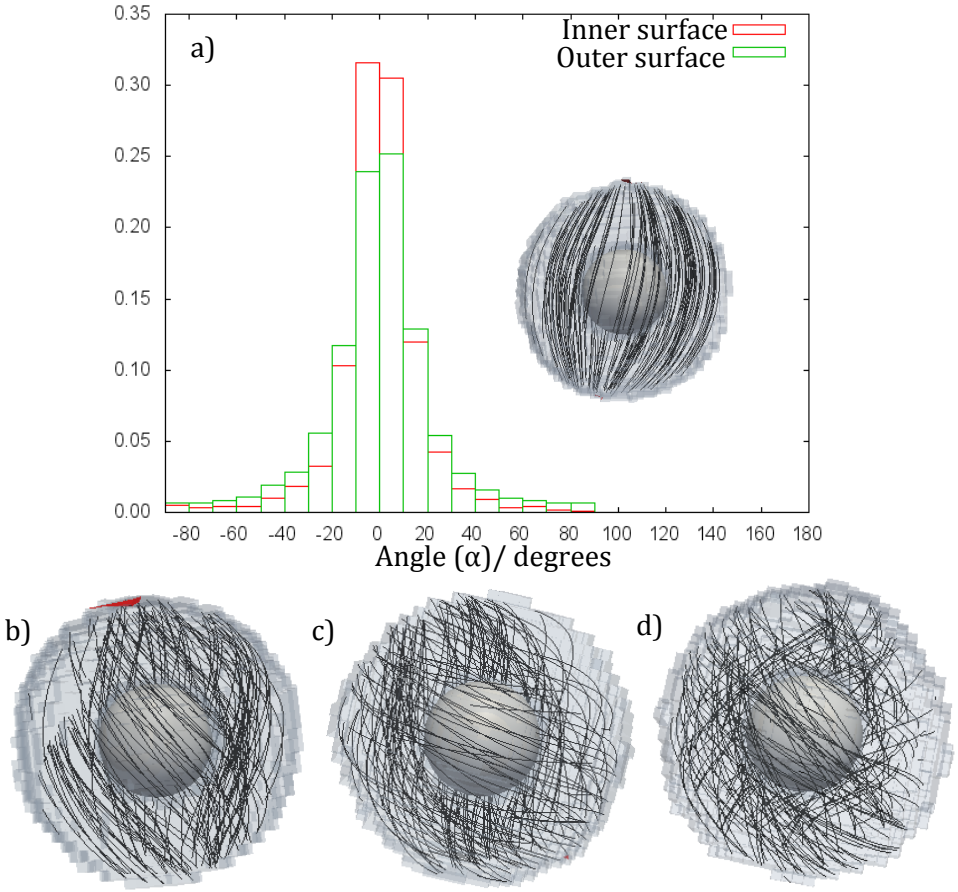

Figure 4.3.6 a) A histogram showing the distribution of twist angle α for a shell thickness of 12σ, $\varepsilon_c = 0$ and the associated visualisation (inset) b)-d) visualisations for a shell thickness of 12σ and b) $\varepsilon_c = 0.05$, c) $\varepsilon_c = 0.10$ and d) $\varepsilon_c = 0.15$

The presence of the bipolar configuration through a wide range of ε_c values including $\varepsilon_c = 0$ allows for a more detailed investigation into the twist angles α and β. In non-chiral nematic shells with planar anchoring, the director can be seen to run along the meridian between the two defects at the poles (Figure 4.3.6) meaning that the twist angle between defects (α) is approximately zero.

As ε_c is increased, the director twists away from the director configuration seen in non-chiral nematic shells. The twist angle between the director and the meridian of the spherical surface (α) is dependent on the thickness of the chiral nematic shell (Table 4.3.3).

As seen in thin shells that form two *s*=+1 defects, the twist angle α increases with increasing shell thickness (Figure 4.3.6). A Gaussian function was fitted to the histograms of angles produced and the mean twist angle at the inner and outer surface is shown in Table 4.3.2.

Table 4.3.2 A table showing the mean twist angle between defects (α) for a shell of thickness 12σ, corresponding to the visualisations in Figure 4.3.6

ε_c	Mean α at the inner surface (degrees)	Mean α at the outer surface (degrees)	Twist through the shell (degrees)
0.00	-0.10	0.47	0.57
0.05	12.80	30.48	17.68
0.10	22.71	57.68	34.97
0.15	24.78	78.46	53.68

The twist through the shell may also be calculated by subtracting α at the inner surface from that at the outer surface, as shown in the last column in Table 4.3.2. The twist angle through the chiral nematic shell increases linearly with increasing ε_c. The resulting graph of twist through the chiral nematic shell against the pitch length divided by the thickness is the same for all shell thicknesses investigated, indicating the main helical twist in the chiral nematic occurs from the inner to outer surface (Figure 4.3.7b).

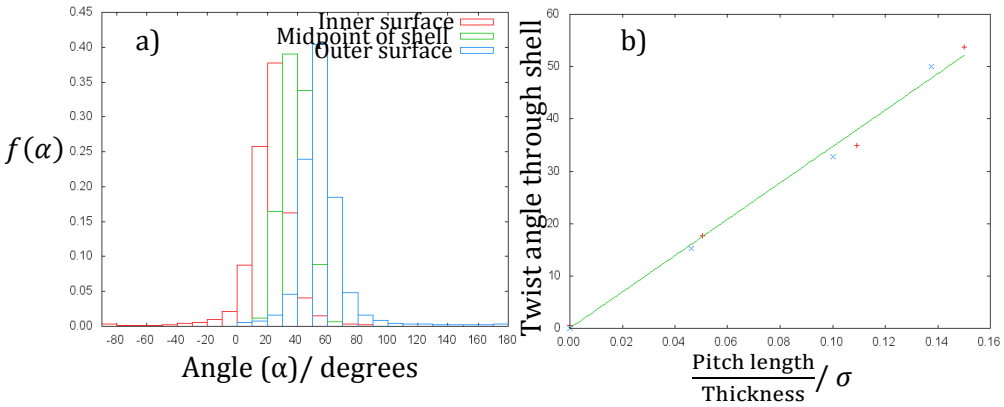

Figure 4.3.7 A histogram showing the distribution of twist angle between defects (α) for a thickness of 11σ,$\varepsilon_c = 0.10$ and b) The linear relationship between the twist through the shell and the proportion of confined pitch length for a thickness of 12σ (red) and 11σ (blue)

The twist angle α at the inner and outer surfaces show the opposite behaviour with increasing shell thickness. The twist angle α at the inner surface increases with decreasing thickness, whereas at the outer surface it decreases with decreasing thickness (Table 4.3.3).

Table 4.3.3 A table showing the mean twist angle between defects (α) for varying shell thicknesses at $\varepsilon_c = 0.15$

Shell thickness/σ	Mean α at inner surface /degrees	Mean α at outer surface /degrees
12	24.8	78.5
11	26.6	76.6
10	27.1	75.3
9	31.6	73.2
8	36.4	71.9

Again, the twist angle out of plane from the surfaces (β) was also measured. For the chiral nematic shell, the director is approximately perpendicular to both $\boldsymbol{v}_1$and $\boldsymbol{v}_2$ meaning β is expected to be approximately zero. However, this is not the case for non-chiral nematic shells ($\varepsilon_c = 0$) β does not favour any angle, this could be because ($\hat{\boldsymbol{n}} \cdot \boldsymbol{v}_1$) and ($\hat{\boldsymbol{n}} \cdot \boldsymbol{v}_2$) are

very small so any fluctuation between them would lead to a large change in $\frac{(\hat{\boldsymbol{n}}\cdot\boldsymbol{v}_1)}{(\hat{\boldsymbol{n}}\cdot\boldsymbol{v}_2)}$ and consequently a large change in β. For systems where $\varepsilon_c > 0$, β is approximately zero showing that there is no twist out of the plane of the surface due to the strong anchoring strength (Figure 4.3.8).

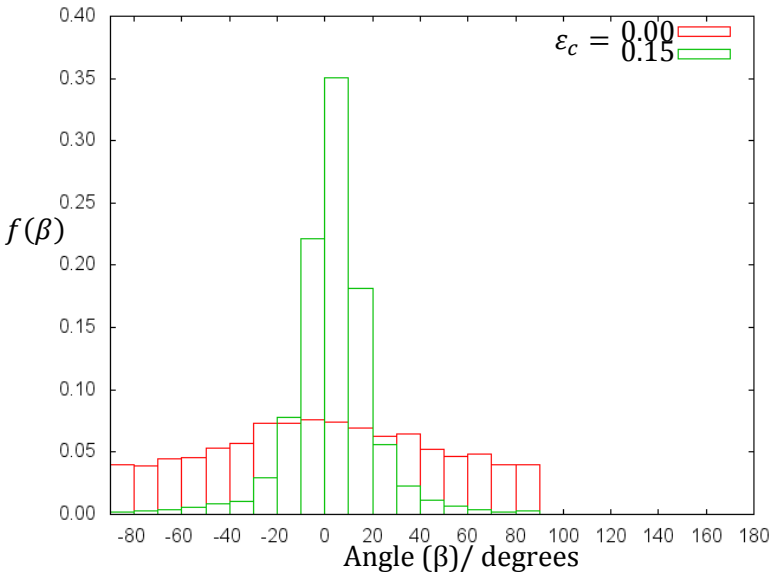

Figure 4.3.8 A histogram of the twist angle out of the surface (β) for a shell of thickness 12σ for both an non-chiral (red) and chiral (green) shell

4.3.4 *End-end interactions favoured (Potential B3)*

For non-chiral nematic shells with planar anchoring, thin shell behaviour consisting of four *s*=+1/2 defects were observed thicker shells for potential B3 than for potential 1. For example, the transition from thin (four defects) to thick (two defects) behaviour occurred at shell thicknesses of approximately 13σ and 10σ for potentials B3 and 1 respectively, with the parameters used in chapter 3. Potential B3 allows for the investigation into the effect of chirality on the four-defect configuration seen in thin shells to be expanded. Two shell thicknesses were investigated, both of which form four *s*=+1/2 defects in a non-chiral nematic shell with planar anchoring. The thicknesses investigated were; a thickness of 12σ

which is near the threshold value for thick behaviour and a thickness of 8σ which is well into the region where four *s*=+1/2 defects are observed for non-chiral nematic shells.

As with potential 1, both shell thicknesses showed a transition from four *s*=+1/2 defects to two *s*=+1 as ε_c is increased, as shown in Table 4.3.4. For the thick shell, this occurred at a similar chirality as the switch for the thickest shell (of thickness 10σ) for potential 1.

Table 4.3.4 The chirality at which the switch from four *s*=+1/2 to two *s*=+1 defect occurs for chiral nematic shells for potential B3

Chiral nematic shell thickness/σ	ε_c and pitch length in brackets at which transition from four to two defects occurs
12	0.06 (160σ)
8	0.18 (53σ)

For the shell of thickness 8σ, the transition from four *s*=+1/2 to two *s*=+1 defects occurred at a much higher chirality for potential B3 ($\varepsilon_c = 0.18$ compared to $\varepsilon_c = 0.13$) than for potential 1. The difference in ε_c at which the transition from four to two defects occurs could be due to the fact that, for a non-chiral nematic shell with planar anchoring, for potential B3 a shell of thickness 8σ is well inside the region where thin behaviour is observed, however for potential 1 8σ is very near the critical thickness where thick behaviour is seen.

Table 4.3.5 A table showing the mean twist angle α for a shell of thickness 8σ and $\varepsilon_c = 0.15$

$\varepsilon_c = 0.15$	Potential 1 (pitch length = 79σ)	Potential B3 (pitch length = 63σ)
Mean α for inner surface	38.01	42.66
Mean α for outer surface	71.86	86.08

The two twist angles α and β were also calculated for simulations using potential B3. As seen with potential 1, it was seen that α increased from the inner to the outer surfaces. It was found that the twist angles between defects (α) for potential B3 were slightly larger than those for potential 1 (Table 4.3.5), as the associated pitch length for each ε_c is slightly shorter for potential B3 than potential 1 (Figure 2.5.4) . The out of plane twist angle (β) was found to be approximately zero for all values of ε_c that formed a chiral nematic phase, in agreement with those seen with potential 1.

4.4 Preliminary studies of confined chiral nematic shells

In the water-liquid crystal-water double emulsions systems investigated in this chapter, there is a limit on the relative thickness of the chiral nematic shell and the pitch length because at high ε_c the planar anchoring at the surface is lost and a cubic blue phase is formed. Whilst it would be possible to increase the relative thickness of the nematic shell to the pitch length by using a larger system size this drastically increases the computational cost of the simulation. In order to increase the thickness and hence the system size without significantly increasing the time taken, systems of confined mesogens without the presence of water were investigated. In these systems, the mesogens are confined to a volume between two spheres. In order to impose planar anchoring at the surfaces, the mesogen-wall interaction took the form;

$$U^{LC-Wall}(\boldsymbol{p}_i, \boldsymbol{r}_{iw}) = \begin{cases} r \leq 0.5\sigma, & \infty \\ 0.5\sigma < r < 1.5\sigma, & U^{LC-Wall}(\boldsymbol{p}_i, \boldsymbol{r}_{iw}) \\ 1.5\sigma \leq r, & 0 \end{cases} \quad (4.4.1)$$

where $\boldsymbol{r}_{iw}$ is the minimum distance from the centre of the mesogen to the wall and

$$U^{LC-Wall}(\boldsymbol{p}_i, \boldsymbol{r}_{iw}) = \varepsilon_{wall} + \varepsilon_A(\boldsymbol{p}_i \cdot \boldsymbol{r}_{ip})^2 \quad (4.4.2)$$

where ε_{wall} is a positive constant and ε_A is as specified in (4.1.5). In a comparison to the interaction potential used in the double emulsion systems it was taken that $\varepsilon_{wall} = 1$ and $\varepsilon_A = 10$. The mesogen-mesogen interaction potential used was the same as that in the systems previously detailed in this chapter, with $J_1 = 1$ and $J_2 = J_3 = 0$ (potential 1).

The starting configurations were produced in a similar manner to that shown in section 4.1.1, with the exception that particles not located within the volume between the two spheres were removed.

Simulations were performed with $\varepsilon_c = 0 - 0.2$ for $r_{in}/r_{out} = 0.6$, with $r_{out} = 20,25,30,35$ and 40σ at $T^*/T^*_{N-I} = 0.9$. By investigating systems with a shell thickness of 24σ systems it was possible to consider systems in which the thickness was approximately half a pitch length, compared to the double emulsion systems where the shell thickness was in the region of a quarter of a pitch length.

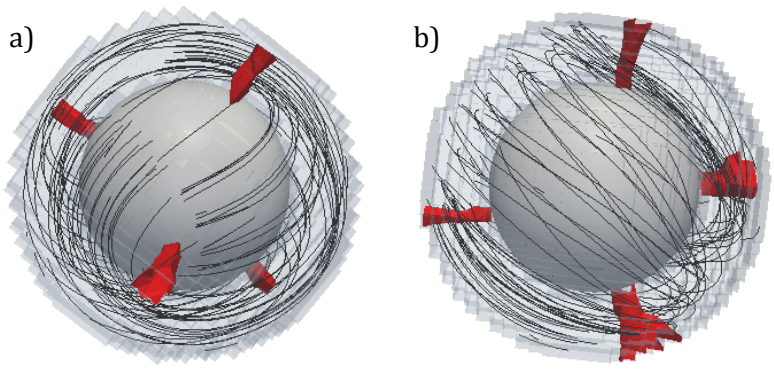

Figure 4.4.1 $r_{out} = 20\sigma, r_{in} = 12\sigma$ showing four *s*=+1/2 defects at a)$\varepsilon_c = 0.13$ and b)$\varepsilon_c = 0.20$

For $r_{out} = 20\sigma$ and $r_{in} = 12\sigma$, the confined nematic system is analogous to the system investigated in the double emulsion systems and as such is predicted to show very similar results to that seen in section 4.3, with a transition from four *s*=+1/2 to two *s*=+1 defects at approximately $\varepsilon_c = 0.13$ (Figure 4.3.2). However, at all values of ε_c investigated, four *s*=+1/2 defects were seen and there was no transition to two *s*=+1 defects. Indeed, the transition from four *s*=+1/2 to two *s*=+1 defects was not observed in any of the systems sizes investigated with four *s*=+1/2 defects always observed except in the largest system investigated, $r_{out} = 40\sigma$ and $r_{in} = 24\sigma$ which formed one *s*=+1 and two *s*=+1/2 defects at $\varepsilon_c = 0.19 \text{ and } 0.20$.

The absence of the transition found in the water-liquid crystal-water systems could be due to the difference in boundaries. In systems with water particles, due to the particle-particle interactions the vector used at the surface may not be perfectly perpendicular to the interface, whereas in the confined systems, by definition the vector used to calculate the anchoring is perpendicular to the interface (Figure 4.4.2).

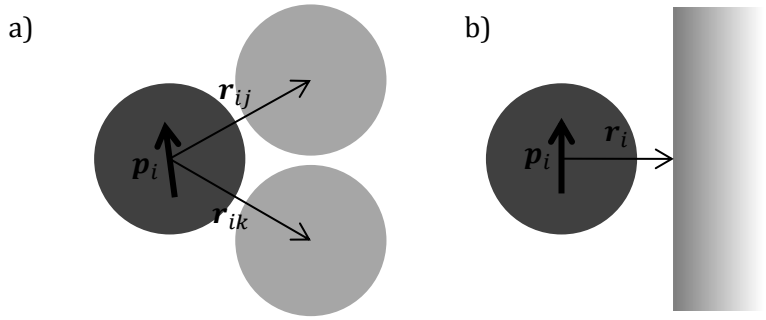

Figure 4.4.2 A schematic representation of the vector used to induce planar alignment at the surface in a) a water-nematic interface and b) a confined nematic using a wall

For an *s*=+1 defect the surrounding director structure means that there is a greater distortion from planar anchoring than for a *s*=+1/2 defect and so the *s*=+1/2 defect is favoured in the confined systems rather than the systems with a water-liquid crystal surface which would allow for some small distortion in the locality of the defect. It may be

possible to see the transition from four *s*=+1/2 to a bipolar structure with lower values of ε_A and ε_{Wall} as the energy penalty for the boojum will be lower.

Whilst there is no transition from four *s*=+1/2 defects to two *s*=+1 defect observed, the director configuration observed in chiral nematic shells is not the same as that seen in the

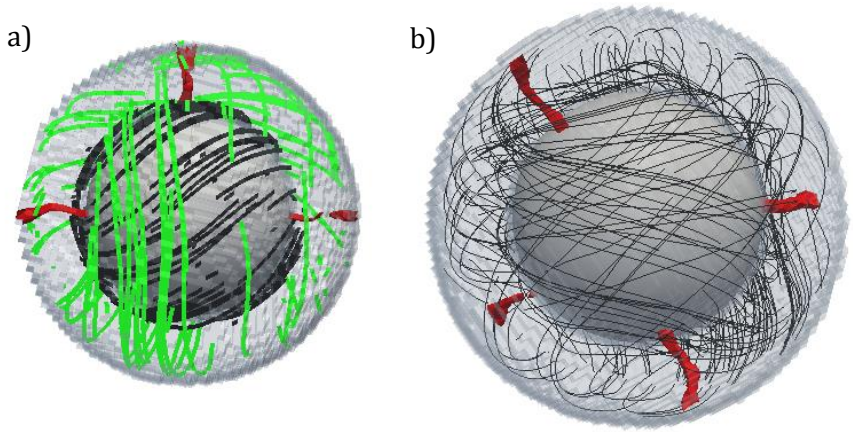

Figure 4.4.3 a) the director streamlines on the inner (black) and outer (green) surfaces for $r_{out} = 35\sigma, r_{in} = 21\sigma, \varepsilon_c = 0.2$ and b) four non-linear *s*=+1/2 defects seen for $r_{out} = 40\sigma, r_{in} = 24\sigma, \varepsilon_c = 0.18$

non-chiral nematic shells. In non-chiral nematic shells, both in the water-liquid crystal-water simulations and the confined nematic shells, the director streamlines at the inner and outer surfaces are parallel. However, as ε_c increases, a twist is observed through the nematic shell meaning the director streamlines on the inner surface are no longer parallel to those on the outer surface (Figure 4.4.3a). The twist seen through the nematic shell with the presence of four defects was similarly seen in the very thin shells in the water-liquid crystal-water systems (section 4.3.1).

In the larger systems investigated, the *s*=+1/2 defects bend and distort away from the linear paths seen in the double emulsion systems investigated earlier in this chapter (Figure 4.4.3b). In non-chiral nematic shells the *s*=+1/2 defects are straight lines through the nematic shell as this minimises the length and therefore the energy of the defect. In the

confined chiral nematic shells investigated here, the defects are now non-linear, in order to preserve the twist through the nematic shell. The distortion in the path *s*=+1/2 defects through the chiral nematic shell was not seen for the very thin double emulsion systems where no bipolar configuration shells were seen due to the small system size. For the very thinnest shells (thickness of 6σ), the size of the analysis boxes means that the shells were only four boxes thick and the resolution of the $c_l < 0.15$ contours was too low to see the bend in the defect path if it did occur in these systems.

4.5 Conclusion

By employing an off-lattice model of a finite thickness nematic shell, for the first time the effect of chirality on a nematic shell with planar anchoring at both surfaces has been simulated. A spontaneous transition from a four *s*=+1/2 defects in a tetrahedral configuration to two *s*=+1 defects at the poles of the shell was seen with increasing chirality (ε_c). The value of ε_c at which the transition occurs at is dependent on the thickness of the nematic shell and the stability of the tetrahedral configuration. For very thin shells, the spontaneous change is not seen for the range of ε_c investigated with the model used, however, it is likely that for systems with shorter pitch lengths this switch would occur.

The range of values that ε_c can take and the associated pitch length is limited by the breakdown of planar anchoring at the surfaces and the formation of a cubic blue phase. In shells where a blue phase has formed, there is a cubic array of *s*=+1 defects surrounded by *s*=-1/2 defects. In all cases the Poincaré-Hopf theorem was fulfilled, that is the total topological charge on both the inner and outer surfaces was equal to +2. The limit on ε_c means that only relatively long pitch lengths compared to the shell thickness could be investigated, with a quarter pitch being the maximum confined to a chiral nematic shell.

The Frank-Pryce like defect structure consisting of one *s*=+2 defect observed in chiral nematic shells produced by Uchida *et al*[41] were not observed in any simulations

investigated in this chapter. For filled chiral nematic droplets, the Frank-Pryce structure is only observed when the pitch length of the chiral nematic is shorter than the radius of the droplet[26]. The reason that the Frank-Pryce like structure is not observed in the systems investigated here is that the accessible pitch lengths using the simple model are much longer than both the radius of the droplet and the thickness of the shell. Future investigation into chiral nematic shells in which the pitch length is shorter than both the droplet radius and shell thickness may indicate a transition analogous to that seen in filled chiral droplets from the twisted bipolar structure to the Frank-Pryce like defect structure.

In order to investigate a larger system, preliminary simulations of a chiral nematic confined between two spherical surfaces were run with ${}^{r_{min}}/_{r_{max}} = 0.6$, which formed four *s*=+1/2 for a non-chiral nematic shell and showed a transition from four *s*=+1/2 to two *s*=+1 defects at approximately $\varepsilon_c = 0.13$ for the double emulsion systems. Unlike the systems with a water-liquid crystal surface no transition from four *s*=+1/2 to two *s*=+1 defects was seen up to $\varepsilon_c = 0.20$ in all sizes investigated, with four *s*=+1/2 defects primarily formed. The inherent twist in the chiral nematic phase was evident from the inner to outer surface and caused the *s*=+1/2 disclination lines to bend and distort from the linear defects seen in the non-chiral nematic shells. Whilst only preliminary work has been carried out into a chiral nematic confined between two spherical surfaces, it gives an interesting insight into the structure of the *s*=+1/2 defects that could not be observed in the double emulsion systems initially investigated. They also highlight the dependence on the surface interactions for the director configuration observed. It is possible, that for weaker mesogen-wall interaction potentials that the expected transition from four defects to a bipolar structure may be found.

The director configuration seen for the bipolar shells is similar to that seen for twisted bipolar droplets (Figure 1.2.3b). The twist angle director and the meridian of the spherical

surface was measured (α) throughout the shell and found to be highly dependent on the pitch length (Table 4.3.2).

In this chapter only uniform thickness shells are investigated, however experimentally produced nematic shells tend to be non-uniform in thickness[29]. Non-uniform thicknesses with four *s*=+1/2 defects, the defects are not located on the vertices of a tetrahedron but rather all at the thinnest part of the shell (chapter 3). The distortion of the director configuration away from a tetrahedral arrangement could lead to the transition to two *s*=+1 defects to occur at a different ε_c.

5 SOLID SPHERICAL AND POLYHEDRAL PARTICLES WITH NEMATIC COATINGS

5.1 INTRODUCTION

In this chapter, the research is expanded upon from nematic shells in double emulsion systems to solid particles with a nematic coating. Unlike systems with a nematic shell surrounding an inner water droplet, the solid particle may be of any geometry. A spherical particle of the same dimensions as the double emulsion systems in chapter 3 is initially investigated before extending to cubic, tetrahedral and octahedral particles with a nematic coating. It is expected that for spherical particles with a nematic coating, the resulting director configurations will be very similar to those seen for systems surrounding a liquid droplet[37].

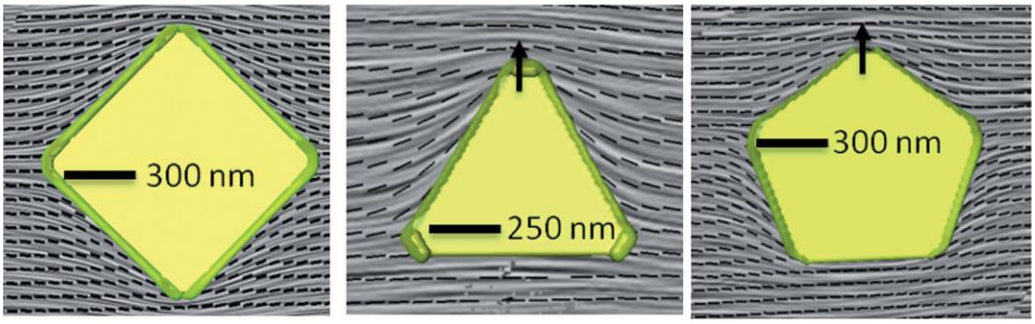

Figure 5.1.1 Taken from Dontabhaktuni *et al* [62]showing faceted platelets with planar anchoring and the defects formed at the corners

Previous work involving on non-spherical solid particles has focussed on the inclusion of such particles in a nematic bulk with both planar and homeotropic anchoring at the surface of the particles. Cubic and triangular prisms[59] along with two dimensional platelets[62] have been investigated, as have colloidal particles of a more complex geometry, such as a multi-

handled body[64]. It has been found that for systems with planar anchoring, defects tend to form at the corners or vertices of the solid particle (Figure 5.1.1).

In this chapter, systems with a nematic coating surrounding a solid polyhedral particle with four (tetrahedron), six (cube) and eight (octahedron) faces[65] is investigated. These three geometries are three of the five platonic solids, the fourth and fifth being a dodecahedron (12 faces) and an icosahedron (20 faces). A platonic solid is a regular, *i.e.* all the sides are the same length, convex polyhedron in which the same number of faces meet at each vertex. In all platonic particles, the Euler characteristic is +2 and so the systems with planar anchoring in the nematic coating must have a total topological charge on the surface of the solid particle of +2.

The boundary conditions at the nematic-water surface are also planar and so must possess a total topological charge of +2. As the outer surface is formed at a liquid-liquid interface, it is expected to be spherical in nature to minimise the surface area and the unfavourable mesogen-water interactions. Indeed, preliminary experiments started from a uniform thickness coating around a cube show that this rapidly changes to become a sphere (section 5.2.2).

5.1.1 *Interaction Potentials*

In this chapter, there are five different interactions to consider; mesogen-mesogen, water-water and the cross mesogen-water interactions as in previous chapters and discussed in detail in chapter 2 and two additional interactions to consider due to the large solid particle in the centre; mesogen-particle interactions and water-particle interactions. As in previous chapters the mesogen-mesogen potential used was,

$$U^{LC-LC}(\boldsymbol{p}_i, \boldsymbol{p}_j, \boldsymbol{r}_{ij}) = \begin{cases} r \leq \sigma, & \infty \\ \sigma < r < 1.5\sigma, & U^{LC-LC}(\boldsymbol{p}_i, \boldsymbol{p}_j, \boldsymbol{r}_{ij}) \\ 1.5\sigma \leq r, & 0 \end{cases} \qquad (5.1.1)$$

Where $\boldsymbol{p}_i$ and $\boldsymbol{p}_j$ are the unit orientation vectors for the particles *I* and *j* respectively, $\boldsymbol{r}_{ij}$ is the vector between the centre of the two particles and $U^{LC-LC}(\boldsymbol{p}_i, \boldsymbol{p}_j, \boldsymbol{r}_{ij})$ is

$$\begin{aligned} U^{LC-LC}(\boldsymbol{p}_i, \boldsymbol{p}_j, \boldsymbol{r}_{ij}) \\ = -\varepsilon \Big[J_1 (\boldsymbol{p}_i \cdot \boldsymbol{p}_j)^2 - 2J_2 (\boldsymbol{p}_i \cdot \boldsymbol{p}_j)(\boldsymbol{p}_i \cdot \hat{\boldsymbol{r}}_{ij})(\boldsymbol{p}_j \cdot \hat{\boldsymbol{r}}_{ij}) \\ + J_3 (\boldsymbol{p}_i \cdot \hat{\boldsymbol{r}}_{ij})^2 (\boldsymbol{p}_j \cdot \hat{\boldsymbol{r}}_{ij})^2 \Big] \end{aligned} \tag{5.1.2}$$

In this chapter, the majority of simulations discussed are run with potential 1 where $J_1 = 1$ and $J_2 = J_3 = 0$. The water-water potential is a simple square well potential where $\varepsilon_W = 0.25$.

$$U^{W-W}(\boldsymbol{r}_{ij}) = \begin{cases} r \leq \sigma, & \infty \\ \sigma < r < 1.5\sigma, & -\varepsilon_W \\ 1.5\sigma \leq r, & 0 \end{cases} \tag{5.1.3}$$

The mesogen-water interaction potential is as before

$$U^{LC-W}(\boldsymbol{p}_i, \boldsymbol{r}_{ij}) = \begin{cases} r \leq \sigma, & \infty \\ \sigma < r < 1.5\sigma, & U^{LC-W}(\boldsymbol{p}_i, \boldsymbol{r}_{ij}) \\ 1.5\sigma \leq r, & 0 \end{cases} \tag{5.1.4}$$

where

$$U^{LC-W}(\boldsymbol{p}_i, \boldsymbol{r}_{ij}) = \varepsilon_{LC-W} + \varepsilon_A (\boldsymbol{p}_i \cdot \hat{\boldsymbol{r}}_{ij})^2 \tag{5.1.5}$$

which favours planar anchoring. Values of $\varepsilon_{LC-W} = 0.25$ and $\varepsilon_A = 5$ were used unless otherwise specified.

Figure 5.1.2 shows a schematic representation of the interaction between a mesogen and the large solid particle, which has the interaction potential

$$U^{LC-P}(\boldsymbol{p}_i, \boldsymbol{r}_{ip}) = \begin{cases} r \leq 0.5\sigma, & \infty \\ 0.5\sigma < r < 1.5\sigma, & U^{LC-P}(\boldsymbol{p}_i, \boldsymbol{r}_{ip}) \\ 1.5\sigma \leq r, & 0 \end{cases} \tag{5.1.6}$$

where r_{ip} is the smallest distance between the surface of the large particle and the centre of the mesogen and

$$U^{LC-P}(\boldsymbol{p}_i, \boldsymbol{r}_{ip}) = -\varepsilon_{LC-P} + \varepsilon'_A(\boldsymbol{p}_i \cdot \hat{\boldsymbol{r}}_{ip})^2 \quad (5.1.7)$$

where ε_{LC-P} and ε'_A are positive constants corresponding to the interaction between the solid particle and the mesogen and the anchoring strength at the surface of the particle. Unless otherwise specified, $\varepsilon_{LC-P} = 3$ and $\varepsilon'_A = 5$ or $\varepsilon'_A = \varepsilon_A$ in (5.1.5) were used. For mesogen-particle interactions, only mesogens close to the large particle interacted with it and the cut off for the mesogen- particle interaction potential was set to be 1.5σ. The potential cut off for the interaction between the mesogen and the solid particle is slightly longer than that of the particle-particle interactions as in preliminary simulations with the cut off of 1.0σ, the nematic did not condense onto the surface of the larger solid particle.

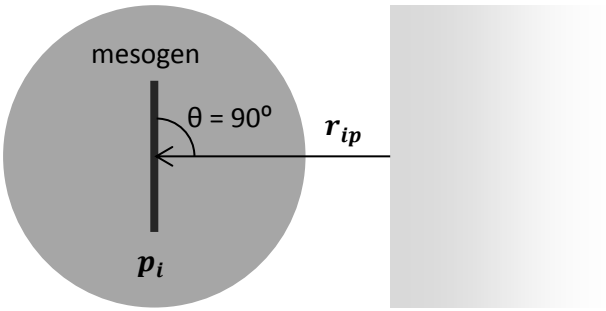

Figure 5.1.2 Diagram showing mesogen- solid particle interaction

For simplicity, water particles were set to not interact with the larger solid particle except through hard body repulsions,

$$U^{W-P}(\boldsymbol{r}_{ip}) = \begin{cases} r \leq 0.5\sigma, & \infty \\ 0.5\sigma < r, & 0 \end{cases} \quad (5.1.8)$$

5.1.2 *DEFECT ANALYSIS*

The angles between defects has been analysed in a similar way to the defects in the nematic shells surrounding water droplets. However, unlike the systems surrounding a water droplet, due to the different geometries of the central particles, it was only possible

to calculate the angle between defects using the defect location on the outer liquid crystal-water surface. However, this allowed for the analysis of the *s*=+1 defects in nematic shells surrounding a solid particle. As previously, a threshold value of $c_l \leq 0.15$ was used to identify the defect positions. The position of the defect on the outer surface is used rather than the inertia tensor method (as used in chapters 3 and 4) as the geometries of the solid particles can lead to very thin regions of the nematic shell. The inhomogeneity of the thickness of the nematic coating leads to the defects being of similar length and width meaning the inertia tensor is hard to define.

The defects are located and the number of defects present is calculated and systems with two, three and four defects are handled separately. If there are more than four defects present, the system is not yet equilibrated (or not yet formed a nematic) and no further analysis is performed.

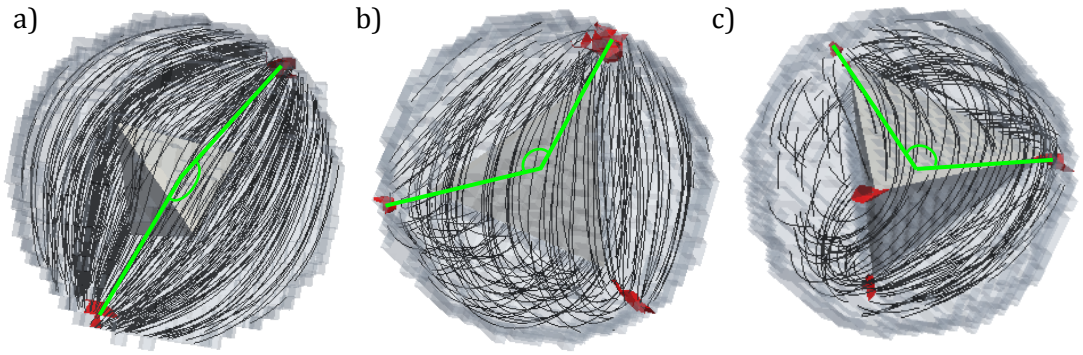

Figure 5.1.3 Angles calculated in the defect analysis for defect configurations with a) two, b) three and c) four defects for different size tetrahedral particles

The angles between individual pairs of defects and the centre is then calculated and averaged across many simulations of the same systems with differing initial random number seeds (Figure 5.1.3). For bipolar structures only one angle is calculated whereas for the three defect structure three angles are calculated and in director configurations with four defects six angles are calculated. Although these angles are between two different types of pairs, a *s*=+1 and a *s*=+1/2 or two *s*=+1/2 defects and are not equivalent, they are

not distinguished between in this defect analysis. In systems that show four *s*=+1/2 defects, the angle formed between three defects is also analysed.

5.1.3 *TRIAL MOVES*

In addition to the particle translations and rotations detailed in section 1.3.2, an additional type of Monte Carlo trial move was employed in simulations in this chapter, in which one water and one mesogen particle are swapped. A water particle and a mesogen particle are selected at random and their respective positions are exchanged. A random orientation vector is generated for the mesogen particle and the new energy is calculated and the trial move accepted or rejected in the normal way. In this chapter, these particle swap trials accounted for 50% of the attempted Monte Carlo moves, with the other trial moves accounting for the same proportion as previously described.

The additional trial move swapping a water and mesogen particle allows the nematic coating to deform in shape more quickly than the small trial translations otherwise taken. Preliminary experiments were run both with and without the particle swap trial moves and it was found that, as expected both methods had the same equilibrated structure and energy, however, by including the particle swaps the system reached equilibrium in less time.

5.2 PRELIMINARY SIMULATIONS

5.2.1 *MESOGEN-WATER MIX*

A series of preliminary simulations were run from a starting configuration where particles were randomly assigned as either water (90% of particles) or mesogens (10% of particles) creating a homogeneous water-mesogen mixture surrounding a cubic particle with sides of 18σ in the centre of the simulation cell at ${T^*}/{T^*_{N-I}} = 0.9$. These systems were investigated to confirm that for a given set of interaction, parameters phase separation occurred between the water and mesogens and that the mesogens coated the solid particle (Figure 5.2.1).

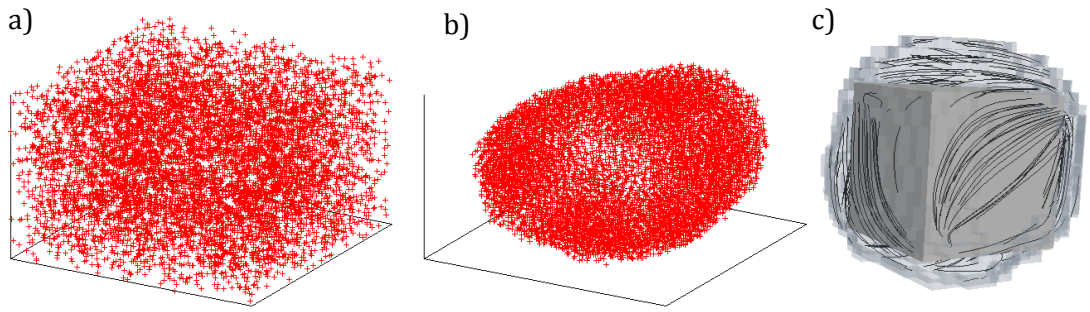

Figure 5.2.1 a) The initial random positions of mesogens and b) and c) show the nematic phase formed on the surface of the cube after 500000MC cycles. Both the cube and water particles are excluded for clarity.

Several different sets of parameters in both the mesogen-water and mesogen-particle interaction potentials were used. It was found that phase separation occurred for all mesogen-water interaction potentials investigated so long as the mesogen-water interaction was repulsive, *i.e.*$\varepsilon_{LC-W} > 0$. Initially a value of $\varepsilon_{LC-P} = 1$ was used in the mesogen-particle interaction potential, however this was not strong enough to drive the nematic formed to condense on the surface of the cube. Therefore a stronger interaction is necessary. At the density of the system investigated ($\rho^* = 0.75$) the resulting phase is a

dense liquid with a similar short range structure to that of a FCC lattice. By considering an FCC lattice on average each particle has 12 nearest neighbours[103]. The presence of the larger solid particle takes the place of two of these nearest neighbours and so a value slightly larger than two was used. Simulations started from a homogeneous mesogen-water mixture run with $\varepsilon_{LC-P} = 3$ showed that the nematic formed now condensed onto the surface.

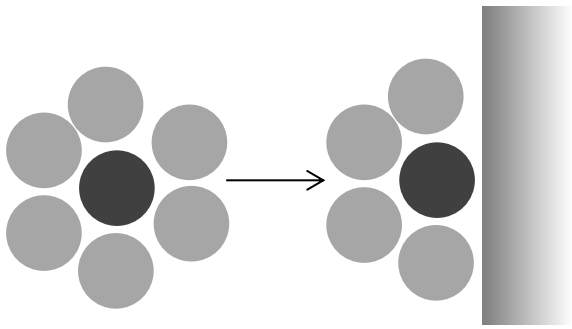

Figure 5.2.2 A schematic showing the loss of nearest neighbours when moving adjacent to the large particle wall. Shown in two dimensions for clarity, there are three neighbours in the planes above and below the selected particle.

5.2.2 *CUBE IN A CUBE*

Simulations starting from a cube surrounded by a cubic shell of mesogens, forming a uniform thickness coating surrounding the solid particle, were also run. Two different thicknesses of coating were investigated, either a thick coating (thickness of 10σ) or a thin coating (thickness of 2σ) both with and without the additional swap trial moves.

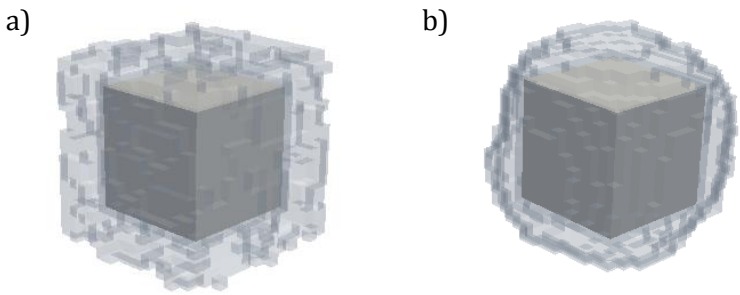

Figure 5.2.3 a) The uniform coating and b) the spherical nematic coating formed after 500000MC cycles.

It was found that, over the simulation, the nematic around the central cube collapsed from its initial shape into a sphere surrounding the solid particle (Figure 5.2.3). For both sizes of cubes, the uniform thickness coating decomposed to form a sphere, minimising the surface area and the unfavourable mesogen-water interactions. The spherical nematic droplet remained approximately centred in the simulation box. Both the simulations run with and without the additional swap trial moves showed the same behaviour, however the simulations in which the additional swap trial moves were included equilibrated in less time.

5.2.3 *MESOGEN-WATER ANCHORING STRENGTH*

Several simulations of spherical, cubic, tetrahedral and octahedral particles with a spherical nematic coating with planar anchoring at both surfaces were run varying the mesogen-water interaction (5.1.5), varying ε_{LC-W} from 0.1 to 10 and ε_A from 1 to 10.

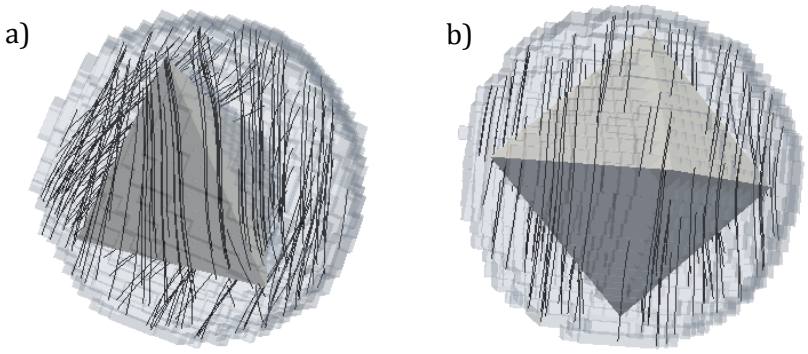

Figure 5.2.4 Systems in which the nematic has contracted away from the water to reduce the unfavourable interactions for a) a tetrahedron and b) an octahedron. Note the lack of planar anchoring due to contraction at the liquid crystal-water surface

It was found that, for the spherical and cubic particles there was very little difference in the final director configurations for the different values of both ε_{LC-W} and ε_A as long as they were both positive and still repulsive. However, the director configurations formed around the tetrahedral and octahedral particles were very sensitive to variations in ε_{LC-W} and ε_A,

particularly variations in the repulsive term, ε_{LC-W}. For values of $\varepsilon_{LC-W} \geq 1$ the nematic contracts away from the water and a void is formed between the nematic and the water. The contraction away from the water means that the nematic does not have any preferred alignment, due to the lack of mesogen-water interaction on the outer surface and behaves as a bulk nematic system, with no defects on the outer surface. Therefore a value of $\varepsilon_{LC-W} = 0.25$ and $\varepsilon_A = 5$ is used unless otherwise stated.

5.3 Simulation Parameters

Simulations were run for 250000MC cycles, cooling slowly from the isotropic phase into the nematic phase and then equilibrated at ${T^*}/{T^*_{N-I}} = 0.9$.All simulations were run at $\rho^* = 0.75$ using cubic analysis cells with sides of 1.5σ. A cubic simulation cell of sides 48σ was used and unless otherwise stated, all simulations were started from an isotropic starting configuration.

The starting configurations were produced in a similar manner to that described in section 3.2 for the double emulsion systems. Initially the simulation cell was filled with hard spheres on a simple cubic lattice around the large solid particle. Particles are then removed at random to obtain the correct density ($\rho^* = 0.75$). These bulk systems were then run at high temperature for a short time to form a liquid phase. A sphere with a radius of 20σ centred in the simulation cell was then carved and particles outside the sphere are assigned as water particles and particles inside the sphere as mesogens (Figure 5.3.1).

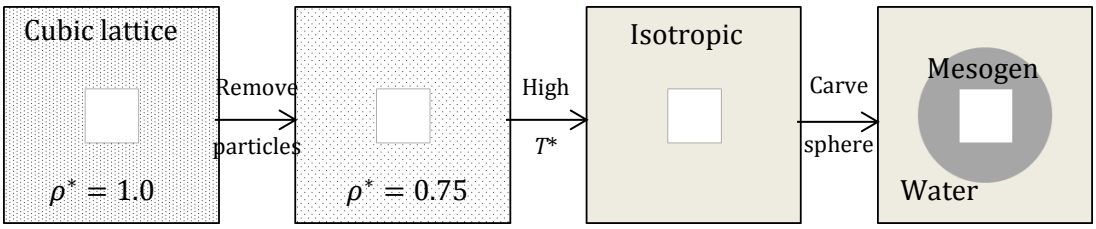

Figure 5.3.1 A schematic of the process used to create the starting configurations

Based on the results of the preliminary simulations discussed in section 5.2, the constant values in the interaction potentials used are as follows, unless otherwise stated. In the mesogen-water interaction potential $\varepsilon_{LC-W} = 0.25$ and $\varepsilon_A = 5$, in the mesogen-particle interaction potential $\varepsilon_{LC-P} = 3$ and $\varepsilon'_A = \varepsilon_A = 5$ and finally the water-water interaction potential has a square well depth of $\varepsilon_{W-W} = 0.25$.

5.4 SPHERICAL PARTICLES WITH A NEMATIC COATINGS

A series of simulations were run with a large solid spherical particle with a nematic coating. These systems are analogous to the uniform nematic shells surrounding water droplets, and as such are used to confirm that the simulation parameters used in this chapter are consistent with the work done in earlier chapters. Solid spheres with radii (r_{in}) of 8,10,11,12 and 14σ were investigated which have an associated nematic coating thickness of 12σ to 6σ with $r_{out} = 20\sigma$ as in chapter 3.

The defect configurations formed for thin coatings were very similar to those formed by the uniform nematic shells enclosing a water droplet, consisting of four *s*=+1/2 defects at the vertices of a tetrahedron. However, thick coatings around a solid spherical particle did not form a bipolar or three defect structure as were seen in nematics shells around a water droplet, but rather formed four *s*=+1/2 in a tetrahedral arrangement as seen in thinner shells, suggesting that the presence of a solid surface stabilises two *s*=+1/2 defects with respect to one *s*=+1, which is also seen in the chiral nematic systems confined between two spherical surfaces in section 4.4. The stabilisation of the two *s*=+1/2 defects with respect to

one *s*=+1 defect may be down to two reasons. The first is as outlined in the chiral nematic confined between two spherical surfaces, that is that at the liquid crystal-water interface the vector used ($\boldsymbol{r}_{ij}$) to drive the anchoring may not be perfectly perpendicular to the surface whereas at the solid particle-liquid crystal interface the vector used ($\boldsymbol{r}_{ip}$) is by definition perpendicular. The slightly longer range of the interaction may also cause the two *s*=+1/2 to become stabilised.

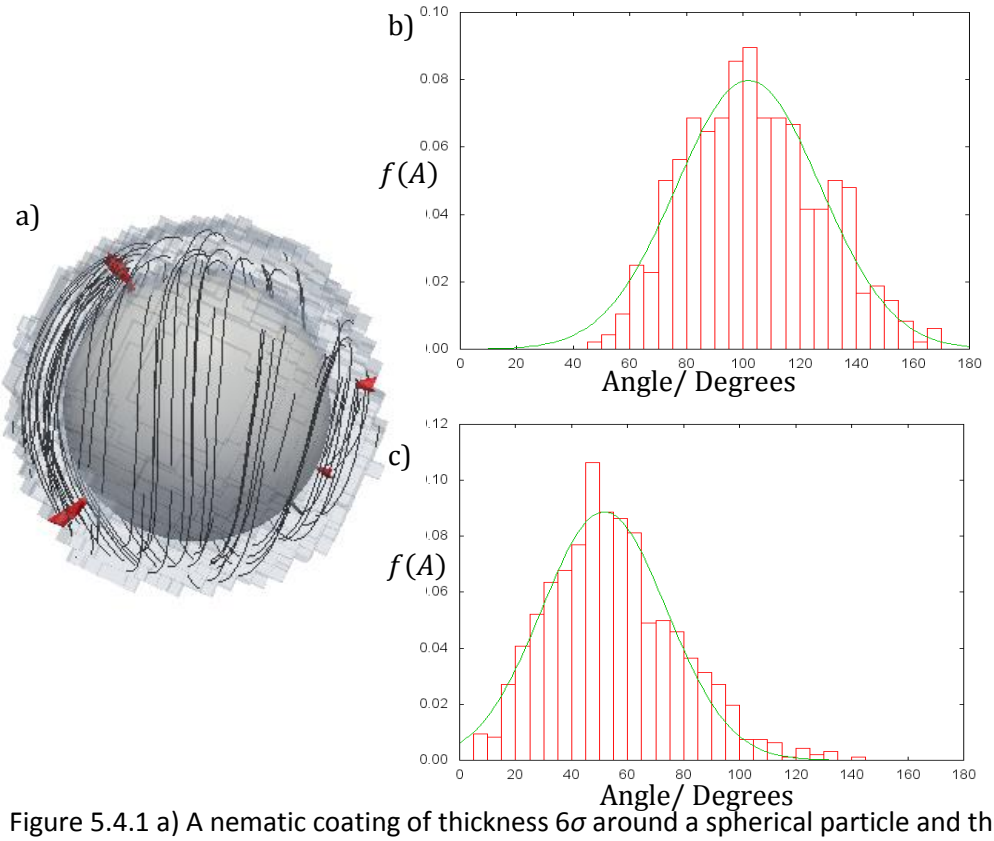

Figure 5.4.1 a) A nematic coating of thickness 6σ around a spherical particle and the assoicated distribution of angles between b) pairs of defects and the centre and c) three defects

In these systems with a large solid particle with a nematic coating, the interaction between the mesogens and the large particle is attractive. In *s*=+1 defects, the hyperbolic half hedgehog found at the inner surface may cause to contraction at the centre of the mesogens away from the surface. In the double emulsion systems this is favourable as the interaction is repulsive, however in the systems with the large solid particle this is disfavoured.

For a sphere of radius 14σ, corresponding to a nematic coating of thickness 6σ, the angle between defects was analysed over twenty simulations and a histogram produced (Figure 5.4.1). A Gaussian function was then fitted to the histogram and the mean angle between defects was found to be the same as that observed for the double emulsion systems (101.8^{o}). The standard deviation for the solid sphere with a nematic coating is similar to that as the comparable standard deviation calculated from the outer points of the defects in the double emulsion systems (25.4^{o} and 23.0^{o} respectively). The difference in the standard deviations calculated for the solid particle with a nematic coating and the double emulsion systems is likely to be statistical and disappear with increasing sample size.

The angle between three defects was also analysed, as in chapter 2. In a tetrahedron, the angle between three vertices is equal to 60^{o}. The mean angle from the simulations however is slightly smaller than this at 51.6^{o}, however this is very similar to that seen in the double emulsion systems where the standard deviation calculated was equal to 53.1^{o}.

5.5 CUBIC PARTICLES WITH NEMATIC COATINGS

After investigating the spherical particles, which are analogues of the systems investigated in the previous chapters, systems of faceted particles with nematic coatings are investigated with planar anchoring at both the liquid crystal-water surface and the large solid particle surface.

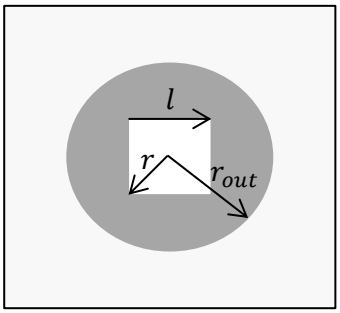

Figure 5.5.1 A schematic representation of the cubic particle with a nematic coating, with the nematic coating in dark grey

A series of simulations were performed for cubic particles in a nematic droplet with sides (*l*) ranging from 10*σ* to 18*σ*. For cubic particles with sides above 18*σ*, the vertices of the cubes were found to pierce the nematic droplet and the cubic particles did not have a complete nematic coating. The distance from the centre of the cubic particle to the vertices (*r*) is

$$r = \frac{l}{\sqrt{3}} \tag{5.5.1}$$

All of the size cubes investigated formed four *s*=+1/2 defects. The smallest cube investigated with $l = 10\sigma$ can be compared to a sphere with a radius of $r \approx 7\sigma$, which, again for a solid sphere using potential 1 also formed four *s*=+1/2 defects. In all cases where *s*=+1/2 disclination lines were observed, the *s*=+1/2 defects were located at the vertices of the cube. The disclination lines are located at the vertices as this is where the nematic coating is thinnest and the corresponding energy of the disclination line (which is proportional to its length) is minimised.

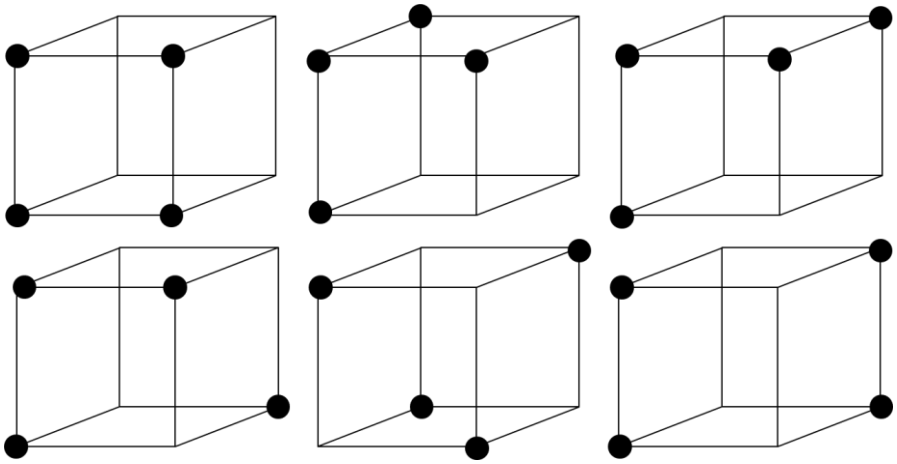

Figure 5.5.2 Six possible defect configurations found in a nematic coating surrounding a cubic particle assuming all defects are found on the vertices.

In systems with four *s*=+1/2 defects there are six possible defect arrangements in which all the defects are located at the vertices of the cube (Figure 5.5.2). The defects with the same sign repel each other to minimise the increase in elastic energy and maximise the distance between one another with the maximum mutual defect separation being achieved by a tetrahedral arrangement. In a tetrahedral arrangement (Figure 5.5.3b), each face of the cube has a defect at two vertices. There is one other possible defect arrangement where each face has two defects located at the vertices, where the defects are diagonally opposite on two faces and adjacent on four faces and can be thought of in an analogous fashion as the great circle defect configuration shown by some nematic shells (Figure 5.5.3a). Other defect arrangements are possible where one face has either three or four defects located at the vertices of one face are possible, although these are higher in energy due to the smaller defect separation. Indeed, no systems with defects at the four vertices of one face were seen in simulations with any potential and no systems with three defects on one face were observed for simulations run using potential 1.

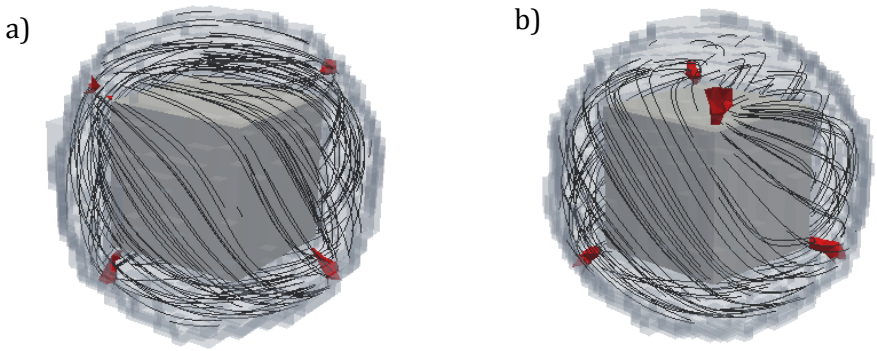

Figure 5.5.3 A cube with four *s*=+1/2 defects in a) a great circle or b) tetrahedral arrangement

The energy difference between the tetrahedral and great circle configurations is very small and within the thermal fluctuations of the simulation and so not possible to measure. In systems that formed four *s*=+1/2 defects, the great circle configuration was formed 65.2% with the tetrahedral configuration being observed in 34.7% of the simulations. The reason that the great circle configuration is more prevalent than the thermodynamic tetrahedral arrangement is kinetic in origin and that once a defect has formed at a vertex of the cube the energy barrier for it to move through the nematic shell onto another vertex cannot be overcome at the temperature investigated. The energy barrier for the defect to move from one vertex to another is present due to the inhomogeneous thickness of the nematic coating. The defect would have to increase in length, and so increase the energy of the system on moving through the thicker part of the nematic coating surrounding the edge and face of the cube. The ratio of the great circle to the tetrahedral arrangement can be explained in the following manner. Assuming there are only two defects on each face and focussing on just one face which has one defect located at one of its vertices, there are two positions adjacent to the first defect that the second defect can form that will lead to the great circle arrangement but only one place diagonally opposite to the first defect where the second defect can form to lead to the tetrahedral arrangement (Figure 5.5.4a).

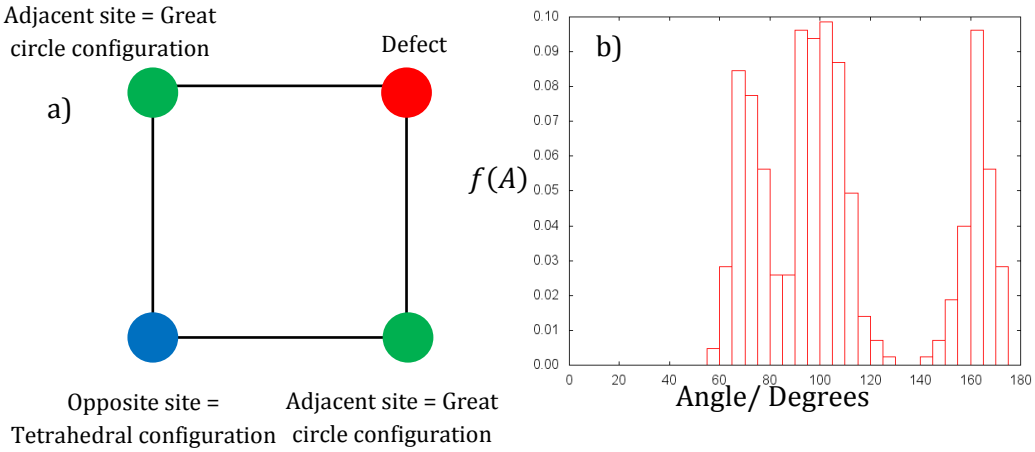

Figure 5.5.4 A schematic of the formation of the tetrahedral and great circle defect configurations and b) a histogram of the angle between defects for a cube (sides of 18σ).

The angle between two defects and the centre was analysed for a cube with sides of 18σ. As previously noted, in a perfect tetrahedral defect configuration the angle between all defects is 109°, however in the great circle configuration, there are three different angles, the angle between adjacent defects, the angle between diagonal defects on a face and the angle between diagonally opposed defects, in a perfect arrangement these would be 71°, 109° and 180° respectively (Figure 5.5.4b). The angle distribution clearly shows three peaks of approximately the same height at 70°, 110° and 160° corresponding to the predicted angles. The function

$$f(A) = t_{Gc}\left[e^{-(A-\mu_1)^2/2\sigma_1^2} + e^{-(A-\mu_2)^2/2\sigma_2^2} + e^{-(A-\mu_3)^2/2\sigma_3^2}\right] + t_{Td}e^{-(A-\mu_2)^2/2\sigma_2^2} \quad (5.5.2)$$

where t_{Gc} and t_{Td} are the proportion of great circle and tetrahedral contributions to $f(A)$ respectively. The value of t_{Td}/t_{Gc} is approximately 0.2 which implies that the tetrahedral arrangement is only observed in a fifth of cases. The value calculated is differs from e number of observed cases as the histogram is averaged over the whole simulation run (after equilibrium is reached), whereas the observed cases are only snapshots.

The function shown in (5.5.2) does not take into account any defect configurations where there are three or four defects on one face or the possibility of the defects not being located on the vertices of the cube. The values $\mu_1, \mu_2 \text{and } \mu_3$ give the centres of each peak as 70.6°, 100.4° and 163.3°, in concordance with the calculated values. The value of the peak at the highest angle, corresponding to the diagonally opposing defects in the great circle defect configuration is lower than expected and can be explained as the fact that this is the largest distance between defect pairs leaving the largest region for fluctuation of the defect centres. The angle between two defects and the centre is calculated by

$$(\boldsymbol{r}_1 \cdot \boldsymbol{r}_2) = r_1 r_2 \cos A \qquad (5.5.3)$$

Where $\boldsymbol{r}_x$ is the vector between the centre of the simulation cell and the average point of defect x, where $x = 1,2$, on the outer surface and r_x is the magnitude of $\boldsymbol{r}_x$. The cosine of 163° and 180° are very close, -0.956 and -1 respectively, so any fluctuations in the dot product will be amplified when looking at the angles.

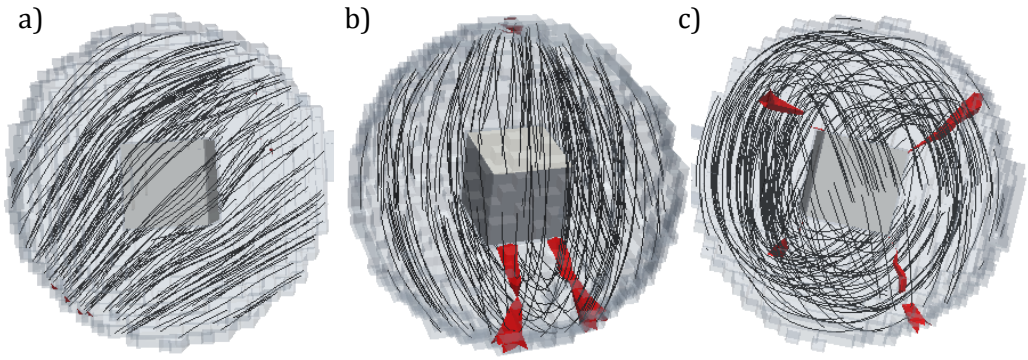

Figure 5.5.5 A cubic particle with sides 10σ for a) potential A3, b) potential B1 and c) potential B3 showing two *s*=+1, one *s*=+1 & two *s*=+1/2 and four *s*=+1/2 defects respectively

So far in this section on cubic particles with a nematic coating, the simulations have employed the simplest mesogen-mesogen interaction, potential 1. Whilst the general behaviour of the systems is the same for all the potentials investigated, the subtle differences between interaction potentials in which the end-end and side-side interactions

are of differing energy are now discussed. For this section, values of $\varepsilon_{LC-W} = 1, \varepsilon_{LC-P} = 10$ and $\varepsilon_A = \varepsilon'_A = 10$ were used along with $\varepsilon_{W-W} = 0.5$. Simulations were run using potentials 1,A1,A3,B1 and B3 with cubes with sides of 10σ to 18σ investigated.

The smallest cubes investigated with potential 1 using the parameters described above showed two *s*=+1 defects, showing the dependence on the interaction potential parameters used and the resulting director configuration. As observed in the double emulsion systems, the A potential series, in which the side-side interactions are lower in energy to the end –end interactions, again favoured the formation of two *s*=+1 defects (Figure 5.5.5a), with the bipolar configuration seen in systems with cubic particles with sides up to 14σ for potential A3. The B potential series, in which the end-end interactions are lower in energy than the side-side interactions, favoured the formation of four *s*=+1/2 defects (Figure 5.5.5c). There were very few occurrences of the intermediate defect configuration consisting of one *s*=+1 and two *s*=+1/2 defects, however they were occasionally observed for cubic particles with sides of intermediate length between those that tend to form two or four defects (Figure 5.5.5b).

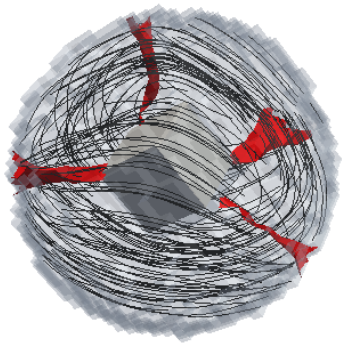

Figure 5.5.6 Four *s*=+1/2 defects initially formed after 5000MC cycles for potential A3 with $l = 10\sigma$

For thick coatings which form two *s*=+1 defects, the defects were located at two diagonally opposed vertices. As with the nematic shells surrounding a water droplet, four *s*=+1/2 defects are initially formed at the vertices of the cube, minimising the length of the

disclination lines. Each pair of defects then combine to form two *s*=+1 defects still located at the vertices (Figure 5.5.6).As in the bipolar director configuration, in the intermediate defect configuration consisting of two *s*=+1/2 and one *s*=+1 defect, the two *s*=+1/2 defects are located at adjacent vertices of the cube. There are three different possible locations for the *s*=+1 defect, either on the opposing face, edge or vertex. Three different angles in three defect configurations are calculated α, β and γ (Figure 5.5.7d).

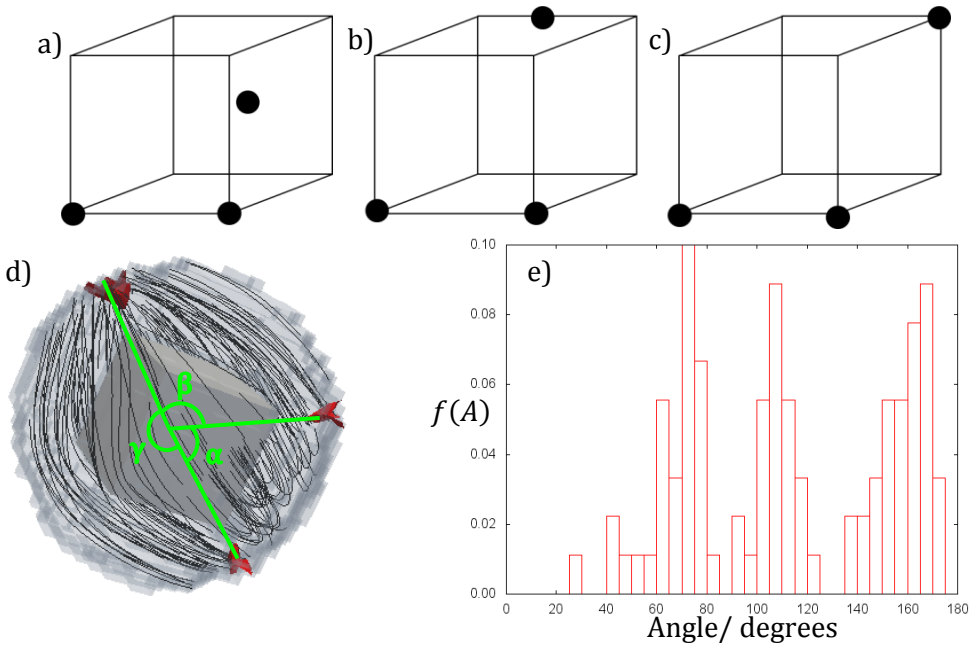

Figure 5.5.7 a)-c) show three possible defect configurations in which the two *s*=+1/2 defects are located at adjacent vertices d) A three defect configuration showing all the defects located at the vertices of the cube for potential B3 and a side of 16σ, and e) the distribution of angles between two defects and the centre calculated over all occurrences of three defect configurations

The angle between the two *s*=+1/2 defects on adjacent vertices is α = 70.6^{o}. In the case where the *s*=+1 defect is located on the face or the edge, β=γ= 125.3^{o} and 144.7^{o} respectively. If the *s*=+1 defect is located at a vertex, then β=109^{o} and γ=180^{o}. By calculating the angle distribution for the angle between two defects and the centre for all occurrences of the three defect configuration it is possible to quantify the location of the

s=+1 defect. The distribution of angles between two defects and the centre clearly shows three peaks and by fitting the sum of three Gaussians,

$$f(A) = t_1\left[e^{-(A-\mu_1)^2/2\sigma_1^2} + e^{-(A-\mu_2)^2/2\sigma_2^2} + e^{-(A-\mu_3)^2/2\sigma_3^2}\right] \qquad (5.5.4)$$

the three peaks are calculated to occur at 72°, 108° and 161° corresponding to the angles α, β and γ respectively, confirming that all defects are located at vertices of the cube.

5.6 SURFACE NEIGHBOUR LIST

For both the spherical and cubic particles there is a quick test to check if the mesogen or water particle interacts with the large solid particle. For a sphere it is merely the distance from the centre of the simulation cell to the centre of the mesogen or water particle (r_i). For a cubic particle, a quick test to check for overlaps with the large particle is

$$r_{ix}, r_{iy}, r_{iz} > \frac{l}{2} \qquad (5.6.1)$$

where r_{ix}, r_{iy}, r_{iz} are the components of $\boldsymbol{r}_i$ in the *x,y* and *z* directions respectively and $\boldsymbol{r}_i$ is the vector between the centre of the simulation and the centre of particle *i*. A similar test can be made to check for interaction with the large cubic particle,

$$r_{ix}, r_{iy}, r_{iz} > \frac{l}{2} + r_{cut} \qquad (5.6.2)$$

where r_{cut} is the potential cut off, in this case $r_{cut} = 1.5\sigma$.

For systems of tetrahedral and octahedral particles with nematic coatings, unlike for spherical and cubic particles, there no quick test to calculate the minimum distance between the large solid particle and the selected mesogen or water particle exists. In order to optimize the simulations, an additional neighbour list was utilised based on the same cubic grid used in the original neighbour list, *i.e.* a cubic grid with sides of 1.5σ (section 1.3.5).

At the start of each simulation, the position of the eight corners of each small cell was calculated with respect to the large solid particle and assigned with one of three indexes. These index environments were; all eight corners within the solid particle (index=1), some corners within the solid particle or with a minimum distance of less than the potential cut-off (index=2) or no corners within either the solid particle or with a minimum distance of less than the potential cut-off (index=3) (Figure 5.6.1).

In a simulation trial move, if any particle enters any small cell with index=1, the move is immediately rejected as the particle has moved within the large solid particle. If the particle is in a cell with index=3 then the particle is too far away from the large polyhedral particle and so the particle is not tested for overlap and interaction with the large solid particle is not calculated as the minimum distance between the centre of the particle and the large solid particle is greater than r_{cut}. If any particle is in a cell with index=2, the interaction between the particle and the large solid particle is calculated, including checking if the mesogen/water has moved to within the large particle. Of course for particles in cells with an index of 2 or 3, the trial move may still be rejected due to overlap with other particles.

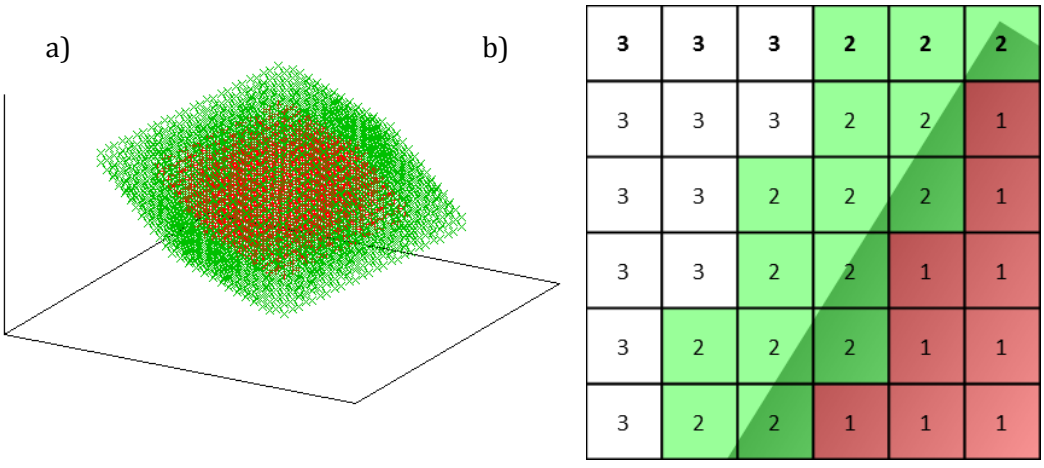

Figure 5.6.1 A schematic of the surface neighbour list used with index=1 (red) and index=2 (green) in a) three dimensions and b) a magnified view in two dimensions. The cells with index = 3 have been omitted for clarity.

Preliminary simulations were performed of identical systems for both a tetrahedral and octahedral particle with and without the additional neighbour list. It was found that the energy at equilibrium was the equivalent for both simulations; however those with the additional neighbour list were faster than those run without the additional neighbour list. In simulations of tetrahedral particle, those run with the additional neighbour list were 5.03% faster than those run without the additional neighbour list. Simulations of octahedral particles showed an even greater increase in speed, with simulations that employed the additional neighbour list running 5.74% faster than those run without the additional neighbour list.

5.7 TETRAHEDRAL PARTICLES WITH A NEMATIC COATINGS

5.7.1 *CENTRED TETRAHEDRAL PARTICLES*

Simulations were also performed of tetrahedral particle with a nematic coating with planar anchoring at both surfaces. The size of the tetrahedral particle is not quoted as the length of the sides (as in the cubic particle systems) but rather in relation to the position of the vertices, x. In systems where the tetrahedron is not shifted, the vertices are located at:

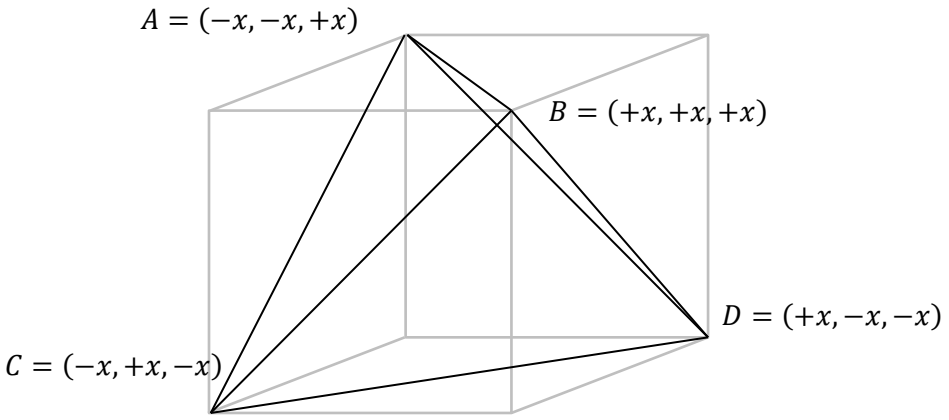

Figure 5.7.1 A schematic of the positions of the vertices of the tetrahedron (inside a cube for clarity).

The length of the sides (l) of the tetrahedron are related to x by

$$l = \sqrt{2}x \tag{5.7.1}$$

and values of $x = 6,7,8,9$ & 10σ were investigated. When $x > 10\sigma$, the vertices of the tetrahedron pierce the spherical nematic coating (with a radius of 20σ) as the distance from the centre of the simulation cell to a vertex (r_{tet}) is related to x by,

$$r_{tet} = \sqrt{3}x \tag{5.7.2}$$

For small tetrahedrons ($x = 6\sigma$), a defect configuration with two *s*=+1 defects in was seen (Figure 5.7.2a). For a relatively large range of values, ($x = 7 - 9\sigma$) a defect configuration consisting of one *s*=+1 and two *s*=+1/2 defects is seen (Figure 5.7.2b) along with both the bipolar and tetrahedral defect configurations, and for $x = 8\sigma$ the three and four defect configurations were equally likely to be observed. Only for the very thinnest shells ($x = 10\sigma$) were only four *s*=+1/2 defects seen (Figure 5.7.2c).

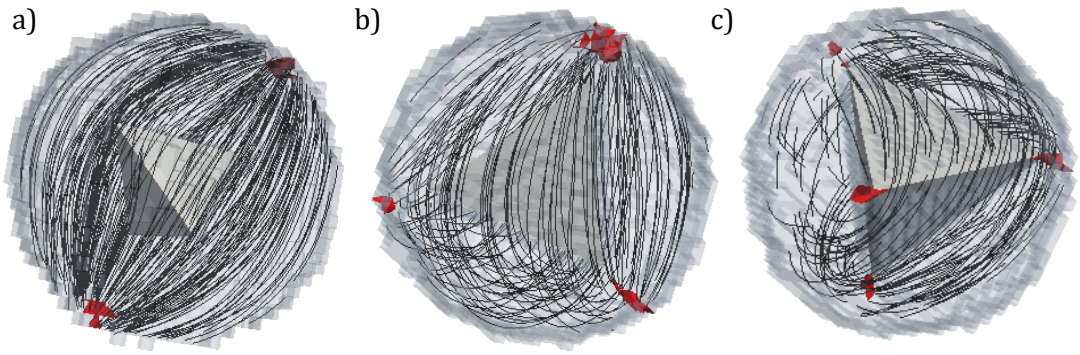

Figure 5.7.2 Un-shifted tetrahedral particles with a nematic coating showing a) two *s*=+1, b) one *s*=+1 & two *s*=+1/2 and c) four *s*=+1/2 defects located at the vertices of the tetrahedron

The small range of formation of the four *s*=+1/2 defects compared to spherical and cubic particles with nematic coatings may be due the inhomogeneity of the spherical nematic coating surrounding the tetrahedral particle. At the faces of the tetrahedron, the nematic coating is very thick and more bulk-like, causing the nematic coating to behave as a thick

shell, forming a bipolar configuration. The decrease in the volume of the large solid particle from a sphere to a tetrahedron can be calculated. The volume of a sphere is

$$V_{sphere} = \frac{4}{3}\pi r^3 \tag{5.7.3}$$

where *r* is the radius of the sphere. Whereas the volume of a tetrahedron is

$$V_{tet} = 3x^3 \tag{5.7.4}$$

leading to the difference in volume between a tetrahedron and a sphere with a radius of r_{tet} is;

$$V_{sphere} - V_{tet} = \frac{4}{3}\pi r_{tet}^3 - 3x^3 = x^3\left(4\sqrt{3}\pi - 3\right) \tag{5.7.5}$$

It is also possible to calculate the approximate number of mesogens in each system, again illustrating the difference in the nematic coating thickness. For $r_{tet} = 12\sigma$ where the radius of the spherical nematic coating is 20σ and $\rho^* = 0.75$, there are approximately 4680 more mesogens in the system with a tetrahedral particle compared to a spherical particle, corresponding to an increase in the number of mesogens of almost 24% from the spherical to tetrahedral particle. The increase in the number of mesogens may account for the dependency of the type and number of defects formed on the geometry of the large solid particle. Indeed, for $r_{tet} = 12\sigma$, the spherical particle formed four *s*=+1/2 defects whereas the tetrahedral particle it is in the region where one *s*=+1 and two *s*=+1/2 defects are observed.

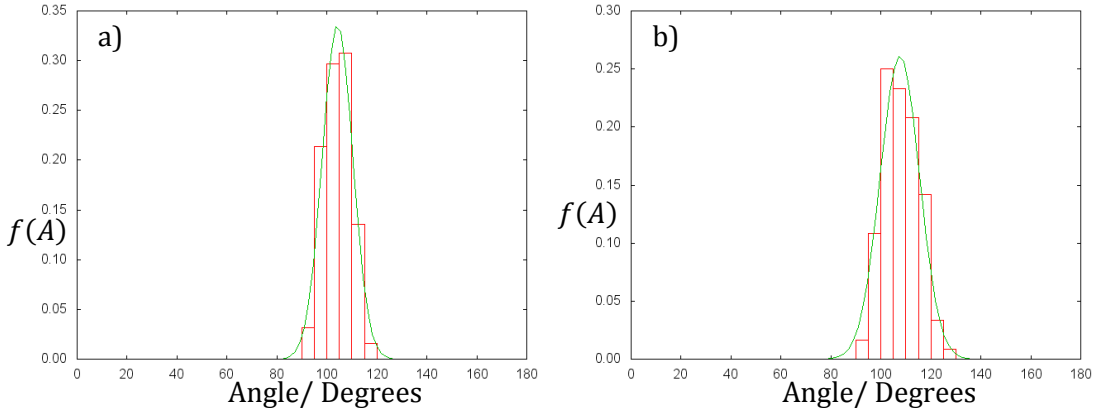

Figure 5.7.3 Distributions of the angle between defects for a) four *s*=+1/2 defects ($x = 10\sigma$) and b) one *s*=+1 & two *s*=+1/2 defects ($x = 8\sigma$)

The angles between two defects and the centre were calculated separately for $x = 10\sigma$ for defect configurations with four *s*=+1/2 defects and a Gaussian function is fitted to the resulting histogram (Figure 5.7.3a). The mean angle from the fitted Gaussian function is 104.2°, which is very close the angle in a perfect tetrahedron (109.5°) and occurs as the defects tend to form at the vertices of the large solid tetrahedral particle. The standard deviation of the fitted Gaussian function is much smaller than that found for a spherical particle, 6.1° and 25.4° for a tetrahedral particle with $x = 10\sigma$ and a spherical particle with $r_{in} = 14\sigma$ respectively. A similar histogram for the distribution of angles between two defects and the centre is seen for the slightly smaller tetrahedral particle when $x = 8\sigma$, when looking at only those configurations with four *s*=+1/2 defects.

For the intermediate defect configuration with one *s*=+1 and two *s*=+1/2 defects the two *s*=+1/2 defects were located on two the vertices of the large tetrahedral particle. On the assumption that the *s*=+1/2 are always located on two vertices of the tetrahedral particles, the angle between the two *s*=+1/2 defects and the centre is approximately 109.5°. There are three possible locations for the *s*=+1 defect (Figure 5.7.4):

1. on the edge between the two ‘empty’ vertices
2. on a vertex
3. on one of the a face of the tetrahedral.

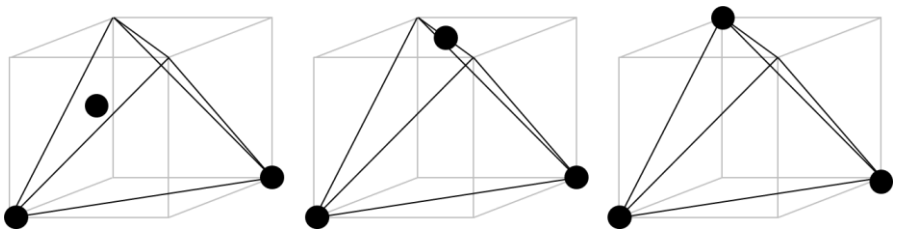

Figure 5.7.4 A schematic representation of the three possible configurations for a three defect system, assuming the two *s*=+1/2 defects are located on the vertices of the tetrahedron

The third option for the location of the *s*=+1 defect is likely to be very high in energy as the separation between the *s*=+1 defect and one of the *s*=+1/2 disclination lines is much less than in option one or two and so is not expected to be found. In option one, the separation between the defects is maximised and the resulting distribution of angles between two defects and the centre would show two peaks with a 1:2 ratio at approximately 109^{o} and 125.3^{o} corresponding to the angle between the two *s*=+1/2 and between the *s*=+1 and one *s*=+1/2, respectively. In option two, all the defects are located at the vertices of the large solid particle, which was found in cubic particles with three defects. The resulting distribution of angles between two defects and the centre would show one peak at approximately 109^{o}.

The defect configuration comprising of one *s*=+1 and two *s*=+1/2 defects was investigated for tetrahedral particles with $x = 8\sigma$ and the distribution of angles between two defects and the centre was analysed (Figure 5.7.3b). The resulting histogram showed one peak at 107.5^{o} with a standard deviation of 7.86^{o}, corresponding to option two where all the defects are located at the vertices of the solid particle. The standard deviation is very similar to that found in the four defect configuration for tetrahedral particles with a

nematic coating, indicating that the energy of defects formed away from the vertices is much higher than those formed at the vertices of the tetrahedron.

5.7.2 *SHIFTED TETRAHEDRAL PARTICLES*

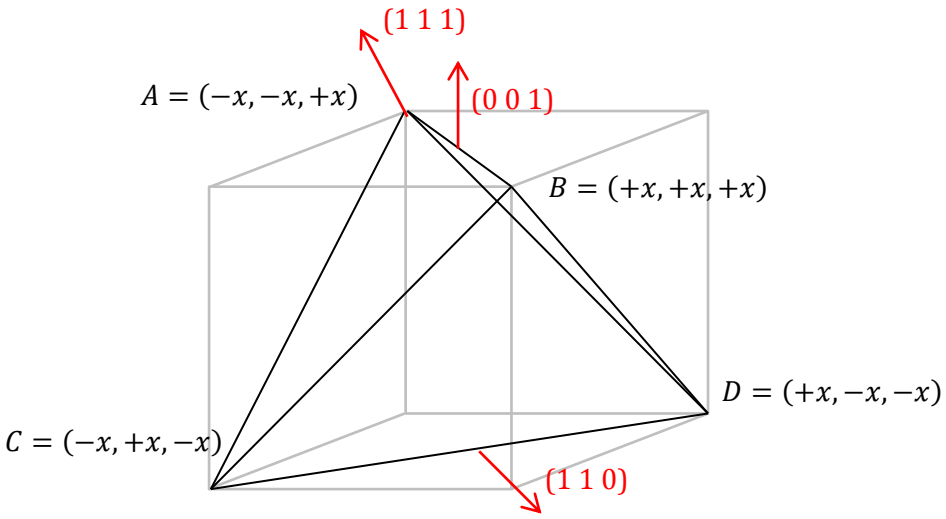

Figure 5.7.5 A schematic of the positions of the vertices of the tetrahedron (inside a cube for clarity). The red arrows show the vectors that the tetrahedron is shifted along

Leading on from the centred tetrahedral particles, a series of simulations were performed in which the centre of tetrahedral particles ($x = 6\sigma$ and 8σ) were shifted with respect to the centre of the simulation cell along one of three vectors, shown in red in Figure 5.7.5. The three vectors are (0 0 1), (1 1 0) and (1 1 1) and correspond to shifting the tetrahedral particle along an edge, face and vertex respectively. For the shifts along (0 0 1) and (1 1 0), shifting the centre of the tetrahedral in either the positive or negative direction are equivalent due to the symmetry of the tetrahedral particle. However, this is not the case when the tetrahedron is shifted along the vector (1 1 1) corresponding to shifting the large particle along a vertex and so both positive and negative shift values are investigated.

The tetrahedral particles were shifted by differing amounts, as shown in Table 5.7.1, for each vector as the magnitudes of the vectors are different. For example, when shifted by y

amount, the magnitudes for the vectors (0 0 1), (1 1 0) and (1 1 1) would be $y, \sqrt{2}y$ and $\sqrt{3}y$ respectively.

Table 5.7.1 The parameters used in shifted tetrahedral particles with nematic coatings

	Shifted amount along each vector/ σ		
	(0 0 1)	(1 1 0)	(1 1 1)
$x = 6\sigma$	2.0,3.0,4.0 & 5.0	2.0,2.5,3.0 & 3.5	$\pm$1.5, $\pm$2.0, $\pm$2.5 & $\pm$3.0
$x = 8\sigma$	1.0 & 2.0	1.0 & 1.5	$\pm$0.5 & $\pm$1.0

To recap, in simulations with an un-shifted tetrahedral particle, when $= 6\sigma$, a bipolar defect configuration with two *s*=+1 defects is favoured. When $x = 8\sigma$, the defect configurations comprising of three and four defects are equally likely to be observed with no bipolar configurations seen. It was not possible to investigate a shifted tetrahedron with $x = 10\sigma$ which only formed four *s*=+1/2 as shifting it would cause the nematic droplet to be pierced resulting in an incomplete nematic coating.

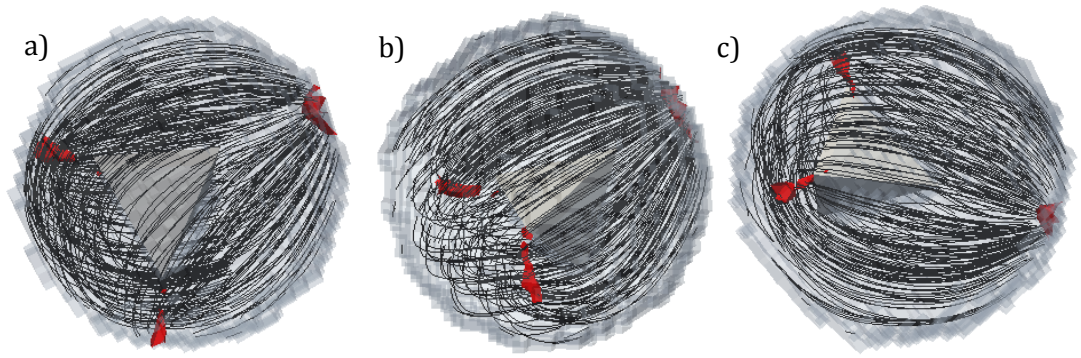

Figure 5.7.6 Three defect configurations for $x = 6\sigma$ a) shifted by 2.5σ along (1 1 0), b) shifted by 2.5σ along (1 1 1) and c) shifted by -2.5σ along (1 1 1)

The percentage of two-, three- and four-defect configurations observed were calculated for all systems investigated and found to be very similar for all systems. For $x = 6\sigma$, the defect configuration consisting of one *s*=+1 and two *s*=+1/2 defects was favoured for all shifted amounts along all vectors investigated and was observed in approximately 50-70% of the simulations for each system. The number of occurrences of the two and four defect configurations was approximately equal and independent from the amount shifted. The most commonly seen defect configuration in systems with $x = 6\sigma$ was with the two *s*=+1/2 defects at the thinner part of the nematic coating, minimising the length of the disclination line through the nematic coating (Figure 5.7.6). The stabilisation of the three defect configuration by shifting the inner particle towards the surface of the nematic droplet is similar to that shown in the non-uniform thickness nematic shells (section 3.5). In both cases, one of the *s*=+1 defects at the thinnest part of the nematic shell splits into two *s*=+1/2 disclination lines.

In systems with $= 6\sigma$, for configurations with three defects, the distribution of angles between two defects and the centre of the simulation cell was calculated for all shifted values. For systems shifted by 2σ along (0 0 1), the distribution of angles between two defects and the centre is similar to that seen for a centred tetrahedral particle with three defects (Figure 5.7.3b) and has a mean angle of 112.5^{o} and a standard deviation of 13.0^{o}, indicating that the defects are centred at the vertices of the tetrahedral particle (Figure 5.7.7a) as found in the un-shifted tetrahedral particles with a nematic coating. The standard deviation is larger than that seen in for an un-shifted tetrahedral particle suggesting that the *s*=+1 boojum is less strongly anchored to the vertex of the tetrahedron than the two *s*=+1/2 disclination lines. For systems shifted by 4σ and larger along (0 0 1), a very different angle distribution is seen with two distinct peaks, at 82.3^{o} and 124.4^{o}(Figure 5.7.7b), indicating that the defects may no longer be located at the vertices of the tetrahedron. The peak at approximately 80^{o} is due to the angle between the two *s*=+1/2

defects and is smaller than expected as the positions of the defects on the outer surface are closer together due to the shifted position of the large particle.

The deviation away from the three defects being located at verticex of a tetrahedron is even more pronounced when the tetrahedral particle is shifted along (1 1 0) or (1 1 1) with the angle distributions showing no favoured angle for many systems.

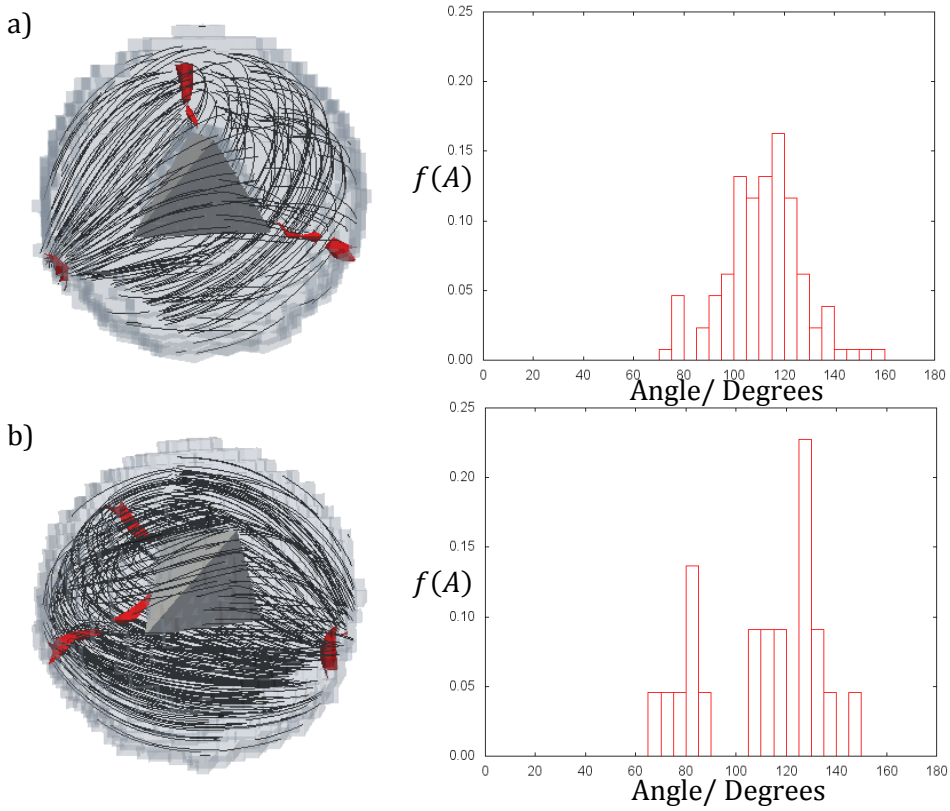

Figure 5.7.7 Tetrahedral particles ($x = 6\sigma$) shifted along (0 0 1) by a)2σ and b)4σ and their respective angle distributions.

For larger tetrahedrons ($x = 8\sigma$) it was possible to investigate the angle between four *s*=+1/2 defects. The distribution of angles between two defects and the centre of the simulation cell was calculated and showed very little change in the mean angle from that for the un-shifted tetrahedron with $x = 8\sigma$, however this could be due to the relatively small shifting amount allowed in these systems (Table 5.7.2). The standard deviation of the Gaussian function fitted to the distribution of angles is much larger than that for the un-shifted tetrahedral particle when shifted along both the (0 0 1) and (1 1 0) vectors, however

it is similar to the unshifted value when shifted along the (1 1 1) vector. The similarity in both the mean angle and standard deviation observed for tetrahedral particles displaced along the (1 1 1) vector can be explained by the limit on the size of the shift possible before the nematic coating 'pops' limiting the maximum displacement possible when $x = 8\sigma$ along (1 1 1) of 1σ, or $0.05r_{out}$, compared with a possible maximum displacement for $x = 6\sigma$ along (0 0 1) of 5σ or $0.25r_{out}$.

Table 5.7.2 The mean angle and standard deviation calculated from a Gaussian function fitted to the distribution of angles between two defects and the centre of the simulation cell for the maximum shifted value for a tetrahedral particle with $x = 8\sigma$ along the vectors investigated

$x = 8\sigma$	Mean angle / degrees	Standard Deviation/ degrees
Unshifted	107.5	7.9
Shifted by 2σ along (0 0 1)	107.9	13.0
Shifted by 1.5σ along (1 1 0)	112.6	12.4
Shifted by 1σ along (1 1 1)	114.0	4.8
Shifted by -1σ along (1 1 1)	108.4	7.2

5.8 OCTAHEDRAL PARTICLES WITH NEMATIC COATINGS

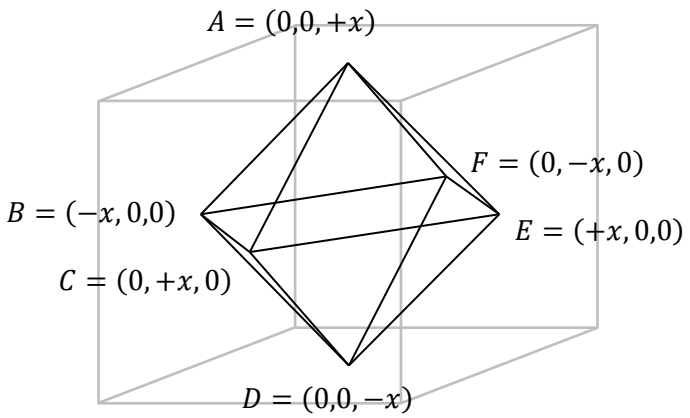

Figure 5.8.1 A schematic of an octahedral particle showing the vertices used

The final platonic solid particle investigated with a nematic coating was an octahedral particle, centred at the centre of the simulation cell. The octahedral particle had vertices as shown in Figure 5.8.1. As in the tetrahedral systems, the size of the octahedral particle is reported as the location of the vertices, x. The octahedral particle has sides of length (l) which are related to x by

$$l = \sqrt{2}x \tag{5.8.1}$$

again the initial nematic shell is spherical in nature with a radius (r_{out}) of 20σ.

Simulations were performed with $x = 12\sigma - 17\sigma$ with most sizes of octahedral particles with a nematic coating forming a bipolar defect configuration consisting of two *s*=+1 defects. It was not possible to run simulations with larger octahedral particles as for $x > 17\sigma$ the nematic coating 'popped' and an incomplete coating was produced. Only the largest octahedral particle ($x = 17\sigma$) investigated were any *s*=+1/2 defects seen. The propensity for the formation of *s*=+1 defects can be explained by the additional bulk character in the nematic shell. The extra volume when an octahedral particle is enclosed in a sphere is even greater than that when a tetrahedral particle is enclosed .The volume of an octahedron is

$$V_{oct} = \frac{4}{3}x^3 \quad (5.8.2)$$

By comparing the volume of the octahedron with a sphere of radius x (5.7.3) the difference in volume is clear,

$$V_{sphere} - V_{oct} = \frac{4}{3}\pi x^3 - \frac{4}{3}x^3 = \pi \quad (5.8.3)$$

The increase in the thickness of the nematic coating means it behaves similarly to a bulk droplet (forming two *s*=+1 defects) with planar anchoring than a thin shell with planar anchoring (forming four *s*+1/2 defects). Indeed, for $x = 12\sigma$, there are approximately 3700 more mesogens in an octahedral particle with a nematic coating compared to a spherical particle with a radius of x with $r_{out} = 20\sigma$ and $\rho^* = 0.75$.

In order to investigate the four defect configuration, a series of simulations were run cooling slowly over 62500MC cycles from the isotropic to a nematic at ${T^*}/{T^*_{N-I}} = 0.9$ were run for $x = 17\sigma$ and resulted in three main defect configurations being seen. One defect configuration formed one *s*=+1 and two *s*=+1/2 defects, the other two consisted of four *s*=+1/2 defects.

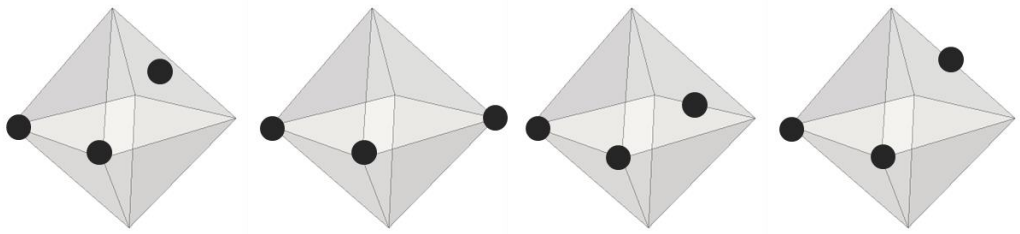

Figure 5.8.2 Four idealised arrangements for three defects assuming the two *s*=+1/2 defects are located on adjacent vertices

In the configurations with three defects which were observed in 42% of the simulations performed for $x = 17\sigma$, as in the cubic and tetrahedral particles with a nematic coating, the two *s*=+1/2 defects were located at adjacent vertices of the octahedral particle. Assuming the two s=+1/2 defects are always located at adjacent vertices and the s=+1

defect is located on the opposing side of the nematic coating, there are four possible defect configurations, one in which the boojum located on a face, one in which the boojum is located on the vertex and two with the boojum located on an edge (Figure 5.8.2).

In order to quantify the preferred arrangement in the three defect configuration, the angle between two defects and the centre was investigated. The predicted angles for the idealised defect configurations in Figure 5.8.2 are shown in Table 5.8.1.

Table 5.8.1 The predicted angles between defects for the four idealised defect configurations shown in Figure 5.8.2 assuming the two *s*=+1/2 defects are located at adjacent vertices. α,β and γ correspond to the angles shown in Figure 5.5.7 for a cubic particle with three defects.

Position of *s*=+1 defect (l-r in Figure 5.8.2)	Predicted Angles / Degrees		
	α	β	γ
Middle of face	90	114	114
Vertex	90	90	180
Edge in plane	90	135	135
Edge out of plane	90	90	135

The resulting distribution of angles between two defects and the centre (Figure 5.8.3b) shows two peaks and by fitting the function

$$f(A) = t_1\left[e^{-(A-\mu_1)^2/2\sigma_1^2} + e^{-(A-\mu_2)^2/2\sigma_2^2}\right] \quad (5.8.4)$$

The peaks are found to be at 79.7^{o} and 135.7^{o} suggesting that the *s*=+1 defect is located on an edge of the octahedral particle, unlike in systems with a cubic or tetrahedral particle where the *s*=+1 defect is located at a vertex. By modifying the function fitted to the resulting histogram, it is possible to estimate the ratio of occurrences of both angles to

differentiate between the configurations where *s*=+1 defect located at the edge in plane and out of plane with the two *s*=+1/2 defects. The predicted value for the ratio I_{80}/I_{135} for the in plane is 0.5, whereas for the out of plane it is 2.0. The calculated value was $I_{80}/I_{135} = 0.66$, indicating that the defect configuration with the *s*=+1 defect in plane was preferred, as shown in Figure 5.8.3a.

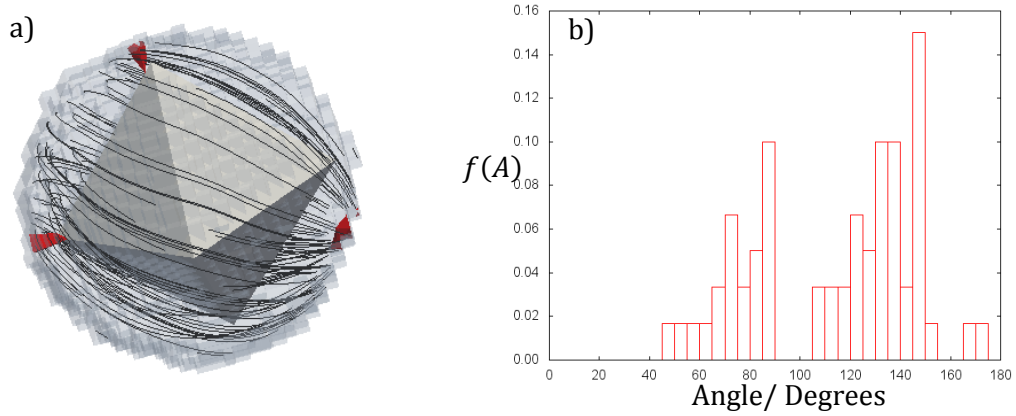

Figure 5.8.3 a) A nematic coating on an octahedral particle with one *s*=+1 and two *s*=+1/2 defects and b) the associated distribution of angles between defects

The resulting defect arrangement for three defects in which the two *s*=+1/2 defects are located at adjacent vertices of the octahedral particle and the *s*=+1 defect is located on the opposing edge in the same plane again highlights the differing nature of the *s*=+1 and *s*=+1/2 defects. The *s*=+1/2 defects are located at the vertices as this corresponds the the thinnest region of the nematic coating, minising the energy of the disclination line, which is proportional to the length of the defect. Due to the three-dimensional character of the *s*=+1 defect, the energy of the boojum is not dependent on the length of the defect and so the energy penalty for the movement of the *s*=+1 defect away from a vertex is smaller than that for a *s*=+1/2 defect. The *s*=+1 defect is located at an edge rather than a face of the octahedral particle due to the hyperbolic half hedgehog on the surface of the large particle. Both the edge and the vertex of the octahedral particle serve to reduce the volume of the

defect on the surface, minimising the associated energy cost due to the loss of nematic order in the defect.

Systems with four *s*=+1/2 defects were also observed in 42% of simulations run. In the simulations with four *s*=+1/2 defects, the defects tended to form at the vertices of the octahedron, however it was not uncommon for a defect to be found partway along one of the edges of the solid particle. Defects that are located along the edges of the octahedral particles occurs are observed as, unlike in cubic and tetrahedral particles with a nematic coating, there is no natural low energy tetrahedral arrangement possible in which all the defects are located on a vertex.

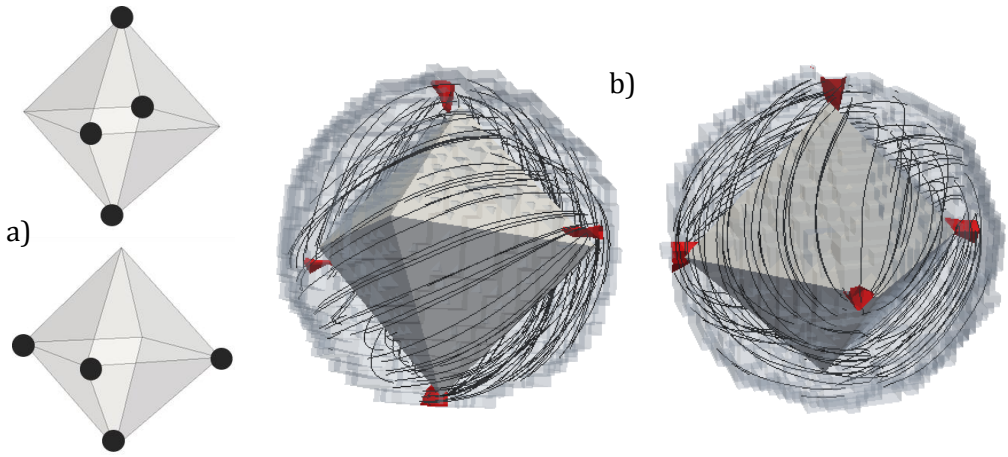

Figure 5.8.4 a) Idealised defect configurations for four *s*=+1/2 defects at the vertices of an octahedral particle. b) shows two visualisations corresponding to the suggested defect arrangements in a)

When the defects were all formed at vertices of the octahedron, there are fifteen ways to arrange four defects at the vertices of an octahedron, however due to the highly symmetrical nature of an octahedron, there are only the two distinct defect configurations. The defect configurations can be defined as the number of defects associated with each face and as such are:

1. one in which each face had two defects at the associated vertices, shown at the top of Figure 5.8.4a;
2. one in which two faces had three defects, two had two defects and two had one defect at the associated vertices, shown at the bottom of Figure 5.8.4a.

Defect configuration 1 is lower in energy than defect configuration 2 as the mean distance between defects is greater.

In a nematic, the defects form simultaneously along with additional defect pairs of opposite and equal strength which then annihilate to leave the equilibrated four defect structure seen. At all times, the total topological charge on the surface is conserved and equal to +2. As mentioned earlier, there are fifteen ways of forming four defects located at the vertices of an octahedral particle, three of these arrangements result in defect configuration 1 whereas twelve of these result in the formation of the defect configuration 2.

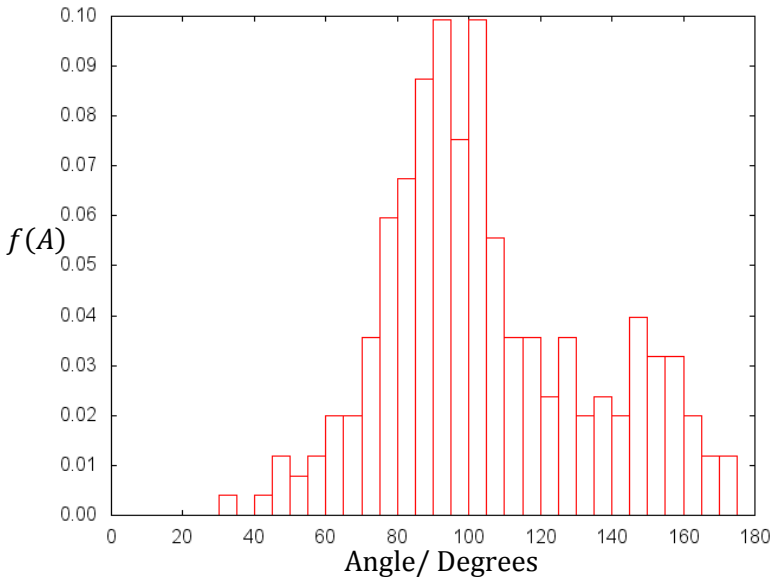

Figure 5.8.5 The distribution function of angles between two defects and the centres of an octahedral particle with $x = 17\sigma$

It is possible to distinguish between the two defect configurations by calculating the distribution of angles between two defects and the centre of the simulation cell. For defect configuration 1, the resulting histogram will have two peaks, one at 90° and one at 180° in approximately a 2:1 ratio. For defect configuration 2, the resulting histogram will again have two peaks at 90° and 180° however with the ratio 5:1. By fitting the function

$$f(A) = t_1 e^{-(x-\mu_1)^2/2\sigma_1^2} + t_2 e^{-(x-\mu_2)^2/2\sigma_2^2} \quad (5.8.5)$$

it is possible to calculate the approximate ratio I_{90}/I_{180}.

The distribution of angles between two defects and the centreshows two peaks as predicted at 93.4° and 148.8°. The slightly lower value than expected for the peak at 180° may be due to similar reasons as explained with the distribution of angles between two defects and the centre for cubic particles in section 5.5. Of course, the deviation from the predicted values may also be due to the defects moving away from the vertices in order to maximise the distance between them. The compulsion for the defects to be located on the edge rather than at the vertices can also be seen in the relatively large standard deviations for the two peaks, 16.1° and 15.2° compared to that for tetrahedral particles (6.1° when $x = 10\sigma$), however the standard deviations are still smaller than that seen for the spherical particle (25.4° for $r_{in} = 14\sigma$) where the only driving force for the defect arrangement is the minimisation of the elastic energy of the nematic. The calculated ratio I_{90}/I_{180} from (5.8.5) fitted to the distribution of angles between two defects and the centre was 2.84, suggesting the preferred arrangement was defect configuration 1.

5.9 CONCLUSION

In this chapter, systems of solid particles with a nematic coating and planar anchoring at both the liquid crystal-water and liquid crystal-particle surfaces were investigated. The use of a solid particle allowed for the investigation into different shaped particles and in particular, particles which were faceted and possessed vertices. Particles of three platonic solids, a cube, a tetrahedron and an octahedron were investigated in addition to a spherical particle, which is analogous to the nematic shells around a water droplet found in previous chapters. In all systems the total topological charge on the surface of the particle was equal to +2, as was the total topological charge on the outer nematic-water surface.

The use of a solid particle introduced additional terms into the interaction parameters to take into account the interaction between mesogen and water particles and the large solid particle. Preliminary simulations confirmed that the nematic bulk formed around the solid particle and the alignment was maintained at both surfaces. Simulations also showed that the nematic coating formed a sphere, minimising the unfavourable mesogen-water interactions.

Systems with a single spherical particle with nematic coating gave similar results to those shown by nematic shells enclosing a water droplet (*e.g.* Figure 3.4.2 and Figure 5.4.1). However, the presence of the solid surface stabilised the four s=+1/2 defect configuration with respect to the bipolar configuration and four s=+1/2 defects were seen in much thick shells than with the water-nematic-water systems.

Simulations of the platonic solid systems showed that the defects tended to form at the vertices of the particle, with only cases of defects not located on a vertex in systems with an octahedral particle where there is no natural tetrahedral arrangement possible in which all the defects are located at a vertex.

In systems that showed four s=+1/2 defects, for both cubic and octahedral particle with a nematic coating two distinct defect configurations were observed, which were very similar in energy (Figure 5.5.3 and Figure 5.8.4). However, for tetrahedral particles with a nematic coating, there are only four vertices and so only one defect configuration is possible in which all the defects are located at the vertices of the large particle. The corresponding distribution of angles between two defects and the centre had a much smaller standard deviation than for spherical particles. By employing tetrahedral particles as opposed to spherical particles, it would increase the possibility of the formation of a three-dimensional colloidal array, as suggested by Nelson[28] which could have applications in forming a photonic crystal at the visible wavelength.

For the tetrahedral and octahedral particles with a nematic coating, the four *s*=+1/2 defect configurations were only seen for very large particles due to the increased bulk-like behaviour of the nematic coating. Indeed, for most sizes of octahedral particles with a nematic coating investigated a bipolar defect configuration similar to that found in a nematic droplet was observed.

The three defect configuration consisting of one s=+1 and two s=+1/2 defects was seen for a range of sizes of tetrahedral particles and all three defects were located at the vertices of the tetrahedron (Figure 5.7.1). The three defect configuration was also found in some systems with a cubic particle (Figure 5.5.7) and again all three defects were located at the vertices of the larger particle. In comparison, for the octahedral particle the three defect configuration was only seen for the largest size particle investigated and whilst the two *s*=+1/2 defects were located at the vertices of the octahedron, the *s*=+1 defect was located mid-way along the opposite edge (Figure 5.8.3).

Systems in which the tetrahedrons that were shifted from the central position along one of three vectors, (0 0 1), (1 1 0) or (1 1 1) were also investigated. Due to the large size of the

tetrahedron compared with the radius of the nematic coating for systems where four *s*=+1/2 defects were seen, only small shifts along these vectors were possible and all simulations showed very similar results to the un-shifted tetrahedrons. In systems with smaller tetrahedrons which formed a bipolar configuration when un-shifted, the three defect configuration were seen consisting of one *s*=+1 and two *s*=+1/2 defects was stabilised compared to the bipolar configuration.

6 NEMATIC AND CHIRAL NEMATIC PHASES CONFINED IN A TORUS

6.1 INTRODUCTION

The lowest energy geometry for a droplet is a sphere as it minimises the surface area, which in turn minimises the unfavourable interactions between the droplet and its surroundings, in this case the mesogens and the surrounding water. In this chapter, a different class of geometry droplets are investigated, namely toroidal or doughnut shaped droplets. Toroidal droplets can be seen in nature, in raindrops[66] and in self-assembly in DNA[67]. In the area of liquid crystals, toroidal droplets of both isotropic[68] and nematic[69] phases have also been formed experimentally by confining the droplet in a gel matrix. By confining the fluid in a gel matrix, the torus is stabilised due to the yield stress of the gel matrix. The size and aspect ratio ξ,

$$\xi = \frac{r_{max}}{r_{min}} \tag{6.1.1}$$

Where r_{max} and r_{min} are as shown in Figure 6.1.1 of toroidal droplets than can be made in this manner is dependent on the interfacial tension between the nematic and the surrounding medium.

A torus is geometrically distinct from a sphere, in that it is not possible to continuously transform one into the other without breaking the system. Mathematically, a sphere and a torus are geometrically distinct as their Euler characteristics (χ) are different, for a sphere χ=2 whereas for a torus χ=0. The Euler characteristic is related to the number of handles in a system (*g*), where *g*=0 for a sphere and *g*=1 for a torus.

$$\chi = 2(1 - g) \tag{6.1.2}$$

The Poincaré-Hopf theorem relates to the Euler characteristic of a system. It states that for an ordered system on a surface, the total topological defect strength on the surface is equal to its Euler characteristic. As seen in previous chapters, spheres have a total topological charge of *s*=+2 on the surface, as expected as for a sphere $\chi = 2$. Of interest in this chapter is systems in which $\chi = 0$, in which a defect free director configuration should be seen. Toroidal systems give the opportunity to investigate this case.

Two different director configurations have been predicted by theory for toroidal nematic droplets with planar anchoring, an untwisted structure running axially around the torus or a twisted configuration. In general, the untwisted structure is seen for thin tori with a large aspect ratio ($r_{min} \ll r_{max}$) and the twisted structure for thicker tori with a smaller aspect ratio[70]. The cause of the spontaneous twist for thick tori is not known and has been suggested to be due to the minimisation of the bend distortion around the torus by transforming into a twisted state as generally $K_2 < K_3$ for calamitic molecules. More recently, it has been suggested that the saddle-splay elastic constant K_{24},[69] which is dependent on the surface of the system has an effect on when the cross over from an untwisted state to a twisted state is seen.

Little work has been done into nematic tori with homeotropic anchoring. A numerical study into nematic tori in magnetic fields[71] investigated three possible director configurations for a nematic tori with homeotropic anchoring, either one *s*=+1 defect or two *s*=+1/2 defects running around the torus or an escaped defect structure as seen in nematic capillaries[104]. Of these three director configurations, for a torus with homeotropic anchoring the two *s*=+1/2 defects was the most stable with no magnetic field due to the minimisation of elastic energy of the system. Indeed, for all magnetic field strengths, the two *s*=+1/2 defect configuration was lower in energy than either the *s*=+1 defect ring or the escaped defect configuration.

In this chapter, simulations of nematic tori and nematic cylinders which can be thought of as a toroidal system in the limit where $r_{max} \to \infty$, are discussed. The nematic tori droplets are simulated by confining the liquid crystal inside a toroidal cavity. These simulations do not contain any water particles as in previous chapters concerning spherical nematic shells and coatings on solid particles (chapters 3 to 5) as this would result in the decomposition to one or more spherical droplets (as seen experimentally). It would be possible for the structure of the external water to be frozen in an analogous manner to the gel matrix used experimentally, however this would drastically increase the number of particles in each simulation, increasing the computational cost without providing any additional insight into the toroidal nematic systems. Indeed, for a typical system investigated with $r_{max} = 30\sigma$ and $r_{min} = 20\sigma$, there are $N = 160331$ at $\rho^* = 0.75$ which would increase to $N = 419904$ with the inclusion of water particles.

6.1.1 *THE GEOMETRY OF A TORUS*

A torus can be obtained by moving a sphere with a radius of r_{min} along a ring with a radius of r_{max} (Figure 6.1.1).

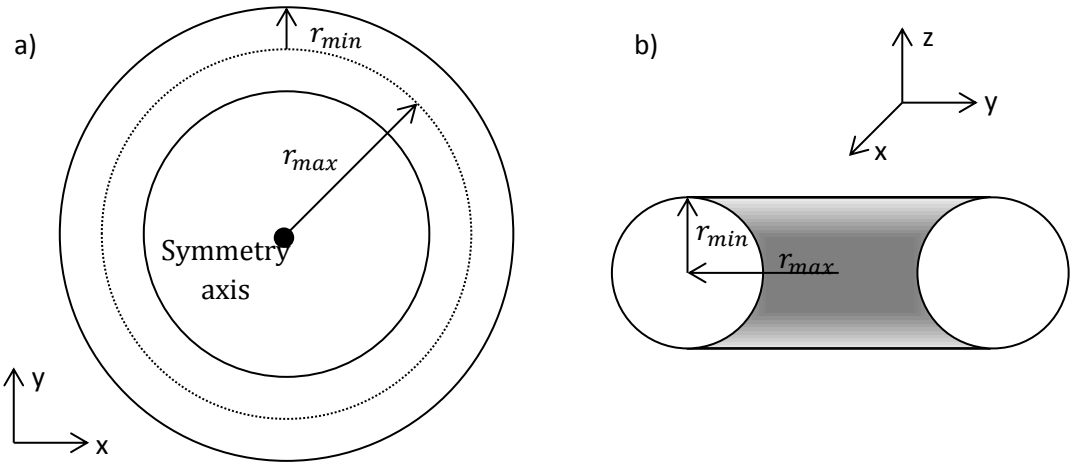

Figure 6.1.1 Parameters used to define a torus. a) Shows the torus from above and b) shows a cross section of the torus

There are three main classes of tori depending on the aspect ratio, ξ (6.1.1) . These are the ring torus ($r_{min} < r_{max}$) , the horn torus ($r_{min} = r_{max}$) and the spindle torus ($r_{min} > r_{max}$), as shown in Figure 6.1.2. As the Euler characteristic is the same for all three tori classes ($\chi = 0$), only the ring torus is considered here and henceforth will be referred to simply as a torus. The symmetry axis of the torus is set to be in the *z*-direction. The volume for a ring torus is

$$V_{tor} = 2\pi^2 r_{min}^2 r_{max} \tag{6.1.3}$$

which is equal to the area of the cross-section of the tube (πr_{min}^2) multiplied by the length (circumference) of the path ($2\pi r_{max}$).

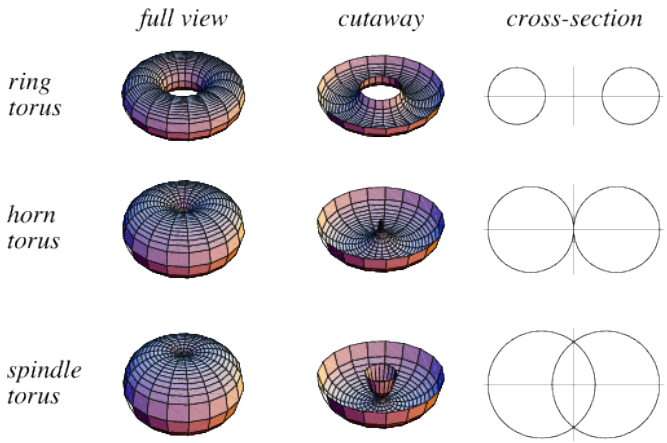

Figure 6.1.2 Examples of the three types of tori. Taken from mathforum.org[105]

6.1.2 *INTERACTION POTENTIALS*

In the systems investigated in this chapter, there are two types of interactions to take into account, mesogen-mesogen interactions and mesogen-wall interactions. The interaction potential used for mesogen-mesogen interactions is as detailed in Chapter2 . To recap, mesogens are modelled using an anisotropic hard sphere well with a unit vector representing the long molecular axis centred in each particle. In this chapter both non-chiral and chiral nematic phases are investigated using the mesogen-mesogen interaction potential ;

$$U^{LC-LC}(\boldsymbol{p}_i, \boldsymbol{p}_j, \boldsymbol{r}_{ij})$$

$$= \begin{cases} r \leq \sigma, & \infty \\ \sigma < r < 1.5\sigma, & U^{LC-LC}(\boldsymbol{p}_i, \boldsymbol{p}_j, \boldsymbol{r}_{ij}) + U^{LC-LC}_{chiral}(\boldsymbol{p}_i, \boldsymbol{p}_j, \boldsymbol{r}_{ij}) \\ 1.5\sigma \leq r, & 0 \end{cases} \quad (6.1.4)$$

where $\boldsymbol{p}_i$and $\boldsymbol{p}_j$ are unit vectors defining the orientations of particles *i* and *j* and $\boldsymbol{r}_{ij}$ is the vector between the centres of *i* and *j.*

$$U^{LC-LC}(\boldsymbol{p}_i, \boldsymbol{p}_j, \boldsymbol{r}_{ij})$$

$$= -\varepsilon \Big[J_1 (\boldsymbol{p}_i \cdot \boldsymbol{p}_j)^2 - 2J_2 (\boldsymbol{p}_i \cdot \boldsymbol{p}_j)(\boldsymbol{p}_i \cdot \hat{\boldsymbol{r}}_{ij})(\boldsymbol{p}_j \cdot \hat{\boldsymbol{r}}_{ij}) \quad (6.1.5)$$

$$+ J_3 (\boldsymbol{p}_i \cdot \hat{\boldsymbol{r}}_{ij})^2 (\boldsymbol{p}_j \cdot \hat{\boldsymbol{r}}_{ij})^2 \Big]$$

$$U^{LC-LC}_{chiral}(\boldsymbol{p_i}, \boldsymbol{p_j}, \boldsymbol{r_{ij}}) = \varepsilon_c [\hat{\boldsymbol{r}}_{\boldsymbol{ij}} \cdot (\boldsymbol{p_i} \times \boldsymbol{p_j})][(\boldsymbol{p}_i \cdot \boldsymbol{p}_j)] \quad (6.1.6)$$

ε_c is the chiral parameter and the pitch of the chiral nematic decreases with increasing ε_c. For non-chiral nematic systems, $\varepsilon_c = 0$. The pitch lengths associated with selected values of ε_c are shown in section 2.5.2 with pitch lengths ranging from approximately 200σ to 60σ. In the simulations performed in this chapter, potential 1 is used with $J_1 = 1, J_2 = 0$ and $J_3 = 0$ unless otherwise stated.

The interaction potential used for mesogen-wall interaction is similar to that used for mesogen-water interactions in previous chapters ,

$$U^{LC-Wall}(\boldsymbol{p}_i, \boldsymbol{r}_i) = \begin{cases} r \leq \sigma, & \infty \\ \sigma < r < 1.5\sigma, & U^{LC-Wall}(\boldsymbol{p}_i, \boldsymbol{r}_i) \\ 1.5\sigma \leq r, & 0 \end{cases} \quad (6.1.7)$$

Where $\boldsymbol{r}_i$ is the vector between the particle and the closet point on the toroidal surface and

$$U^{LC-Wall}(\boldsymbol{p}_i, \boldsymbol{r}_i) = +\varepsilon_A (\boldsymbol{p}_i \cdot \hat{\boldsymbol{r}}_i)^2 \quad (6.1.8)$$

$$U^{LC-Wall;}(\boldsymbol{p}_i, \boldsymbol{r}_{ip}) = -\varepsilon_A (\boldsymbol{p}_i \cdot \hat{\boldsymbol{r}}_i)^2 \quad (6.1.9)$$

corresponding to planar and homeotropic anchoring respectively.

6.1.3 *SIMULATION PARAMETERS*

All simulations in this chapter were run at $\rho^* = 0.75$ using cubic analysis cells with sides of 1.5σ. All simulations were started from an isotropic configuration and run at ${T^*}/{T^*_{N-I}} = 0.9$ unless otherwise stated.

Isotropic starting configurations were made by filling the torus with a cubic lattice of $\rho^* = 1$ with $\boldsymbol{p}_i = (0\ 0\ 1)$, then removing particles at random to reach the required number of particles corresponding to $\rho^* = 0.75$. These were then run for a short time at a high temperature ($T^* = 1000$) to produce an isotropic phase.

6.2 Nematics confined in a cylinder

Cylinders can be considered as a toroidal system in the limit where $r_{max} \rightarrow \infty$. Simulations were run varying both the radius, which is analogous to r_{min} in a torus, and length of the cylinder (

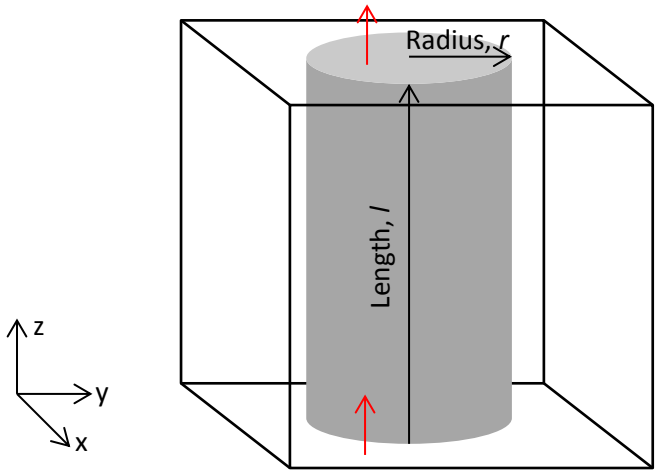

Figure 6.2.1 Schematic of cylinder simulations

Table 6.2.1) with both planar and homeotropic anchoring. The cylinder is set to run in the *z*-direction and there is a periodic boundary condition in the *z*-direction as shown by the red arrows in Figure 6.2.1.

Table 6.2.1 Cylinder parameters used

Radius (*r*)/σ	Length (*l*)/σ
12	48
16	24,36,48,72,96
20	48

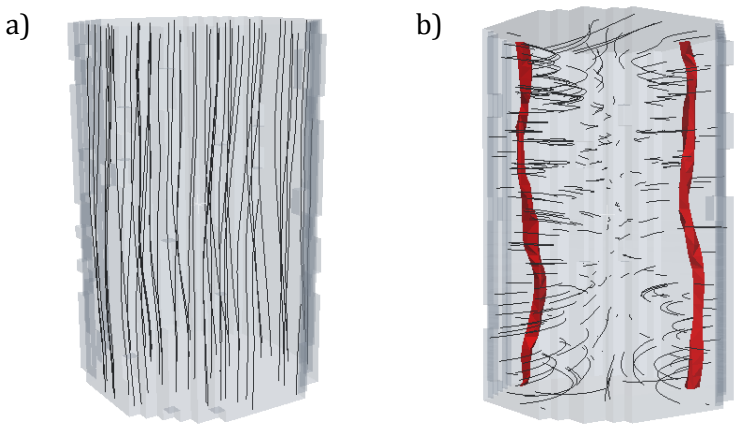

Figure 6.2.2 A cylinder with a) planar anchoring and b) homeotropic anchoring where

$$T^*/T^*_{N-I} = 0.9,\ r = 16\sigma, l = 48\sigma$$

In all simulations of a cylinder with planar anchoring, a defect free director configuration is observed in which the director runs through the cylinder (Figure 6.2.2a). However, in a cylinder with homeotropic anchoring, unlike the cylinder with planar anchoring it is not possible for a defect-free director configuration to form. There are three possible defect

configurations, similar to those discussed briefly at the start of the chapter in relation to a torus with homeotropic boundary conditions. These are either one *s*=+1 (Figure 6.2.3a) or two *s*=+1/2 (Figure 6.2.3b) defect line(s) running the length of the cylinder or an escaped-like director configuration in which the director escapes into the third dimension to remove the disclination line (Figure 6.2.3c). It has been found that the type of director configuration observed is dependent on both the radius of the cylinder and the elastic properties of the nematic[106]. The *s*=+1 disclination line tends to be found in small capillaries or close to the nematic-isotropic transition, but is unstable with respect to two *s*=+1/2 disclination lines at the radius increases. For large *r*, the escaped director configuration is most stable, however it is very rarely observed, instead manifesting as a periodic array of $s = \pm 1$ defects with partially escaped domains between the defects[107].

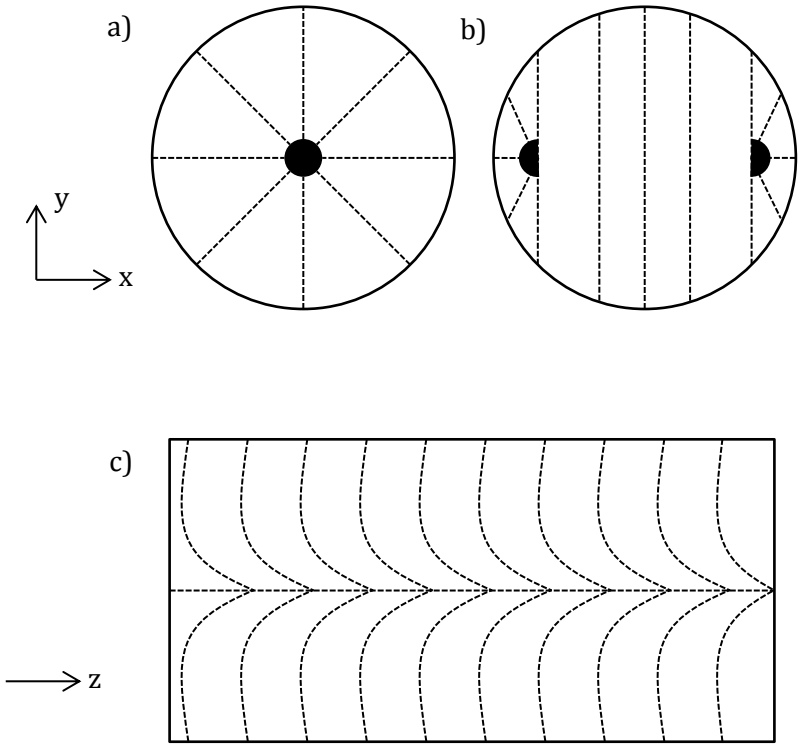

Figure 6.2.3 Idealised schematic representations of a) one *s*=+1 defect configuration and b) two *s*=+1/2 defects configuration and c) an escaped director configuration

In all simulations performed of a nematic cylinder with homeotropic anchoring, two *s*+1/2 defect lines were seen (Figure 6.2.2b).The energy of a disclination line is proportional to s^2 and so is less for two *s*=+1/2 disclination lines compared to one *s*=+1 disclination line. An escaped director configuration (Figure 6.2.3c) is not seen due to the periodic boundary conditions which do not allow the director to escape into the third dimension.

6.3 NEMATICS CONFINED TO A TOROIDAL GEOMETRY

6.3.1 *NEMATIC TORI WITH PLANAR ANCHORING*

For an ordered system, in this case a nematic with planar anchoring, the total topological charge on the surface must be equal to the Euler characteristic (χ) of the geometry investigated. For a single torus $\chi = 0$, and so the ground state director configuration for a nematic torus with planar anchoring defect-free. A defect free director configuration was occasionally observed when started from an isotropic phase, however, this was not always the case. Director configurations with one or more boojum-like defects were also seen (Figure 6.3.1). The boojum-like defects consisted of one *s*=+1 and *s*=-1 hedgehog defect on the inner and outer regions respectively, thus conserving the total topological charge as required by the Euler constraint, and were stable and once formed remained for the rest of the simulation suggesting that the energy barrier for the defects of the opposing sign to meet and annihilate was larger than the thermal energy of the system.

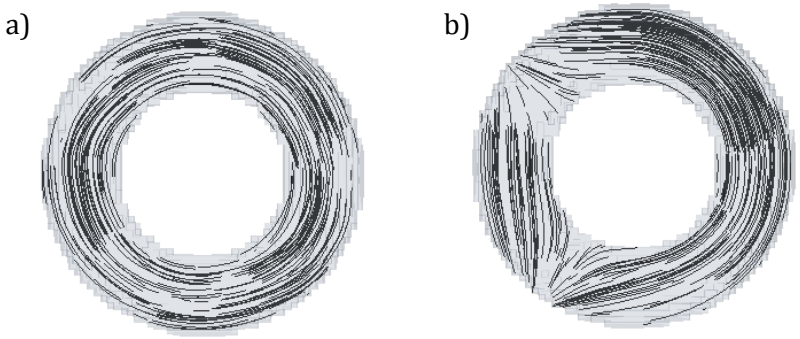

Figure 6.3.1 A torus with planar anchoring with a director configuration with a) no defects and b) two boojums

Previous work, by both experimentally by Pairam *et al*[69] and theoretically by Kulic *et al*[70] have found the presence of a twisted director configuration in nematic tori with planar anchoring. In order to investigate the spontaneous twisting of the director, a defect free system is needed. To form a defect free director configuration, the simulation was started from a perfect alignment around the torus by setting the orientation vector to;

$$\boldsymbol{p}_i = \frac{(r_{ix}, -r_{iy}, 0)}{|r|} \qquad (6.3.1)$$

where $\boldsymbol{r}_i$ is the position vector from the centre of the simulation cell.

The spontaneously twisted director configurations was not observed in simulations run either from an isotropic or from a defect-free starting configuration for any values of r_{max} and r_{min}. To investigate the difference in energy between the twisted state and the axial state, systems were started from a twisted configuration and an axial configuration. The starting configurations were produced by applying a local field

$$E_{twist} = \varepsilon_{field}\left[\hat{\boldsymbol{s}}\left(1 - \varepsilon_{twist}\frac{r_i}{r_{min}}\right) + \hat{\boldsymbol{t}}\left(\varepsilon_{twist}\frac{r_i}{r_{min}}\right)\right] \qquad (6.3.2)$$

$\hat{\boldsymbol{s}}$ is a unit vector around the torus and $\hat{\boldsymbol{t}}$ is a unit vector perpendicular to both $\boldsymbol{r}_c$ and $\hat{\boldsymbol{s}}$ (Figure 6.3.2a) and ε_{field} is the field strength. The two limiting director configurations are $\varepsilon_{twist} = 0$ where the director is axial and $\varepsilon_{twist} = 1$ where the director goes round the tube of the torus on the surface and runs round the torus in the centre of the tube (Figure 6.3.2b & c).

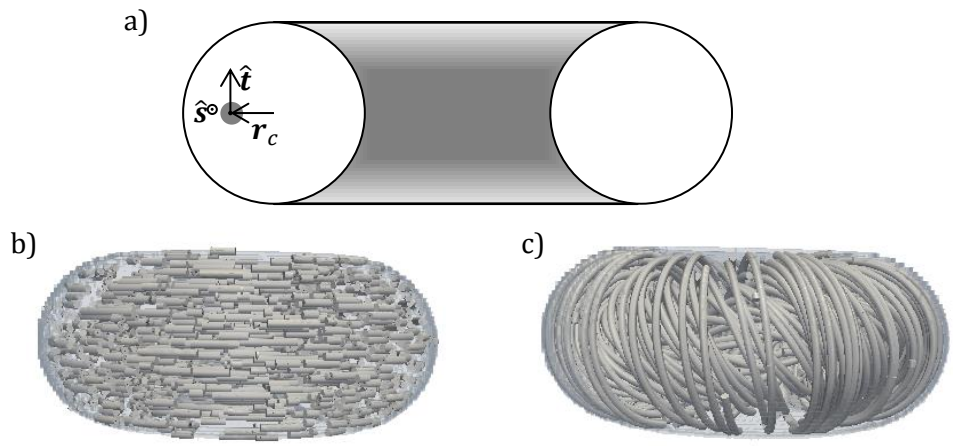

Figure 6.3.2 a) A schematic showing $\boldsymbol{r}_c, \hat{\boldsymbol{t}}$ and $\hat{\boldsymbol{s}}$. $\hat{\boldsymbol{s}}$ is into the page and b) and c) show a torus with planar anchoring with $\varepsilon_{twist} = 0$and $\varepsilon_{twist} = 1$ respectively

By running simulations at varying values of ε_{field}, due to the linear relationship between mean energy per particle and the local field strength (Figure 6.3.3a), it is possible to extrapolate to $\varepsilon_{field} = 0$ and estimate the energy difference between director configurations. Simulations were run with $\varepsilon_{twist} = 0, 0.2, 0.4\ 0.5, 0.6, 0.8$ and 1.0 for $r_{max} = 30\sigma, r_{min} = 20\sigma$ at ${T^*}/{T^*_{N-I}} = 0.95$.

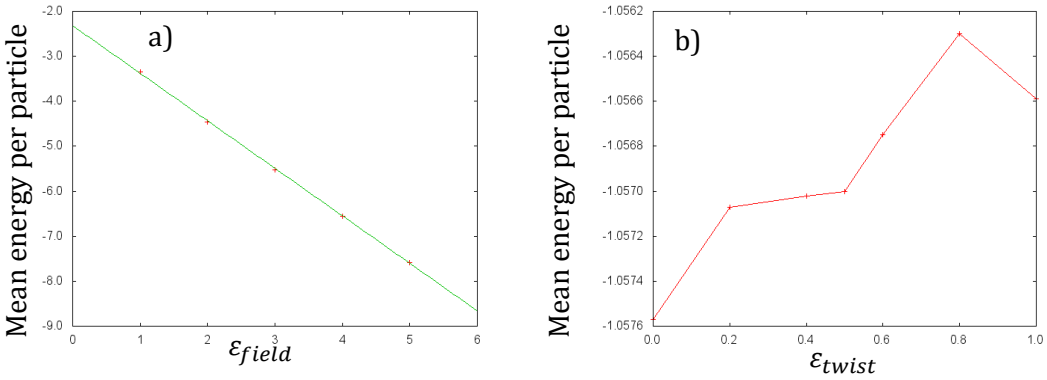

Figure 6.3.3 a) shows the linear relationship between ε_{field} and the mean energy per particle for $\varepsilon_{twist} = 1$. b) shows the estimated energy at for each value of ε_{twist} for $r_{max} = 30\sigma, r_{min} = 20\sigma$

The calculated mean energy per particle for the different director configurations confirms that the untwisted director configuration where $\varepsilon_{twist} = 0$ is lowest in energy (Figure 6.3.3b).

Simulations were also performed potentials A1-3 and B1-3 detailed in chapter 2 to vary the energy between end-end and side-side interactions. The difference in energy between these interactions leads to a variation in the twist bend elastic constant ratio, ${K_2}/{K_3}$.For example, ${K_2}/{K_3} = 1.23$ and 0.72 for potentials A3 and B3 respectively. Tori with $r_{max} = 30\sigma, r_{min} = 10\sigma, 15\sigma,$ and 20σ were run corresponding to $\xi = 3 - 1.5$. For all cases, the director untwisted, showing that, for the potential based on hard sphere with orientation vectors, the twisted director configuration is unstable. The instability of the twisted director configuration may indicate that the potentials developed and utilised here

have a value of $^{K_{24}}/_{K_2}$ below the threshold calculated by Pairam *et al*[69] where K_{24} is the saddle-splay elastic constant. It is not possible to calculate K_{24} or $^{K_{24}}/_{K_2}$ from the simulations as K_{24} is a surface dependent elastic constant. The lack of the twisted director configuration can then lead to an estimation that $^{K_{24}}/_{K_2} < 0.9$ for all potentials used.

6.3.2 *Nematic tori with Homeotropic anchoring*

As with nematic cylinders with homeotropic anchoring (section 6.2), it is not possible for a nematic tori with homeotropic anchoring to form a defect free director configuration. All values of r_{max} and r_{min} showed the same defect configuration consisting of two *s*=+1/2 defect lines on the surface of the torus, one running around the inside of the ring torus and one around the outside.

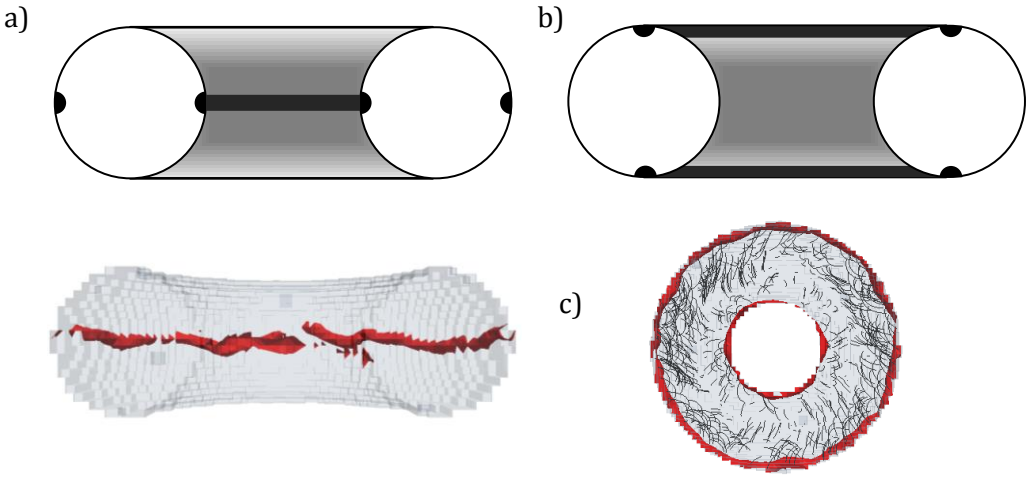

Figure 6.3.4 Schematics of a torus with homeotropic anchoring with two *s*=+1/2 defect lines with the defect lines a) around the inside& outside and b) the top & bottom and c) a cut through showing the defect configuration. The director streamlines are removes for clarity

There were two possible positions for the defects lines which maximised the distance between them, either running along the inside and outside (Figure 6.3.4a), or along the top

and the bottom (Figure 6.3.4b). Both possible defect positions have the same total defect length of $4\pi r_{max}$ and the same distance between them, $2r_{min}$. Only defect configurations with the disclination lines on the inside and outside were seen. It is likely that the elastic energy of the defect configuration in which the disclination lines run along the top and bottom of the torus are is higher than that for the defects at the inner and outer regions due to the intrinsic bend of the torus. When the defects are located at the top and bottom, there is a greater splay distortion in the nematic than when the defects are located on the inside and outside of the torus.

6.4 GAY-BERNE SIMULATIONS OF NEMATIC TORI WITH PLANAR ANCHORING

In section 6.3.1, it has been demonstrated that for the simple model the twisted director configuration observed experimentally and predicted by theory is not formed. Whilst it is not possible to calculate and vary the ratio K_{24}/K_2, in an earlier paper by Kulic *et al*[70] the formation of a twisted director configuration is dependent on the ratio K_2/K_3. The simple model used previously does not allow a wide range of elastic constant ratios and so the Gay-Berne potential is employed. The elastic constants for the Gay-Berne potential have previously been calculated for both thick platelets[98] and ellipsoidal particles[97] and were found to be much larger than the simpler potential used previously.

The Gay-Berne model is an anisotropic version of the Lennard-Jones potential and it takes into account both short- and long-range interactions. The potential is based on ellipsoidal particles with length *l* and breadth *d* where *l*>*d* , σ_e and σ_s are the end-to-end and the side-to-side diameters respectively and ε_e and ε_s the end-to-end and side-to-side well depths. The potential is given by [76];

$$U(\boldsymbol{p}_i, \boldsymbol{p}_j, \boldsymbol{r}_{ij}) = 4\varepsilon(\boldsymbol{p}_i, \boldsymbol{p}_j, \hat{\boldsymbol{r}}_{ij})\left[\left(\frac{\sigma_s}{r_{ij} - \sigma(\boldsymbol{p_i}, \boldsymbol{p_j}, \hat{\boldsymbol{r}}_{\boldsymbol{ij}}) + \sigma_s}\right)^{12} - \left(\frac{\sigma_s}{r_{ij} - \sigma(\boldsymbol{p_i}, \boldsymbol{p_j}, \hat{\boldsymbol{r}}_{\boldsymbol{ij}}) + \sigma_s}\right)^{6}\right] \quad (6.4.1)$$

where $\boldsymbol{p}_i$ and $\boldsymbol{p}_j$ are unit vectors representing the orientations of the molecules and $\boldsymbol{r_{ij}}$ the separation between the molecules. The orientation dependent part of the Gay-Berne potential is;

$$\sigma(\boldsymbol{p_i}, \boldsymbol{p_j}, \hat{\boldsymbol{r}}_{\boldsymbol{ij}}) = \sigma_s \Bigg/ \sqrt{1 - \frac{\chi}{2}\left\{\frac{\left[\hat{\boldsymbol{r}}_{ij} \cdot (\boldsymbol{p}_i + \boldsymbol{p}_j)\right]^2}{1 + \chi(\boldsymbol{p}_i \cdot \boldsymbol{p}_j)} + \frac{\left[\hat{\boldsymbol{r}}_{ij} \cdot (\boldsymbol{p}_i - \boldsymbol{p}_j)\right]^2}{1 - \chi(\boldsymbol{p}_i \cdot \boldsymbol{p}_j)}\right\}} \quad (6.4.2)$$

For spherical particles this reduces to σ_s which is the spherical diameter, or $\sqrt{2}d$[85].

$\varepsilon(\boldsymbol{p}_i, \boldsymbol{p}_j, \hat{\boldsymbol{r}}_{ij})$ affects the well depths in the potential.

$$\varepsilon(\boldsymbol{p}_i, \boldsymbol{p}_j, \hat{\boldsymbol{r}}_{ij}) = \varepsilon_s \boldsymbol{\varepsilon}'^{\nu}(\boldsymbol{p}_i, \boldsymbol{p}_j)\varepsilon''^{\mu}(\boldsymbol{p}_i, \boldsymbol{p}_j, \hat{\boldsymbol{r}}_{ij}) \quad (6.4.3)$$

$$\varepsilon'(\boldsymbol{p_i}, \boldsymbol{p_j}) = 1 \Bigg/ \sqrt{1 - \chi^2(\boldsymbol{p}_i \cdot \boldsymbol{p}_j)^2} \quad (6.4.4)$$

$$\boldsymbol{\varepsilon}''(\boldsymbol{p_i}, \boldsymbol{p_j}, \hat{\boldsymbol{r}}_{\boldsymbol{ij}}) = 1 - \frac{\chi'}{2}\left\{\frac{\left[\hat{\boldsymbol{r}}_{ij} \cdot (\boldsymbol{p}_i + \boldsymbol{p}_j)\right]^2}{1 + \chi'(\boldsymbol{p}_i \cdot \boldsymbol{p}_j)} + \frac{\left[\hat{\boldsymbol{r}}_{ij} \cdot (\boldsymbol{p}_i - \boldsymbol{p}_j)\right]^2}{1 - \chi'(\boldsymbol{p}_i \cdot \boldsymbol{p}_j)}\right\} \quad (6.4.5)$$

$$\chi = \frac{\kappa^2 - 1}{\kappa^2 + 1} \text{ and } \chi' = \frac{\kappa^{\frac{1}{\mu}} - 1}{\kappa^{\frac{1}{\mu}} + 1} \quad (6.4.6)$$

Where $\kappa = \frac{\sigma_e}{\sigma_s}$ and $\kappa = \frac{\varepsilon_s}{\varepsilon_e}$.

In the original paper, values of $\kappa = 3, \kappa' = 5, \mu = 2$ and $\nu = 1$ or GB(3,5,2,1) where GB(κ,κ',μ,ν), were used. Bulk systems using these parameters, form both a nematic and an isotropic phase. By varying the parameters κ, κ', μ and ν, it is possible to tune both the position and relative depths of the potential wells for the four limiting particle interactions,

shown in Figure 6.4.1. Consequent work varying the parameters used found that more ordered mesophases may be formed using the Gay-Berne potential, for example GB(4.4,20,1,1)[87] forms a smectic phase in addition to a nematic and isotopic phases.

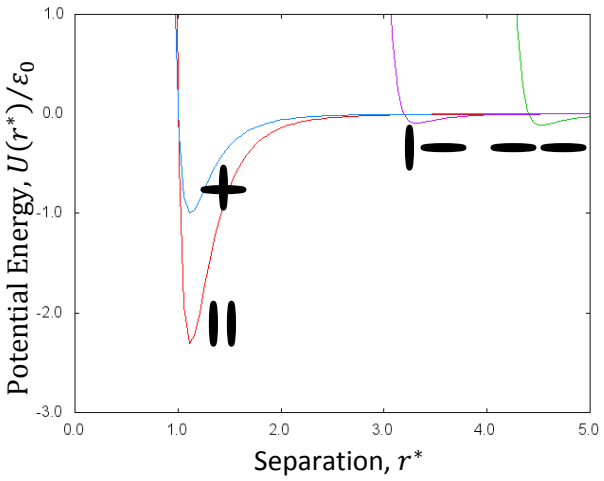

Figure 6.4.1 The dependence of the GB(4.4,20,1,1) for the scaled separation ($r^* \equiv {}^{r_{ij}}/_{\sigma_s}$) for the four limiting cases; side-side (red), cross (blue), side-end (purple) and end-end (green)

6.4.1 *Mesogen-Wall interaction potential*

The anchoring potential used in simulations employing the Gay-Berne interaction potential were as shown in (6.1.7) and (6.1.8), corresponding the planar anchoring. To recap the mesogen-wall potential is

$$U^{LC-Wall}(\boldsymbol{p}_i, \boldsymbol{r}_i) = \begin{cases} r \leq \sigma_s, & \infty \\ \sigma_s < r < 1.5\sigma_s, & U^{LC-Wall}(\boldsymbol{p}_i, \boldsymbol{r}_i) \\ 1.5\sigma_s \leq r, & 0 \end{cases} \qquad (6.4.7)$$

However, due to the elongated nature of the Gay-Berne particles, additional constraints to the mesogen-wall interaction were required,

$$U^{LC-Wall}(\boldsymbol{p}_i, \boldsymbol{r}_i) = \begin{cases} |(\boldsymbol{r}_i \pm 1.0\sigma_s \boldsymbol{p}_i)| < \sigma_s, & \infty \text{ for GB(3,5,2,1)} \\ |(\boldsymbol{r}_i \pm 1.7\sigma_s \boldsymbol{p}_i)| < \sigma_s, & \infty \text{ for GB(4.4,20,1,1)} \end{cases} \qquad (6.4.8)$$

to ensure that the entirety of the mesogen is confined within the torus and that the ends cannot leave the toroidal cavity.

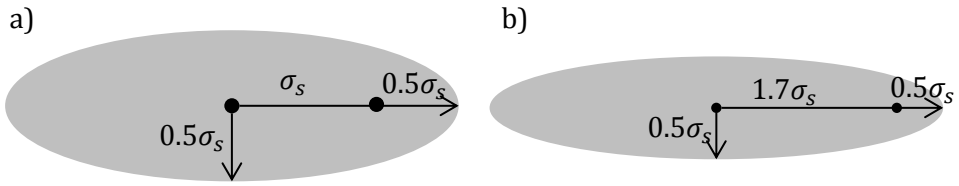

Figure 6.4.2 A schematic representation of the ellipsoidal Gay-Berne particles showing the parameters for the additional constraint on the mesogen-wall interaction for a) GB(3,5,2,1) and b) GB(4.4,20,1,1)

6.4.2 *SIMULATION PARAMETERS*

In this chapter, two sets of parameters were used to investigate the nematic phase when confined to a toroidal cavity; GB(3,5,2,1) and GB(4.4,20,1,1). GB(3,5,2,1) is using the original values proposed[76] and GB(4.4,20,1,1) is using values first proposed by Luckhurst and Simmonds[86] as a more realistic model for a mesogen based on *p*-terphenyl. A potential cut-off distance (r_{cut}) of $4.5\sigma_s$ and $5.5\sigma_s$were used for the GB(3,5,2,1) and GB(4.4,20,1,1) potentials respectively. The elastic constants for both models have been previously calculated by Allen *et al*[97]and were re-calculated for this work. The resulting elastic constant ratios are shown in Table 6.4.1 and Table 6.4.2.

The Gay-Berne potential is much more computationally intensive than the previous model based on hard spheres so in order to investigate tori of comparable size to those run with the simpler potential only a small section of a torus was simulated, with both a quarter (Figure 6.4.3a) and an eighth (Figure 6.4.3b) of a torus investigated. There are periodic boundaries at both the *x*-axis and either the *y*-axis in quarter simulations, or along *y=x* in eighth of a torus simulations (Figure 6.4.3).

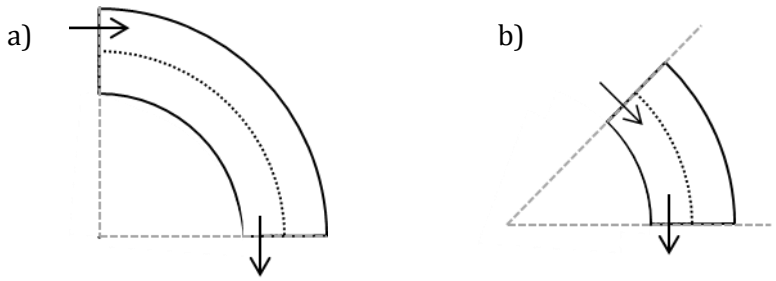

Figure 6.4.3 Schematics of the a) quarter and b) eighth of a torus simulations. The arrows show the movement of a particle out of the bottom of the simulation into the top

Several different systems were investigated for both Gay-Berne models. There is a constraint on the system size investigated due to the arc of the inner surface (which has a radius of $r_{max} - r_{min}$),

$$\frac{\pi(r_{max} - r_{min})}{M} > r_{cut} \tag{6.4.9}$$

Where *M*=4 for a quarter and *M*=8 for an eighth. When the arc is smaller than the potential cut-off used, the periodic boundary conditions could lead to an unrealistic result. The size of the tori investigated is $r_{max} = 30\sigma_s, r_{min} = 10\sigma_s, 15\sigma_s$ and $20\sigma_s$, $r_{max} = 40\sigma_s, r_{min} = 20\sigma_s$ and $r_{max} = 48\sigma_s, r_{min} = 16\sigma_s$ for both models and tori sections as long as the aforementioned constraint is met, *e.g.* no eighths of a torus where $r_{max} = 30\sigma_s, r_{min} = 20\sigma_s$ were investigated as the inequality in (6.4.9) is not true. The tori parameters investigated correspond to varying the aspect ratio from $\xi = 1.5 - 3$.

The starting configurations were produced by gradually elongating spherical particles by gradually increasing κ at a high temperature above the nematic-isotropic transition.

6.4.3 *GB(3,5,2,1) NEMATIC TORI WITH PLANAR ANCHORING*

For the Gay Berne model with parameters $\kappa = 3, \kappa' = 5, \mu = 2 \text{ and } \nu = 1$ simulations were run at a reduced density of $\rho^* = 0.35$. The bulk properties were calculated using the same method as for the simpler potential in chapter 2 and can be seen in Table 6.4.1.

Table 6.4.1 Bulk properties for GB(3,5,2,1) at $\rho^* = 0.35$

	$\rho^* = 0.35$
T^*_{N-I}	2.8
K_1/K_3	At $T^* = 2.0, 0.2954$
K_2/K_3	At $T^* = 2.0, 0.2685$

Simulations were run from an isotropic starting configuration for all tori sizes investigated. Additionally for $r_{max} = 30\sigma_s\ r_{min} = 20\sigma_s \text{ and} r_{max} = 40\sigma_s\ r_{min} = 20\sigma_s$ simulations were run from a series of aligned states. The aligned stated were produced by applying a strong ($\varepsilon_{field} = 1000$) local field at a temperature much higher than the nematic-isotropic transition temperature. The local field used is identical to the one used for the simpler potential (6.3.2). Simulations were then run at $T^* = 2.0$ ($\approx 70\% T^*_{NI}$) and for selected systems at $T^* = 2.5$ ($\approx 90\% T^*_{NI}$) for $\varepsilon_{twist} = 0.0, 0.2, 0.4, 0.5, 0.6, 0.8 \text{ and } 1.0$. Note that $\varepsilon_{twist} = 0$ corresponds to an untwisted director configuration.

As with the simulations run using the simpler potential, no twisted director configurations were seen from those started from an isotropic configuration and those started from a twist configuration untwisted when the local field was removed. It is possible however, by calculating the mean energy per particle for different values of ε_{field} to extrapolate backwards to estimate the energy difference between differing twist amounts due to the linear relationship between the field strength (ε_{field}) and the mean energy per particle

(Figure 6.4.4a). For an eighth of a torus with $r_{max} = 30\sigma_s, r_{min} = 20\sigma_s$ and $r_{max} = 40\sigma_s, r_{min} = 20\sigma_s$values of $\varepsilon_{twist} = 0.0, 0.2, 0.4, 0.5, 0.6, 0.8 \text{ and } 1.0$ where $\varepsilon_{twist} = 0$ corresponds to an untwisted director configuration were run with a series of ε_{field} values.

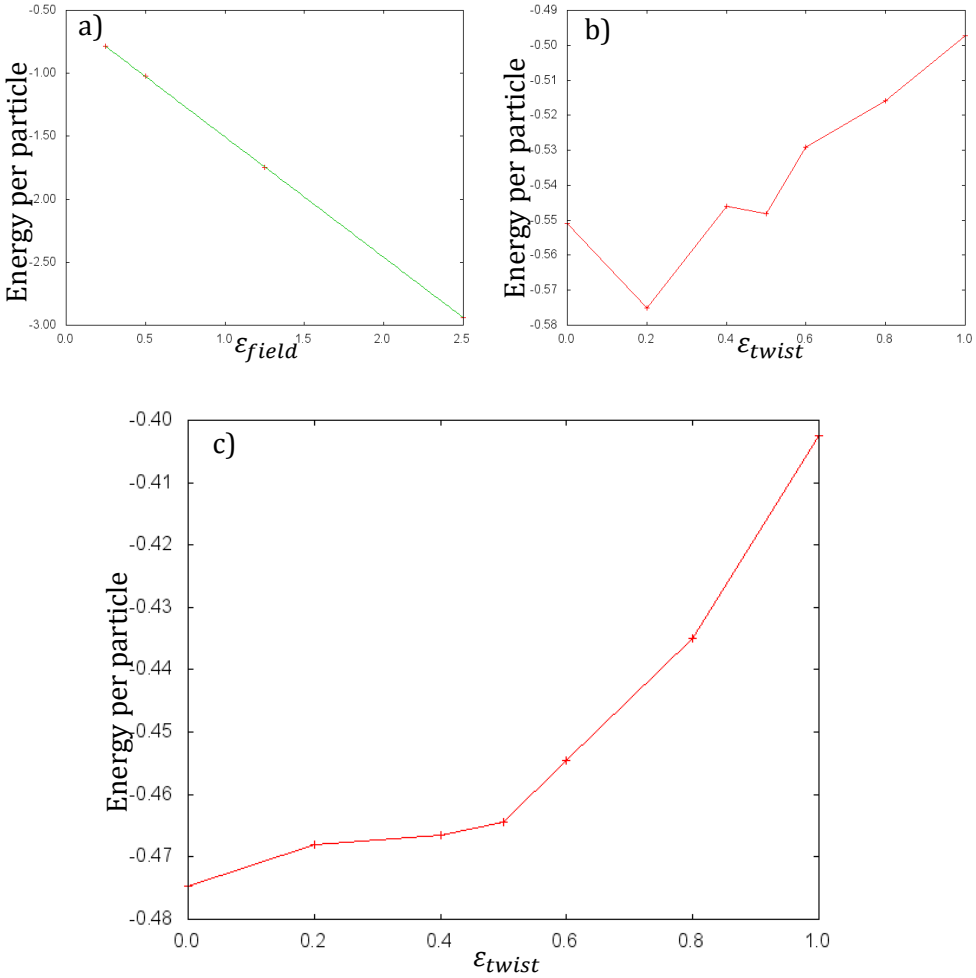

Figure 6.4.4 a) The linear relationship between the mean energy per particle and the local field strength and b) and c) the extrapolated energy with no field for different values of ε_{twist} for $r_{max} = 30\sigma_s, r_{min} = 20\sigma_s$ and $r_{max} = 40\sigma_s, r_{min} = 20\sigma_s$ respectively.

The extrapolated mean energy per particle for different twist amounts is shown in Figure 6.4.4b and c for $r_{max} = 30\sigma_s, r_{min} = 20\sigma_s$ and $r_{max} = 40\sigma_s, r_{min} = 20\sigma_s$ corresponding to an aspect ratio of $\xi = 1.5$ and $\xi = 2$ respectively. For both systems, the highly twisted director configuration is higher in energy than the untwisted director configuration, which is the most stable and lowest in energy for $\xi = 2$. For the slightly thinner torus where $r_{max} = 30\sigma_s, r_{min} = 20\sigma_s$ however it appears that the slightly twisted director

configuration with $\varepsilon_{twist} = 0.2$ is the lowest energy state. As shown in Table 6.4.1, for the GB(3,5,2,1) model ${K_2}/{K_3} = 0.2685$. The cross over between a twisted and untwisted director configuration predicted by Kulic *et al* for this elastic constant ratio occurs at approximately $\xi = 1.4$, which is very close to the aspect ratio where the slightly twisted director configuration was lowest in energy and may be the cause of the lowest energy configuration found for $\xi = 1.5$.

The previous work by Pairam *et al* allows for an estimation of the ratio ${K_{24}}/{K_2}$ as for $\xi = 2$ the untwisted director configuration was the ground state. The cross over between an untwisted and twisted director configuration for $\xi = 2$ occurs at approximately ${K_{24}}/{K_2} = 0.7$ indicating that for the GB(3,5,2,1) ${K_{24}}/{K_2} < 0.7$.

6.4.4 *GB(4.4,20,1,1) NEMATIC TORI WITH PLANAR ANCHORING*

Unlike the original Gay-Berne model, GB(3,5,2,1), the GB(4.4,20,1,1) potential shows a transition from the nematic phase to a smectic phase that is dependent on the density and temperature of the system. All the reduced densities investigated below form a nematic phase. The bulk properties of the densities investigated are shown in Table 6.4.2.

Table 6.4.2 Bulk properties for GB(4.4,20,1,1)

	$\rho^* = 0.16$	$\rho^* = 0.17$	$\rho^* = 0.1756$
T^*_{NI}	1.6	2.2	2.7
K_1/K_3	At $T^* = 1.2, 0.6412$	At $T^* = 1.8, 0.5203$	At $T^* = 1.6, 0.4567$
	At $T^* = 1.3, 0.5571$		
	At $T^* = 1.4, 0.5692$		
K_2/K_3	At $T^* = 1.2, 0.3721$	At $T^* = 1.8, 0.2517$	At $T^* = 1.6, 0.1931$
	At $T^* = 1.3, 0.3671$		
	At $T^* = 1.4, 0.3727$		

In total, five different points on the phase diagram for GB(4.4,20,1,1) were investigated. These were; $\rho^* = 0.16, T^* = 1.2, 1.3 \text{ \& } 1.4$; $\rho^* = 0.17, T^* = 1.8$; $\rho^* = 0.1756, T^* = 1.6$. Simulations were run starting from an isotropic phase or from a twisted or untwisted director configuration, produced as detailed for the GB(3,5,2,1) simulations (section 6.4.3). As with GB(3,5,2,1), no twisted director configurations found for all tori investigated. However, the lack of observation of the twisted director configuration does not agree with the findings of Kulic *et al* who state that for $\rho^* = 0.1756, T^* = 1.6$ corresponding to $K_2/K_3 = 0.1931$, a twisted director configuration is predicted for $\xi \leq 1.6$. The disparity between the simulation results and those predicted by Kulic *et al* suggests that the director

configuration is not solely dependent on the twist-bend ratio, rather there are more complicated factors influencing the director configuration seen.

Due to the long time needed for these systems to reach equilibrium and the time constraints imposed, it was not possible to repeat the series of simulations run for the GB(3,5,2,1) model varying the local field strength in order to extrapolate the energy for each director configuration with no local field.

6.5 CHIRAL NEMATICS CONFINED IN A CYLINDER

As with the non-chiral nematic systems, preliminary simulations of a chiral nematic phase confined in a cylindrical cavity were run. The same size cylinders were investigated for a confined chiral nematic phase as for the non-chiral nematic phase, shown in

Table 6.2.1, in order to investigate the dependence of the director configurations on both the length (*l*) and radius (*r*) of the cylinder whilst varying the chiral parameter, ε_c(6.1.5). Simulations were run with both planar and homeotropic anchoring.

6.5.1 *CHIRAL NEMATIC CYLINDERS WITH PLANAR ANCHORING*

For systems with planar anchoring, a defect-free configuration was formed (Figure 6.5.1). In the centre of the cylinder, the director is running along the length of the cylinder, parallel to the surface as seen in the non-chiral nematic case (Figure 6.2.2a). However, as the distance from the centre of the cylinder increases, the director twists away from the vertical. For the highest chirality systems investigated, the director at the surface is nearly perpendicular to the director at the centre of the cylinder (Figure 6.5.1f) as half a pitch length is approximately equal to the diameter of the cylinder (30σ and 32σ respectively).

The twist in the director at the surface of the cylinder was independent on the length of the cylinder, however, as expected more twists were seen along the cylinder as l increases. As the radius of the cylinder was increased, the twist at the surface increases, as the distance from the centre of the cylinder increases so a greater amount of the chiral pitch is seen.

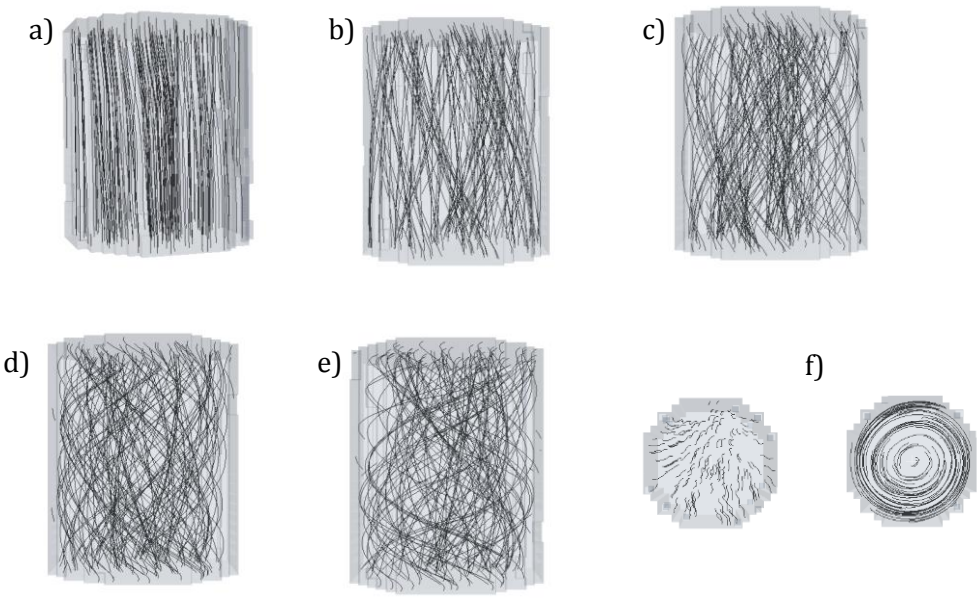

Figure 6.5.1 A cylinder (with ${T^*}/{T^*_{N-I}} = 0.9, r = 16\sigma\ l = 36\sigma$) showing the change in director twist with increasing chirality, a) $\varepsilon_c = 0.00$, b) $\varepsilon_c = 0.06$, c) $\varepsilon_c = 0.12$, d) $\varepsilon_c = 0.18$ and e)$\varepsilon_c = 0.24$. f) shows views along the cylinder for $\varepsilon_c = 0.00$ & 0.24

6.5.2 *CHIRAL NEMATIC CYLINDERS WITH HOMEOTROPIC ANCHORING*

It was found for chiral nematic cylinders with homeotropic anchoring that, as for the non-chiral analogue, two *s*=+1/2 disclination lines were formed in all cases. For the chiral systems, the two *s*=+1/2 defect lines twist around each other in a helix.

Due to the periodic boundary conditions is was only possible to simulate cylinders of finite length and the defects in the simulation can only twist by *nπ* where *n* is an integer (Figure 6.5.2b-e).

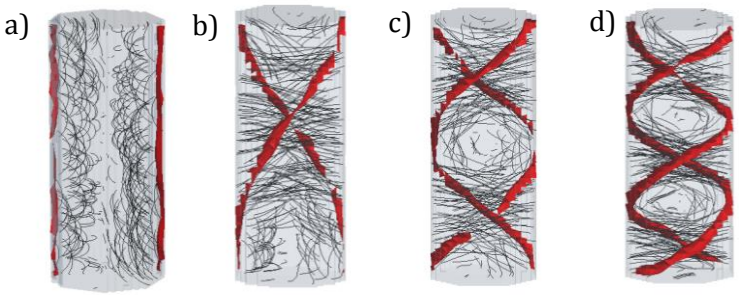

Figure 6.5.2 Cylinders with $r = 16\sigma, l = 96\sigma$ showing b) 0 c)π, d) 2π and e) 3π defect twists

Simulations run from an initial isotropic phase gave a range of different defect twist values in the final configuration, indicating that there was little or no energy difference between them. In order to investigate the different energies of the defect configurations and estimate the twist repeat unit, ten simulations were run at ${T^*}/{T^*_{N-I}} = 0.75$ starting from each defect configuration with *n*=0 to 3 with $\varepsilon_c = 0.00, 0.06, 0.12, 0.18 \text{ and } 0.24$. The mean energy per particle for each ε_c can be seen (Figure 6.5.3a) for the longest cylinder investigated. By fitting a parabola to the resulting curve it is possible to estimate the lowest energy twist in each cylinder and from that the repeat length for the defect twist, that is the length for the defects to twist by 2π. (Figure 6.5.3b).

In non-chiral nematic cylinders with homeotropic anchoring, the defect line configuration consisting of no twist was lowest in energy, as expected as there is no inherent twist present in a nematic. The value of *n* for the most stable state for each value of ε_c investigated was found to be independent of the diameter of the cylinder and over the three systems investigated ($r = 12\sigma, 16\sigma \text{ and } 20\sigma$) there was no clear trend in the defect twist repeat unit. The estimated defect twist repeat unit shows a similar trend to the pitch length of the chiral nematic with increasing ε_c as both are governed by the intrinsic twist present in a chiral nematic, however the defect repeat unit is longer than the chiral nematic pitch length.

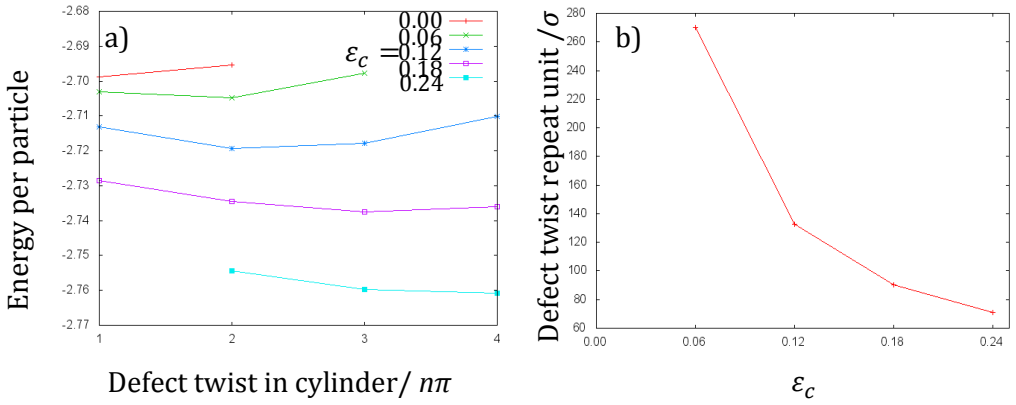

Figure 6.5.3 a) the mean energy per particle for a cylinder of $r = 16\sigma, l = 96\sigma$. b) The calculated defect twist repeat unit for each ε_c value investigated

6.6 CHIRAL NEMATICS CONFINED TO A TOROIDAL GEOMETRY

Whilst nematic tori modelled using both the Gay-Berne potential (section 6.4) and the simpler potential (section 6.3.1) did not spontaneously twist, it is possible to impose a twist in the tori by the addition of a chiral term (6.1.6) in order to simulate a chiral nematic phase. Simulations of chiral nematic tori with both planar and homeotropic anchoring were run for $\varepsilon_c = 0.06, 0.12, 0.18$ and 0.24 from an isotropic configuration for tori of sizes $r_{max} = 30\sigma, r_{min} = 10\sigma, 15\sigma$ & 20σ and $r_{max} = 40\sigma, r_{min} = 20\sigma$ corresponding to a range of aspect ratios from $\xi = 1.5 - 3$.

6.6.1 *CHIRAL NEMATIC TORI WITH PLANAR ANCHORING*

Chiral nematic tori with planar anchoring showed a twist along the tube of the tori, forming a defect free structure. The director in the centre of the tube is running axially around the torus, as in the nematic tori with planar anchoring. As the distance increases from the centre of the torus the director begins to twist around the torus rather than running axially (Figure 6.6.1b inset), this is analogous to that seen in a chiral nematic cylinder with planar anchoring (Figure 6.5.1f).

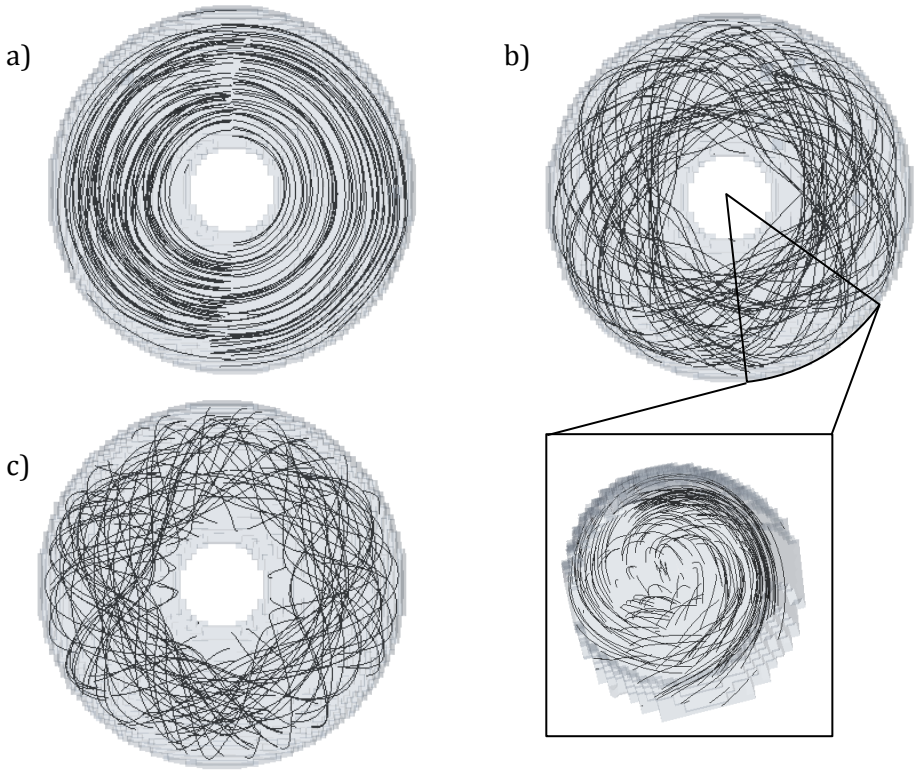

Figure 6.6.1 A torus where $r_{max} = 30\sigma, r_{min} = 20\sigma$ with a) $\varepsilon_c = 0.00$, b) $\varepsilon_c = 0.12$ with an inset showing a cut through section of the torus and c)$\varepsilon_c = 0.24$

The amount of twist seen around the tori is greater for thicker tori with a small aspect ratio than thin tori with a large aspect ratio. The greater twist seen for thicker tori is due to the fact there is a greater distance between the centre of the torus ring where the director is running axially and the surface of the torus where the director is twisted.

The pitch length of the chiral nematic can be much longer than both r_{max} and $r_{min}$and yet still show a twisted director configuration, indicating that these systems are very sensitive to the increasing chirality. Even very thin tori show a twisted director configuration at the lowest chiral parameter investigated, which has an associated pitch length of approximately 200σ, much larger than both r_{min} and r_{max}. As the chirality of the system increased, the amount of twist around the tori increased, this is due to the decreasing pitch length (Figure 6.6.1).

6.6.2 *CHIRAL NEMATIC TORI WITH HOMEOTROPIC ANCHORING*

In non-chiral nematic tori with homeotropic anchoring two *s*=+1/2 disclination lines running on the inside and outside of the torus are seen (section 6.3.2). In chiral nematic tori with homeotropic anchoring again *s*=+1/2 disclination lines are seen however, as seen in the chiral nematic cylinders with homeotropic anchoring (section 6.5.2), the disclination lines twist around one another to form a helix due to the intrinsic twist present in the chiral nematic, perpendicular to the director. The torus is a closed system with fixed length, and as such the defect lines must be continuous around the torus and so rotate by $n\pi$ where *n* is an integer. When *n* is even, two *s*=+1/2 defect lines are seen as interlocking rings where *n*> 0, however when *n* is odd, only one defect line is seen as the inner and outer disclination lines seen for a non-chiral nematic join one another. In systems with one *s*=+1/2 defect line the defect line circled the torus twice, once on the outer surface and once on inner surface (*i.e.* Figure 6.6.2c).

A series of simulations were run at $T^*/T^*_{N-I} = 0.9$ from an isotropic phase for the parameters specified in section 6.6. As with the chiral nematic cylinders with homeotropic anchoring, a variety defect configurations of differing twists around the torus were seen in different simulation runs for the same parameters, indicating that the energy difference between each defect configuration was small. In general, as the chirality of the system increased, the number of twists the defects make around the torus (*n)* increases.

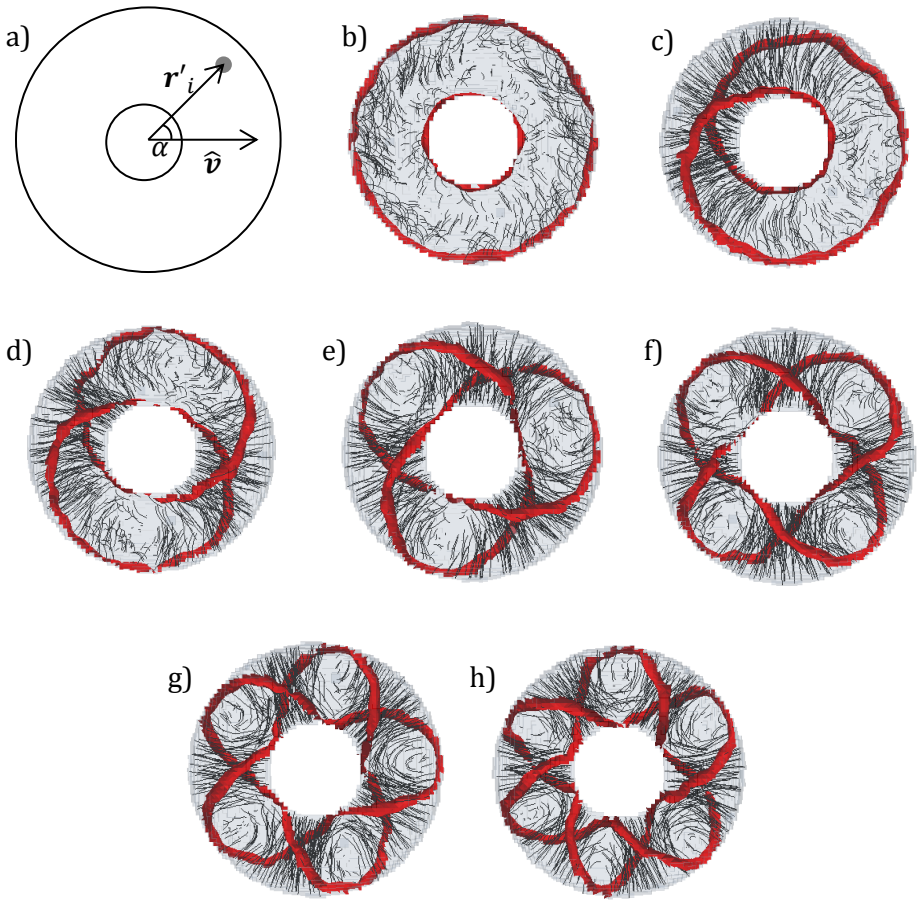

Figure 6.6.2 a) A schematic showing $\boldsymbol{r'_i}, \hat{\boldsymbol{v}}$ and α used to created idealised director configurations and defect configurations for a torus with homeotropic anchoring showing defect twists of b) 0, c) π, d) 2π, e)3π, f)4π, g) 5π and h)6π for $r_{max} = 30\sigma, r_{min} = 15\sigma$

To investigate the lowest energy value of *n*, simulations were started from idealised director configurations at $T^*/T^*_{N-I} = 0.75$ for $r_{max} = 30\sigma, r_{min} = 10,12,15, \text{and } 20\sigma$. These were produced by calculating the angle (α) between the vector between the centre of the torus and the position of the particle ($\boldsymbol{r'_i}$) and the vector $\hat{\boldsymbol{v}} = (1\ 0\ 0)$, shown in Figure 6.6.2a and setting the *z*-component of the orientation vector to $-\sin n\pi$ and the *x*- and *y*-components along $\boldsymbol{r'_i}$. The negative sign in the *z*-component is due to the handedness of the chiral potential.

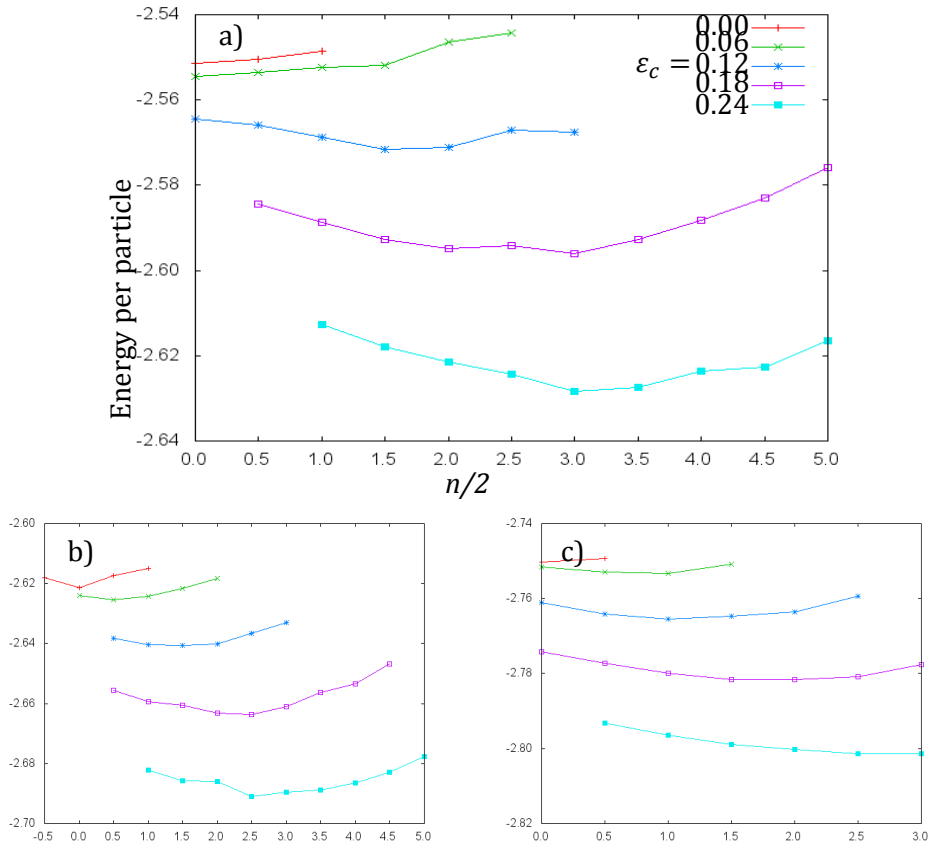

Figure 6.6.3 A graph showing how the energy per particle varies with $\frac{n}{2}$ for $r_{max} = 30\sigma$ and a)$r_{min} = 10\sigma$, b) $r_{min} = 12\sigma$ and c) $r_{min} = 20\sigma$

From the systematic study, it was found that for a non-chiral nematic the untwisted, *i.e.* *n* = 0, defect configuration was the most stable state, as seen in section 6.3.2. The lowest energy defect configuration for each tori size and chirality is given in Table 6.6.1.

As ε_c increases, the number of twists in the ground state defect configuration increases. The value of *n* for the lowest energy defect configuration for each value of ε_c is a complex balance between the proportion of a chiral nematic pitch length across the tube of the torus and the length of the disclination lines. For low ε_c as the aspect ratio decreases and the torus gets thicker, *n* increases as the diameter of the tube increases and a larger proportion of a pitch length of the chiral nematic can be found in the tube. For larger values of ε_c, the opposite is true, with decreasing aspect ratio the lowest energy *n*

decreases as the length of the disclination lines increase with increasing *n.* The length of the disclination lines increase as *n* increase as the defects loop around the circumference of the tube and the circumference of the tube is proportional to r_{min} .

Table 6.6.1 The lowest energy *n* for each system investigated

ε_c	*n* Ground state for each aspect ratio, ξ			
	3	2.5	2	1.5
0.06	0	1	1	2
0.12	3	3	3	3
0.18	5	5	4	4
0.24	6	6	*	*

*= uncertain as high enough values of *n* were not run

6.7 CONCLUSION

In this chapter both chiral and non-chiral nematics confined within a single torus have been investigated with both planar and homeotropic anchoring. At the limit where $r_{max} \to \infty$, a cylinder is formed and both non-chiral and chiral nematics confined within a cylindrical cavity were also investigated with both planar and homeotropic anchoring.

Cylinders of a nematic with planar anchoring formed a defect-free configuration with the director running along the tube. A related structure was seen in nematic tori with planar anchoring where the director running axially along the tube of the torus. In some simulations of a nematic torus with planar anchoring started from an isotropic phase, one or more boojum-like defects consisting of a *s*=-1 and a *s*=+1 defect located on the inner and outermost regions of the torus respectively were formed. Once formed these defects were present for the remainder of the simulation as the thermal energy present was insufficient to overcome the energy barrier needed for these defects to annihilate.

Previous work[69] has shown that for a nematic torus with planar anchoring a spontaneous twisting of the director can be seen for fat tori, however this was not seen in simulations performed in this chapter. The presence of a twisted director configuration has been postulated by Kulic *et al*[70] to be due to the ratio of the twist and bend elastic constants, K_2/K_3 however subsequent work by Pairam *et al*[69] suggests that the presence of a twisted director configuration is due to the ratio of the saddle-splay and twist elastic constants, K_{24}/K_2.

The lack of stable twisted director configuration observed for a nematic tori with planar anchoring could be down two reasons, either all the tori investigated may be too thin or ratio of elastic constants (either K_2/K_3 or K_{24}/K_2) may not be in the region where it is predicted that a twisted director structure is seen. Future work with larger simulations, either of whole tori or sections of tori (as in section 6.4.2) could be performed. By employing a twisted local field it was possible to extrapolate back to the energy of different director configurations with no field present which confirmed that the untwisted director configuration was lowest in energy. From this, using the work by Pairam *et al* it is possible to estimate that $K_{24}/K_2 < 0.9$ for these systems. If, in future work the transition from an untwisted to a twisted director configuration can be observed, it could be used as a way to estimate K_{24}, which is otherwise not possible.

In order to investigate a larger K_2/K_3 ratio, sections of a torus were simulation using the Gay-Berne potential for which the K_2/K_3 ratio has previously been calculated[97]. Again only non-twisted defect configurations were observed in all systems investigated and a local twisted field was employed to estimate the mean energy per particle for twisted director

configurations with no field present. It was found that, in agreement with Kulic *et al* a torus with an aspect ratio (ξ) of 2, the untwisted director configuration was the ground state.

The addition of a chiral term to the potential causes a chiral nematic phase to be formed with an inherent twist perpendicular to the director. In systems with planar anchoring, the inherent twist causes the chiral nematic to twist along either the cylinder or the tube of the torus. The director in a chiral nematic torus runs axially at the centre of the tube and as the distance from the centre of the increases the director begins to twist until it reaches the maximum twist angle seen at the surface of the torus or cylinder.

Nematic cylinders with homeotropic anchoring have three possible defect configurations; one s=+1 or two s=+1/2 defect line(s) running the length of the cylinder or an escaped structure where the s=+1 defect escapes into the third dimension. However in all simulations only two s=+1/2 disclination lines were observed, running the length of the cylinder. Nematic tori with homeotropic anchoring also showed a defect configuration consisting of two s=+1/2 defects on the surface of the torus, with one circling the centre of the torus and one travelling around the outer surface of the torus. In all cases, these defect lines were seen midway through the torus, as opposed to the top and the bottom of the torus.

In chiral nematic cylinders with homeotropic anchoring, the intrinsic twist in the plane normal to the director causes the two s=+1/2 defect lines seen to twist around one another and form a helical structure. Due to the boundary conditions, twist in the defects must be $n\pi$ where n is an integer. A series of simulations from the isotropic phase showed multiple possible values of n for each system investigated and so a series of simulations started from each value of n were run to calculate the twist repeat length (*i.e.* the length for one defect to rotate by 2π) for a range of values of ε_c. It was found that as the chirality increases the

defect twist repeat length decrease as it is clearly related to the associated pitch length of the chiral nematic which also decreases with increasing ε_c.

In chiral nematic tori with homeotropic anchoring as in the non-chiral analogues, *s*=+1/2 defect lines are observed, however, unlike in the non-chiral case, the defect lines rotate around the tube of the torus by $n\pi$ where *n* is an integer. When *n* is even two interlocked *s*=+1/2 disclination rings are seen and when *n* is odd one *s*=+1/2 disclination line traversing both the inner and outer regions is formed.

As with the chiral nematic cylinders with homeotropic anchoring, when started from an initial isotropic phase several values of *n* were seen for each system. In order to calculate the most stable value of *n* for each system, a series of simulations were run from idealised starting configurations. These series of simulations confirmed that for a non-chiral nematic (*i.e.* $\varepsilon_c = 0$) an untwisted defect configuration with the defects located on the inner and outer regions was most stable. As ε_c increased the value of *n* for the ground state also increases. The most stable value of *n* for each system is a complex balance of the proportion of the chiral nematic pitch length in the tube and the total length of the disclination lines traversing the surface of the torus. At low values of ε_c, the increasing proportion of chiral nematic pitch length dominates and the value of *n* for the lowest energy state increases with increasing thickness, however at high values of ε_c, the total length of the disclination lines dominates with the value of *n* for the lowest energy state decreasing with increasing thickness.

7 CHIRAL NEMATICS IN N-FOLD TORI

7.1 INTRODUCTION

The previous chapter considered the case of nematic and chiral nematic phases inside a toroidal geometry with both planar and homeotropic anchoring. Nematic tori with planar anchoring formed a defect free ground state with the director running axially around the torus. The addition of chirality caused the director to twist around the tube of the torus, with the director at the centre of the tube running axially along the tube and the director twisting away from the axial vector as the distance from the centre of the tube increased (section 6.6.1).

Nematic tori with homeotropic anchoring all formed two *s*=+1/2 defect lines, one circling the inner ring and one running around the outermost surface of the torus. The addition of chirality caused the defect lines to twist around one another and form a helical structure with the twist of the defects in multiples of $n\pi$ where *n* is an integer. When *n* is even, two interlocking *s*=+1/2 disclination rings are formed however when *n* is odd, one disclination ring is seen traversing both the inner and outermost surfaces of the torus.

In this chapter the study is extended from single torus systems to *n*-tori systems by combining two or more tori to create *2-, 3-* and *4-* genus handled bodies. As in chapter 6 all the multiple torus systems investigated here are created from ring tori ($r_{min} < r_{max}$).

For nematic *n*-tori with planar anchoring, as for the single tori systems, the total topological defect charge on the surface is equal to the Euler characteristic[108], χ ,

$$\chi = 2(1 - g) \tag{7.1.1}$$

where *g* is the number of handles or genus of the system. The Euler characteristic for a single torus is zero, hence a defect-free director configuration is possible for a single torus.

Table 7.1.1 The total topological charge on the surface of nematic *n*-tori systems with planar anchoring

Number of handles (*g*)	Euler Characteristic, χ and total topological charge on the surface
0 (sphere)	2
1 (single torus)	0
2	-2
3	-4
4	-6

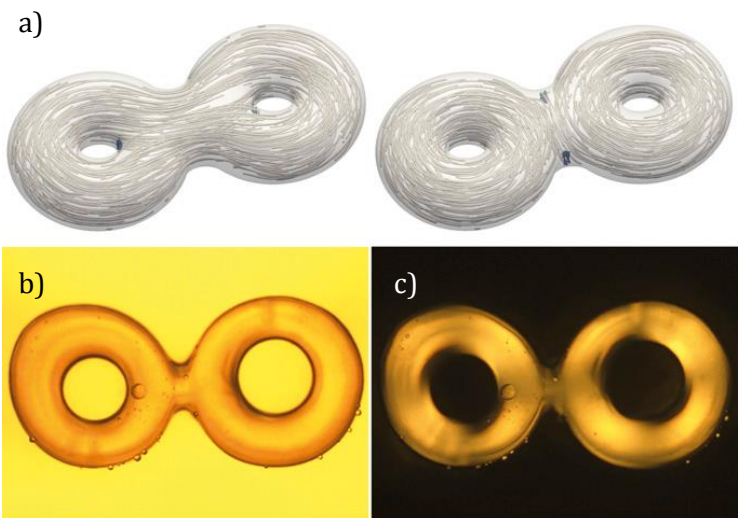

Figure 7.1.1 Previous work showing double tori with two *s*=-1 defects. a) shows computer simulations of two director configurations b) and c)shows experimental results where the two *s*=-1 defects are located at the outermost surface where the two tori join. b) is the bright field view and c) the associated view under cross polarisers. (from Pairaim *et al*[69])

Previous research both experimentally and simulations employing a lattice-based model[69] have shown that the constraint on the total topological charge on the surface of a *n*-fold handled body is fulfilled with the required number of *s*=-1 defects based on the genus of the system . These *s*=-1 defects are hyperbolic in structure located on the surface located at areas of negative Gaussian curvature, either at the outermost region of the surface where two tori join or the inner ring of each torus (Figure 7.1.1). Gaussian curvature (*K*) is defined as the product of two orthogonal planes of principle curvature (κ_1 and κ_2).

$$K = \kappa_1 \kappa_2 \qquad (7.1.2)$$

The Gaussian curvature is negative at a saddle surface where the planes of principle curvature are of different signs (Figure 7.1.2).

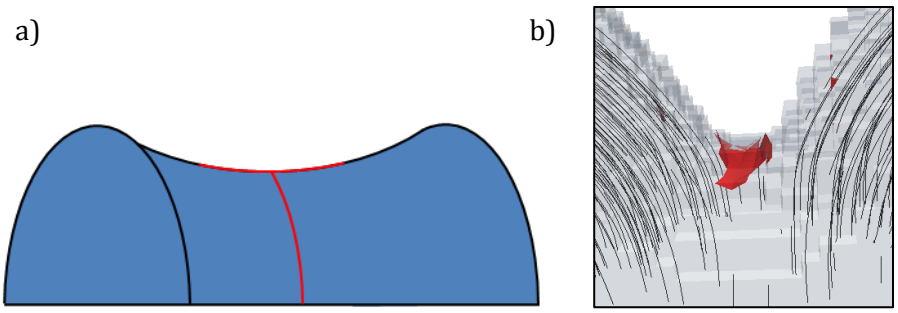

Figure 7.1.2 a) A schematic representation of a saddle surface with negative Gaussian curvature. The curves on the surface in the planes of principle curvature are shown in red. b) shows a *s*=-1 defect located at a region of negtive Gaussian curavture in a double torus

There has been little or no previous research into nematic droplet systems with multiple handles with homeotropic anchoring. These systems with homeotropic anchoring are not held by the constraint that the total topological charge on the surface must equal the Euler characteristic of the system; however, it is not possible to create a defect-free director configuration in a *n*-fold torus system with homeotropic anchoring due to the boundary conditions.

It is possible to predict the defect structure in the *n*-tori systems with homeotropic anchoring away from the join between tori as these behave as the single torus systems in the previous chapter. Utilising this idea, it is predicted that for a nematic *n*-fold handled body, away from the join that there will be two *s*=+1/2 defect lines, one running around the inner ring and one around the outer. However, what occurs at the join between tori in *n*-tori systems is unknown.

In this chapter both nematic and chiral nematic phases confined in a *n*-torus cavity with both planar and homeotropic anchoring are investigated using the off-lattice model previously employed to investigated both shells and single torus systems. An insight into the effect of chirality on the director configurations observed in these systems is hoped to

be gained and the behaviour of a nematic handled body with homeotropic anchoring investigated for the first time.

7.1.1 *INTERACTION POTENTIALS*

The same interaction potentials are used as previously detailed in section 6.1.2. To recap, there are two interaction potentials; a mesogen-mesogen interaction and a mesogen-wall interaction. The mesogen-mesogen interaction is,

$$U^{LC-LC}(\boldsymbol{p}_i, \boldsymbol{p}_j, \boldsymbol{r}_{ij}) = \begin{cases} r \leq \sigma, & \infty \\ \sigma < r < 1.5\sigma, & U^{LC-LC}(\boldsymbol{p}_i, \boldsymbol{p}_j, \boldsymbol{r}_{ij}) + U^{LC-LC}_{chiral}(\boldsymbol{p}_i, \boldsymbol{p}_j, \boldsymbol{r}_{ij}) \\ 1.5\sigma \leq r, & 0 \end{cases} \quad (7.1.3)$$

where $\boldsymbol{p}_i$and $\boldsymbol{p}_j$ are unit vectors centred on the middle of particles *i* and *j* respectively and $\boldsymbol{r}_{ij}$ is the vector between the centre of *i* and *j* and

$$U^{LC-LC}(\boldsymbol{p}_i, \boldsymbol{p}_j, \boldsymbol{r}_{ij}) = -\varepsilon\left[J_1(\boldsymbol{p}_i \cdot \boldsymbol{p}_j)^2 - 2J_2(\boldsymbol{p}_i \cdot \boldsymbol{p}_j)(\boldsymbol{p}_i \cdot \hat{\boldsymbol{r}}_{ij})(\boldsymbol{p}_j \cdot \hat{\boldsymbol{r}}_{ij}) + J_3(\boldsymbol{p}_i \cdot \hat{\boldsymbol{r}}_{ij})^2(\boldsymbol{p}_j \cdot \hat{\boldsymbol{r}}_{ij})^2\right] \quad (7.1.4)$$

$$U^{LC-LC}_{chiral}(\boldsymbol{p_i}, \boldsymbol{p_j}, \boldsymbol{r_{ij}}) = \varepsilon_c[\hat{\boldsymbol{r}}_{\boldsymbol{ij}} \cdot (\boldsymbol{p_i} \times \boldsymbol{p_j})][(\boldsymbol{p}_i \cdot \boldsymbol{p}_j)] \quad (7.1.5)$$

where ε and ε_c are positive constants relating to the potential well depth and the chirality of the cholesteric phase. In this chapter, only the most simple mesogen-mesogen potential, potential 1 where $J_1 = 1, J_2 = 0 \text{ and } J_3 = 0$ is investigated as the resulting director configurations for a single torus system were very similar for all potentials investigated (section 6.3.1).

The model can be used to simulate a chiral nematic with a pitch length ranging from approximately 200σ to 60σ before the planar surface anchoring is lost and a blue phase is formed. In this chapter, four values of ε_c are investigated and the corresponding pitch lengths are shown in Table 7.1.2.

Table 7.1.2 A table showing the ε_c values investigated and associated pitch length used throughout this chapter

ε_c	Associated pitch length /σ
0.00	∞ (a regular nematic)
0.06	202
0.12	101
0.18	62
0.24	48

The mesogen-wall interaction used was;

$$U^{LC-Wall}(\boldsymbol{p}_i, \boldsymbol{r}_i) = \begin{cases} r \leq \sigma, & \infty \\ \sigma < r < 1.5\sigma, & U^{LC-Wall}(\boldsymbol{p}_i, \boldsymbol{r}_i) \\ 1.5\sigma \leq r, & 0 \end{cases} \quad (7.1.6)$$

where $\boldsymbol{r_i}$ is the minimum distance between the wall and the centre of the mesogen and $U^{LC-Wall}(\boldsymbol{p}_i, \boldsymbol{r}_i)$ takes the general form

$$U^{LC-Wall}(\boldsymbol{p}_i, \boldsymbol{r}_i) = \varepsilon_{LC-Wall} + \varepsilon_A(\boldsymbol{p}_i \cdot \hat{\boldsymbol{r}}_i)^2 \quad (7.1.7)$$

$$U^{LC-Wall}(\boldsymbol{p}_i, \boldsymbol{r}_i) = (\varepsilon_A + \varepsilon_{LC-Wall}) - \varepsilon_A(\boldsymbol{p}_i \cdot \hat{\boldsymbol{r}}_i)^2 \quad (7.1.8)$$

for planar and homeotropic anchoring respectively. In this chapter, as in the previous chapter,

$$U^{LC-Wall}(\boldsymbol{p}_i, \boldsymbol{r}_i) = \pm(\boldsymbol{p}_i \cdot \hat{\boldsymbol{r}}_i)^2 \quad (7.1.9)$$

where $+(\boldsymbol{p}_i.\hat{\boldsymbol{r}}_i)^2$ corresponds to planar anchoring and $-(\boldsymbol{p}_i.\hat{\boldsymbol{r}}_i)^2$ corresponds to homeotropic anchoring.

7.1.2 *SIMULATION PARAMETERS*

The simulations were run by placing the *n*-tori boundary inside a rectangular box. As with the single torus simulations in the previous chapter, the simulations were run at $\rho^* = 0.75$ and ${T^*}/{T^*_{N-I}} = 0.9$using cubic analysis cells with sides of 1.5σ from an isotropic starting configuration unless otherwise stated. The isotropic starting configuration was produced using the method outlined in section 6.3.1. That is, the *n*-fold handled body was filled with a simple cubic lattice of mesogens with $\rho^* = 1$ and the orientation vectors of all the particles were set along the *z*-axis. 25% of the particles were then removed at random to gain the desired density of $\rho^* = 0.75$. A short simulation at a high temperature ($T^* = 1000$) was then run to produce an isotropic starting configuration.

To confirm that the simulations were being run at the correct reduced density, the volume of the systems was calculated. Unlike single tori, there is no simple algebraic formula to calculate the volume of an *n*-fold torus, meaning the volume had to be calculated numerically. To calculate the volume, a MC simulation was performed using random trial insertions into the rectangular box containing the *n*-torus boundary system. The number of insertions found to be inside the toroidal volume (N_{in}) divided by the total number of trial insertions ($N_{trial} = 5 \times 10^8$) gives the ratio of the volumes of the *n*-torus and the box. Multiplying this by the volume of the rectangular box (V_{sim}) gives the volume of the *n*-torus system **(V_{tor})**.

$$V_{tor} = \left(\frac{N_{in}}{N_{trial}}\right) V_{sim} \tag{7.1.10}$$

From the calculated volume, it was confirmed that the simulations were performed at the correct density, $\rho^* = 0.75$.

7.2 GEOMETRY OF A DOUBLE TORUS

The first system considered in this chapter is the double torus ($g = 2$). To simulate a double torus four tori are needed, two are the tori joined together to form the system (Figure 7.2.1) and two are ghost tori used to control the curvature at the join between the two real tori. The two ghost tori are needed to provide a smooth region between the joined tori, as found in experimental systems (Figure 7.1.1). Without the ghost tori, a cusp is formed with a discontinuity on the surface. The use of the ghost tori allow for R_{sep} to be larger than $R_{max} + R_{min}$, which is when the two tori are just touching (Figure 7.2.2a). The opposing limit to the cusp occurs when r_t tends to infinity, the curvature between torus 1 and 2 decreases until it appears as a cylinder (Figure 7.2.2b).

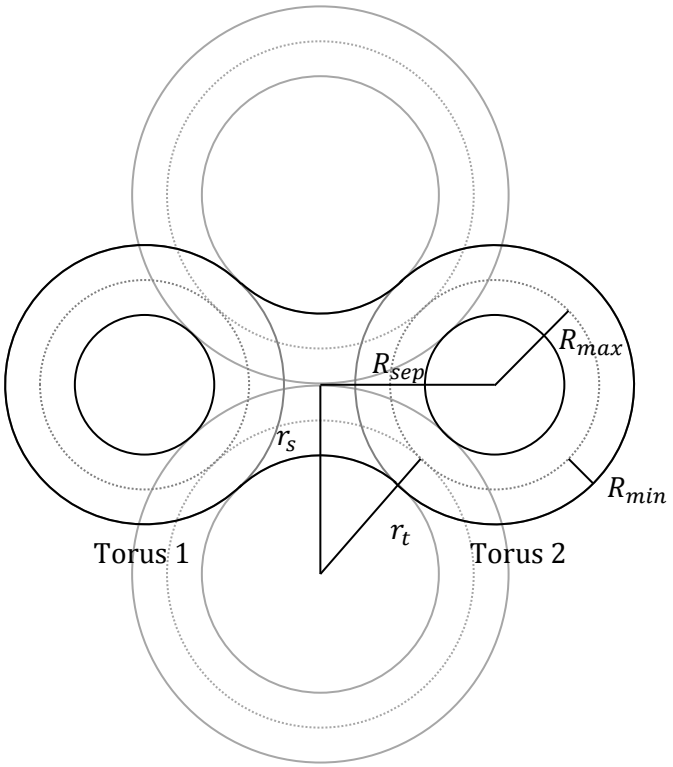

Figure 7.2.1 A schematic of double torus simulations.

Figure 7.2.1 also shows the parameters used to assign the double tori. As in single torus simulations, there are two parameters used to describe the torus itself; R_{max} which is the radius of the circular path and R_{min} which is the radius of the tube. There are three

additional parameters used in these simulations, R_{sep}, which is the separation from the midpoint of each torus from the centre of the simulation cell. The minimum value that R_{sep} can take is R_{max} as any smaller would result in a hole in the centre. The last two parameters relate to the ghost tori. They are r_t, which is the circular path (R_{max}) for the ghost torus and r_s which is the separation of the midpoint of each ghost torus from the centre of the simulation cell (R_{sep}).

The variables used in this chapter are R_{sep} and r_t, with,

$$R_{max} = 25\sigma \;\&\; R_{min} = 12.5\sigma \left(\frac{1}{2}R_{max}\right) \qquad (7.2.1)$$

for both torus 1 and 2 for all systems. The values of r_t and R_{sep} used are equal for torus 1 and 2 in individual systems, meaning the distance between the centre of torus 1 and 2 is $2R_{sep}$.

The value of r_s is dependent on R_{max}, R_{sep} and r_t and is;

$$r_s = \sqrt{(R_{max} + r_t)^2 - R_{sep}^2} \qquad (7.2.2)$$

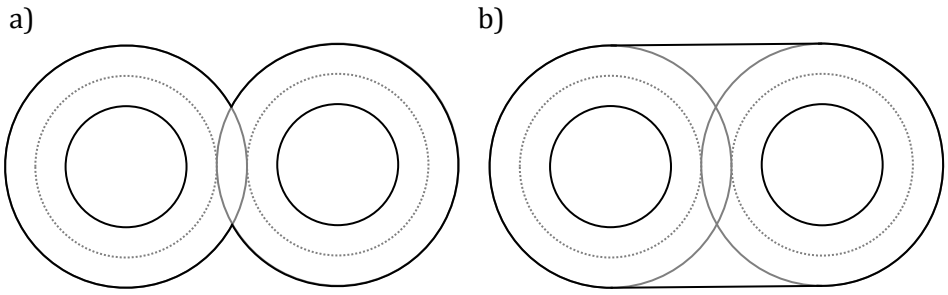

Figure 7.2.2 A schematic of a double torus as a) $r_t \rightarrow 0$ and b) $r_t \rightarrow \infty$

r_t is constrained to be above a minimum value (r_t^{min}) due to the thickness of the central part between torus 1 and 2. For r_t below the threshold value, r_s would be small, meaning that the join between the two tori would have a thickness in the *z*-direction of less than $2R_{min}$ and for very small values of r_t when $R_{sep} > R_{max} + R_{min}$, the two tori would not

be joined at all. The threshold value for r_{min} can be calculated using the right angled triangle formed by r_s, R_{sep} and $(R_{max} + r_t)$ and setting $r_t = r_s$ giving

$$r_t^{min} = \frac{R_{sep}^2 - R_{max}^2}{2R_{max}} \tag{7.2.3}$$

The maximum thickness of the double tori at the join is equal to the diameter of the tube, $2R_{min}$ which leads to a flat region on both the top and bottom of the system when $r_t > r_t^{min}$.

7.3 NEMATIC DOUBLE TORI WITH PLANAR ANCHORING

7.3.1 *PRELIMINARY STUDIES*

A series of simulations were run with planar anchoring varying both R_{sep} and r_t cooling slowly from the isotropic phase to the nematic phase at $T^*/T^*_{N-I} = 0.9$ over a period of 62500MC cycles.

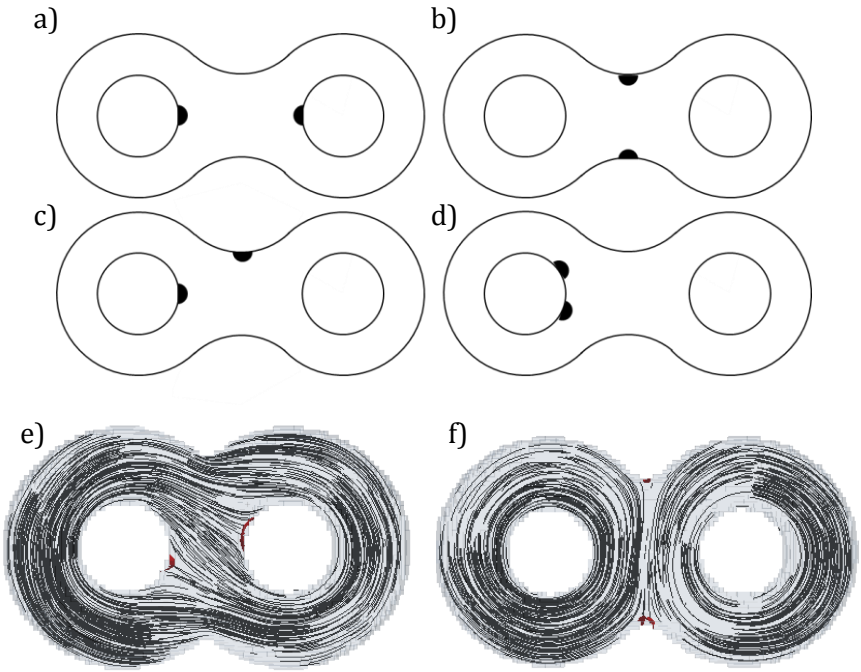

Figure 7.3.1 a)-d) show four possible defect configurations, e) and f) show the two defect configurations found

In systems of all sizes, the total topological charge on the surface was equal to -2 and the resulting defect configuration consisted of two *s*=-1 defects, in agreement with previous research[69]. These defects were found on the surface of the double torus at the areas of negative Gaussian curvature [109](Figure 7.1.2b). The location of the *s*=-1 defects at points of negative Gaussian curvature agrees with theoretical studies of two dimensional curved nematics, where defects are attracted to regions with the same sign Gaussian curvature, *.i.e.* defects with *s*<0 are attracted to locations of negative Gaussian curvature, and defects with *s*>0 are attracted to locations of positive Gaussian curvature[110].

To preserve the director alignment around each handle, the defects must form at the join of the two tori. There are two distinct environments for the defects to form in, either the innermost surface of either torus, or the outer region at the join of the two tori. There are four possible defect configurations (Figure 7.3.1a-d). Of these four defect configurations, when cooled slowly from the isotropic phase into a nematic phase, only two configurations were seen; consisting of either one defect on the innermost surface of each torus (Figure 7.3.1e) or one defect at each join between the tori (Figure 7.3.1f).

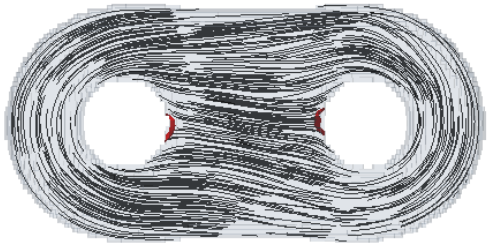

Figure 7.3.2 A double torus with no regions of negative Gaussian curvature on the outermost region of the surface ($r_t = 1000\sigma$) showing the two *s*=-1 defects on-axis

For systems at the limit where $r_t \to \infty$, there are no regions of negative Gaussian curvature on the outermost surface at the join between the two tori. Due to this, the defects are forced to be located on the innermost region of the surface on one or both of the tori. No

defect configurations were seen when cooled from the nematic in which both defects were located around the same torus.

For the defect configuration consisting of two defects on the inside edges of the double torus, the defects could either be on-axis (Figure 7.3.2) or off-axis (Figure 7.3.1e). The off-axis configuration was more commonly seen for small values of R_{sep} due to the smaller distance between defects meaning the defects repel each other until they are off-axis. Defects of the same sign repel each other due to the increase in elastic energy from the distortions of the director. At high values of R_{sep}, the defects are on-axis as the increase in elastic energy is overcome by the preservation of nematic order seen between the defects when on axis.

It was seen that at small r_t , the defects were more commonly found at the outermost region of the surface (Figure 7.3.1f) and as r_t increased the defects moved to the innermost region. Indeed, for $r_t = 1000\sigma$, only the defect configuration with the defects on the innermost surface was seen (Figure 7.3.2).

7.3.2 *SYSTEMATIC STUDIES*

In principle, many simulations cooling from an isotropic phase into a nematic phase could be run and count the number of each type of director configuration seen in order to calculate the differing stability of the four possible defect configurations. Here however, an alternative approach of starting from a known director configuration and calculating the mean energy per particle is used to allow for comparison of the stability of different defect configurations. Simulations were run at $T^*/T^*_{N-I} = 0.90$ for the parameters shown in Table 7.3.1. from initial defect configurations in which both defects are located on either the outermost or innermost regions of the surface.

Table 7.3.1 Parameters used to investigate energy between defects at the inner and outer edges

R_{sep}/σ	r_t/σ
25 (R_{max})	6.25 ($\frac{1}{2}R_{min}$), 7,8,9,10,11,12.5(R_{min}),15
31.25 ($R_{max} + \frac{1}{2}R_{min}$)	8 (r_t^{min}) ,9,10,11,12.5(R_{min}),15,16
37.5 ($R_{max} + R_{min}$)	16(r_t^{min}),16.5,17,17.5,18,18.5,19,19.5
43.75 ($R_{max} + \frac{3}{2}R_{min}$)	26(r_t^{min}),27,28,29,30

Additionally, for $R_{sep} = 31.25\sigma$, the defect configuration with one defect on the innermost and one on the outermost surfaces was also investigated. For the values of r_t shown, the defect configuration with two defects on the innermost region of one handle were unstable and a defect was found to migrate to either the outermost region or the opposing handle.

For systems with intermediate R_{sep} $(31.25\sigma \text{ and } 37.5\sigma)$ for small r_t, the director configuration with the defects at the join between the two tori (at the outermost surface) is lower in energy than the defect configuration in which the defects are located at the innermost region of the handles. As r_t increases the comparative stability between the two states decreases until for large r_t the defect configuration with the defects on the outermost surface is unstable and the defect configuration with one defect located on each handle is most stable ($r_t > 19.5\sigma$ for $R_{sep} = 37.5\sigma$) (Figure 7.3.3b & c).

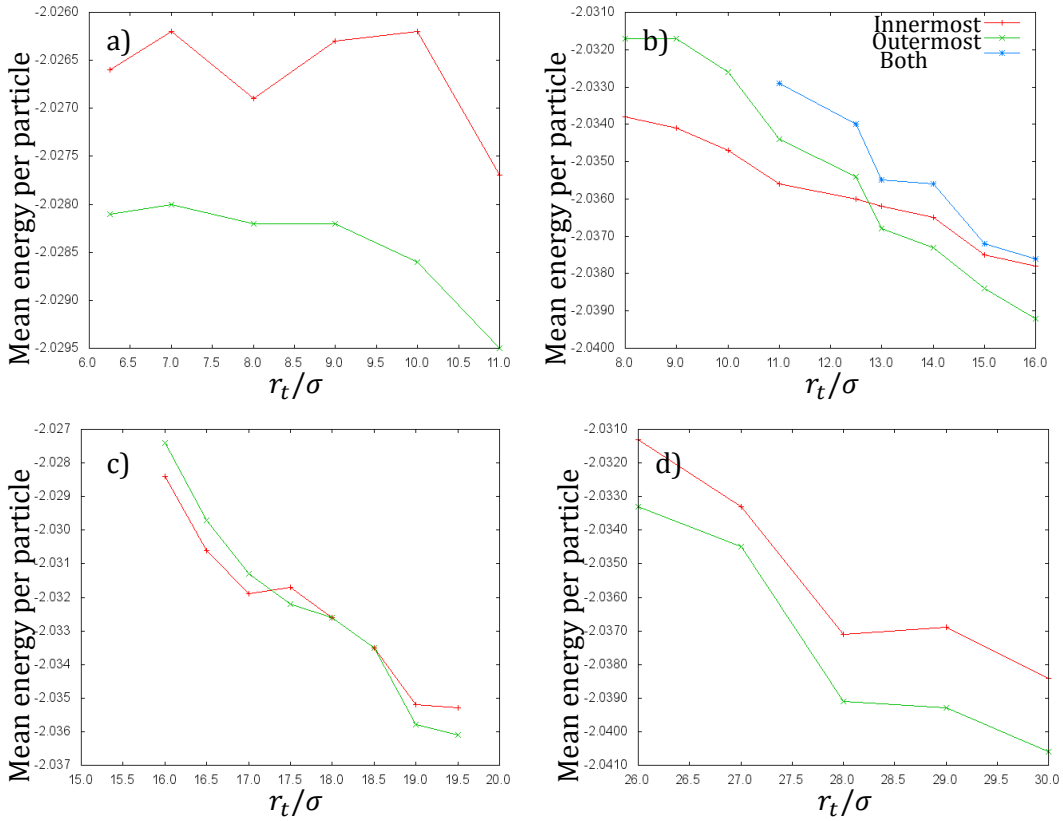

Figure 7.3.3 Graphs showing the relative stability of the director configurations with the defects located at the outermost surface (red) and the innermost surface (green) for a)$R_{sep} = 25\sigma$, b) $R_{sep} = 31.25\sigma$, c) $R_{sep} = 37.5\sigma$ and d) $R_{sep} = 43.75\sigma$. b) also shows the relative stability of the director configuration with one defect at located the innermost surface and one defect located at the outermost surface (blue)

For systems with small R_{sep} (25σ) , there is no such crossover in the most stable defect configuration, with the director configuration with the defects at the innermost surface more stable for all values of r_t. Above $r_t = 11\sigma$ the director configuration with the defects at the join between the two tori is unstable. The reduced stability of the defect configuration with the defects located at the join between the two tori at small separations could be due to the cusp-like nature at the outermost surface leading to a discontinuity on the surface.

For systems where the two tori are not touching, *i.e.* $R_{sep} > R_{max} + R_{min}$, $\left(R_{sep} = 43.75\sigma\right)$ the director configuration with the defects on the innermost surface always being most stable. The director configuration with the defects at the join between the two tori is relatively high in energy as the large value of R_{sep} means the defects located here are very broad, with a larger core area of disorder compared to defects formed on the innermost surface.

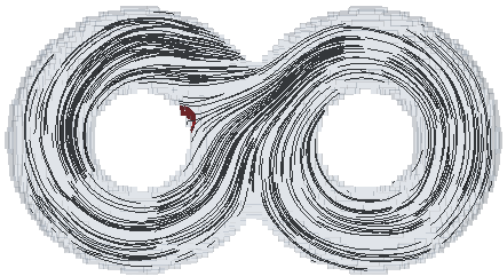

Figure 7.3.4 A double torus with planar anchoring showing one defect on the innermost surface and one defect on the outermost surface for

$$R_{sep} = 31.25\sigma, r_t = 14\sigma$$

As can be seen in Figure 7.3.3b, the director configuration with one defect on both the innermost and outermost surface (Figure 7.3.4) is unstable with respect to both defects being located in the same environments. The relatively high energy of the defect configuration in which one defect is located on the innermost surface and one is located on the outermost surface at the join of the two tori can be explained by the relative orientation of the director to the vector between the two defects. In the both defect configurations where the defects are located in the same environment, the director is parallel to the vector between the two defects (Figure 7.3.1e and f), however in the defect configuration where the defects are in different environments, the director is perpendicular to the vector between defects, leading to a larger region of distortion around the defects (Figure 7.3.4).

A series of simulations in which both defects are on the same handle were also run for $R_{sep} = 31.25\sigma$ for the values of r_t shown in Table 7.3.1, however all were unstable and the defects migrated to form the defects on the outermost surface at the join of the two tori, showing that, due to the close proximity of the two defects, the defect configuration in which both defects are on the same handle is higher in energy than the other three defect configuration investigated.

In order to investigate the relative stability of two defects located on one handle, a series of simulations with no regions of Gaussian curvature on the outermost surface, $r_t = 1000\sigma$ with $R_{sep} = 31.25\sigma$, were run from an initial defect configuration with either one defect on each handle or both defects on one handle (Figure 7.3.5).

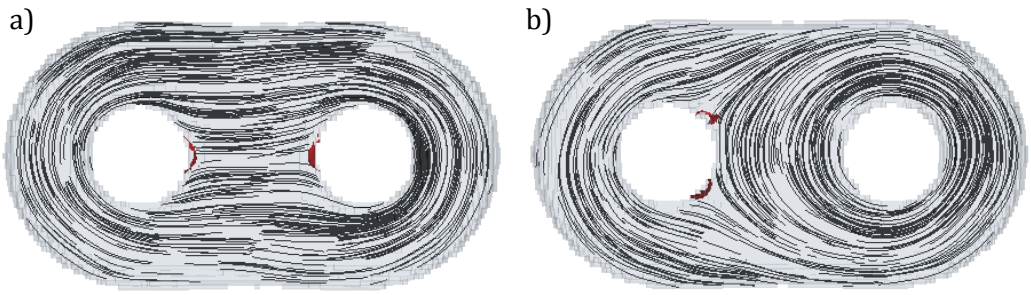

Figure 7.3.5 A double torus with planar anchoring with no regions of negative Gaussian curvature on the outermost surface showing a) one defect on either handle and b) two defects on one handle

It was found that, for $R_{sep} = 31.25\sigma$ and $r_t = 1000\sigma$, the mean energy per particle for the director configuration was -2.0609 and -2.0587 for one defect on each handle and both defects located on the same handle respectively. The energy difference between the two director configurations is an order of magnitude greater than that seen in Figure 7.3.3 for the difference in energy between two defects located on the inner or outermost surfaces.

7.4 CHIRAL NEMATIC DOUBLE TORI WITH PLANAR ANCHORING

Further to the nematic double tori discussed previously, the effect of chirality on the observed defect configuration is investigated. A series of simulations were run cooling slowly from the isotropic phase to a nematic phase at $T^*/T^*_{N-I} = 0.9$ for $R_{sep} = 37.5\sigma\ (R_{max} + R_{min})$, varying r_t and ε_c. The values of ε_c and the associated chiral nematic pitch lengths are detailed in Table 7.1.2.

In chiral nematic double tori with planar anchoring, the director twists along the handles of the system. As seen in chiral nematic single tori with planar anchoring (section 6.6.1), at the centre of the tube the director is running axially along the tube and as the distance from the centre of the tube increases the director twists until the maximum twist is seen at the surface. For both single and double tori systems, the amount of twist observed at the surface increases with increasing ε_c, *i.e.* decreasing pitch length.

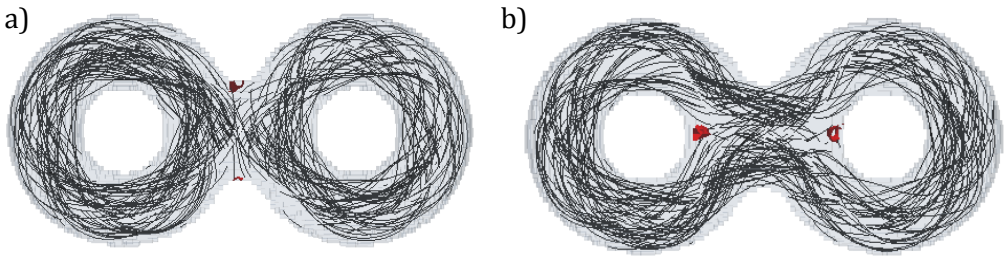

Figure 7.4.1 Two chiral nematic double tori with $\varepsilon_c = 0.12$ showing two *s*=-1 defects at a) the outermost surface and b) the innermost surface

In all the double tori systems with planar anchoring the total topological charge on the surface was equal to -2, in agreement with (7.1.1). For simulations of low chirality ($\varepsilon_c = 0.06$ and 0.12) similar director configurations were seen as for the non-chiral nematic double tori with planar anchoring consisting of two *s*=-1 at either the innermost surface around the inner rings of the tori (Figure 7.4.1a) or the outermost surface at the join between the two tori (Figure 7.4.1b).

As $\varepsilon_c$increases and the pitch length decreases, the defects become untethered from the surface and become axial defect lines of strength *s*=-1/2 through the chiral nematic bulk (Figure 7.4.2). The total topological surface defect charge in these systems is still -2 as each defect line has two points of strength *s*=-1/2 on the surface. These defects through the chiral nematic bulk appear wider at the surfaces than at the centre of the chiral nematic. As with the *s*=-1 defects, the two *s*=-1/2 defects in the centre were found to be either on-axis (Figure 7.4.2a) or off-axis (Figure 7.4.2b), however there was no obvious correlation to either r_t or R_{sep}.

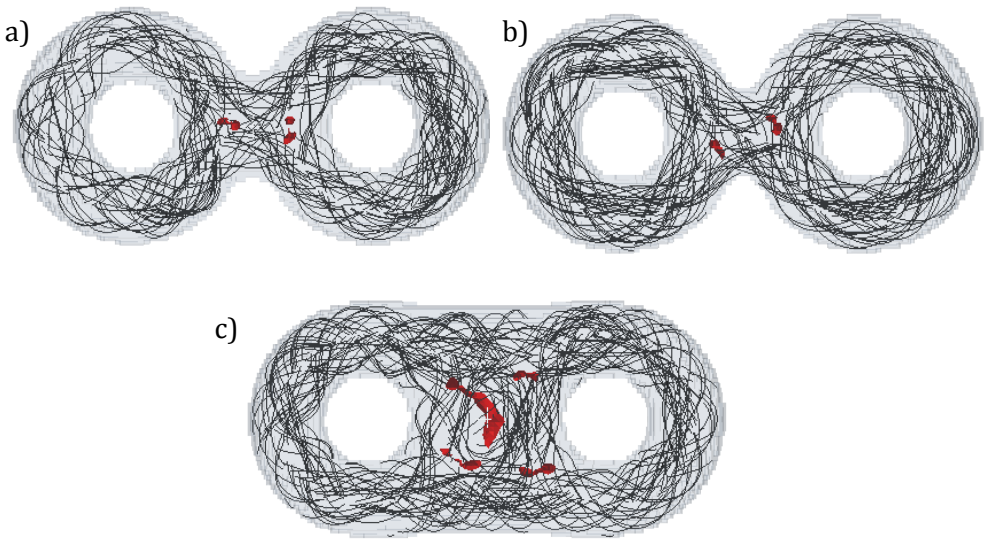

Figure 7.4.2 a) and b) show two *s*=-1/2 lines through the chiral nematic bulk on-axis and off-axis respectively. c) shows a system with no regions of negative Gaussian curvature on the outermost surface with one *s*=+1 and four *s*=-1/2 defects

For systems with no regions of negative Gaussian curvature on the outermost surface ($r_t = 1000\sigma$) at the highest chirality investigated a defect configuration consisting of one escaped *s*=+1 defect surrounded by four *s*=-1/2 defects on both the top and the bottom faces of the double torus was seen (Figure 7.4.2c), again the total topological charge was equal to -2 as required by (7.1.1) .The *s*=+1 defect is the centre of a helix that is formed at right angles to the surface which has been created to fill the space between a helix running

around both the handles and the outer edge of the double torus. The extra helix in the centre of the double torus is not seen for systems with regions of negative Gaussian curvature on the outermost surface as there is not enough space for the two helices around the handles to join and form a loop.

7.5 NEMATIC AND CHIRAL NEMATIC DOUBLE TORI WITH HOMEOTROPIC ANCHORING

In this section, both nematic and chiral nematic double tori with homeotropic anchoring are investigated. A series of simulations were performed varying R_{sep} and r_t, again cooled slowly over a period of 62500MC cycles from an isotropic to a nematic or chiral nematic phase. As for the chiral nematic systems with planar anchoring, the pitch lengths investigated for chiral nematic systems are as shown in Table 7.1.2.

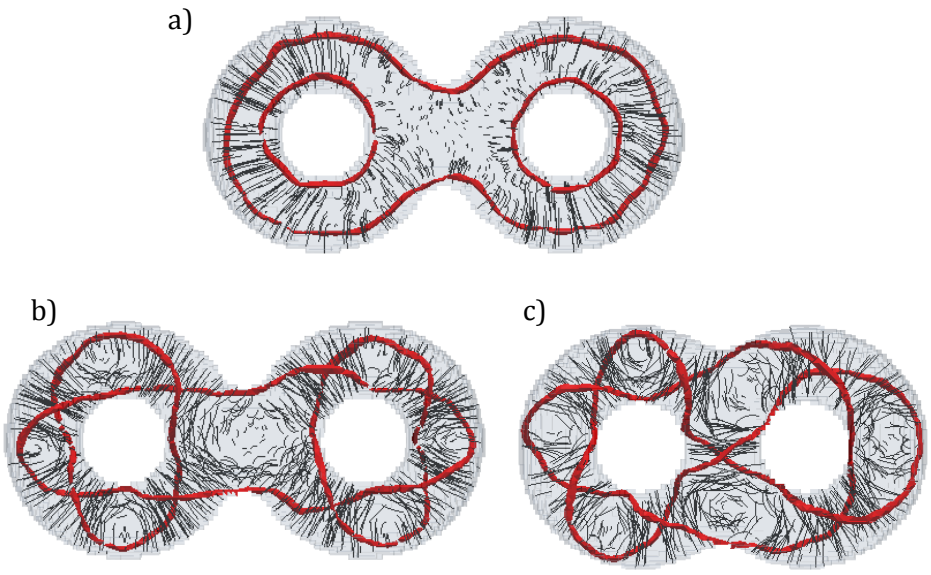

Figure 7.5.1 A double torus with homeotropic anchoring showing where a)$\varepsilon_c = 0$ with three *s*=+1/2 defect lines, b)$\varepsilon_c = 0.12$ with three *s*=+1/2 defect lines and c) $\varepsilon_c = 0.18$ with two *s*=+1/2 defect lines

For a single nematic torus with homeotropic anchoring two *s*=+1/2 disclination lines are observed on the outermost and innermost of the torus (section 6.6.2). In a nematic double

torus, three *s*=+1/2 disclination lines are also observed, one around the centre of each torus and a third around the outermost surface of the torus (Figure 7.5.1a). The resulting defect configuration for a nematic double torus with homeotropic anchoring can be thought of as the sum of two single tori where the outer disclination lines join in order to minimise the total defect length in the system.

In a single torus, the addition of chirality into the system causes the two *s*=+1/2 disclination lines to twist around one another to form a helix. The finite length of the torus decrees that the disclination lines must twist by $n\pi$, where *n* is an integer. For chiral nematic double tori systems with homeotropic anchoring, in an analogous manner the defects form a helix around both handles, again by multiples of $n\pi$. There is no correlation between the number of twist amount around each torus in a double torus system and *n* may be the same (Figure 7.5.1b) or different (Figure 7.5.1c). The value of *n* for each handle of the double tori systems for a given value of ε_c is consistent with that observed for the single tori systems.

7.6 Triple and Quadruple Tori

The following section now expands the research to triple and quadruple tori, or three and four handled systems. There are many ways of joining multiple tori and only four are considered here. The geometries considered are; a linear (Figure 7.6.1a) or triangular (Figure 7.6.1b) triple tori and a square or rectangular quadruple tori (Figure 7.6.1c).

As with the double tori systems, ghost tori are required to produce a smooth surface between the joined tori. The number of ghost tori used is dependent on the geometry of the systems, for example the triangular triple tori requires three ghost tori whereas the linear triple tori and both the quadruple tori systems studied here require four ghost tori. The number of ghost tori is equivalent to the number of regions of negative Gaussian curvature on the outermost surface.

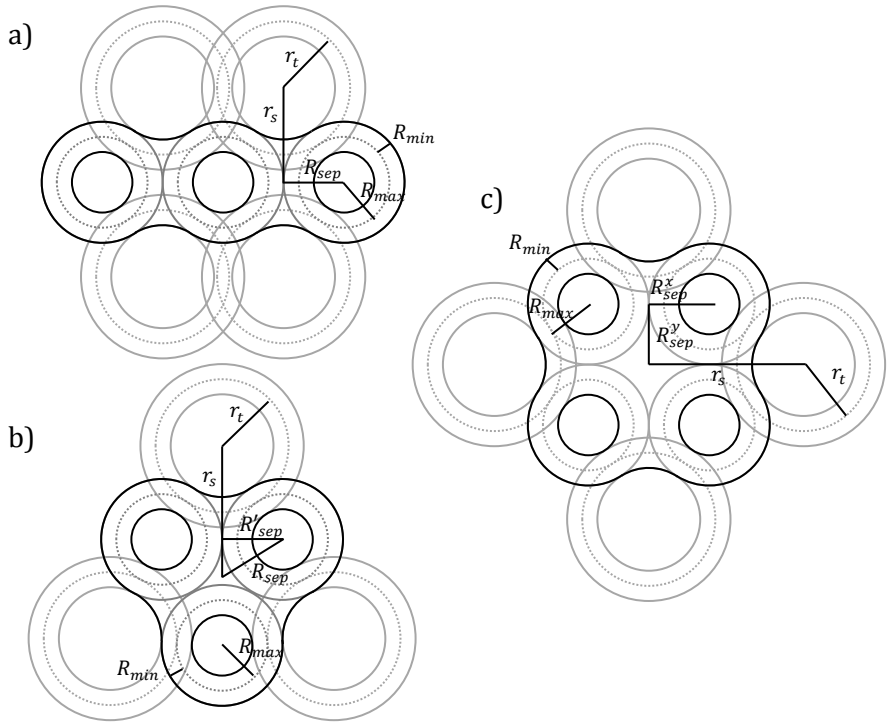

Figure 7.6.1 Schematics of a) a linear triple torus b) a triangular triple torus and c) a quadruple torus that when $R^x_{sep} = R^y_{sep}$is square and when $R^x_{sep} \neq R^y_{sep}$it is rectangular

The parameters used for the triple and quadruple torus systems are analogous to those used in the double torus simulations earlier in this chapter and are shown in Figure 7.6.1 for each system investigated. Again R_{max} and R_{min} are related to the single tori in each system and are 25σ and 12.5σ respectively. r_t and r_s are again related to the ghost tori with the same constraints on a r_t as shown in section 7.2. In the triple torus and square quadruple torus simulations, r_t and r_s are the same for all the ghost tori however in the rectangular quadruple torus simulations where $R^x_{sep} \neq R^y_{sep}$ the pairs of ghost tori opposite each other have the same r_t and r_s but adjacent ghost tori do not. As in the double torus simulations the parameters are dependent upon one another and the variables used in this section are R_{sep} , R^x_{sep} and R^y_{sep} in the quadruple tori systems.

In the triangular triple torus systems the separation from the centre of the simulation cell (R_{sep}) is not the separation between the centre of the single torus (R'_{sep}) as it is in the linear system and is related by

$$R'_{sep} = \frac{2R_{sep}}{\sqrt{3}} \quad (7.6.1)$$

In order for the triangular triple torus systems to be compared to the other systems investigated we shall report the systems in terms of R'_{sep}. In the quadruple torus systems there are two different separation variables, R^x_{sep} and R^y_{sep}, which are the separation between the centres of two tori in the *x* and *y* direction respectively. In square *4*-torus systems, $R^x_{sep} = R^y_{sep} = R_{sep}$.

Due to the large system size only the limits of r_t^{min} and $r_t \to \infty$ are investigated for two separations, $R_{sep} = 25\sigma(R_{max})$ and $37.5\sigma\ (R_{max} + R_{min})$. In the rectangular quadruple torus systems, $R^x_{sep} = 25\sigma\ (R_{max})$ and $R^y_{sep} = 37.5\sigma\ (R_{max} + R_{min})$ was investigated. Simulations were run with both planar and homeotropic anchoring for the values of ε_c shown in Table 7.1.2, simulating both a chiral and non-chiral nematic. Simulations were cooled slowly over 62500MC cycles from the isotropic phase to a nematic phase at $T^*/T^*_{N-I} = 0.9$.

7.6.1 *NEMATIC N-TORI WITH PLANAR ANCHORING*

The Euler characteristic of the system is dependent on the number of handles (7.1.1), with each additional handle contributing -2 to the Euler characteristic. The change in Euler characteristic (χ) means that for systems with planar anchoring, with each additional handle the total topological charge on the surface increases by -2, *i.e.* for a triple torus the total topological charge on the surface must equal -4 and for a quadruple torus, both square and rectangular, it must be -6.

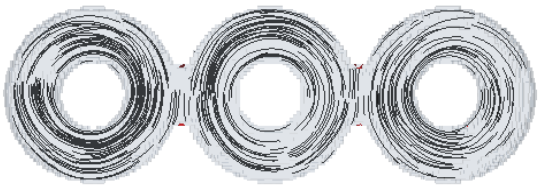

Figure 7.6.2 Linear triple tori showing four *s*=-1 defects with $r_t = r_t^{min}$

For all nematic systems with planar anchoring it was found that there were χ *s*=-1 defects located at areas of negative Gaussian curvature, either at the innermost surface on the rings of the torus or at the outermost surface at the join between two tori. It was found that the regions of negative Gaussian curvature at the outermost surface could only contain one *s*=-1 defect however there could be two or more *s*=-1 defects at the innermost surfaces.

For the linear triple tori systems with $r_t = r_t^{min}$, there were four areas that the defects could form on the outermost surface and defect configurations in which all four *s*=-1 defects are located at the joins between tori were seen (Figure 7.6.2).

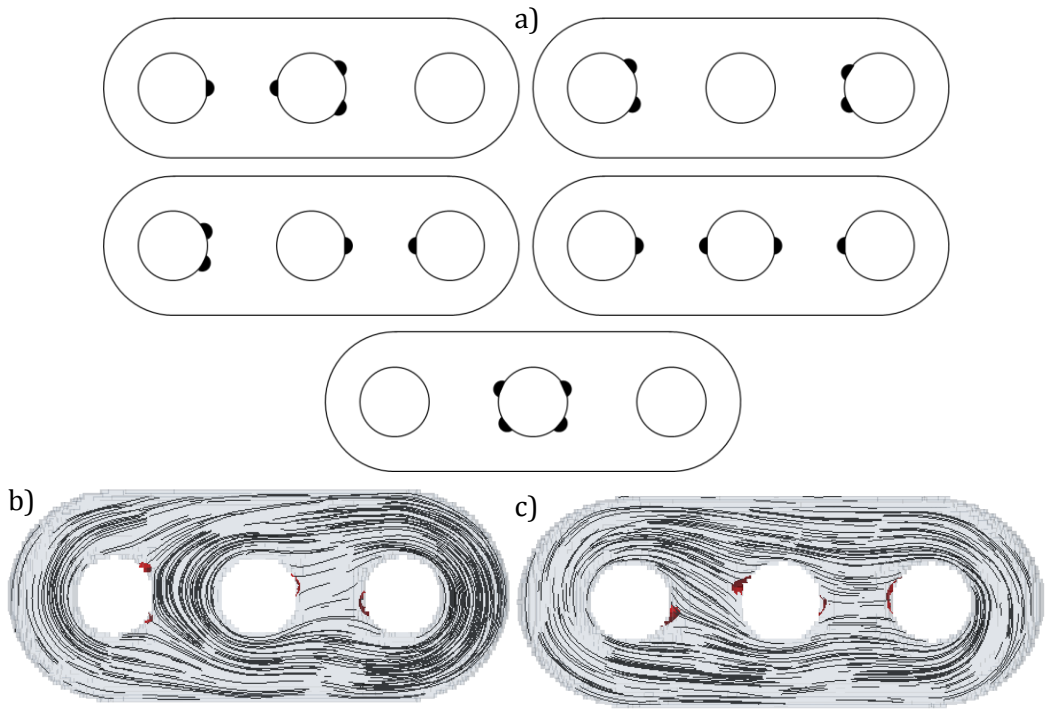

Figure 7.6.3 a) The five possible defect configurations for a linear triple torus where $r_t \to \infty$ with planar anchoring. b) and c) show the two most commonly observed defect configurations

For linear triple tori with no areas of negative Gaussian curvature on the outermost surface ($r_t \to \infty$), there are only three regions of negative Gaussian curvature meaning that one ring must have two (or more) defects present. There are five possible defect arrangements

in linear tori with $r_t \to \infty$, with those in which two holes have one defect and one hole two defects being observed in 90% of the simulations. The other defect configurations predicted are higher in energy as in all the distance between two (or more) defects is much smaller. In the two defect configurations observed, with two defects located at the centre hole (Figure 7.6.2c) or at one of the edge holes (Figure 7.6.2b), the energy difference was in the range of the fluctuations of the simulations and so it was not possible to calculate. However, due to the larger distance between defects when two are located at the centre hole this is likely to be lower in energy and was observed in 60% of the simulations. The presence of more than one defect configuration suggests that, once formed there is not enough energy present in the system for the defects to migrate to the lowest energy configuration.

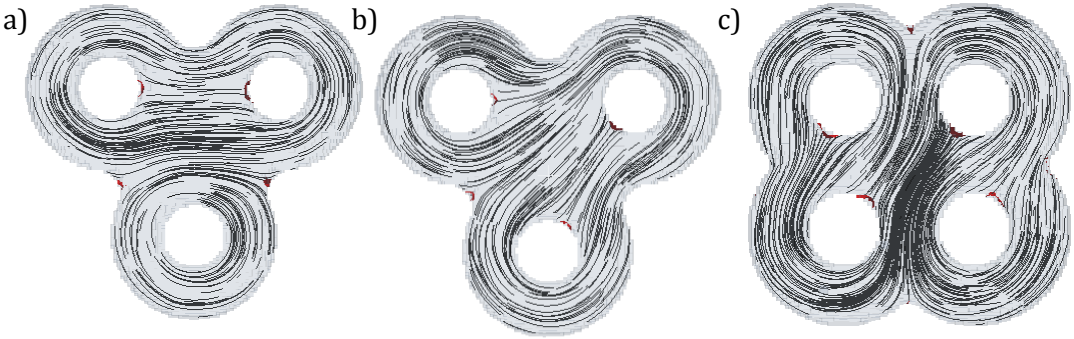

Figure 7.6.4 a) and b) show triangular triple tori showing two and one *s*=-1 defects at the outermost surface respectively and c) a square quadruple torus showing two *s*=-1 defects at the outermost surface

For triangular triple tori and quadruple tori where $r_t = r_t^{min}$ there are less regions of negative Gaussian curvature on the outermost surface than required to exclusively form the *s*=-1 defects at the join between tori. For the triangular triple torus, systems were seen with two (Figure 7.6.4a) or one (Figure 7.6.4b) *s*=-1 defects located at the outermost surface (leaving one or two joins between tori free) but there were no occurrences where a defect was located at each join as it is not possible to do this without introducing extra

defects into the system. The same is true for the quadruple torus systems with defect configurations with two (Figure 7.6.4c) or three defects located at the join between tori, leaving two or one joins defect free respectively.

For systems at the limit where $r_t \to \infty$, the defects all form at the holes of the tori as there are no regions of negative Gaussian curvature on the outermost surface of the systems, leading to two or more defects being located at a single hole. Whilst no defect configurations with more than two defects at any one hole were observed in the simulations run, it is possible to form a defect configuration in which there are three defects located at a single hole. However, the possible defect configurations with three defects on one hole are significantly higher in energy due to the decreased distance between defects. In quadruple tori, six *s*=-1 defects are required to fulfil the constraint on the total topological charge. The defect configuration observed comprised of two holes with two defects and two holes with one defect. The holes with two defects may be either adjacent or at diagonally opposite. Both cases were observed and, and as with the linear triple tori the the energy difference between the two defect configurations was within the energy fluctuation of the simulation and could not be calculated.

7.6.2 *CHIRAL NEMATIC N-TORI WITH PLANAR ANCHORING*

In chiral nematic systems with planar anchoring, as in the non-chiral nematic systems, the total topological charge was equal to the Euler characteristic, in triple tori χ=-4 and in quadruple tori χ=-6, in all cases. The effect of chirality on the triple and quadruple torus systems is similar to that seen for the chiral nematic double torus. For systems with low chirality ($\varepsilon_c = 0.06$) and a long associated pitch length (202σ), similar defect configurations were seen as for the non-chiral nematic case. That is, the required number of *s*=-1 defects were seen at areas of negative Gaussian curvature at either the innermost or outermost surfaces.

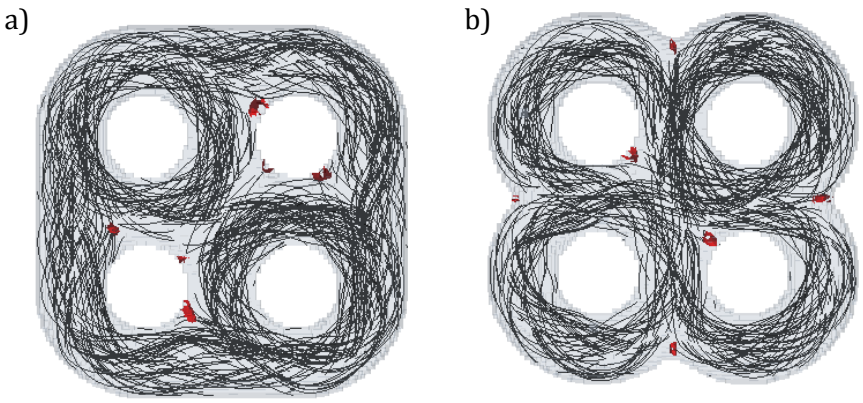

Figure 7.6.5 Chiral nematic quadruple tori with $\varepsilon_c = 0.12$ showing a) three defects on two holes and b) four defects on the outermost surface

At $\varepsilon_c = 0.12$ the defects become detached from the surface of the system and begin to move into the chiral nematic bulk as *s*=-1/2 lines. These lines conserve the total topological charge as each has two points of *s*=-1/2 at the surface of the system. In systems at this intermediate chirality, the defects are still slightly anchored to the surface and more defect configurations not seen for a non-chiral nematic are seen, including systems with three defects on one hole (Figure 7.6.5a) or defects at all regions of negative Gaussian curvature on the outermost surface (Figure 7.6.5b).

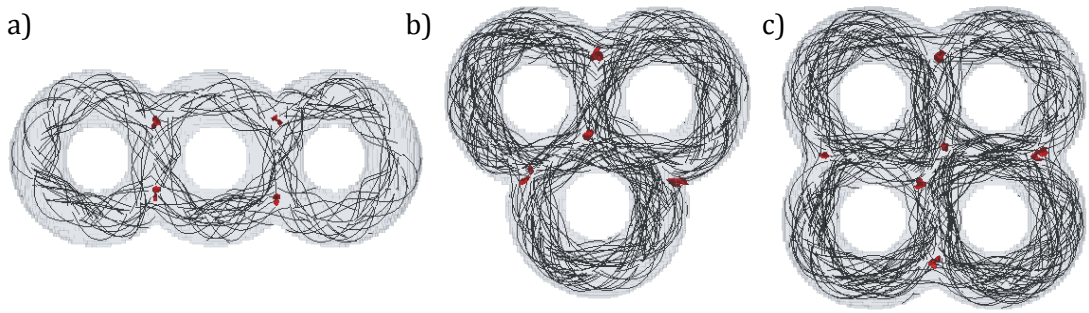

Figure 7.6.6 Chiral nematic systems with planar anchoring with *s*=-1/2 defects.

a) A linear triple torus, b) a triangular triple torus and c) a square quadruple torus

As ε_c continues to increase, the defects become fully detached from the surface and form an ordered structure maximising the distance between defects (Figure 7.6.6). The defect structure formed is independent on R_{sep} and r_t with the same defect configuration observed at both $r_t = r_t^{min}$ and $r_t \to \infty$. In the quadruple tori, the pair of defects at the centre can appear either on- or off- axis in an analogous manner to the defects observed in chiral nematic double tori with planar anchoring. Whilst it is not possible to calculate the energy difference between the on-axis and off-axis defect configurations, the configuration in which the defects off-axis was more commonly observed as the distance between the two defects is larger and so it is likely to be lower in energy than the on-axis defect configuration.

In the quadruple tori systems, at high chirality ($\varepsilon_c = 0.18 \text{ and } 0.24$) a novel defect configuration was seen with an additional *s*=+1 at the centre of the top and bottom of the surface surrounded by eight *s*=-1/2 defects, analogous to that seen in the double tori systems with $r_t = 1000\sigma$. The total topological charge was conserved by the addition of positive and negatively charged defects with the same total magnitude, leading to a total topological charge of -6. The *s*=+1 defects are located in the centre of a helix that perpendicular to the top and bottom surface of the system. The arrangement of the *s*=-1/2 defects around the centre differed in the square and rectangular quadruple tori.

The *s*=+1 defects were seen at lower chirality ($\varepsilon_c = 0.18$) for systems where $r_t \to \infty$ and $R_{sep} = 37.5\sigma$ in comparison to $R_{sep} = 25\sigma$ and/or $r_t = r_t^{min}$due to the increase in the volume at the centre of the system. A similar defect configuration was also seen for the triangular triple torus when $R'_{sep} = 37.5\sigma$ but not for the linear triple torus, as in the linear arrangement there is no larger volume between the join of three or more tori. It can be expected that in a linear torus with a large enough separation between tori and $r_t \to \infty$, at a high chirality two helices perpendicular to the top and bottom surfaces will form, one either side of the central hole in a manner analogous to that seen in double tori (Figure 7.4.2c).

7.6.3 *N-TORI WITH HOMEOTROPIC ANCHORING*

Nematic and chiral nematic triple and quadruple tori systems were also investigated with homeotropic anchoring. As in the single and double torus systems, *s*=+1/2 disclination lines were observed in all systems investigated.

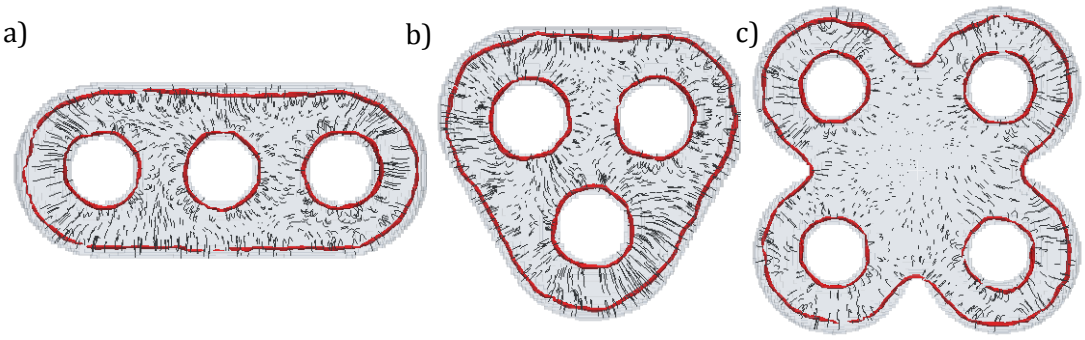

Figure 7.6.7 Nematic systems with homeotropic anchoring showing *g*+1 *s*=+1/2 defect lines, a)linear triple torus, b) triangular triple torus and c) square quadruple torus

In non-chiral nematic systems with homeotropic anchoring $g + 1$ *s*=+1/2 defect lines were observed where *g* is the number of handles. In all cases, one disclination line runs around the outside of the system with a disclination line circling each hole of the system (Figure 7.6.7). Again all the defects were located midway through the system in the *z*-direction, as observed for the single tori. In an analogous manner to the nematic double tori systems

with homeotropic anchoring, the defect arrangements can be thought of as the combination of *g* single tori with homeotropic anchoring with the outer defect lines joined to minimise the energy of the system.

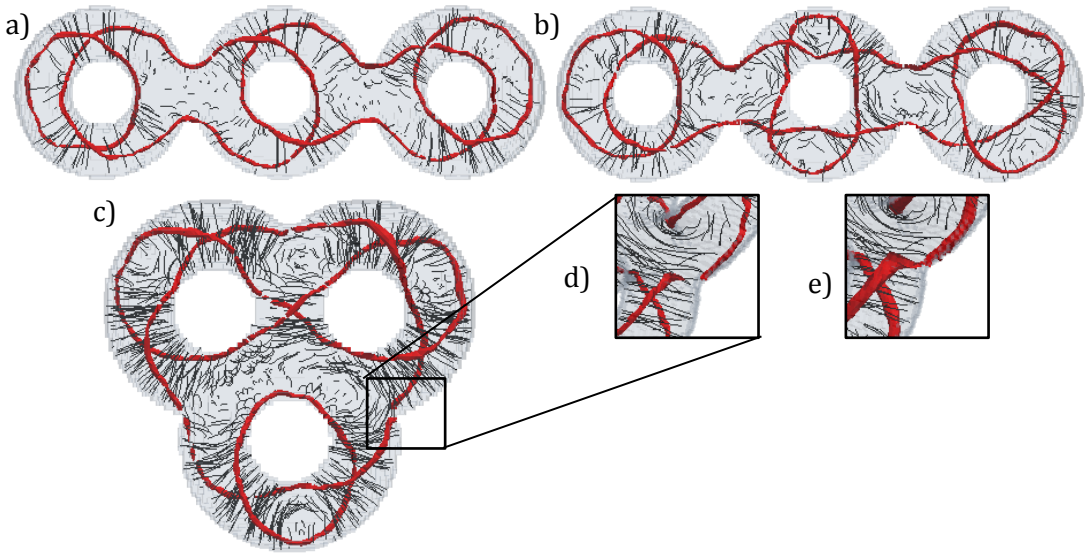

Figure 7.6.8 a) and b) are linear triple tori with homeotropic anchoring showing the same and differing values of *n* around each centre respectively. c) is a triangular triple torus with homeotropic anchoring. Inserts d) and e) the join between two tori and the defect line at

$$c_l = 0.12 \text{ and } 0.20 \text{ respectively}$$

Chiral nematic systems with homeotropic anchoring also show *s*=+1/2 defect lines. The intrinsic twist in the chiral nematic causes the disclination lines to twist around one another to form a helix which run round the handles of the system. The triple and quadruple tori systems can be thought of as joining of single tori components and as such, the defects must twist by $n\pi$ where *n* is an integer in order for the ends of the defects to meet and a closed ring to form. If the defects twist by an amount that isn't a multiple of π a discontinuity is produced which, due to the increased region of disorder, is much higher in energy.

The value of *n* round each handle is independent from the value of *n* found for the other handles in the system and may be the same (Figure 7.6.8a) or different (Figure 7.6.8b & c).

Whilst the lowest value of *n* for each handle is the same as it is dependent on ε_c, the energy difference between *n* and $n\pm1$ is very small (approximately 0.01 for single tori in section 6.6.2) and the energy needed to convert between *n* around each handle once the defects are formed is larger than the thermal energy of the simulation as, in order to convert between *n*, the disclination lines must break.

As observed in both single tori and double tori systems, as the pitch length of the chiral nematic decreases (*i.e.* ε_c increases), the value of *n* around each hole increases. As with the triple and quadruple tori with planar anchoring, it was not possible to calculate the energy difference between different defect configuations for the same value of ε_c as the energy difference was within the range of the energy fluctuations and could not be resolved.

The number of disclination lines in a system depends on *n* around each single torus centre. A chiral nematic linear triple torus with homeotropic anchoring can be thought of as an expansion of a chiral nematic double torus with homeotropic anchoring and both show very similar defect configurations. For chiral nematic linear triple tori with homeotropic anchoring the number of *s*=+1/2 defect lines (N_{def}) is equal to the number of *s*=+1/2 defect lines in a nematic system (*i.e.* $g+1$)minus the number of cases where *n* is odd.

$$N_{def} = 1 + g - n_{odd} \tag{7.6.2}$$

For example, for in the linear triple tori in Figure 7.6.8, in a) the defect rotates by 2π around each holes and so $n_{odd} = 0$ and $N_{def} = 4$ whereas in b) the defects rotate by $2\pi, 4\pi$ and 3π when looking from left to right and so $n_{odd} = 1$ and $N_{def} = 3$.

The formula for the number of *s*=+1/2 disclination lines only holds for linear triple tori but can be used as a guide for the other multiple tori systems investigated. In the triangluar triple torus systems with $r_t = r_t^{min}$, in the visualisations there appears to be a discontinuity in the defect lines at the areas of negative Gaussian curavature on the outermost surface

(Figure 7.6.8). By using a higher threshold for c_l (Figure 7.6.8e) it is possible to see that there is no break in the defect lines and the appearance may be due to the resoluation obtained using the cubic analysis cells with sides of 1.5σ.

In chiral nematic square quadruple torus systems with homeotropic anchoring the defect configuration seen was dependent on R_{sep}. In systems where $R_{sep} = 25\sigma$, the small

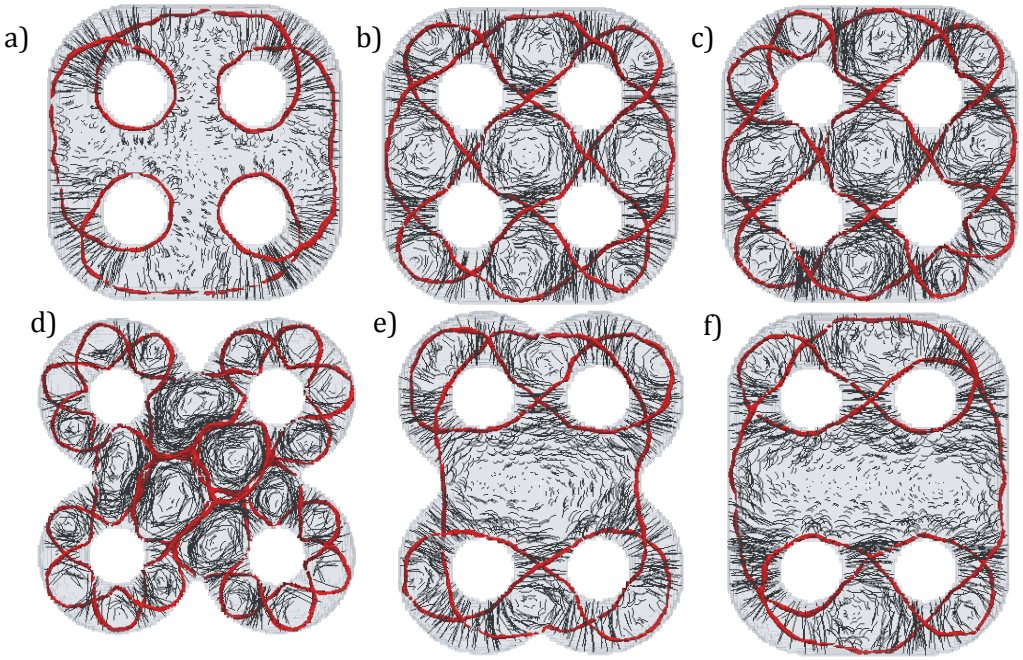

Figure 7.6.9 Chiral nematic quadruple tori with homeotropic anchoring showing *s*=+1/2 defects. a)-d) are square quadruple tori and e)&f) are rectangular quadruple tori.

distance between the holes leads to an ordered defect structure with the same value of *n* around each hole (Figure 7.6.9a-c). However, in systems where $R_{sep} = 37.5\sigma$, the larger distance between the holes meant that different values of *n* were seen in the same system.

In the chiral nematic rectangular quadruple torus systems with homeotropic anchoring the defect loops that circled two holes tended to enclose the two separated by the smaller distance (Figure 7.6.9e&f)whereas in the analogous square quadruple torus systems diagonally opposed holes tended to be enclosed by one loop (Figure 7.6.9b&c). The difference in defect structure between the rectangular and square quadruple tori shows

the competing contributions to the total energy of the system, in the rectangular case the length of the defect is the limiting factor whereas in the square case maintaining the helix of the director is the limiting factor.

At high chirality, the *s*=+1/2 defects join to form a network at the centre of the systems (Figure 7.6.9d). The formation of a network is more pronounced in systems with $R_{sep} = 37.5\sigma$ as there is a larger volume between the join of four tori in which this can occur.

7.7 Conclusion

In this chapter, the study has been expanded from a single torus in the previous chapter to systems comprised of two or more nematic and chiral nematic tori. Five different geometries were investigated; double tori, linear and triangular triple tori and square and rectangular quadruple tori, with both planar and homeotropic anchoring.

It was found that multi-handled bodies with planar anchoring have a total topological charge on the surface equal to $2(g-1)$, *i.e.* -2,-4 or -6 for double, triple and quadruple tori respectively (7.1.1).

For nematic systems with planar anchoring, the constraint on the total topological charge on the surface is fulfilled with the required number of *s*=-1 defects found in regions of maximum negative Gaussian curvature of which there are two distinct regions; either on the innermost surface of each handle or the outermost surface at the join of two tori. The location of the defects at these two distinct regions is highly dependent on both R_{sep} and r_t and systematic investigations with double tori systems showed a cross over in the most stable defect configuration from the two defects located at the join between two tori to the innermost surfaces for intermediate values of R_{sep} with the increase in r_t. At both small and large values of R_{sep}, the defects were more stable when located at the

innermost surface (section 7.3.2). The defect configuration with one defect located in either environment was unstable with respect to both the defects being located in the same environment.

The dependence on R_{sep} and r_t observed in double tori systems is likely to also apply to triple and quadruple tori systems, however the small energy difference meant it was not possible to investigate systematically in systems with more than two tori. In systems with no regions of negative Gaussian curvature on the outermost surface all the defects were located on the innermost surface (*e.g.* Figure 7.3.2 and Figure 7.6.2b & c). In double tori with no regions of negative Gaussian curvature on the outermost surface, the energy difference between one defect on either hole and two defects on one hole was investigated. The difference in energy was found to be an order of magnitude larger than that seen in the previous systematic study, explaining why for systems with regions of negative Gaussian curvature on the outermost surface, two defects on the same hole are not observed and unstable with one defect migrating to the other handle.

In triangular triple tori and quadruple tori systems, more *s*=-1 defects are required to fulfil the constraint on the total topological charge than there are regions of negative Gaussian curvature on the outermost surface between the join of two tori. For nematic systems no defect configurations with a defect at each join were seen as this would create additional defects in the director configuration (Figure 7.6.4).

For chiral nematic systems with a long associated pitch length ($\varepsilon_c = 0.06$), similar defect configurations were seen as in the nematic systems. As the chirality of the system increases, the defects detach from the surface and move into the bulk as *s*=-1/2 defect lines. The *s*=-1/2 defect lines still contribute -1 to the total topological charge at the surface as there are two regions of *s*=-1/2, one on the top and one on the bottom of the system. At intermediate values of ε_c, the defects are still weakly anchored to the surface and more

unusual defect configurations are found (Figure 7.6.5) that were not observed for a non-chiral nematic system.

For highly chiral systems investigated ($\varepsilon_c = 0.24$) a new defect configuration was seen consisting of a *s*=+1 line through the bulk surrounded by *s*=-1/2 lines (*e.g.* Figure 7.4.2c) which occurs as the helical twist of the director is perpendicular to the surface, with the *s*=+1 line at the centre of the helix. In all simulations, the total topological charge was equal to the Euler characteristic of the system.

Multi-handled nematic systems with homeotropic anchoring all formed $g + 1$ *s*=+1/2 disclination lines, with one around each hole and one around the outside of the system (*e.g.* Figure 7.5.1a and Figure 7.6.7).

In chiral nematic systems with homeotropic anchoring the director rotates by $n\pi$ where *n* is an integer around each handle as seen in a single torus in the previous chapter. The value of *n* for each handle in the system is dependent on ε_c but independent from the other handles in the system. The total number of defect lines in the systems varies with the director configuration and for linear multiple tori is equal to $g + 1 - n_{odd}$ (7.6.2) where n_{odd} is the number of handles that *n* is an odd number. For triangular triple tori and quadruple tori systems this relationship does not hold true but can be used as a general guide. In these systems, at high chirality ($\varepsilon_c = 0.24$) the *s*=+1/2 defect lines join to form a network which is most apparent when $R_{sep} = 37.5\sigma$ due to the increased volume at the join between three or four tori at centre of the system (Figure 7.6.9d).

The work in this chapter forms a substantial basis for further investigation into nematic and chiral nematic multiple torus systems. The findings in this chapter agree with those found experimentally[69] and may be used to predict director configurations in future work. The systems investigated and the results obtained may be applied to larger multiples and

systems where the single tori are of different sizes. It may be possible in future work to employ boundary conditions that allow for the investigation of larger system sizes, *e.g.* half of a double torus.

8 CONCLUSIONS

In this thesis, a simple off-lattice model was developed in order to investigate nematics with curved surfaces within confined geometries. The model was based on hard spheres with an embedded orientation vector at the centre of each particle. The simplicity of the developed model allows for large system sizes to be investigated.

The first system investigated was nematic shells, in which a water droplet is encompassed in a slightly larger nematic droplet. Nematic shells were first made experimentally by Fernandez-Nieves *et al.* in 2007[29] after Nelson's[28] paper proposed the presence of a tetrahedral arrangement of defects in systems with planar anchoring. For systems with planar anchoring, the total topological charge on the surface of the sphere must be equal to +2, as specified by the Poincaré-Hopf theorem. The nematic shells are thought to order through the defects, which for thin shells with a tetrahedral array of defects would lead to a lattice similar to that found in diamond on the micrometre scale. This would act as a photonic crystal and could find applications in light-modulating devices.

The research conducted in this thesis found that, for shells with planar anchoring at both surfaces, the number and position of the defects formed was highly dependent on the shell thickness. In thin shells where four *s*=+1/2 defects were observed which favoured a tetrahedral arrangement and for thick shells, a bipolar defect configuration was seen consisting of two *s*=+1 defects. A third defect configuration was occasionally observed for intermediate thickness shells consisting of one *s*=+1 and two *s*=+1/2 defects. The dependence of the defect configuration on the thickness of the nematic shell agrees with previous work, both experimental[31] and from simulation.[32]

An extended potential was employed to vary the ratio of the elastic constants, in particular K_3/K_1. It has been seen previously that as $K_3/K_1 \rightarrow \infty$, which occurs at the transition to a

smectic phase[39,40] or for systems of infinitely long hard rods[35], in thin shells the four defects migrate to a great circle arrangement. Unfortunately, for all the models employed in this work, the elastic constants were very similar and the tetrahedral arrangement was observed for all potentials investigated. For the **A** series of potentials, which favoured side-side interactions, the transition from thick to thin shell behaviour occurred in thinner shells than for potential **1**. Conversely, for the **B** series of potentials, which favoured end-end interactions, the transition from thick to thin shell behaviour occurred in thicker shells than potential **1**. The difference in the transition from thick to thin shell behaviour between the simpler potential and both the **A** and **B** series shows that it is not only the ratio of elastic constants that effects the defect configuration but also the subtle interactions between particles.

Future work, utilising a more complex model, may be possible to vary K_1/K_3 in order to observe the prevalence of the great circle arrangement of defects in thin shells. A model the encompasses the transition from a nematic to a smectic phase would also be of interest, as whilst this has been observed experimentally, no such simulations have been performed.

In experimental systems, due to a slight difference in density between the nematic and the inner water droplet, the nematic shells are not of uniform thickness and the inner droplet moves upwards, producing a thinning of the shell at the top of the system and a thickening at the bottom. Therefore, systems in which the inner water droplet was shifted were also investigated here. In thin shells with four defects, the defects migrate to the thinnest part of the shell, minimising the total length of the defects, overcoming the repulsion between defects.

The intermediate defect configuration, consisting of one *s*=+1 and two *s*=+1/2 defects which was occasionally observed in uniform thickness shell was stabilised in the non-

uniform thickness shells. The two *s*=+1/2 defects most commonly found at the thinnest part of the nematic shell. This finding is consistent with that found by Seyednejad *et al.*[32] and may explain the prevalence of the observed in experimental work.

Koning *et al.*[36] discuss the effect of shifting the inner water droplet in thick shells that form two *s*=+1 defects and suggest a transition from a 'deconfined' defect configuration with one defect at each pole to a 'confined' defect configuration in which both defects are located at the thinnest part of the nematic shell. In all simulations where two *s*=+1 defects were observed the defects were located at the poles of the droplet *i.e.* the 'deconfined' defect configuration. However, all the systems investigated here fall within the region where only the 'deconfined' configuration is expected. Future, larger simulations in which the inner water droplet is more shifted may show the predicted transition.

By employing a non lattice-based model, it was possible to investigate the effect of chirality on the defect configuration observed in nematic shells with planar anchoring. Chiral nematic shells have only very recently been fabricated experimentally by Uchida *et al.*[41]. In thin shells where four defects are observed for a non-chiral nematic, at a threshold chirality a transition from four *s*=+1/2 to two *s*=+1 defects is observed and a twisted bipolar director configuration is seen. The twist bipolar configuration is similar to that found in filled chiral nematic droplets for chiral nematics with a long pitch length.[26] In the chiral nematic shells fabricated by Uchida *et al.*, a single *s*=+2 defect is observed, which is similar to the Frank-Pryce structure found for filled chiral nematic droplets in which the pitch length of the chiral nematic is much smaller than the radius of the droplet. In the systems investigated here, the shortest chiral pitch length possible is still much longer than the shell thickness due to the loss of surface anchoring, which may explain why the twisted bipolar structure is observed rather than one with *s*=+2 defects.

Future work in which the pitch-length-to-shell-thickness ratio is decreased may show a second transition to a structure similar to that found experimentally. To this end, preliminary simulations of a confined nematic and chiral nematic between two spherical surfaces were performed. By not including the water particles, the ratio of shell thickness to pitch length can be increased as larger system sizes can be run. It was found that the chiral nematic between two spherical surfaces forms four *s*=+1/2 defects rather than the twisted bipolar structure observed in the systems with the water molecules included. The absence of the transition from four *s*=+1/2 to two *s*=+1 defects is due to the intrinsic difference in anchoring strengths. Future work is likely to show the same transition from four to two defects as found in the systems with a liquid crystal-water interface. The transition from four to two defects with decreasing pitch length gives a way to control and vary the number of defects that previously has been done by external forces, such as an electric field[37].

The use of solid colloidal particles with a nematic coating were then investigated with planar anchoring, allowing for the investigation of non-spherical particles. Preliminary simulations from an initial, non-spherical coating found that the nematic droplet became spherical, minimising the surface area and repulsive interactions between the mesogens and the water particles. As expected, the defect configurations observed for solid, spherical particles with a nematic coating are similar to those found in nematic shells with an internal water droplet. Due to the difference in anchoring strength, the thin shell behaviour consisting of four *s*=+1/2 defects is stabilised.

It was found that the defects form at the vertices of the large solid particle where the nematic coating is thinnest, thus minimising the length of the defects. For a tetrahedral particle, this leads to a stabilisation of the tetrahedral defect configuration seen in thin shells. However, due to the difference in the volumes of the spherical nematic droplet and

the large tetrahedral particle, four *s*=+1/2 were only seen for large tetrahedral particles. This behaviour suggests that by using tetrahedral particles with thin nematic coatings, the desired diamond-like lattice formed by self-assembly of the shells through the defects may be stabilised. Systems in which smaller tetrahedral particles were shifted from the centre of the nematic droplet were also investigated. It was found that, as with the non-uniform nematic shells, the three-defect configuration was stabilised with two *s*=+1/2 defects forming at the thinnest part of the nematic coating. Both the *s*=+1/2 defects and the *s*=+1 defect were found at the vertices of the tetrahedral particle.

Cubic and octahedral particles with a nematic coating were also investigated. As observed with the tetrahedral particles, for octahedral particles the increased bulk-like nature of the nematic droplet meant that a bipolar configuration was observed for all but the largest particles. Unlike the case with cubic and tetrahedral particles, defects were observed along the edges of the particle as there was no way of arranging the defects in a tetrahedron on the vertices of the octahedron.

For cubic particles with a nematic coating, four *s*=+1/2 defects were most commonly observed, with two defect arrangements in which each face has two defects associated with it. This may be thought of as analogous to the tetrahedral and great circle arrangements seen in nematic shells. Of these two defects arrangements, the great circle was observed approximately five times more often than the tetrahedral arrangement due to the high energy cost for the defects to move vertices once formed. Other defect arrangements with three defects associated with a face were occasionally observed but were higher in energy due to the closer proximity of the defects.

All the systems consisting of both mesogen and water particles highlight the sensitive nature of the resulting defect configuration on the mesogen-water potential. For all systems, the mesogen-water interaction is negative stabilising the nematic shells. Whilst for the nematic shells surrounding a water droplet the observed defect configuration was very similar for all anchoring strengths, for large solid particles with a nematic coating the resulting defect configuration was very sensitive to the constants used in the mesogen-water potential. For the solid particles with a nematic coating, most noticeably for the tetrahedral and octahedral particles, for $\varepsilon_{LC-W} \geq 1$ the nematic contracts away from the liquid crystal-water interface and the preferred surface anchoring is lost. As such, the mesogen-water potential used in chapter 5 is different to the previous chapters.

The resulting defect configuration is also highly dependent on the type of surface, *i.e.* whether the surface is solid, as found in the preliminary chiral nematic between confined between two spherical surface and between the large solid particle and the mesogens, or between water and mesogen particles. The different surfaces produce slightly different results, as evidenced by the solid sphere with a nematic coating or the confined chiral nematic shells. The solid surfaces have an intrinsic stronger anchoring due to the definition of the vector used to compute the dot product term in the anchoring potential. With solid surfaces, this vector is defined as the shortest distance between the centre of the mesogen particle and the wall, however for liquid crystal-water interfaces the vector used is the distance between the centre of the two particles. The difference in the defect configurations observed with solid or mesogen-water interfaces again highlight the sensitivity of the defect configurations on the type and strength of the surface anchoring.

Finally, nematic and chiral nematic droplets with handles were investigated. Whilst a sphere is the lowest energy geometry as a sphere minimises the surface area of the droplet and so the unfavourable mesogen-water interactions, other geometries, such as a torus,

may be stabilised by external forces. A torus is geometrically distinct from a sphere, that is it is not possible to transform continuously between a sphere and a torus. For a droplet with planar anchoring, the total topological charge on the surface is equal to its Euler characteristic. The Euler characteristic for a single torus is zero and a defect-free director configuration may therefore be observed.

Recently, Pairam *et al.*[69] fabricated both single and multiple nematic tori *via* microfluidic means and stabilised the droplets in a gel matrix, finding that the director configuration in nematic tori with planar anchoring twists spontaneously for fat tori. Kulic *et al.*[70] suggest that the transition to a twisted director configuration from an untwisted defect configuration observed for thin tori is governed by the ratio $^{K_2}/_{K_3}$, however the later paper by Pairam *et al,* suggests that the ratio of $^{K_{24}}/_{K_2}$, where K_{24} is the saddle-splay elastic constant, is of importance. Finding the aspect ratio of the tori where the transition from an untwisted to twisted director configuration occurs lead to a method to estimate the saddle-splay elastic constant, which is otherwise not possible. In all the simulations performed using the simple potential based on hard spheres, a twisted director configuration was not observed. By employing an external field, it was possible to extrapolate to a zero field strength for a twisted configuration and it was confirmed that the twisted state was higher in energy for the systems investigated.

In order to vary $^{K_2}/_{K_3}$, the Gay-Berne[76] potential was employed. Due to the increased computational cost of the Gay-Berne potential compared to the simple potential developed, sections (a quarter and an eighth) of a torus were simulated. As with the simpler potential, it was found that the twisted director configuration was unstable and higher in energy than the untwisted director configuration. The lack of twisted director configuration observed may be due to the limited sizes of torusinvestigated. Further

simulations of fat tori with small aspect ratios are needed to detect the transition to a twisted director configuration; however a smaller aspect ratio leads to a larger system size which is computationally more expensive.

For the first time the effect of chirality on the director configuration in both single and multiple tori was investigated. A twisted director configuration in nematic tori with planar anchoring was produced by the inclusion of chirality into the system.

Both nematic and chiral nematic tori with homeotropic anchoring were also investigated. Unlike nematic tori with planar anchoring, a defect-free director configuration is not possible. For non-chiral nematic tori, two s=+1/2 disclination lines are observed running around the inner and the outermost surface of the torus. The presence of the defect lines again highlights the different nature between a toroidal droplet and spherical shell, as for spherical nematic shells with homeotropic anchoring a defect-free director configuration is observed.

On the addition of chirality, the two disclination lines twist around one another to form a helical structure. Due to the closed nature of the system, the defect lines must twist by multiples of $n\pi$ where n is a positive integer. When n is even there are two s=+1/2 disclination lines, however when n is odd, one disclination line circles both the innermost and outermost surface of the torus.

Nematic and chiral nematic double, triple and quadruple tori were also investigated with both planar and homeotropic anchoring. With the addition of each handle, the Euler characteristic decreases by -2, as does the total topological charge on the surface of the droplet with planar anchoring. Therefore, the total topological charge on the surface is -2, -4 and -6 for double, triple and quadruple tori respectively. For non-chiral nematics with planar anchoring, the constraint on the total topological charge is fulfilled by the required

number of *s*=-1 at regions of negative Gaussian curvature, either at the join between two tori or the innermost surface of one of the handles.

For double tori, the relative stabilities of the locations of the two *s*=-1 defects were calculated. It was found that, for both small and large separations between the two tori, the defect configuration in which both defects are on the innermost surface was most stable. For intermediate separations between two tori, for small values of r_t, where r_t controls the curvature on the outermost surface at the join between two tori, the defect configuration in which the defects at the outermost surface is most stable. As r_t increases, there is a crossover in stability until the defect configuration in which both defects are located at the innermost surface is lowest in energy. Both these configurations where the defects are located in the same environment are lower in energy than when the defects are located in different environments.

For all *n*-fold chiral nematic tori with planar anchoring, as the pitch length decreases the defects detach from the surface and become *s*=-1/2 disclination lines through the bulk, linking the top and bottom of the system. The *s*=-1/2 disclination lines still fulfil the constraint on the total topological charge on the surface as each contributes two regions of *s*=-1/2 character on the surface. At very high chirality, a new defect configuration is often observed consisting of a *s*=+1 defect surrounded by the required number of *s*=-1/2 defects to fulfil the constraint on the total topological charge on both the top and bottom of the systems. The *s*=+1 defect is at the centre of a helix formed by the director.

For *n*-fold nematic tori with homeotropic anchoring, the resulting defect configuration may be thought of as the combination of *n* tori, with one *s*=+1/2 disclination line circling each hole and one running along the outermost surface of the system. As in the single tori, with the addition of chirality, the disclination lines twist around one another to form a helix. The value of *n* around each handle is independent from the other handles in the system.

By investigating different geometry nematic droplets with planar anchoring, the dependence of the total topological charge on the surface can clearly be seen, with a total charge of +2 on both surfaces observed in all spherical shells and the presence of a defect-free director configuration observed for a toroidal droplet. In all cases with defects present, the addition of chirality into the system causes a new, previously unobserved defect configuration to manifest. The new defect configurations observed for confined chiral nematic systems allow for the preservation of the chiral helix. At very high chirality, due to the potential employed, a transition to a more complex defect structure consisting of a s=+1 defect at the centre of the helix surrounded by the required number of s=-1/2 defects to fulfil the constraint on the total topological charge. The s=-1/2 defects are found between the helices of the liquid crystal phase.

ABBREVIATIONS AND DEFINITIONS

5CB	4-Cyano-4'-pentylbiphenyl, a commonly used mesogen
BP	Blue phase
c_l	One of three Westin Metrics used to identify the location of defects
ρ^*	Reduced density, defined in (2.4.1)
K_1	Splay elastic constant of a nematic phase
K_2	Twist elastic constant of a nematic phase
K_3	Bend elastic constant of a nematic phase
K_{24}	Saddle-splay elastic constant of a nematic phase
LC	Liquid Crystal
MC	Monte Carlo
MC cycle	*N* Monte Carlo trial moves where *N* is the number of particles in the simulation
N	Number of particles in the simulation
$\hat{\boldsymbol{n}}$	The director
σ	Particle diameter
T^*	Reduced temperature, defined in (2.4.2)
T_{N-I}	The nematic-isotropic transition temperature

REFERENCES

[1] P. J. Collings and M. Hird, *Introduction to Liquid Crystals: Chemistry and Physics*, CRC Press, London, **1997**, 312.

[2] H. Takezoe and Y. Takanishi, *Jpn. J. Appl. Phys., Part 1* **2006**, *45*, 597-625; G. Pelzl, S. Diele and W. Weissflog, *Adv. Mater.* **1999**, *11*, 707-724.

[3] D. Demus, J. Goodby, G.W. Gray, H. –W. Spiess and V. Vill, *Low Molecular Weight Liquid Crystals I*, Wiley-VCH, Wurzburg, **1998**, 530.

[4] P. G. de Gennes and J. Prost, *The Physics of Liquid Crystals*, Clarendon Press, Oxford, **1993**, 596.

[5] S. Jen, N. A. Clark, P. S. Pershan and E. B. Priestley, *Phys. Rev. Lett.* **1973**, *31*, 1552-1556.

[6] F. C. Frank, *Discuss. Faraday Soc.* **1958**, 19-28.

[7] D. A. Dunmur, *Physical Properties of Liquid Crystals: Nematics, Vol 25,* eds. D. A. Dunmur, A. Fukuda and G. R. Luckhurst, EMIS Datareview Series, INSPEC, IEE, London, **2000**, 216-229.

[8] S. Singh, *Liquid Crystals Fundamentals*, World Scientific Publishing Co. Pte. Ltd, Singapore, **2000**, 370-403.

[9] M. R. Fisch, *Liquid Crystals, Laptops and Life*, World Scientific Publishing Co Pte Ltd, Singapore, **2004**, 376.

[10] E. R. Waclawik, M. J. Ford, P. S. Hale, J. G. Shapter and N. H. Voelcker, *J. Chem. Educ.* **2004**, *81*, 854-858; Y. B. Sun, H. M. Ma, Z. D. Zhang and S. T. Wu, *J. Appl. Phys.* **2002**, *92*, 1956-1959.

[11] P. P. Crooker, *Chirality In Liquid Crystals.* eds. H.-S. Kitzerow and C. Bahr, Springer, York PA, **2001**, 186-222.

[12] H. Choi, H. Higuchi, Y. Ogawa and H. Kikuchi, *Appl. Phys. Lett.* **2012**, *101*, 131904.

[13] H. J. Coles and M. N. Pivnenko, *Nature* **2005**, *436*, 997-1000.

[14] Z. B. Ge, S. Gauza, M. Z. Jiao, H. Q. Xianyu and S. T. Wu, *Appl. Phys. Lett.* **2009**, *94*, 101104.

[15] D. Coates and G. W. Gray, *Phys. Lett. A* **1973**, *A 45*, 115-116.

[16] I. W. Stewart, *The Static and Dynamic Continuum Theory of Liquid Crystals*, Taylor and Francis, London, **2004**, 360.

[17] M. Kleman and O. D. Lavrentovich, *Philos. Mag.* **2006**, *86*, 4117-4137.

[18] N. D. Mermin, *Boojums all the way through: communicating science in a prosaic age*, Cambridge University Press, Cambridge, United Kingdom, **1990**, 332.

[19] J. M. Brake, A. D. Mezera and N. L. Abbott, *Langmuir* **2003**, *19*, 8629-8637.

[20] R. J. Carlton, C. D. Ma, J. K. Gupta and N. L. Abbott, *Langmuir* **2012**, *28*, 12796-12805.

[21] S. Sivakumar, J. K. Gupta, N. L. Abbott and F. Caruso, *Chem. Mater.* **2008**, *20*, 2063-2065.

[22] M. Vennes and R. Zentel, *Macromol. Chem. Phys.* **2004**, *205*, 2303-2311.

[23] A. Fernandez-Nieves, G. Cristobal, V. Garces-Chavez, G. C. Spalding, K. Dholakia and D. A. Weitz, *Adv. Mater.* **2005**, *17*, 680-684.

[24] A. Kilian, *Liq. Cryst.* **1993**, *14*, 1189-1198.

[25] O. D. Lavrentovich, *Liq. Cryst.* **1998**, *24*, 117-125.

[26] F. Xu and P. P. Crooker, *Phys. Rev. E* **1997**, *56*, 6853-6860.

[27] T. C. Lubensky and J. Prost, *J. Phys. II* **1992**, *2*, 371-382.

[28] D. R. Nelson, *Nano Lett.* **2002**, *2*, 1125-1129.

[29] A. Fernandez-Nieves, V. Vitelli, A. S. Utada, D. R. Link, M. Marquez, D. R. Nelson and D. A. Weitz, *Phys. Rev. Lett.* **2007**, *99*, 157801.

[30] V. Vitelli and D. R. Nelson, *Phys. Rev. E* **2006**, *74*, 021711.

[31] T. Lopez-Leon, V. Koning, K. B. S. Devaiah, V. Vitelli and A. Fernandez-Nieves, *Nature Phys.* **2011**, *7*, 391-394.

[32] S. R. Seyednejad, M. R. Mozaffari and M. R. Ejtehadi, *Phys. Rev. E* **2013**, *88*, 012508.

[33] M. A. Bates, *J. Chem. Phys.* **2008**, *128,* 104707

[34] S. Dhakal, F. J. Solis and M. O. de la Cruz, *Phys. Rev. E* **2012**, *86*, 011709.

[35] H. Shin, M. J. Bowick and X. J. Xing, *Phys. Rev. Lett.* **2008**, *101*, 037802.

[36] V. Koning, T. Lopez-Leon, A. Fernandez-Nieves and V. Vitelli, *Soft Matter* **2013**, *9*, 4993-5003.

[37] G. Skacej and C. Zannoni, *Phys. Rev. Lett.* **2008**, *100,* 197802.

[38] T. Lopez-Leon, M. A. Bates and A. Fernandez-Nieves, *Phys. Rev. E* **2012**, *86,* 030702.

[39] H. L. Liang, S. Schymura, P. Rudquist and J. Lagerwall, *Phys. Rev. Lett.* **2011**, *106*, 247801.

[40] T. Lopez-Leon, A. Fernandez-Nieves, M. Nobili and C. Blanc, *Phys. Rev. Lett.* **2011**, *106*, 247802.

[41] Y. Uchida, Y. Takanishi and J. Yamamoto, *Adv. Mater.* **2013**, *25*, 3234-3237.

[42] M. A. Bates, G. Skacej and C. Zannoni, *Soft Matter* **2010**, *6*, 655-663.

[43] S. Kralj, R. Rosso and E. G. Virga, *Soft Matter* **2011**, *7*, 670-683.

[44] I. Musevic and M. Skarabot, *Soft Matter* **2008**, *4*, 195-199.

[45] P. Poulin and D. A. Weitz, *Phys. Rev. E* **1998**, *57*, 626-637.

[46] J. D. Joannopoulos, S. G. Johnson, J. N. Winn and R. D. Meade, *Photonic Crystals: Molding the Flow of Light (Second Edition)*, Princeton University Press, Singapore, **2008**, 304.

[47] Y. Fink, A. M. Urbas, M. G. Bawendi, J. D. Joannopoulos and E. L. Thomas, *J. Lightwave Technol.* **1999**, *17*, 1963-1969.

[48] A. Blanco, E. Chomski, S. Grabtchak, M. Ibisate, S. John, S. W. Leonard, C. Lopez, F. Meseguer, H. Miguez, J. P. Mondia, G. A. Ozin, O. Toader and H. M. van Driel, *Nature* **2000**, *405*, 437-440.

[49] A. K. Raub and S. R. J. Brueck, *J. Vac. Sci. Technol., B* **2010**, *28*, C6O38-C36O44.

[50] Z. W. Mao, H. L. Xu and D. Y. Wang, *Adv. Funct. Mater.* **2010**, *20*, 1053-1074.

[51] C. K. Harnett, K. M. Satyalakshmi and H. G. Craighead, *Langmuir* **2001**, *17*, 178-182.

[52] M. Tasinkevych, N. M. Silvestre and M. M. T. da Gama, *New J.Phys.* **2012**, *14*, 073030.

[53] H. Stark, *Phys. Rep.* **2001**, *351*, 387-474.

[54] Y. Kimura, K. Takahiro, K. Kita and N. Kondo, *J. Phys. Soc. Jpn* **2012**, *81*, SA007.

[55] I. Musevic, M. Skarabot, U. Tkalec, M. Ravnik and S. Zumer, *Science* **2006**, *313*, 954-958.

[56] F. E. Mackay and C. Denniston, *Europhys. Lett.* **2011**, *94*, 50004.

[57] I. Musevic, *Phil.l Trans. R. Soc. A* **2013**, *371*, 20120266.

[58] S. C. Glotzer and M. J. Solomon, *Nat. Mater.* **2007**, *6*, 557-562.

[59] F. R. Hung and S. Bale, *Mol. Simul.* **2009**, *35*, 822-834.

[60] P. M. Phillips, N. Mei, L. Reven and A. Rey, *Soft Matter* **2011**, *7*, 8592-8604.

[61] C. P. Lapointe, T. G. Mason and I. I. Smalyukh, *Science* **2009**, *326*, 1083-1086.

[62] J. Dontabhaktuni, M. Ravnik and S. Zumer, *Soft Matter* **2012**, *8*, 1657-1663.

[63] C. P. Lapointe, K. Mayoral and T. G. Mason, *Soft Matter* **2013**, *9*, 7843-7854.

[64] Q. K. Liu, B. Senyuk, M. Tasinkevych and I.I. Smalyukh, *Proc. Natl. Acad. Sci. U.S.A.,* **2013**, *110*, 9231-9236.

[65] M. S. Atiyah, Paul, *Milan J. Math.* **2003**, *71*, 33-58.

[66] M. Buckley, F. Bernard and F. Veron, *American Physical Society Meeting, Division of Fluid Dynamics*, Long Beach, **2010**.

[67] N. V. Hud, M. J. Allen, K. H. Downing, J. Lee and R. Balhorn, *Biochem.Biophys. Res. Commun.* **1993**, *193*, 1347-1354.

[68] E. Pairam and A. Fernandez-Nieves, *Phys. Rev. Lett.* **2009**, *102*. 234501

[69] E. Pairam, J. Vallamkondu, V. Koning, B. C. van Zuiden, P. W. Ellis, M. A. Bates, V. Vitelli and A. Fernandez-Nieves, *Proc. Natl. Acad. Sci. U.S.A* **2013**, *110*, 9295-9300.

[70] I. M. Kulic, D. Andrienko and M. Deserno, *Europhys. Lett.* **2004**, *67*, 418-424.

[71] J. Stelzer and R. Bernhard. cond-mat/0012394, **2000**.

[72] L. Onsager, *Ann. N. Y. Acad. Sci.* **1949**, *51*, 627-659.

[73] W. Maier and A. Saupe, *Z. Naturforsch., A: Phys. Sci.* **1959**, *14*, 882-889.

[74] S. Riniker, J. R. Allison and W. F. van Gunsteren, *Phys. Chem. Chem.Phys.* **2012**, *14*, 12423-12430.

[75] M. R. Wilson, *Int. Rev. Phys. Chem.* **2005**, *24*, 421-455.

[76] J. G. Gay and B. J. Berne, *J. Chem. Phys.* **1981**, *74*, 3316-3319.

[77] P. A. Lebwohl and G. Lasher, *Phys. Rev. A* **1972**, *6*, 426-429.

[78] G. R. Luckhurst and C. Zannoni, *Nature* **1977**, *267*, 412-414.

[79] D. Frenkel, *J. Phys. Chem.* **1987**, *91*, 4912-4916.

[80] P. Bolhuis and D. Frenkel, *J. Chem.Phys.* **1997**, *106*, 666-687.

[81] M. A. Bates and D. Frenkel, *J. Chem. Phys.* **2000**, *112*, 10034-10041.

[82] M. P. Allen, *J. Chem. Phys.* **2000**, *112*, 5447-5453.

[83] P. J. Camp and M. P. Allen, *Physica A* **1996**, *229*, 410-427.

[84] A. Speranza and P. Sollich, *J. Chem. Phys.* **2002**, *117*, 5421-5436; G. Odriozola, *J. Chem. Phys.* **2012**, *136*, 134505.

[85] D. J. Cleaver, C. M. Care, M. P. Allen and M. P. Neal, *Phys. Rev. E* **1996**, *54*, 559-567.

[86] G. R. Luckhurst and P. S. J. Simmonds, *Mol. Phys.* **1993**, *80*, 233-252.

[87] M. A. Bates and G. R. Luckhurst, *J. Chem. Phys.* **1999**, *110*, 7087-7108.

[88] U. Fabbri and C. Zannoni, *Mol. Phys.* **1986**, *58*, 763-788.

[89] C. Chiccoli, P. Pasini, G. Skacej and C. Zannoni, *Mol. Cryst. Liq. Cryst.* **2005**, *429*, 255-264.

[90] N. Metropolis, A. W. Rosenbluth, M. N. Rosenbluth, A. H. Teller and E. Teller, *J. Chem. Phys.* **1953**, *21*, 1087-1092.

[91] M. P. Allen and D. J. Tildesley, *Computer Simulation of Liquids*, Clarendon Press, Ipswich, **1989**, 408.

[92] A. C. Callan-Jones, R. A. Pelcovits, V. A. Slavin, S. Zhang, D. H. Laidlaw and G. B. Loriot, *Phys. Rev. E* **2006**, *74*, 061701.

[93] C. F. Westin, S. Peled, H. Gubjartsson, R. Kikinis and F. A. Jolesz *, Proceedings 5th Annual ISMRM,* **1997** 1742.

[94] W. J. Gossens, *Mol.Cryst. Liq. Cryst.* **1971**, *12*, 237-244.

[95] S. Varga and G. Jackson, *Chem. Phys. Lett.* **2003**, *377*, 6-12.

[96] E. G. Noya, C. Vega and E. de Miguel, *J. Chem. Phys.* **2008**, *128*, 154507.

[97] M. P. Allen, M. A. Warren, M. R. Wilson, A. Sauron and W. Smith, *J. Chem. Phys.* **1996**, *105*, 2850-2858.

[98] P. A. C. O'Brien, M. P. Allen, D. L. Cheung, M. Dennison and A. Masters, *Soft Matter* **2011**, *7*, 153-162.

[99] J. Saha and M. Saha, *Mol. Simul.* **1997**, *19*, 227-235.

[100] T. Lopez-Leon and A. Fernandez-Nieves, *Colloid Polym. Sci.* **2011**, *289*, 345-359.

[101] R. Ondriscrawford, E. P. Boyko, B. G. Wagner, J. H. Erdmann, S. Zumer and J. W. Doane, *J. Appl. Phys.* **1991**, *69*, 6380-6386.

[102] M. V. Kurik and O. D. Lavrentovich, *Mol. Cryst. Liq. Cryst.* **1982**, *72*, 239-246; J. Bezic and S. Zumer, *Liq.Cryst.* **1992**, *11*, 593-619; D. Sec, T. Porenta, M. Ravnik and S. Zumer, *Soft Matter* **2012**, *8*, 11982-11988.

[103] J. P. Hansen and I. R. McDonald, *Theory of Simple Liquids*, Academic Press Inc, London, **2006**, 428.

[104] C. Williams, Pieranski.P and P. E. Cladis, *Phys. Rev. Lett.* **1972**, *29*, 90-92.

[105] Lmasis1 in *Image:Tori.gif*, from http://mathforum.org/mathimages/index.php/Image:Tori.gif, **2009**, access 20/11/2013.

[106] G. De Luca and A. D. Rey, *J. Chem.Phys.* **2007**, *127*, 104902.

[107] I. Vilfan, M. Vilfan and S. Zumer, *Phys. Rev. A* **1991**, *43*, 6875-6880.

[108] H. G. Flegg, *From Geometry to Topology*, The English Universities Press Limited, London, **1974**, 1

[109] T. Frankel, *The Geometry of Physics: An Introduction*, Cambridge University Press, Cambridge, **2009**, 241

[110] M. J. Bowick and L. Giomi, *Adv. Phys.* **2009**, *58*, 449-563.